Michihiko Nagumo

Fundamentals of Hydrogen Embrittlement

Springer

Fundamentals of Hydrogen Embrittlement

Michihiko Nagumo

Fundamentals of Hydrogen Embrittlement

Springer

Michihiko Nagumo
Professor Emeritus
Laboratory for Materials Science
and Technology
Waseda University
Tokyo
Japan

ISBN 978-981-10-0160-4 ISBN 978-981-10-0161-1 (eBook)
DOI 10.1007/978-981-10-0161-1

Library of Congress Control Number: 2015960841

Printed on acid-free paper

This Springer imprint is published by SpringerNature
The registered company is Springer Science+Business Media Singapore Pte Ltd.

Preface

Hydrogen embrittlement or degradation of mechanical properties by hydrogen is a latent problem for structural materials. The problem is serious particularly for high-strength steels, and its importance is increasing with recent needs for hydrogen energy equipment.

Hydrogen embrittlement has been studied for many decades, but its nature is still an unsettled issue. Two reasons are most likely: one is its interdisciplinary attribute covering electrochemistry, materials science, and mechanics, making comprehensive understanding difficult. The other is experimental difficulty in detecting hydrogen behaviors directly. Hydrogen, the lightest element on the periodic table, is mobile and insensitive to external excitations. Coupled with normally very low concentrations of hydrogen, information on its states in materials is limited and most notions must remain speculative about the function of hydrogen. However, recent remarkable advances in experimental techniques in analyses of hydrogen states and of microstructures of materials are unveiling the entity of embrittlement and stimulating new aspects on the mechanism of hydrogen embrittlement. Now is the time to put in order diverse results and notions on hydrogen embrittlement and to prepare the direction to establish principles for materials design and usage against hydrogen problems.

This book provides students and researchers engaging in hydrogen problems with a comprehensive view on hydrogen embrittlement, reviewing previous studies and taking in recent advances. Hydrogen effects must be considered along operating principles in each field, and basic rather than phenomenological stances are adopted in referring to the literature. Emphases are put on experimental facts, but their meanings rather than phenomenological appearance are paid particular attention. Experimental facts are noticed on adopted conditions since the operating mechanism of hydrogen might differ by materials and environments. For theories, assumptions and premises employed are given attention so as to examine their versatility.

Consecutive rather than fragmental setup of contents is attempted so as to facilitate readers' systematic understanding of the problem. The interdisciplinary attribute of the subject requires an understanding of elementary concepts in the wider field. The task demands textbooks for each field, but brief descriptions of fundamental ideas are presented when necessary.

This book consists of roughly two parts. The first part, from Chaps. 1, 2, 3, 4, and 5, covers basic behaviors of hydrogen in materials after the entry into materials, and the second part, from Chaps. 6, 7, 8, 9, and 10, deals with characteristics of the degradation of mechanical properties and fracture caused by hydrogen.

I am pleased to acknowledge my colleagues, particularly my former students at Waseda University, many of whom are coauthors of my works. I also appreciate works by Prof. K. Takai of Sophia University in devising ingenious methods to clarify the function of hydrogen in embrittlement.

A book of the same title in Japanese was published by Uchida Rokakuho Publishing, Tokyo, Japan, in 2008. The present book fully revised and reorganized the former one, removing some of its contents and adding recent advances. I would like to acknowledge the courtesy of Uchida Rokakuho for permitting the publication of this new book in the present form.

Michihiko Nagumo

Contents

Chapter 1
Solid Solution

1.1 Solubility

Hydrogen that brings about degradation of metallic materials comes from environments. Hydrogen adsorbs on the surface of metal in the form of H_2 molecule or H_3O^+ ion, dissociates to atoms, and diffuses into the bulk. Hydrogen atoms locate at various sites in metals with respective energies at sites as schematically shown in Fig. 1.1. The role of hydrogen in embrittlement is the central subject in this book, and interactions of hydrogen with various lattice defects are of crucial importance. Hydrogen atoms in solid solution, i.e., at interstitial sites of the regular lattice, are only a part of the total hydrogen atoms in most cases at thermal equilibrium, but interstitial sites are dominating in the number and control the transport and partition of hydrogen at various trap sites.

The temperature dependence of the solid solubility θ of hydrogen in various metals in hydrogen gas of 0.1 MPa are compared in Fig. 1.2 [1]. The negative slope in the Arrhenius plot for iron means an endothermic reaction for hydrogen absorption, i.e., the energy of hydrogen in solid solution is higher than that in hydrogen molecule as Fig. 1.1 indicates. It is in contrast with Ti and V that have higher affinities with hydrogen than Fe. The amount of absorbed hydrogen in iron at high temperatures is readily measured by chemical analysis. Thus, determined solid solubility data for pure iron under hydrogen gas environments above 300 °C are shown in Fig. 1.3 [2]. The ordinate denotes $\boldsymbol{\theta}$ in atomic ratio normalized by $\sqrt{p}$, where p is the hydrogen gas pressure in the unit of 0.1 MPa. Solubility data at lower temperatures are shown in Sect. 2.1 concerning trapping of hydrogen in lattice defects.

In Fig. 1.3, the level of $\boldsymbol{\theta}$ in face-centered cubic (fcc) $\boldsymbol{\gamma}$-iron is higher than that in body-centered cubic (bcc) $\boldsymbol{\alpha}$-iron, and a slight departure from the Arrhenius plot appears at temperatures lower than about 500 °C. The departure was discussed to originate in simultaneous occupations of tetrahedral and octahedral sites in α-iron [2]. Definitive values of $\boldsymbol{\theta}$ in $\boldsymbol{\alpha}$-iron in the room temperature regime are few, and

M. Nagumo, *Fundamentals of Hydrogen Embrittlement*,
DOI 10.1007/978-981-10-0161-1_1

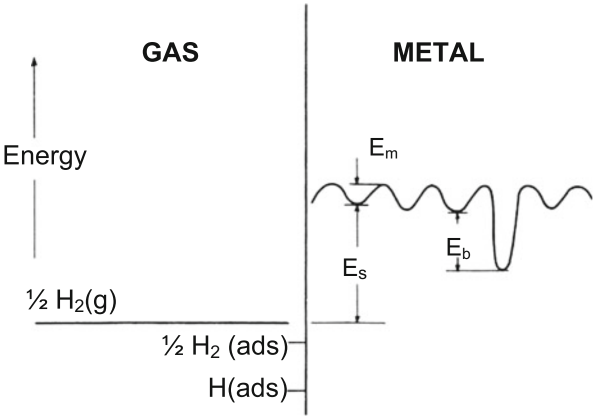

Fig. 1.1 Energies of hydrogen in gas-metal equilibria. E_s, energy of solid solution; E_m, migration energy; E_b, trap binding energy

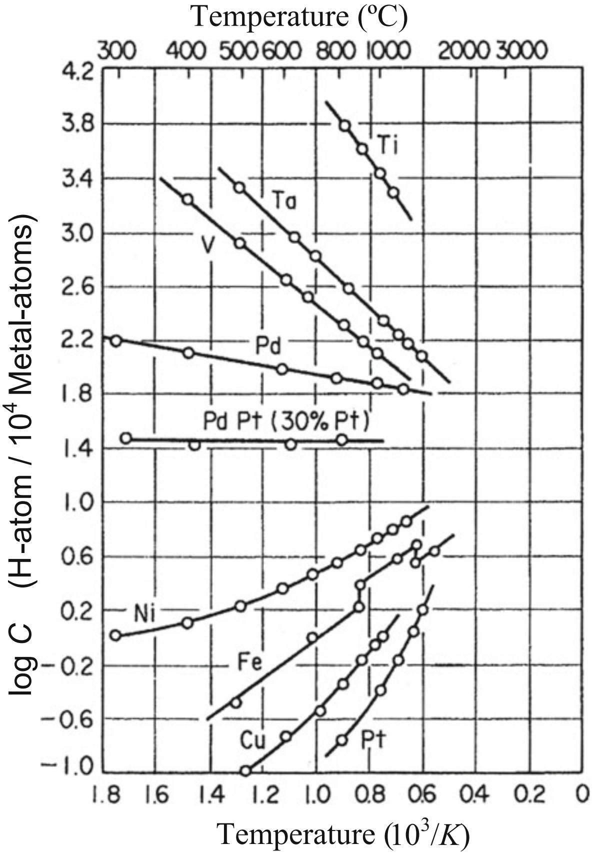

Fig. 1.2 Temperature dependence of hydrogen solubility in various metals in equilibrium at 0.1 MPa hydrogen gas (Huang et al. [1]. Reprinted with permission from The Japan Inst. Metals)

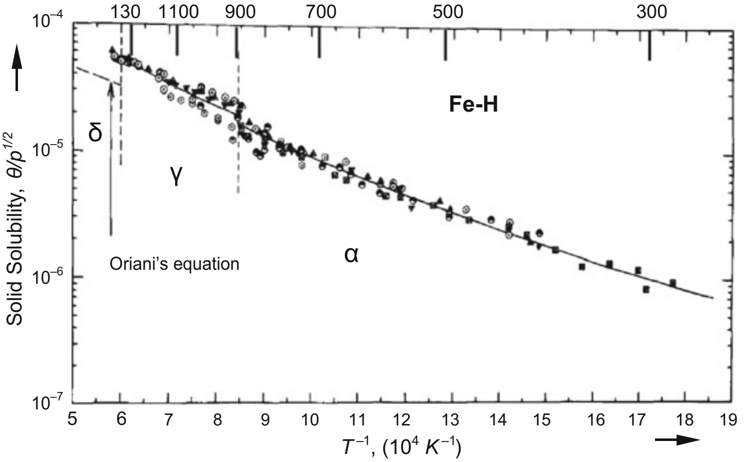

Fig. 1.3 Solid solubility of hydrogen in iron above 300 °C (Different marks are by literatures in the original paper. Da Silva et al. [2])

Hirth collected reliable data and expressed θ (in atomic ratio) in hydrogen gas of pressure p (in 0.1 MPa) in the form

$$\theta = 0.00185\sqrt{p}\,\exp\left(-3440/T\right) \tag{1.1}$$

with T in Kelvin [3]. The heat of solution of hydrogen in α-iron obtained from the temperature dependence of θ is 28.6 kJ/mol-H.

The $\sqrt{p}$ dependence of θ is known as Sieverts' law. It is originally an experimental relation for diatomic molecular gases, but it is also derived from thermodynamics. The entry of hydrogen into metal is initiated by the dissociation of adsorbed hydrogen molecules on the metal surface followed by the diffusion of hydrogen atoms into the metal. For the equilibrium reaction,

$$\frac{1}{2}H_2 \rightleftarrows H_{\mathrm{sol}}\,, \tag{1.2}$$

where the chemical potential μ is equal in both sides, i.e.,

$$\frac{1}{2}\mu_{H_2} = \mu_{H_{\mathrm{sol}}}. \tag{1.3}$$

Expressing μ in terms of the value at the standard state, μ^0, and the activity of hydrogen, a, in the form of

$$\mu = \mu^0 + RT \ln a, \tag{1.4}$$

where R is the gas constant, the change of the Gibbs energy associated with the absorption is written as

$$-\Delta G^0 = \frac{1}{2}\mu^0_{H_2} - \mu^0_{H_{\text{sol}}} = RT \ln \frac{a_{H_{\text{sol}}}}{a^{1/2}_{H_2}}. \tag{1.5}$$

Since

$$\Delta G^0 = \Delta H^0 - T\Delta S^0, \tag{1.6}$$

where H and S denote respectively enthalpy and entropy, Eq. (1.5) is rewritten as

$$a_{H_{\text{sol}}} = a^{1/2}_{H_2} \exp\left(-\frac{\Delta H^0}{\mathrm{R}T}\right) \exp\left(\frac{\Delta S^0}{\mathrm{R}}\right) \tag{1.7}$$

leading to the form of Sieverts' law.

It is to be noticed that the hydrogen concentration is expressed in terms of activity a and thus is related to pressure in terms of fugacity f:

$$a = \frac{f}{f^0} = \frac{\varphi p}{\varphi^0 p^0}, \tag{1.8}$$

where φ is the fugacity coefficient and the superscript "^{0}" denotes the standard state. Accordingly, for the estimation of the equilibrium hydrogen concentration using Eq. (1.1), p should be replaced by f. The conversion is important in practice for high pressures, since φ increases with p. Calculated values of φ are tabulated in Ref. [4], e.g., 1.06, 1.41 and 2.06 for p of 10, 50 and 100 MPa hydrogen gas at 300 K, but the values vary according to the equation of state employed for the calculation.

The equilibrium hydrogen concentration in α-iron at room temperature expected from Eq. (1.1) is very small, *ca* 2×10^{-8} (in atomic ratio), in 0.1 MPa hydrogen gas. Then, normally observed hydrogen concentrations of the order of mass ppm in ferritic steels are mostly the amount of trapped hydrogen in various lattice defects except under nonequilibrium situations.

The solubility of hydrogen in steels is substantially altered by alloying. In austenitic stainless steels, the heat of solution of hydrogen is about 16 kJ/mol-H [5], much less than that in pure γ-iron. Solubility data for stainless steels are shown in Fig. 1.4 [5]. Higher solubilities in austenitic stainless steels than those in ferritic stainless steels are due not only to the crystal structures but also to alloying elements such as Ni and Cr. Most data in Fig. 1.4 were obtained by permeation experiments. It is to be noticed that very inhomogeneous distributions of hydrogen are often present in austenitic stainless steels because of the low diffusivity of hydrogen as described in Sect. 4.1. At elevated temperatures, the increased

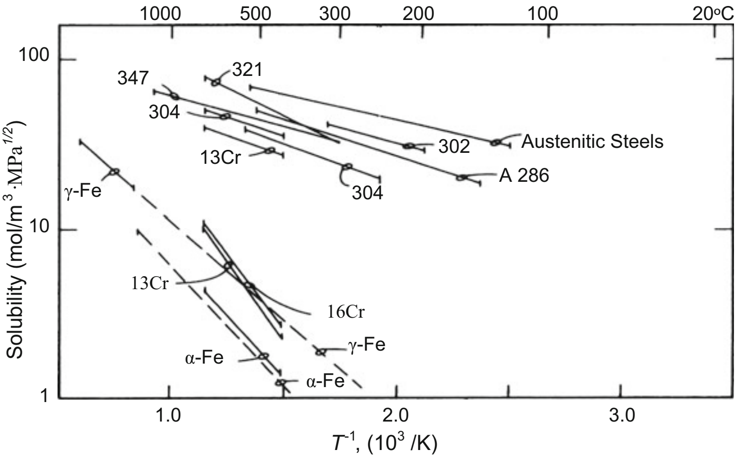

Fig. 1.4 Solid solubility data of hydrogen in stainless steels (Caskey [5])

diffusivity favors homogeneous distribution and the hydrogen content in Type 316 L stainless steel measured directly by means of thermal desorption is about 40 mass ppm in 70 MPa hydrogen at 90 °C [6].

1.2 Lattice Location

Hydrogen atoms locate at interstitial sites in the elementary lattice of α-iron. Direct determination of the location is difficult because of the small solubility and the high diffusivity of hydrogen, but the preferential occupancy at the tetragonal site (T-site) than at the octahedral site (O-site) has been shown by calculations of the total energy of the solution described in Sect. 1.4. Analyses of thermodynamic data also show that the T-site occupancy is favored at low temperatures, but the O-site occupancy increases as the temperature increases [2, 7].

A powerful method to detect directly the lattice location of hydrogen in metals is a channeling analysis utilizing a nuclear reaction ^{1}H(^{11}B,α) αα using ^{11}B beam. The location of hydrogen can be precisely determined by measuring the angular profile of emitted α particles on tilting a single crystal specimen against the incident ^{11}B beam. Hydrogen occupancy at the T-site was successfully confirmed for bcc single crystals of the group V_a metals (Nb, V, Ta) and their alloys [8–11]. In vanadium, a reversible displacement of hydrogen from the normal T-site was observed when a compressive stress of 70 MPa was applied along the <100> axis [8]. In Nb-Mo alloys with Mo of less than 10 %, the position of hydrogen atom shifts from the center of the T-site to a neighboring Mo atom as shown schematically in Fig. 1.5 [10]. The shift decreases with increasing Mo concentrations and disappears at 20 at % of Mo, showing a direct evidence for hydrogen trapping by alloying elements.

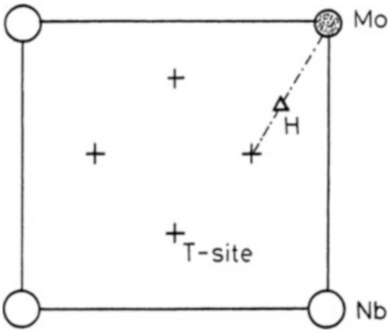

Fig. 1.5 Location of hydrogen atom in Nb-Mo alloy determined by a ^{1}H (^{11}Bα)αα nuclear reaction channeling method (Yagi [10]. Reprinted with permission from The Iron & Steel Inst. Japan)

1.3 Partial Molar Volume and Strain Field

The entry of hydrogen into metals accompanies volume expansion, and the partial molar volume of hydrogen, $\overline{V}_{\mathrm{H}}$, is directly obtained from dilatation measurements. While a substantial scatter of data is inevitable, a reliable value of $\overline{V}_{\mathrm{H}}$ for α-iron wires exposed in hydrogen gas is 2.0×10^{-6} m^3/mol-H at the temperature range from 600 °C to 800 °C [12]. At room temperature, electrochemical hydrogen permeation experiments have been used to determine the value of $\overline{V}_{\mathrm{H}}$. The steady-state permeation current in iron is affected by the applied elastic stress, and this effect is ascribed to the change of the hydrogen solubility. The chemical potential of hydrogen in metal is altered by applied stress, and an additional flow of hydrogen takes place to keep equilibrium. The hydrogen concentration is evaluated from the permeation current density, and $\overline{V}_{\mathrm{H}}$ is given as [13],

$$\overline{V}_{\mathrm{H}} = RT\left[\frac{\partial \ln\left(C_{\sigma}/C_{0}\right)}{\partial \sigma_{h}}\right], \tag{1.9}$$

where C_{σ} and C_0 are respectively hydrogen concentrations with and without the application of external hydrostatic stress σ_{h}. The values of C_{σ} and C_0 are estimated from reversible permeation current densities on cyclic stressing. The values of $\overline{V}_{\mathrm{H}}$ thus calculated for pure iron and AISI 4340 steel are 2.66 and 1.96×10^{-6} m^3/mol-H, respectively [13], which are close to the value obtained from dilatation measurements at high temperatures. The value of $\overline{V}_{\mathrm{H}}$ is insensitive to temperature and microstructures. The value of 2.0×10^{-6} m^3/mol-H, i.e., about 0.3 nm^3/H-atom, is almost common for all metals [7]. However, Hirth noticed [3] that the internal volume change δv due to lattice hydrogen to be used for calculating interactions with elastic fields was 1.22×10^{-6} m^3/mol-H when elastic relaxations at the free surface were taken into account for evaluating $\overline{V}_{\mathrm{H}}$.

The volume change around hydrogen atom plays a crucial role in interaction energies of hydrogen with various types of lattice defects. In α-iron, the local strain field around a single hydrogen interstitial atom has tetragonal symmetry in both the *T*- and *O*-sites [3], but the tetragonality is considered to be small. Accordingly, in the elastic regime, the hydrogen concentration, C_{h}, under hydrostatic stress σ_{h}, or C_{σ} under a uniaxial stress σ, at a constant hydrogen fugacity f is given respectively as

$$C_h = C_0 \exp\left(\frac{\sigma_{\mathrm{h}}\overline{V}_{\mathrm{H}}}{RT}\right)_f , \tag{1.10}$$

or

$$C_\sigma = C_0 \exp\left(\frac{\sigma\overline{V}_{\mathrm{H}}}{3RT}\right)_f , \tag{1.11}$$

where C_0 is the value at zero stress [14].

Accumulation of hydrogen in stress-concentrated areas such as notch root has been revealed in steels by means of hydrogen microprint technique [15]. It should be noticed, however, that the increase in the hydrogen concentration by stress also results from trapping of hydrogen in various lattice defects created by plastic strain.

1.4 Atomistic Calculations of the Heat of Solution

In the crystalline lattice of metals, the electronic state of hydrogen differs from that of free atom because of partial sharing of electrons with host metallic ions. The heat of solution, H_s, is the difference between the energy of hydrogen atom in solid solution and a half of the energy of hydrogen molecule as shown in Fig. 1.1. Atomistic calculations of binding energies of hydrogen with metals have been conducted by various methods. The first-principles calculations are generally time consuming, and some approximate methods have been devised.

The effective medium theory (EMT) replaces the complicated inhomogeneous host by an effective host consisting of a homogeneous electron gas. The embedding energy ΔE of an atom is defined as the energy difference between the combined atom-host system minus the energies of the separated atom and the host. The host density is not homogeneous in general, and the core regions of host atoms have very large variations in the electrostatic potential. Nørskov took into account the interaction of the hydrogen $1s$ level with the valence bands, particularly $3d$ band, of the host and calculated ΔE of hydrogen at the T-site of α-iron in transition metals [16]. Thus, calculated value of ΔE for α-iron was -212 kJ/mol. The heat of solution is the embedding energy minus the binding energy of hydrogen molecule (-232 kJ/mol), and the resultant 20 kJ/mol is close to experimentally obtained 29 kJ/mol [3, 17].

A generalization of the EMT using a pair-wise interaction is the embedded atom method (EAM) [18, 19]. It considers each atom in a system as embedded in a host lattice consisting of all other atoms. An approximation is that the embedding energy depends only on the environment immediately around the impurity or locally uniform electron density. The energy of an impurity atom in a host consists of two terms: the one is a function of the electron density of the host without impurity and the other is the short range electrostatic interaction. The total energy is a sum over all individual contributions of the host and the impurity. Daw and Baskes determined the embedding energies semiempirically and calculated the adsorption energies on the surfaces of Pd and Ni. Agreements with experimental values were fairly good for Pd, but calculated values were much smaller than experiments for Ni. For the bcc iron-hydrogen system, Wen et al. proposed a new potential to be used for the EAM calculation [20]. Using empirically determined parameters for fitting, Wen et al. obtained good agreements between calculated and experimental values for the heat of solution, migration energy, binding energy to vacancies of hydrogen.

On the other hand, the local electronic structure or the bond nature of hydrogen in α-Fe was investigated using a molecular orbital cluster method [21]. The one-electron Hamiltonian for the cluster consists of kinetic energy, Coulomb potential and exchange-correlation interaction potential terms. The last term was expressed in a form proportional to the cubic root of the spin density, and the discrete variational method (DV-Xα) was applied to calculate the elements of the secular matrix equation. Calculations of the density of states for α-Fe clusters of 32 atoms with and without 1 hydrogen atom showed that the main bonding peak was due to H-1s and Fe-4s hybridization with smaller contributions of Fe-3d and 4p. The charge transfer of about 0.6e from the first and second neighbor Fe atoms to H was shown to decrease metallic bond strength. The bond order as a measure of bond strength was calculated as a function of the Fe-H interatomic distance [21]. Interstitial hydrogen notably decreases Fe-Fe bond strength, but acts over a small distance within 0.3 nm. The Fe-H bond strength increases by nearby vacancies associated with a shift of the position of hydrogen atom toward the vacancy.

The total energy of many-electron system at the ground state is determined by using functions of the spatially dependent electron density. The density functional theory (DFT) using a pseudo-potential and a plane-wave basis set was applied by Tateyama et al. to calculate the total energy of H-α-Fe system [22]. A supercell consisting of 54-atoms (53 Fe atoms + 1 H-atom) was adopted locating hydrogen at a T-site as the ground state. The calculated heat of solution was 32.8 kJ/mol-H, which corresponded to an experimentally determined value of 29 kJ/mol-H. Effects of the supercell size or applied pressure on the total energy of the system were also calculated [23]. The calculated heat of solution was a decreasing function of hydrostatic tensile stress that increased cell volume. It is a natural consequence of the repulsive nature of solid solution. It was deduced that the hydrogen concentration in a stress-concentrated region, e.g., ahead of a crack tip, increases about 100-fold by 2–5 GPa of hydrostatic tensile stress.

References

1. Y.G. Huang, K. Fujita, H. Uchida, Bull. Jpn. Inst. Metals **18**, 694–703 (1979)
2. J.R.G. da Silva, S.W. Stafford, R.B. McLellan, J. Less Common Metals **49**, 407–420 (1976)
3. J.P. Hirth, Metall. Trans. A: **11A**, 861–890 (1980)
4. H.P. van Leeuwen, in *Hydrogen Degradation of Ferrous Alloys*, ed. by R.A. Oriani, J.P. Hirth, M. Smialowski (Noyes Pub., Park Ridge, 1985), pp. 16–35
5. G.R. Caskey Jr., in *Hydrogen Degradation of Ferrous Alloys*, ed. by R.A. Oriani, J.P. Hirth, M. Smialowski (Noyes Pub., Park Ridge, 1985), pp. 822–862
6. K. Takai, K. Murakami, N. Yabe, H. Suzuki, Y. Hagiwara, J. Jpn. Inst. Metals **72**, 448–456 (2008)
7. K. Kiuchi, R.B. McLellan, Acta Metall. **31**, 961–984 (1983)
8. Y. Yagi, T. Kobayashi, S. Nakamura, F. Kano, K. Watanabe, Y. Fukai, S. Koike, Phys. Rev. B **33**, 5121–5123 (1986)
9. Y. Yagi, T. Kobayashi, Y. Fukai, K. Watanabe, J. Phys. Soc. Jpn. **52**, 3441–3447 (1983)
10. E. Yagi, ISIJ Int. **43**, 505–513 (2003)
11. C. Sugi, E. Yagi, Y. Okada, S. Koike, T. Sugawara, T. Shishido, K. Ogiwara, J. Phys. Soc. Jpn. **82**, 074601 (2013)
12. H. Wagenblast, H.A. Wriedt, Metall. Trans. **2**, 1393–1397 (1971)
13. J. O'M Bockris, P.K. Subramanyan, Acta Metall. **19**, 1205–1208 (1971)
14. H.A. Wriedt, R.A. Oriani, Acta Metall. **18**, 753–760 (1970)
15. K. Ichitani, M. Kanno, S. Kuramoto, ISIJ Int. **43**, 496–504 (2003)
16. J.K. Nørskov, Phys. Rev. B **26**, 2875–2885 (1982)
17. W.J. Arnoult, R.B. McLellan, Acta Metall. **21**, 1397–1396 (1973)
18. M.S. Daw, M.I. Baskes, Phys. Rev. Lett. **50**, 1285–1288 (1983)
19. M.S. Daw, M.I. Baskes, Phys. Rev. B **29**, 6443–6453 (1984)
20. M. Wen, X.-J. Xu, S. Fukuyama, K. Yokogawa, J. Mater. Res. **16**, 3496–3502 (2001)
21. Y. Itsumi, D.E. Ellis, J. Mater. Res. **11**, 2206–2213 (1996)
22. Y. Tateyama, T. Miyazaki, T. Ohno: Phys. Rev. B, 67, 174105-1-10 (2003)
23. Y. Tateyama, T. Ohno, ISIJ Int. **43**, 573–578 (2003)

Chapter 2
Hydrogen Trapping and Its Detection

2.1 Manifestations and Analyses of Hydrogen Trapping

2.1.1 Solid Solubility at Low Temperatures

Hydrogen contents in steels are often of the order of 1 mass ppm. The values far exceed the solid solubility of hydrogen in iron at room temperature under ordinary environments and mostly result from trapping in various lattice defects. Figure 2.1 [1] is the extension of Fig. 1.2 for iron to lower temperatures. Data in the temperature range $1/T > 20 \times 10^{-4}$ substantially scatter, and the specimens are mostly given cold-straining and successive annealing that produce various types of lattice defects.

Direct measurements of the solubility are difficult for very low concentrations of hydrogen at low temperatures. Hydrogen diffusivity is a measure of trapped states in lattice defects and is utilized for the estimation of hydrogen concentration even in case where weak hydrogen trapping exists. Permeation techniques are often employed for this purpose and the following is a brief description of the procedure.

The steady-state flow of hydrogen, J_∞, in metal is described by Fick's first law of diffusion:

$$J_\infty = -D_\mathrm{H}\frac{\mathrm{d}C}{\mathrm{d}x}, \tag{2.1}$$

where D_H is the diffusion coefficient of hydrogen and C is the hydrogen concentration. Assuming Sieverts' law for hydrogen concentrations at the input and output surfaces of the specimen, the total flux j_t of hydrogen permeating through a disk of area A and thickness L is expressed in terms of the permeability coefficient Φ as

M. Nagumo, *Fundamentals of Hydrogen Embrittlement*,
DOI 10.1007/978-981-10-0161-1_2

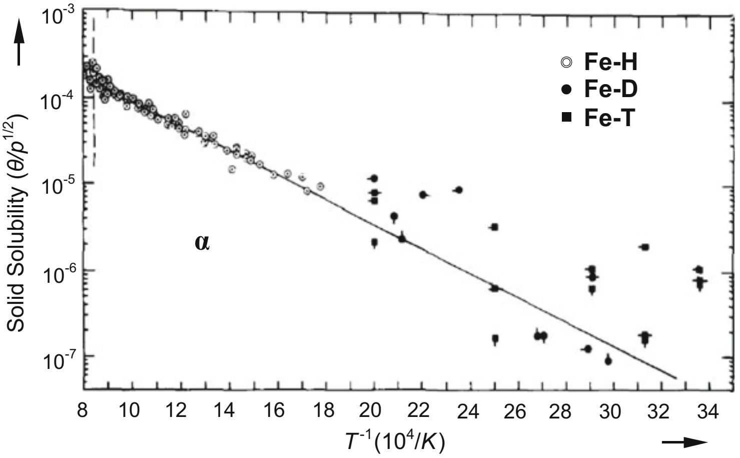

Fig. 2.1 Solid solubility of hydrogen in iron in the temperature range from 20 °C to 900 °C (da Silva et al. [1])

$$j_t = \Phi\frac{A}{L}\left(p_i^{1/2} - p_0^{1/2}\right), \tag{2.2}$$

where p_i and p_o are pressures in the input and output surfaces, respectively. The numerical value of Φ obtained for α-iron above 100 °C is [2]

$$\Phi = (2.9 \pm 0.5) \times 10^{-3} \exp\left[(-35 \pm 1.8\ \mathrm{kJ/mol})/RT\right], \tag{2.3}$$

where the units of Φ is $[\mathrm{cm}^3(\mathrm{ntp\ H_2}) \cdot \mathrm{cm}^{-1} \cdot \mathrm{s}^{-1} \cdot \mathrm{atm}^{-1/2}]$.

Electrochemical techniques are also used for hydrogen permeation from the gas phase through sheet specimens [3]. The permeability coefficient for pure iron thus obtained in temperature and pressure ranges of 0–60 °C and 0.01–1 atm, respectively, is

$$\Phi = 2.6 \times 10^{17} \exp\left[(-36 \pm 2.5\ \mathrm{kJ/mol})/RT\right], \tag{2.4}$$

where the unit of Φ is $[\mathrm{atom\text{-}H} \cdot \mathrm{cm}^{-1} \cdot \mathrm{s}^{-1} \cdot \mathrm{atm}^{-1/2}]$.

When the hydrogen pressure at the output surface is negligible, the hydrogen concentration at the input surface C_i in equilibrium with hydrogen gas of pressure p_i is obtained from Eqs. (2.1) and (2.2) using observed Φ and D_H as

$$C_\mathrm{i} = \frac{\Phi\sqrt{p_\mathrm{i}}}{D_\mathrm{H}}. \tag{2.5}$$

Equation (2.1) is also applied to the hydrogen entry by cathodic polarization, where C_i $[\mathrm{atoms\text{-}H} \cdot \mathrm{cm}^{-3}]$ is calculated from the steady-state current J_∞ $[\mathrm{atoms\text{-}H} \cdot \mathrm{cm}^{-2} \cdot \mathrm{s}^{-1}]$ as

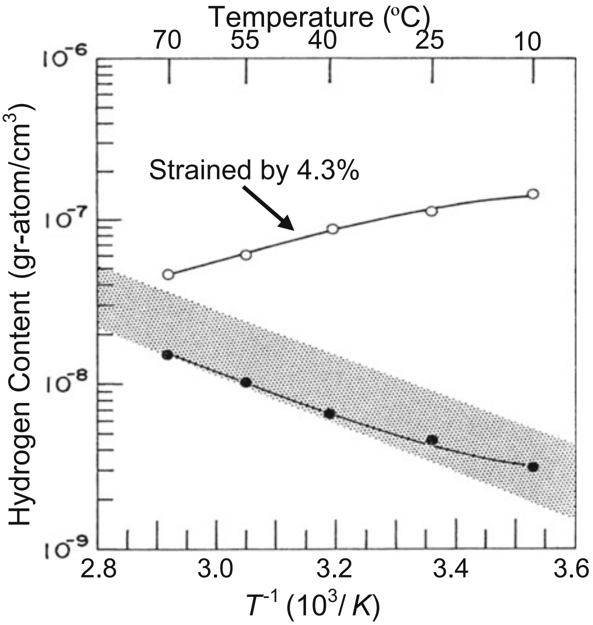

Fig. 2.2 Temperature dependence of hydrogen content in iron with (○) and without (●) plastic strain of 4.3 % (Yamakawa et al. [4]. Reprinted with permission from The Japan Society of Corrosion Engineering)

$$C_{\mathrm{i}} = \frac{J_{\infty} L}{D_{\mathrm{H}}}. \tag{2.6}$$

Figure 2.2 [4] shows the result of an electrochemical permeation experiment with α-iron single crystal specimens with/without prestraining. Tensile prestrain of 4.3 % was given at liquid nitrogen temperature, and the hydrogen concentration was calculated from the steady-state hydrogen flux. The temperature dependence of C_{i} for specimens without prestrain is consistent with the lower limit of the solubility data in Fig. 2.1 and shows the endothermic nature of the solid solution. On the contrary, the prestrain increases the hydrogen content to a large extent and also changes the hydrogen solutioning from endothermic to exothermic.

It is to be noticed that hydrogen composing C_i in Eqs. (2.5) and (2.6) is a quantity calculated from the boundary condition of the diffusion equation. The concentration of "diffusive" hydrogen includes not only hydrogen in solution but also weakly trapped hydrogen reversible to the solid solution to keep local equilibrium. The driving force of diffusion is the concentration gradient of lattice hydrogen, but the loss of lattice hydrogen by diffusion is compensated locally by reversibly trapped hydrogen.

In electrochemical permeation experiments, the entry of hydrogen is controlled by the electrolyte and the applied cathodic polarization potential. The condition for electrolysis is crucial not only for the concentration of hydrogen in solution but also for trapped states of hydrogen. In this respect, the effective hydrogen fugacity in electrochemical experiments is an important quantity. Table 2.1 lists some reported

Table 2.1 Effective hydrogen fugacity on the surface of electrode at cathodic electrolysis

Materials	Electrolyte	Current density (mA/cm^2)	Hydrogen fugacity (atm)	Hydrogen pressure (atm)
99.5 iron	25 °C, distilled water	–	5.7×10^{-5}	5.7×10^{-5}
Armco iron	25 °C, 0.1 N NaOH	8.1	2.2×10^1	2.2×10^1
99.8 iron	25 °C, 0.1 N H_2SO_4	0.4	5.4×10^2	4.5×10^2
99.9965 iron	24 °C, 1 N $H_2SO_4 + 5$ g/L As_2O_3	4.5	1.2×10^8	1.8×10^4
99.8 iron	25 °C, 0.1 N NaOH	1.8	1.1×10^0	1.1×10^0
99.8 Ferrovac E	25 °C, 0.1 N NaOH	11.3	2.9×10^1	2.9×10^1
AISI 1045	0.1 N $H_2SO_4 + 0.5$ mg/L As_2O_3	0.4	$>1.4 \times 10^4$	
AISI 1045	0.1 N NaOH + 10 mg/L As_2O_3	0–0.6	$0 - 3 \times 10^3$	

Kumnick et al. [3] and Oriani et al. [5]

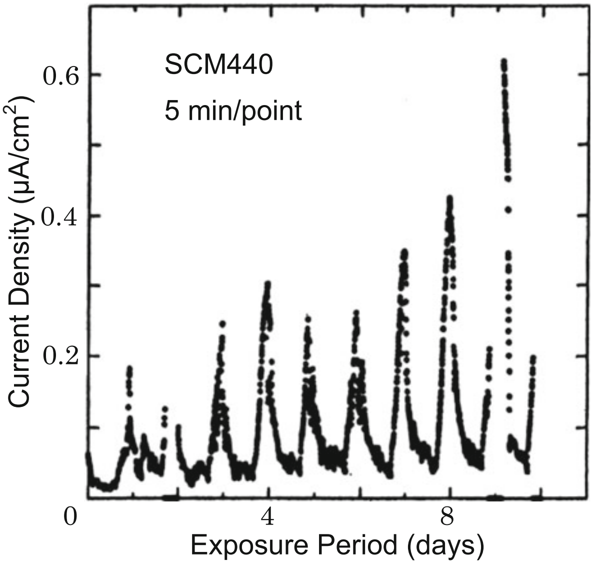

Fig. 2.3 Alternating variation of the permeation current density through iron specimen exposed to natural atmospheric environment (Yamakawa et al. [6]. Reprinted with permission from The Iron & Steel Inst. Japan)

values pf hydrogen fugacity for iron and AISI 1045 steel estimated using Eq. (2.2) and permeability coefficients [3, 5].

Under corrosive atmospheric environments, the hydrogen entry into materials is controlled by electrochemical reactions on the surface, and the equivalent hydrogen fugacity varies with ambient atmospheres. Figure 2.3 [6] shows records of hydrogen permeation currents for a high strength Cr-Mo steel foil specimen, outer side of which is exposed to atmospheric environment. The variation of the permeation current corresponds to daily alternations of humidity.

Permeation experiments are used for the measurement of the hydrogen diffusion coefficient that manifests hydrogen trapping. Details of the procedures and thus obtained information are described in Sect. 4.1.

2.1.2 Hydrogen Thermal Desorption Analysis

Analyses of the desorption of adsorbed gases from the metal surface under a controlled temperature ramp provide information on various parameters such as the number and populations of adsorbing phases, and the activation energy of desorption [7]. The thermal desorption spectroscopy (TDS) developed for characterizing adsorbed gases on the surface of material has been applied to hydrogen diffusing out from bulk specimens of metals [8–10]. The desorption-rate profile against temperature is affected by not only hydrogen states in the metal but also experimental parameters such the specimen size and the temperature-ramp rate. Accordingly, the terminology thermal desorption analysis (TDA) is more appropriate than TDS for the analysis of hydrogen states in metals.

In TDA, the measured quantity is the desorption rate of lattice hydrogen that diffuses out through the material undergoing trapping and detrapping processes. The rate-determining process of desorption during the temperature ramp differs by trapped states of hydrogen. When trapping is weak and local equilibrium exists between lattice and trapped hydrogen, thermally activated diffusion through lattice is the rate-determining process with a diffusion coefficient that depends on the density of and the binding energy with trap sites. On the other hand, when trapping is fairly strong, the thermally activated dissociation of trapped hydrogen with elevating temperature is the rate-determining process of desorption. Normally, desorption of strongly trapped hydrogen takes place at high temperatures, but the distinction between the two extreme processes is not simple and careful examinations of TDA are necessary.

Figure 2.4 [11] shows TDA profiles of hydrogen introduced to eutectoid steels cold-drawn to various reductions of area. Hydrogen was introduced by immersing the steel wires of 5 mm in diameter in a 20 % NH_4SCN aqueous solution at 323 K for 24 h, and the heating rate of TDA was 200 K/h. The specimen without cold-drawing shows a single desorption-rate peak with the peak temperature located at about 420 K. The amount of desorbed hydrogen increased with increasing reductions on cold-drawing, and an additional desorption peak appeared at higher temperatures. The increase initially appeared in TDA profiles for the lower temperature peak and successively for the higher temperature one.

Hydrogen states corresponding to the two peaks are quite different. For TDA of the specimen cold-drawn by 85 %, the lower temperature peak almost totally disappeared after exposing the specimen at room temperature for 2 weeks, indicating that hydrogen composing the lower temperature peak is diffusive. On the

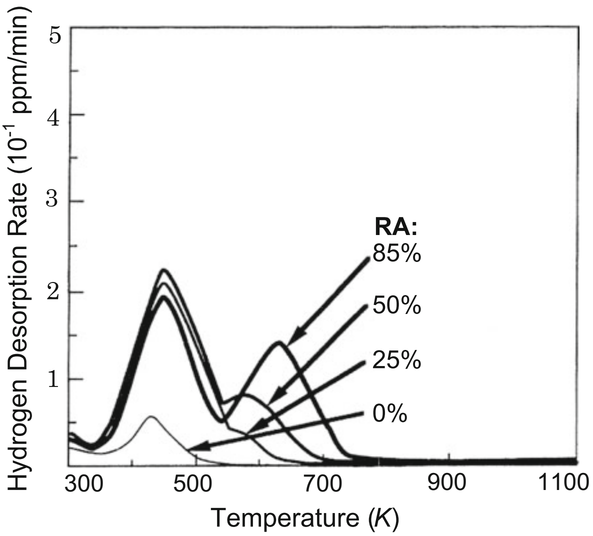

Fig. 2.4 Thermal desorption curves of hydrogen introduced to eutectoid steel specimens cold-drawn to various reductions of area (Takai et al. [11])

contrary, the higher temperature peak was hardly affected by room temperature exposure, indicating non-diffusive nature of trapped hydrogen.

For pure iron, the hydrogen absorption capacity increases by cold-drawing, but only a single desorption peak appears at about 400 ~ 500 K on TDA profiles depending on the specimens size [11]. The peak disappears when hydrogen-charged specimens are exposed at room temperature, indicating diffusive nature of hydrogen. Lattice defects that concern with the single peak in TDA profile is described in Chap. 3. On the other hand, the trap sites of non-diffusive hydrogen that composes the higher temperature peak in Fig. 2.4 for cold-drawn eutectoid steels must be created by heavy deformation of eutectoid cementite, but the entity of trapping is not definite.

(a) Dissociation-controlled desorption

The quantities that describe hydrogen trapping are density of trap site, hydrogen occupancy therein and binding energy of hydrogen therewith. Some procedures have been devised to estimate these quantities from TDA. Kissinger expressed the reaction rate of thermal dissociation of minerals, e.g., solid → solid + gas, in the form [12]

$$\frac{\mathrm{d}X}{\mathrm{d}t} = A(1-X)^n \exp\left(-\frac{E_\mathrm{a}}{RT}\right), \tag{2.7}$$

where X is the fraction reacted, A is the reaction constant, n is the order of the reaction and E_a is the activation energy of the reaction. This type of equation was applied to the thermal desorption of gases from metal surfaces [7] and also to the thermal detrapping of hydrogen from trap sites in metals [8].

The peak temperature T_p at which the dissociation rate is maximum is obtained by differentiating Eq. (2.7) with t, i.e.,

$$\frac{\mathrm{d}}{\mathrm{d}t}\left(\frac{\mathrm{d}X}{\mathrm{d}t}\right) = \frac{\mathrm{d}X}{\mathrm{d}t}\left[\frac{\varphi E_\mathrm{a}}{RT^2} - A\exp\left(-\frac{E_\mathrm{a}}{RT}\right)\right] = 0, \tag{2.8}$$

or

$$\frac{\varphi E_a}{RT_p^2} = A\exp\left(-\frac{E_a}{RT_p}\right), \tag{2.9}$$

for a reaction of the first order ($n = 1$) and a linear heating rate,

$$T = T_0 + \varphi t. \tag{2.10}$$

Differentiation with $1/T_\mathrm{p}$ of the logarithm of Eq. (2.9) gives

$$\frac{\partial \ln\left(\varphi/T_p^2\right)}{\partial\left(1/T_\mathrm{p}\right)} = -\frac{E_a}{R}, \tag{2.11}$$

Then, the activation energy of detrapping, E_a, is obtained from the gradient of the plot of ln (φ/T_p^2) vs. ($1/T_\mathrm{p}$) using measured T_p at various heating rates.

It should be noticed that the above method of evaluating E_a is valid when the desorption is rate-limited by the dissociation of trapped hydrogen rather than by diffusion of hydrogen in lattice. The condition is satisfied for strongly trapped hydrogen, and a criterion for the applicability is the magnitude of the binding energy with traps. Suggested magnitudes of E_a at the border of reversible or irreversible traps are 26.4 kJ/mol for E_a [13] or 64 kJ/mol for E_b [14] for iron at room temperature. The experimentally determined E_a of the higher temperature peak in Fig. 2.2 according to Eq. (2.11) was 65 kJ/mol [15].

Turnbull et al. noticed from a more rigorous treatment [16] that the application of Kissinger's equation, Eq. (2.7), is valid for a very low trap occupancy in case of low lattice hydrogen contents as described in (c) of this section. An experimental method to check whether desorption is dissociation-controlled or not is the dependence of TDA profiles on the specimen size. For the dissociation-controlled desorption, TDA profiles are unaffected by the specimen size since A in Eq. (2.7) is a constant irrelevant to the specimen size.

(b) Diffusion-controlled desorption

On the other hand, when the desorption rate is limited by diffusion of hydrogen in metals, parameters of hydrogen trapping are estimated by modeling TDA profiles. Basic diffusion theories are described in Sect. 4.2, and some examples of the use of trapping parameters for modeling TDA profiles are presented here.

Trapping and detrapping sequences during the migration process of hydrogen are incorporated in the diffusion coefficient. Fick's diffusion law, Eq. (2.1), for the flow of lattice hydrogen is applied to the gradient of total hydrogen concentration C_T that includes trapped hydrogen in equilibrium with lattice hydrogen. The diffusion equation is expressed using the apparent or effective diffusion coefficient D_eff that depends on trapped states, i.e.,

$$J = -D_\mathrm{eff}\frac{\mathrm{d}\,C_\mathrm{T}}{\mathrm{d}x}\,. \tag{2.12}$$

Oriani expressed D_eff considering equilibrium between atomic populations in the normal lattice and traps [14]. When hydrogen occupies a fraction θ of available sites, the equilibrium constant K is the ratio of the activity of hydrogen in the trap sites to that in lattice sites. For very low C_L, i.e., $\theta_\mathrm{L} << 1, K$ is expressed in terms of the fractional occupancy in the form of

$$K = \frac{1}{\theta_L}\left(\frac{\theta_x}{1-\theta_x}\right), \tag{2.13}$$

where suffices x and L denote trapping and normal lattice sites, respectively. The local equilibrium that Oriani assumed was that a change of the lattice hydrogen concentration is compensated in the same time interval by the same amount of trapped hydrogen to keep equilibrium.

When the hydrogen concentration C is defined as the number of hydrogen atoms per unit volume, C is the product of the number of sites per unit volume, N, and the fractional occupancy, θ, thereof. Then,

$$C_L = \mathrm{N}_L\theta_L, \tag{2.14}$$

and

$$C_x = \mathrm{N}_x\theta_x. \tag{2.15}$$

It is to be noticed that N includes the coordination number available for hydrogen around one lattice or defect site of host metals.

Comparing Eqs. (2.1) and (2.12) for Fick's first law, D_eff is related to the normal diffusivity D_L and trapping parameters in Eqs. (2.13) and (2.15) in the form of

$$D_\mathrm{eff} = D_L\frac{\mathrm{d}C_L}{\mathrm{d}C_T} = D_L\left[1+\frac{\mathrm{N}_x\mathrm{N}_LK}{(\mathrm{N}_L+KC_L)^2}\right]^{-1} \tag{2.16}$$

or

$$D_\mathrm{eff} = D_L\frac{C_L}{C_L+C_x(1-\theta_x)} \tag{2.17}$$

For $\theta_\mathrm{x} << 1$, i.e., for a very low occupancy of trapping sites,

$$D_{\mathrm{eff}} = D_L \frac{C_L}{C_T}. \tag{2.18}$$

When C_L is very small, Eq. (2.16) is written in terms of the density of trap sites, Γ_x ($= \mathrm{N}_x/\mathrm{N}_L$), and the binding energy E_b as

$$D_{\mathrm{eff}} = D_L \left[1 + \Gamma_x \exp \left(\frac{E_\mathrm{b}}{RT} \right) \right]^{-1}. \tag{2.19}$$

Ono and Meshii considered dynamic equilibrium between trapping and detrapping processes and obtained an expression of D_{eff} similar to Eq. (2.19), multiplying the exponential factor therein by entropy factor [10].

The desorption rate is calculated from the solution of Fick's second law of diffusion,

$$\frac{\partial C}{\partial t} = D \frac{\partial^2 C}{\partial x^2}, \tag{2.20}$$

with proper initial and boundary conditions. Ono and Meshii simulated TDA profiles of quenched-in hydrogen from high temperatures in pure iron specimens. Observed TDA profiles showed a single desorption peak at about 420 K, excluding an artifact peak at 220 K due to desorption of water molecules from the metal surface. Computations by means of a finite difference method gave simulated TDA profiles coincident with observed ones using D_{eff} with $E_\mathrm{b} = 51$ kJ/mol and $\Gamma_x = (4 \sim 15) \times 10^{-5}$ in Eq. (2.19).

Effects of trapping parameters in TDA profiles were examined by Yamaguchi and Nagumo using effective diffusion coefficients [17]. The specimens were martensitic steel plates and experimental variables were the plate thickness, the amount of prestrain to vary the density of defects, the hydrogen-charging time to vary the initial distribution of hydrogen in specimen and the heating rate. Hydrogen as a tracer of lattice defects was introduced to deformed specimen by fairly mild cathodic electrolysis using a 3 % NaCl + 3 g/*l* NH_4SCN aqueous solution at a current density of 5 A/m^2. The mild condition prevented to induce extraneous defects. Simulations of TDA profiles were conducted using Eq. (2.20) with D_{eff} defined by Eq. (2.19) that includes Γ_x and E_b as fitting parameters.

Figure 2.5 [17] compares observed and simulated TDA profiles for specimens of 2 mm in thickness with increasing heating rates. For the calculation, Γ_x and E_b were assumed to be 8.5×10^{-2} and 17 kJ/mol, respectively. Figure 2.6 [17] also compares observed and simulated TDA profiles for specimens given different amounts of strain. For the calculation, E_b was fixed at 20 kJ/mol and Γ_x was varied.

The peak temperature T_p at which the desorption rate is maximum shifts to higher temperatures with increasing E_b, as shown in Fig. 2.7(a) [17], but T_p is also a function of Γ_x as shown in Fig. 2.7(b) [17]. Accordingly, a unique combination of Γ_x and E_b is not determined by modeling an observed T_p. Another measure of fitting

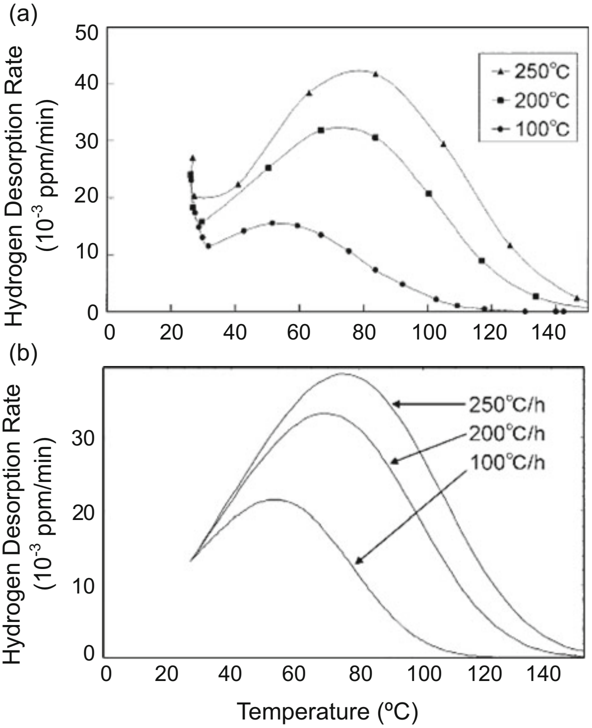

Fig. 2.5 Thermal desorption curves of hydrogen from martensitic steel specimens of 2 mm in thickness at various heating rates. (**a**) Experimental curves, (**b**) simulation curves (Yamaguchi et al. [17])

is the desorption-rate peak width. The peak width at the same T_p is broader when calculated using larger Γ_x and smaller E_b values. A proper characterization of TDA profile in addition to T_p is necessary in utilizing modeling to estimate trapping parameters. It is also to be noticed that TDA profiles depend on geometries of specimen in case of the diffusion-controlled desorption.

TDA gives useful information on lattice defects that affect hydrogen-related failure, but one should be aware that an exact estimation of trapped states of hydrogen is not straightforward in the case of diffusion-controlled desorption.

(c) General treatments in case of multiple traps

Desorption peaks in TDA often exhibit asymmetry accompanying broadening of the width and hump(s) or sub-peak(s). Such features manifest the existence of multiple types of trap. A general formulation of diffusion accompanying trapping processes was given by McNabb and Foster [18] by adding a term for the interchange of hydrogen atoms between diffusing and trapped states in Fick's second law. The equation is

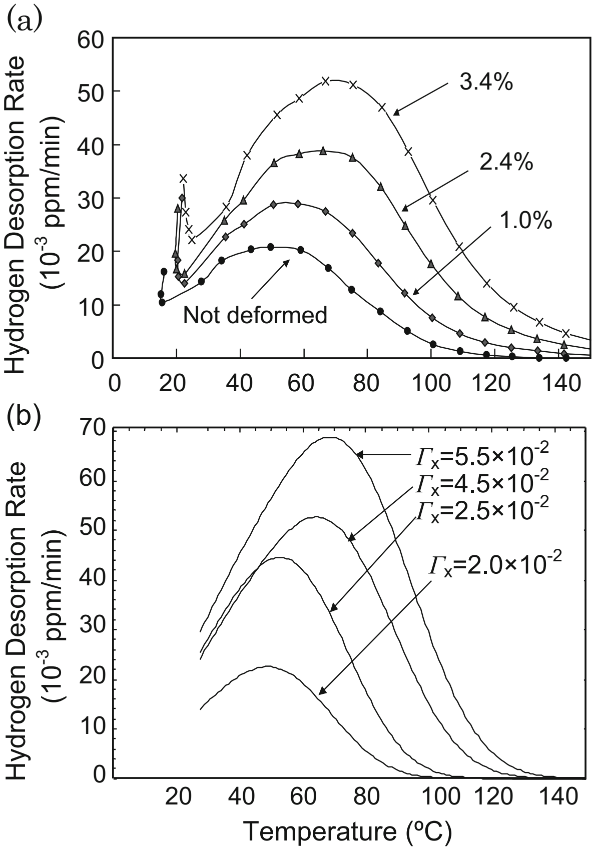

Fig. 2.6 Thermal desorption curves of hydrogen from martensitic steel specimens of 2 mm in thickness given various amounts of strain. (**a**) Experimental curves, (**b**) simulation curves for traps of the binding energy of 20 kJ/mol and different densities Γ_x. The heating rate is 100 °C/h (Yamaguchi et al. [17])

$$\frac{\partial C_L}{\partial t} + \sum_{\mathrm{i}} \mathrm{N_i} \frac{\partial \theta_{\mathrm{i}}}{\partial t} = D_L \tilde{\mathrm{N}}^2 C_L \,, \tag{2.21}$$

with

$$\frac{\partial \theta_{\mathrm{i}}}{\partial t} = k_{\mathrm{i}} C_L (1 - \theta_{\mathrm{i}}) - p_{\mathrm{i}} \theta_{\mathrm{i}} \,, \tag{2.22}$$

where N, C_L and θ are defined in Eqs. (2.14) and (2.15) and k and p are respectively trapping- and detrapping-rate parameters. The terms $k_{\mathrm{i}}C_{\mathrm{L}}(1-\theta_{\mathrm{i}})\mathrm{N_i}$ and $p_{\mathrm{i}}\theta_{\mathrm{i}}\mathrm{N_i}$ are respectively the number of hydrogen atoms captured at and released from the i-th trap in unit volume per second.

Trapping and detrapping are thermally activated processes, and k and p are related to potential energies denoted in Fig. 2.8. Expressions of k and p are given as [16]

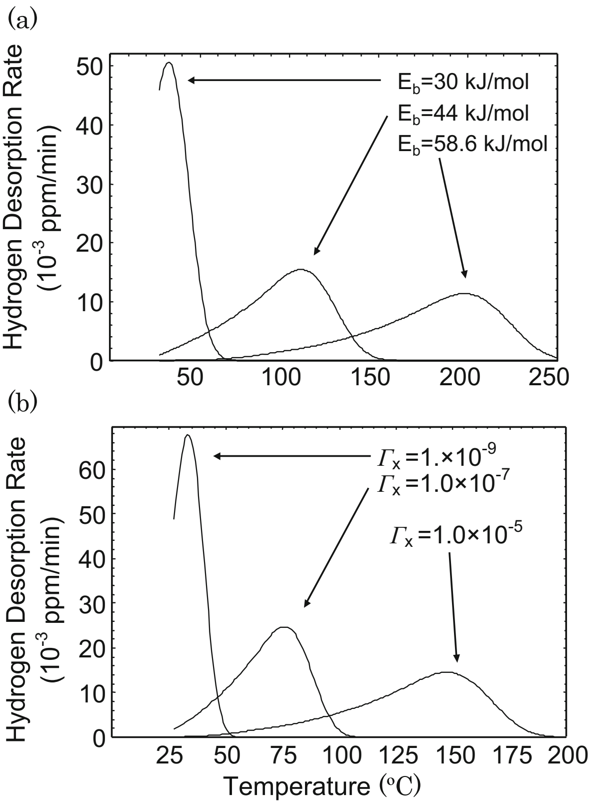

Fig. 2.7 Effects of (**a**) the binding energy with hydrogen and (**b**) the density of the trap on simulated thermal desorption curves. (**a**) The trap density is fixed at 1.0×10^{-4}; (**b**) the binding energy is fixed at 58.6 kJ/mol. The plate thickness is 2 mm and the heating rate is 100 °C/h (Yamaguchi et al. [17])

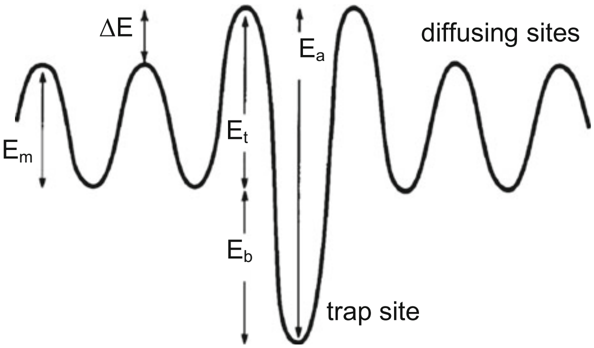

Fig. 2.8 Schematic illustration of energy states of lattice and trapped hydrogen in metals

$$\begin{aligned} k &= k_0 \exp\left(-\frac{E_t}{RT}\right), \\ p &= p_0 \exp\left(-\frac{E_b + E_t}{RT}\right). \end{aligned} \tag{2.23}$$

In Fig. 2.8, the change in the saddle point energy ΔE is either positive or negative according to the relative magnitude of E_t and E_m. Parameters p and k are not independent. When the occupation of hydrogen in the trap is low enough, the ratio k/p in the steady-state condition ($\partial\theta/\partial t = 0$) gives

$$\frac{k_0}{p_0} = \frac{1}{\mathrm{N}_L(1-\theta)} \approx \frac{1}{\mathrm{N}_L} = \text{constant}. \tag{2.24}$$

The general solution of Eqs. (2.21) and (2.12) is difficult. McNabb and Foster derived an approximate solution for thick specimens, i.e., for the case where frequent trapping and detrapping take place during the time of diffusion, under dynamic equilibrium between trapped and lattice hydrogen [18]. When the hydrogen concentration is low enough, Eq. (2.21) is reduced to Fick's first law by using D_eff defined as

$$D_\mathrm{eff} = D_L\left(1 + \mathrm{N}_x\frac{k}{p}\right)^{-1}. \tag{2.25}$$

Equation (2.25) is a kinematic expression of Oriani's D_eff, Eq. (2.19), which is derived from the local equilibrium concept. Further descriptions on hydrogen diffusion process are in Sect. 4.2 about permeation experiments.

TDA profiles are affected by trapping parameters as described in Sect. 2.1.2(b). Turnbull et al. simulated TDA profiles by solving Eqs. (2.21) and (2.22) using a finite differential method [16]. In the analysis, the ratio k/p is important and the functional form of D_eff in Eq. (2.25) is similar to that in Eq. (2.19). Then, calculated TDA profiles obtained using Eqs. (2.19) and (2.25) are similar. For the case of a single trap, key material variables that determine TDA profile are the density of trap sites and the binding energy. Their effects are similar to those shown in Figs. 2.5 and 2.6 obtained by using the effective diffusivity. The peak hydrogen flux and the peak temperature have no marked dependence on the magnitude of rate constants k_0 and p_0 [16]. Impacts of test parameters such as the heating rate and the sample thickness are also similar between the two modeling methods [16, 17]. The increase in C_0 enhances the desorption in the lower temperature side of the peak and shifts the desorption peak to lower temperature [17]. An explanation is that the higher C_0 causes the higher occupancy of traps and reduces retrapping of diffusing lattice hydrogen, resulting in the faster diffusion at lower temperatures.

Turnbull et al. extended their calculations to the case of two types of traps [16], i.e., $i = 1$ and 2 in Eq. (2.21). The calculated TDA profile for two traps with binding energies of 48 and 68 kJ/mol, respectively, exhibits two discrete peaks. Each peak is the same as the one expected for the case of a single trap of 48 or 68 kJ/mol in the binding energy. However, when binding energies are closer, *e.g.*, 48 and 58 kJ/mol, the two peaks merge into one peak. In the calculation, the densities of the two traps are assumed to be the same. The appearance of discrete peaks should depend not only on the difference of the binding energies but also on their magnitudes and on the densities of traps.

Modeling of TDA profiles using McNabb-Foster's equation were attempted by Enomoto et al. using a finite difference method [19]. The observed TDA profile of hydrogen from martensitic steel showed a single peak, and Enomoto et al. assumed trapping of hydrogen in the elastic strain field of dislocations. The binding energy of 27 kJ/mol and the density of trap sites were assumed from the literature, and the fractional occupancy was estimated from the observed amount of hydrogen. Trapping and detrapping parameters in Eq. (2.23) were determined so as to match the calculated peak temperature and desorption rate to observed ones. Thus, determined ratio p_0/k_0 of the order of $10^{29}/\mathrm{m}^3$ is nearly coincident with the values employed by Turnbull et al. [16].

Enonoto et al. also simulated TDA profiles that exhibited two desorption-rate peaks as shown in Fig. 2.4 for a cold-drawn eutectoid steel bar specimen [19]. They assumed that the two peaks were due to the elastic strain field and the core of dislocation with binding energies of 27 and 50 kJ/mol, respectively, from the literature. The trap densities and the initial fractional occupancies of the traps were estimated by assuming the dislocation density of 10^{16} m^{-2} and observed hydrogen fluxes of the two peaks. For the ratio p_0/k_0, the value formerly determined for martensitic steel was also used. A part of hydrogen introduced into specimen diffused out during room temperature exposure, and the simulation satisfactorily reproduced the observed decay of the lower temperature peak in TDA profiles. However, it should be noticed that a set of parameters is not unique to a given TDA profile. Their assignments of trap sites to microstructures are not reasonable, and many assumptions requisite for calculations must be carefully examined.

(d) Technical and intrinsic problems

TDA is a powerful tool for investigating trapped states of hydrogen in metals, but the analyses described above have some limitations for identifying trapped states of hydrogen. At conventional TDA procedures, a substantial amount of hydrogen is lost prior to the start of the temperature ramp. A new method, low temperature thermal desorption spectroscopy (LTDS), starts the temperature ramp from a temperature as low as 70 K [20]. The desorption takes place in low diffusivity range, and early parts of desorption is correctly measured without an inevitable loss of hydrogen that happens in conventional TDA. LTDS enables to obtain the complete form of TDA profile as shown in Fig. 2.9 [20] that compares conventional TDA and LTDS profiles of hydrogen introduced into a plastically deformed pure iron specimen of 0.5 mm in thickness. Examples of LTDS are also shown in Figs. 3.10 and 3.11 in Sect. 3.2.3(b).

Trapping parameters, *k* and *p* in Eq. (2.22), are used in the form of *k*/*p* for modeling. A method to separate the parameters was devised by Pound

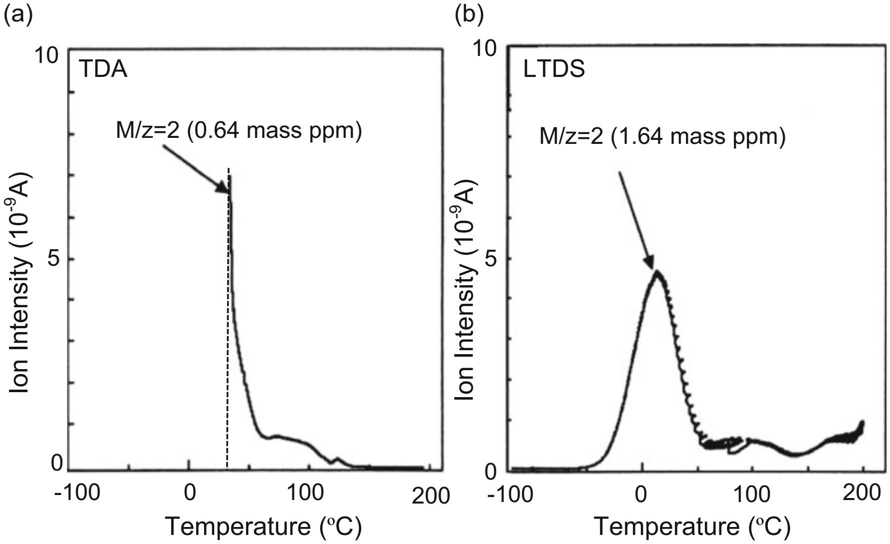

Fig. 2.9 Comparison of TDA and LTDS curves of hydrogen from 90 % cold-rolled iron specimens of 0.5 mm in thickness. Hydrogen is charged by immersing the specimens in 20 % NH_4SCN aq at 50 °C for 24 h (Sato et al. [20], Reprinted with permission from The Iron & Steel Inst. Japan)

et al. [21]. On electrochemical permeation, a double-step method was devised to introduce hydrogen into the metal specimen, firstly at a cathodic potential for a short time and then stepping-up the potential to a more positive value to remove diffusive hydrogen. The amount of removed hydrogen was counted as the anodic charge from the transient anodic current, and the difference between the total charge passed into the metal and the charge passed out during the discharge gave the amount of irreversibly trapped hydrogen. It was assumed that the change of hydrogen concentration with time was due to the diffusional flow and the capture in irreversible traps. The trapping-rate parameter, κ, was defined as

$$\kappa = kN_x(1 - \theta_x), \tag{2.26}$$

including trapping parameters k and N_x defined in Eqs. (2.21) and (2.22). Experiments conducted for iron in aqueous H_2S solutions gave the values of κ of 0.25 s^{-1} that decreases to 0.05 s^{-1} by annealing, but the nature of the irreversible trap sites were not definite.

On TDA measurements, temperature ramping occasionally alters defect structures in materials. Microstructures of steels are not always thermally stable as envisaged on tempering of martensite or recovery of plastically strained materials. In such cases, thermal desorption of hydrogen takes place not only by the activated diffusion or thermal release from traps but also is associated with alterations of trapping defects themselves, such as precipitation of carbides, reconfiguration of dislocations and annihilation of point defects. Analysis of TDA profile taking into account such structural alterations during temperature ramp has not been established.

The binding energy of hydrogen with traps is a major factor that determines the desorption rate. Local equilibrium that is a premise for the diffusion-controlled desorption is viable for E_b lower than a border value. However, the border value is a function of temperature [14], and the rate-controlling process for desorption occasionally changes during the temperature ramp. Such situations pose difficulties in selecting proper approximations for the analyses. In the case of diffusion-controlled desorption from multiple types of traps, separation of respective traps is difficult when hydrogen in each trap is in local equilibrium with lattice hydrogen. LTDS has been devised to improve the precision of analysis and also to separate desorption peaks arising from traps with close E_bs. Separation of weakly trapped states of hydrogen using LTDS is described in Sect. 3.2.3(b), but modeling of observed LTDS profiles is not yet conducted.

It is again to be noticed that trapping parameters estimated from a TDA profile, such as the binding energy and the trap density, do not straightly indicate microscopic entities of the trap. The parameters for a supposed type of defect are to be determined separately, and their consistency with modeling of TDA profiles is a proper procedure to identify hydrogen traps by means of TDA.

2.2 Partition of Hydrogen Among Different Traps

2.2.1 Equilibrium Distribution

The number of hydrogen atoms trapped in a type of defect is the product of the number of sites and the fractional occupancy by hydrogen. The distribution function for the partition of hydrogen among different sites was discussed by Hirth and Carnahan [22] with respect to the adsorption of hydrogen at dislocations and cracks in iron. From thermodynamics viewpoint, McLellan derived the distribution of hydrogen among trap sites and neighboring normal lattice sites in terms of the Fermi-Dirac distribution provided that the fractional occupancy was low and mutual interactions of trapped hydrogen atoms were negligible [23].

The Fermi-Dirac distribution expresses the probability $f(E)$ that a particle will have energy E as

$$f(E) = \frac{1}{1 + \exp\left[(E - E_F)/k_B T\right]}, \tag{2.27}$$

where k_B is the Boltzmann constant and E_F is the Fermi energy. Then, the numbers of hydrogen atoms N_H in two energy states, E_0 and $E_1 = E_0 - E_b$, are given as

$$\frac{\mathrm{N_{H0}}}{\mathrm{N_0} - \mathrm{N_{H0}}}\exp\left(-\frac{E_0}{k_B T}\right) = \frac{\mathrm{N_{H1}}}{\mathrm{N_1} - \mathrm{N_{H1}}}\exp\left(-\frac{E_1}{k_B T}\right). \tag{2.28}$$

by changing the sign of a binding energy to be negative. N and $\mathrm{N_H}$ denothe the number of a site and the number of hydrogen in the site, respectively [24]. Denoting the state 0 and 1 for the normal lattice and trapped state, respectively, Eq. (2.28) is written in terms of fractional occupancy, θ, as

$$\begin{aligned} \frac{\theta_x}{1-\theta_x} = & \frac{\theta_L}{1-\theta_L}\exp\left(1 - \frac{E_L - E_x}{k_B T}\right) = \frac{\theta_L}{1-\theta_L}\exp\left(\frac{E_b}{k_B T}\right) \\ \approx & \ \theta_L \exp\left(\frac{E_b}{k_B T}\right), \end{aligned} \tag{2.29}$$

showing an approximate Boltzmann distribution when $\theta_x << 1$.

The variation of θ_x against E_b calculated from Eq. (2.29) is shown in Fig. 2.10 for iron under hydrogen gas environments at 300 and 500 K, using θ_L calculated from Sieverts' law. Under a constant pressure, *ln* θ_x is proportional to E_b for low θ_x, but

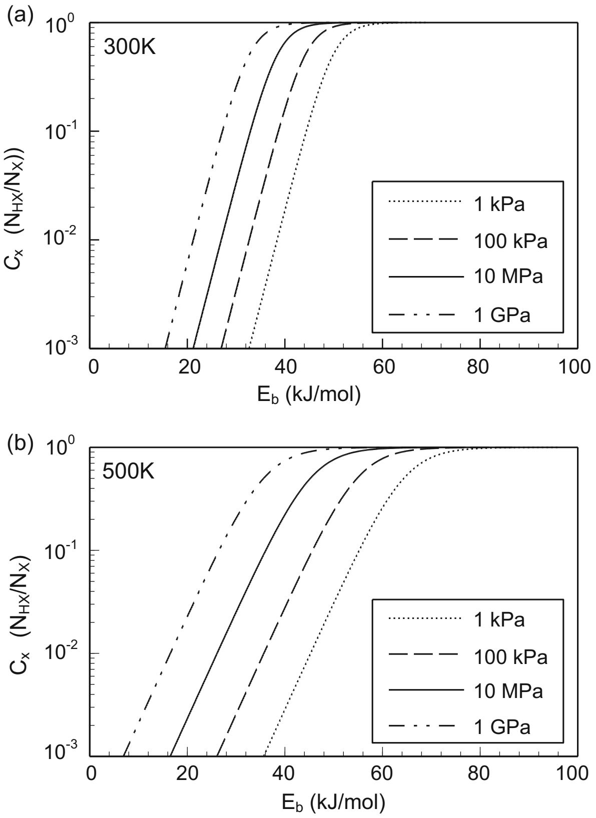

Fig. 2.10 Calculated hydrogen occupation of traps in iron with various binding energies under hydrogen gas environments at (**a**) 300 K and (**b**) 500 k. Calculation is conducted using the Fermi-Dirac distribution and the occupation is denoted in terms of the atomic ratio at traps

the linear relationship no longer holds when θ_x approaches saturation exceeding *ca.* 0.3 under high pressures. Accordingly, the ratio of the amounts of hydrogen trapped in sites of different E_b is not constant but varies by environments. From Eq. (2.29), the ratio of θ_x of two trap sites with different E_b is

$$\frac{\theta_{x1}}{\theta_{x2}} = \frac{1-\theta_{x1}}{1-\theta_{x2}} \exp\left(\frac{E_{b1}-E_{b2}}{k_B T}\right). \tag{2.30}$$

The ratio is a function of θ_L which varies with the fugacity of hydrogen. Under a constant fugacity, θ_x at a site of a higher E_b is larger than that at sites of lower E_b. When fugacity increases and θ_x at a site of a higher E_b approaches saturation, the ratio of θ_xs tends to deviate from the linear relationship. In laboratory tests to assess the susceptibility to hydrogen embrittlement, introduced hydrogen distributes among various lattice defects that play different roles in embrittlement. The hydrogen occupancy is crucial for a specific type of defect to operate in the fracture process. Thus, a proper choice of hydrogen-charging conditions, such as electrolyte and current density in the case of cathodic electrolysis, is necessary for discriminating defects that contribute to hydrogen embrittlement.

2.2.2 Kinetics of Hydrogen Trapping

Fracture events most often proceed under nonequilibrium conditions. Trapping of hydrogen in various defects proceeds sequentially on the entry of hydrogen and

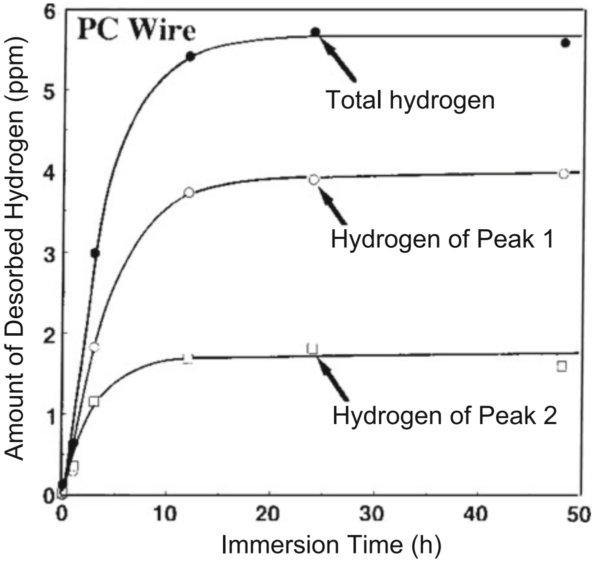

Fig. 2.11 The amount of desorbed hydrogen from cold-drawn eutectoid steel wires subjected to the FIP test for increasing periods. The reduction of specimens at cold-drawing is 75 % (Takai et al. [25]. Reprinted with permission from The Iron & Steel Inst. Japan)

during loading. Figure 2.11 [25] shows the increase in the two peaks in TDA profiles of a eutectoid steel cold-drawn by 75 % and subjected to sustained loading in a 20 % NH_4SCN aqueous solution at 323 K. The TDA profile of the steel without loading is shown in Fig. 2.4. The applied stress is 0.5 of the ultimate tensile strength, and the higher temperature peak reaches saturation faster than the lower temperature peak, implying that the occupancy proceeds faster in sites of higher E_b.

The occupancy of trap sites proceeds through trapping and detrapping processes of hydrogen as a function of trapping parameters, k and p, in the McNabb-Foster diffusion equation. Kasuya and Fuji numerically solved Eqs. (2.21) and (2.22) for two classes of traps [26]. The traps were characterized by the magnitude of N_ik_i/p_i of 20 and 3 respectively for the first and second class of traps, i.e., deeper trapping in the first class. Calculations were conducted for the entry of hydrogen from one side of a plate specimen, and the calculated distributions along the thickness of the plate before the steady state was attained showed that the occupancy of the deeper trap sites proceeded slower in the middle part of the specimen. The result is in contrast with Fig. 2.11 and Eq. (2.30) for the equilibrium partition. Effects of trapping parameters and/or initial conditions on kinetics of partition are subjects to be examined.

2.3 Visualization of Hydrogen Distribution

Effects of microstructures on embrittlement are to be examined firstly with respect to interactions of hydrogen with microstructural elements. However, experimental information on hydrogen effects is mostly averaged over the whole or a bulky portion of specimen. The observation of the location of hydrogen is then useful for distinguishing the role of microstructural elements in embrittlement.

Tritium is a radioactive isotope of hydrogen, and tritium autoradiography is a well-established technique for visualizing hydrogen distributions [27, 28]. Tritium autoradiography exhibits the distribution of Ag particles in a nuclear emulsion layer decomposed of AgBr by the 18.6 keV β-ray emitted from tritium. The emulsion film is deposited normally over a very thin intermediate collodion layer on the surface of tritiated specimen. Microstructures of the metal corresponding to the distribution of Ag particles can be revealed simultaneously when the metal surface has been prepared for metallographic observation. The penetration depth of the β-ray is about 1 μm in iron-base alloys [28], and the spatial resolution of autoradiography is limited by the size of AgBr particles. Before coating the emulsion film, the tritiated specimens are normally exposed at room temperature so as to diffuse out extraneous tritium for the safety on manipulation. In this case, observed Ag particles exhibit strongly trapped sites for non-diffusive tritium.

Figure 2.12 [29] shows a tritium autoradiograph of a low-carbon ferritic steel specimen strained by 5 % at 193 K. Besides accumulation along grain boundaries, the arrows A and B in Fig. 2.12 indicate a columnar distribution and a band-like assembly, respectively, while the distribution within a grain is fairly uniform when

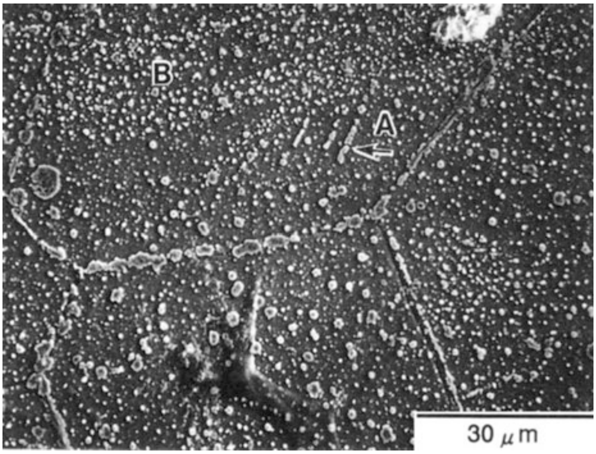

Fig. 2.12 Tritium autoradiograph of a ferritic steel tensile strained by 5 % at −80 °C (Aoki et al. [29])

deformed at room temperature. The distributions exhibit strongly trapped sites of tritium, and the sites correspond well to slip bands that appeared on the surface of specimens.

Alternatively, a digital image technique using imaging plate (IP) in terms of tritium radioluminography has been developed [30]. The IP technique utilizes photostimulated luminescence and has a high sensitivity with a large dynamic range of about five orders. The IP enables to obtain not only two-dimensional distributions but also the concentrations of tritium. However, the IP needs a long exposure time of more than several tens hours, and the spatial resolution is limited by the size of pixels, currently a few tens μm.

Decomposition of AgBr in nuclear emulsion takes place also by chemical reactions with hydrogen. Hydrogen microprint technique (HMT) is a method to reduce AgBr in the nuclear emulsion coated on the surface by hydrogen diffusing out from the specimen [31]. Microscopic observation of Ag particles after fixing to remove unreacted AgBr reveals the distribution of emission sites of hydrogen on the surface. Since the development process is not necessary in HMT, the spatial resolution of Ag particles is generally better than tritium autoradiography. A substantial improvement of HMT has been devised, and 0.1 μm in the spatial resolution of Ag particles and 40 % in the detection efficiency of hydrogen have been reported [32]. Figure 2.13 [32] is a SEM micrograph of HMT of a ferrite-pearlite steel plate specimen of 1.8 mm in thickness to which hydrogen was introduced from the opposite side. Preferential evolution of hydrogen from the interface of cementite in pearlite phase is clearly revealed.

Similarly, the silver decoration technique utilizes reduction of Ag^+ ion in a solution by hydrogen. The specimen is immersed in a solution containing $AgNO_3$ and a small amount of KCN and then is rinsed with water and dried. Adsorbed atomic hydrogen on the metal surface is thought to reduce Ag^+ to Ag. Experiments with hydrogen-charged nickel specimens demonstrated different densities of Ag

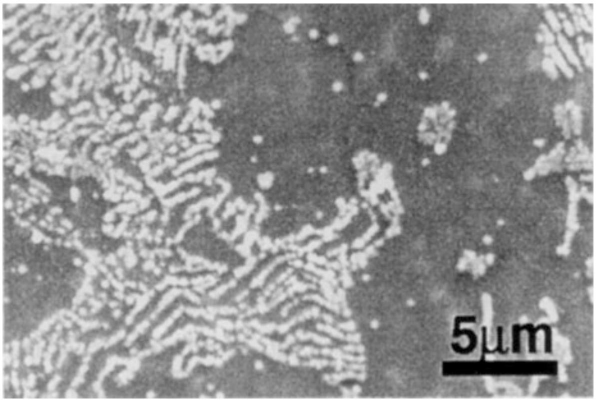

Fig. 2.13 Scanning electron micrograph of hydrogen microprint using gelatin-hardening for a ferrite-pearlite steel (Ichitani et al. [32]. Reprinted with permission from The Iron & Steel Inst. Japan)

particles between neighboring grains or in annealing twins [33]. High densities along slip lines and at grain boundary junctions were also revealed [33].

It should be noticed that states of detected hydrogen in specimen are not always the same between HMT and tritium autoradiography, diffusive in the former while normally non-diffusive in the latter. Observed distributions of Ag particles by HMT indicate desorption sites of hydrogen diffusing out from the surface while autoradiography shows stably trapped sites of hydrogen. Accordingly, the two methods are complementary to each other and the use of the two together is useful for examining interactions of microstructures with hydrogen.

Scanning secondary ion mass spectroscopy (SIMS) is a high sensitivity tool for detecting hydrogen of concentrations as low as the order of ppb. Sputtering the surface of the specimen with a focused primary ion beam ejects secondary ions and exhibits the distribution of elements [34]. The mass/charge ratio of secondary ions is measured with a mass spectrometer. The SIMS method is useful to detect the distribution of hydrogen interacting with different elements. Figure 2.14 [25] shows distributions of D^-, Si^- and P^- in a cold-drawn eutectoid steel specimen subjected to a delayed fracture test in a corrosive solution containing deuterium. Accumulation of deuterium in segregation zones of Si and P is evident. Repeated sputtering of the same area by the primary ion in SIMS measurement gives a three-dimensional distribution image, and the vacuum environment for SIMS enables to distinguish diffusive and non-diffusive types of trapping in the specimen.

Response of hydrogen to external excitations is generally very weak, but neutron interacts strongly with proton. Neutron tomography (NT) is a technique to produce three-dimensional images of the absorbance of neutrons in materials. Hydrogen distributions around blisters formed in iron by electrochemically introduced hydrogen were detected using NT with a spatial resolution of about 25 μm [35]. Hydrogen-charging produced cracks and blisters, and a hydrogen-enriched zone of 50 μm wide was detected surrounding cracks. Hydrogen also accumulated at the sample surface having the highest concentration at blistered areas. The hydrogen accumulation around the cracks could be removed like diffusive hydrogen by a mild temperature treatment.

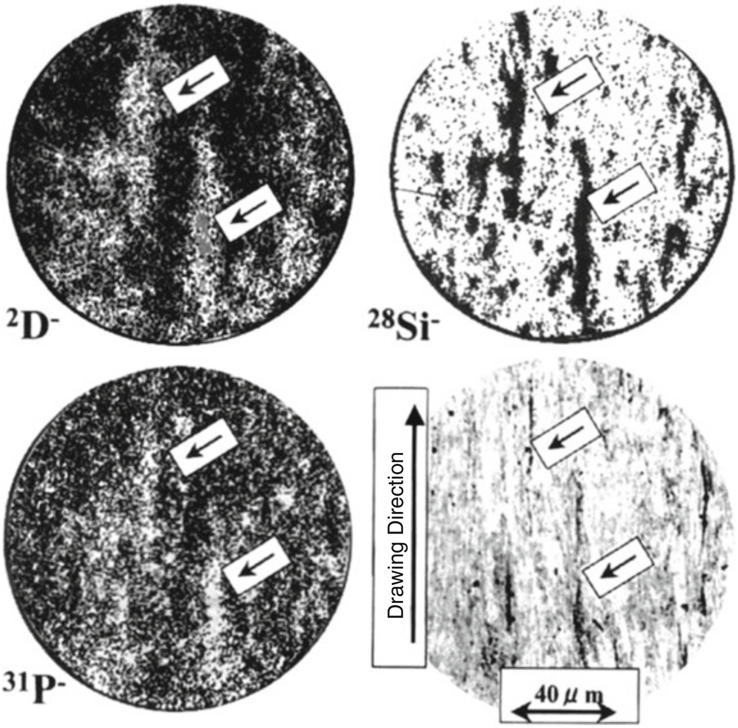

Fig. 2.14 Scanning secondary ion mass spectrometry images of cold-drawn eutectoid steel specimens dipped in a 20 % NH_4SCN deuterium-added aqueous solution. The lower right micrograph shows microstructures (Takai et al. [25]. Reprinted with permission from The Iron & Steel Inst. Japan)

References

1. J.R.G. da Silva, S.W. Stafford, R.B. McLellan, J. Less Common Met. **49**, 407–420 (1976)
2. O.D. Gonzalez, Trans. Metall. Soc. AIME **245**, 607–612 (1969)
3. A.J. Kumnick, H.H. Johnson, Metall. Trans. A **6A**, 1087–1091 (1975)
4. K. Yamakawa, T. Tsuruta, S. Yoshizawa, Boshoku-Gijutsu **30**, 443–449 (1981)
5. R.A. Oriani, P.H. Josephic, Acta Metall. **27**, 997–1005 (1979)
6. K. Yamakawa, in *Advances in Delayed Fracture Solution* (Iron and Steel Institute of Japan, Tokyo, 1997), pp. 77–81
7. P.A. Redhead, Vacuum **12**, 203–211 (1963)
8. W.Y. Choo, J.Y. Lee, Metall. Trans. A **13A**, 135–140 (1982)
9. J.L. Lee, J.Y. Lee, Metall. Trans. A **16A**, 468–471 (1985)
10. K. Ono, M. Meshii, Acta Metall. **40**, 1357–1364 (1992)
11. K. Takai, G. Yamauchi, M. Nakamura, M. Nagumo, J. Jpn. Inst. Metals **62**, 267–275 (1998)
12. H.E. Kissinger, Anal. Chem. **29**, 1702–1706 (1957)
13. J.Y. Lee, J.L. Lee, Philos. Mag. A **56**, 293–309 (1987)
14. R.A. Oriani, Acta Metall. **18**, 147–157 (1970)
15. K. Takai, R. Watanuki, ISIJ Int. **43**, 520–526 (2003)

16. A. Turnbull, R.B. Hutchings, D.H. Ferriss, Mater. Sci. Eng. **A238**, 317–328 (1997)
17. T. Yamaguchi, M. Nagumo, ISIJ Int. **43**, 514–519 (2003)
18. A. McNabb, P.K. Foster, Trans. Metall. Soc. AIME **227**, 618–627 (1963)
19. M. Enomoto, D. Hirakami, T. Tarui, ISIJ Int. **46**, 1381–1387 (2006)
20. Y. Sato, K. Fujita, H. Suzuki, K. Takai, Y. Hagiwara, K. Maejima, N. Miyabayashi, CAMP ISIJ **21**, 1375 (2008)
21. B.G. Pound, G.A. Wright, R.M. Sharp, Acta Metall. **35**, 263–270 (1987)
22. J.P. Hirth, B. Carnahan, Acta Metall. **26**, 1795–1803 (1978)
23. R.B. McLellan, Acta Metall. **27**, 1655–1663 (1979)
24. D.N. Beshers, Acta Metall. **6**, 521–523 (1958)
25. K. Takai, J. Seki, Y. Homma, Tetsu-to-Hagané **81**, 1025–1030 (1995)
26. T. Kasuya, M. Fuji, J. Appl. Phys. **83**, 3039–3048 (1998)
27. P. Lacombe, M. Aucouturier, J. Chéne, in *Hydrogen Embrittlement and Stress Corrosion Cracking*, ed. by R. Gibara, R.F. Hehemann (ASM, Metals Park, 1984), pp. 79–102
28. J. Chéne, A.M. Brass, in *Hydrogen Effects in Materials*, ed. by A.W. Thompson, N.R. Moody (TMS, Warrendale, 1996), pp. 47–59
29. M. Aoki, H. Saito, N. Mori, Y. Ishida, M. Nagumo, J. Jpn. Inst. Metals **58**, 1141–1148 (1994)
30. H. Saitoh, T. Hishi, T. Misawa, T. Ohnishi, Y. Noya, T. Matsuzaki, T. Watanabe, J. Nucl. Mater. **258/263**, 1404–1408 (1998)
31. J. Overjero-Garcia, J. Mater. Sci. **20**, 2623–2629 (1985)
32. K. Ichitani, M. Kanno, S. Kuramoto, ISIJ Int. **43**, 496–504 (2003)
33. T. Shober, C. Dieker, Metall. Trans. A **14A**, 2440–2442 (1983)
34. K. Takai, J. Seki, Y. Homma, Mater. Trans. JIM **36**, 1134–1139 (1995)
35. A. Griesche, E. Dabah, T. Kannengiesser, N. Kardjilov, A. Hilger, I. Manke, Acta Mater. **78**, 14–22 (2014)

Chapter 3
Interactions of Hydrogen with Lattice Defects

The potential energy of hydrogen atom close to lattice defects in metals is mostly lower than that in regular interstitial lattice sites due to elastic and electronic interactions as schematically shown in Fig. 1.1. Various lattice defects are produced in materials during thermal and mechanical processing, and the defects interact with hydrogen in their specific ways. The interactions are crucial for hydrogen embrittlement due to variations of hydrogen concentration around defects and to alterations of the densities and structures of defects. Observed hydrogen effects comprise contributions of various types of defects, but the separation of individual contribution is not easy.

3.1 Dislocations

3.1.1 Experimental Results

Hydrogen embrittlement takes place under applied stress more or less associated with plastic deformation. Dislocations are the primary player in plastic deformation, and hydrogen effects on mechanical properties have been ascribed mostly to interactions of hydrogen with dislocations. However, structures of dislocations associated with their movements are complicated like kinks, jogs, tangles and networks. Further, dislocation movements actually accompany creations of point defects like vacancies and interstitial atoms. Accordingly, the origin of hydrogen effects in plastic deformation is not simple, and experimentally determined parameters of interactions between hydrogen and dislocations must be carefully examined.

(a) Internal friction

Internal friction (IF) exhibits a specific response of dislocations to mechanical stimulations [1]. The IF is the dissipation of mechanical energy of vibration within

M. Nagumo, *Fundamentals of Hydrogen Embrittlement*,
DOI 10.1007/978-981-10-0161-1_3

the elastic range imposed on the specimen. It is normally expressed in terms of the reciprocal loss factor Q^{-1} defined as $\Delta W/2\pi W$, where W and ΔW are the maximum elastic stored energy and the energy dissipation during one cycle, respectively. The Q^{-1} spectrum against temperature rise for deformed iron exhibits two peaks, α- and γ-peaks, due to the movement of dislocations [1]. Various mechanisms of IF associated with the movement of dislocations have been proposed [2], and the α- and γ-peaks are ascribed to double-kink formation of non-screw and screw dislocations, respectively [3].

On the other hand, when hydrogen is introduced into deformed iron, a peak newly appears at intermediate between α- and γ-peaks, and it is named as the hydrogen cold-work peak (HCWP). An excellent correlation of the peak height with hydrogen concentration was observed [4]. The origin of HCWP is interactions of hydrogen with dislocations, but details are not straightforward. Hirth summarized three basic models of HCWP [5]. A simple model of dislocation motion is the string model of a damped oscillation between pinned points on a dislocation line. Schoeck's model is that dislocation drags hydrogen atmosphere as it bows out under oscillating stress [6]. Dislocation motion dragging hydrogen is a thermally activated process accompanying diffusion of neighboring hydrogen. The relaxation time τ of IF, the characteristic time to reach equilibrium, is temperature dependent since it is proportional to the concentration of hydrogen accumulated in dislocations and inversely proportional to the diffusion coefficient of hydrogen near the dislocation core. Then, τ is expressed in terms of the activation energy E_a which is the sum of the binding energy of hydrogen with dislocation E_b and the migration energy of hydrogen E_m. The magnitude of τ is obtained experimentally from the peak temperature vs. oscillation frequency relationship, i.e.,

$$2\pi f \cdot \tau = 1, \tag{3.1}$$

$$\tau = \tau_0 \exp\left(\frac{E_a}{RT}\right), \tag{3.2}$$

$$E_\mathrm{a} = E_\mathrm{b} + E_\mathrm{m}. \tag{3.3}$$

Estimation of E_b from observed E_a is somewhat ambiguous, since the mobility of hydrogen close to the core may differ from that in the bulk. For the case of high hydrogen concentrations close to saturation, E_a is simply equal to E_m.

Alternatively, kink-pair formation accompanying drag of hydrogen has been proposed for HCWP [7, 8]. The model is similar to that for α- and γ-peaks, and Eq. (3.3) is replaced by

$$E_\mathrm{a} = \ 2E_\mathrm{k} + E_\mathrm{m}^{'}, \tag{3.4}$$

where E_k is the kink formation energy and E'_m is the activation energy of diffusion along the core. In the literature, most estimations of E_b were made from experiments conducted following Schoeck's model, and reported values of E_b are around 25 kJ/mol in iron and steels [9–11] as tabulated in Table 3.1. The viability of an

Table 3.1 Experimentally estimated interaction energies of hydrogen with traps in cold-worked iron and steels

Material	Strain (%)	E_a (kJ/mol)	E_b (kJ/mol)	E_m (kJ/mol)	Measuring method	Note	Ref
Very high purity iron	10	32.6			IF		[9]
0.018 % C steel	15	29.6			IF		[9]
Pure iron	16	30	17–25	8.4–12.5	IF		[4]
High purity iron	25	35.1	27	8.4	IF		[10]
Mild steel	20	33	26	7	IF		[11]
Type 430 steel	20	75	43	32	IF		[11]
0.16%C steel	30		25		H-absorption		[12]
0.16%C steel	60		36		H-absorption		[12]
Ferritic steels			20		H-permeation		[12]
AISI 4340			30.5		H-permeation	High occupancy	[12]
0.23 % C steel			25		H-desorption	High occupancy	[12]
Pure iron	0–80		59.9		H-permeation	High occupancy	[13]

E_a, detrapping activation energy; E_b, binding energy; E_m,.migration energy; *IF* internal friction; high occupancy, under high hydrogen concentrations

employed model depends on experimental conditions such as microstructures, applied stress, temperature and hydrogen concentration.

(b) Hydrogen permeation

Trapping parameters are involved in the effective diffusion coefficient D_{eff}, Eqs. (2.16 and 2.17). which is obtained by permeation experiments. The temperature dependence of D_{eff} gives the apparent activation energy of permeation as included in the right-hand side of the equation:

$$\frac{\partial \ln D_{\mathrm{eff}}}{\partial(1/T)} = -\frac{E_m}{R} + \frac{K\mathrm{N}_x/\mathrm{N}_L}{1+K\mathrm{N}_x/\mathrm{N}_L}\frac{E_b}{R}, \tag{3.5}$$

in the domain of low coverage [12]. Oriani analyzed data in the literature on hydrogen permeation or evolution for various steels with and without cold-work [12]. The estimated binding energies, E_b, were in the range of 25 ~ 35 kJ/mol, and the density of trapping sites, N_x, was of the order of 10^{25} m^{-3} in steels without cold-work. Both E_b and N_x increased with increasing amount of cold-work. However, Oriani suggested that microcrack surfaces are more important than dislocations for hydrogen trapping in cold-worked steels.

On the other hand, Kumnick and Johnson conducted hydrogen gas permeation-transient measurements for pure iron specimens given cold-work up to 60 % [13]. Kumnick and Johnson measured the time lag of the permeation and analyzed data using the McNabb-Foster equation for the diffusion accompanying trapping process. Details of permeation experiments and definitions of the time lag are described in Sect. 4.1. The time lag defined as the intersection of the integrated flux and the time axis varies according to the concentration of lattice hydrogen C_0 which is a function of the external hydrogen pressure following Sieverts' law given in Sect. 1.1. According to the McNabb-Foster equation, the time lag was expressed in terms of trap parameters p and k given in Eq. (2.22). The time lag with trapping, t_T, was proportional to the purely lattice time lag t_L, and the ratio $t_\mathrm{T}/t_\mathrm{L}$ was shown to vary according to hydrogen pressure as schematically shown in Fig. 3.1 [13]. For the dilute occupancy region C in Fig. 3.1 for traps under low hydrogen pressures, $t_\mathrm{T}/t_\mathrm{L}$ was independent of lattice hydrogen concentration and was approximated as

$$\frac{t_T}{t_L} = 1 + \mathrm{N}_T \frac{k}{p} = 1 + \frac{\mathrm{N}_T}{\mathrm{N}_L} \exp\left(\frac{E_b}{RT}\right), \tag{3.6}$$

where $\mathrm{N_T}$ and $\mathrm{N_L}$ are densities of trap and lattice hydrogen sites, respectively. On the other hand, for near saturation region A of traps under high hydrogen pressures, the ratio $t_\mathrm{T}/t_\mathrm{L}$ was given as

$$\frac{t_T}{t_L} = 1 + \frac{3\mathrm{N}_T}{\mathrm{C}_0}. \tag{3.7}$$

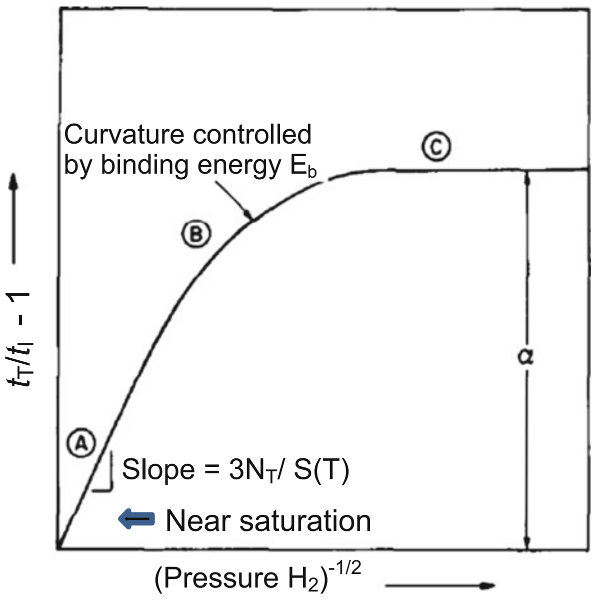

Fig. 3.1 Schematic diagram of variation of time lag with input hydrogen gas pressure for specimen with saturable traps. t_T and t_L are time lag with and without trapping. S(T) is Sieverts' law coefficient (Kummnick et al. [13])

Trap parameters were determined so as to fit calculated t_T/t_L with observed values. Thus, determined E_b was as high as 59.9 kJ/mol for iron given cold-work to 60 % at 318 K. Inferred trap densities were a little less than 10^{21} m^{-3} for annealed iron and a little more than 10^{23} m^{-3} for heavily deformed iron. Experiments were conducted under hydrogen gas pressures lower than 0.1 MPa. The pressure was fairly low, but observed time lags decreased with increasing hydrogen pressure, suggesting that experiments were in a range for saturated traps.

The entity of the trap corresponding to a high E_b of 59.9 kJ/mol is not definite. Kumnick and Johnson suggested some heterogeneous sites along dislocation core, like jogs or point defect debris left behind by moving dislocations. Kumnick and Johnson also noticed that sensitivities of experimental techniques to defects might differ by the range of trapping parameters.

Values of E_b and N_T obtained by IF and permeation experiments are included in Table 3.1. The materials were cold-worked iron and steels, and a single type of trap was assumed. The binding energies extending in a substantial range were not ascribed simply to dislocations. Multiple kinds of traps make transient permeation behaviors dependent on hydrogen concentration, and kinetics of filling traps differ by E_b of each trap as described in Sect. 2.2.2. Data obtained by IF techniques in Table 3.1 may be fairly reliable as interaction energies of hydrogen with dislocations in iron, but details of interactions as the origins of data obtained by different methods are not yet established experimentally.

(c) Thermal desorption analysis

The hydrogen absorption capacity in steels generally increases by plastic straining, indicating the increase in the density of lattice defects that trap hydrogen. Choo and Lee conducted TDA of hydrogen introduced to cold-drawn iron bar specimens of 5 mm in diameter [14]. Hydrogen was introduced under 0.2 MPa hydrogen pressure at 673 K, and TDA measurements were conducted after degassing mobile hydrogen at room temperature for 6 h. Application of Eq. (2.11) gave 19.2 kJ/mol for E_b after subtracting 7.6 kJ/mol for E_m from E_a. Choo and Lee assumed that remained hydrogen was trapped in dislocations and that desorption was dissociation-controlled. On the other hand, Ono and Meshii conducted TDA of hydrogen electrochemically introduced to a cold-rolled single crystal of pure iron. Assuming diffusion-controlled desorption under dynamic equilibrium between trapping and detrapping processes described in Sect. 2.1.2 (b), E_b of 47 kJ/mol gave good agreement between simulated and experimental TDA profiles [15].

The hydrogen absorption capacity increases associated with plastic straining, but the increase cannot be ascribed simply to dislocations. Figure 3.2 [16] shows the amounts of tritium introduced by cathodic electrolysis into low-carbon ferritic steel given tensile strain up to 25 % at 25 °C and −50 °C. The TDA measurement was conducted up to 800 °C, and the amount of tritium was expressed in terms of radioactivity. Thermal desorption almost totally took place in the temperature range between 120 and 150 °C showing a single desorption-rate peak. Tritium acts as the tracer of lattice defects, and the amount of desorbed tritium is a measure of the density of strain-induced defects. A noteworthy result was that the increase in the

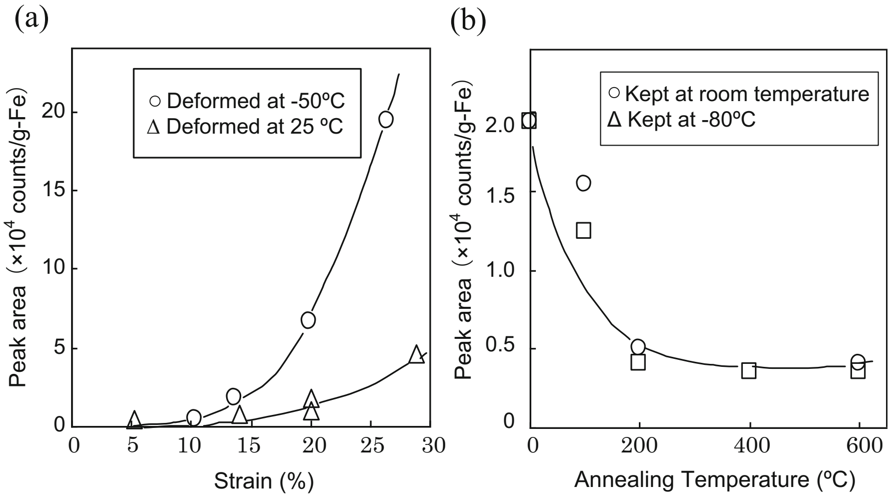

Fig. 3.2 Amounts of tritium absorbed in strained low-carbon ferritic steel. (**a**) Dependence on the amount of strain, (**b**) on the annealing temperature after straining by 20 % at −50 °C. Keeping temperature after straining was room temperature or −80 °C (Nagumo et al. [16])

hydrogen absorption capacity was almost totally reduced by aging the deformed specimens at temperatures as low as 200 °C. The density of dislocations must increase with strain, but annealing experiment implies that lattice defects concerned with the increase in absorbed tritium are point defects, mostly vacancies, rather than dislocations. The deformation temperature dependence of the hydrogen absorption capacity also implies that dislocations are not the primary sites of hydrogen trapping in this case. It is to be reminded that the partition of hydrogen among multiple traps is dependent on hydrogen fugacity as shown in Fig. 2.10. The cathodic electrolysis to introduce tritium in Fig. 3.2 was conducted using 1 N NaOH tritated aqueous solution at a current density of 25 A/m^3 for 2 h. The condition is fairly mild so as to avoid the formation of extraneous damage in the specimen. Further, Fig. 2.10 for the preferential partition of hydrogen at traps of different binding energies implies that deeper traps than dislocations, like vacancies, operate as predominant sites of hydrogen trapping.

3.1.2 Theoretical Estimation of Hydrogen-Dislocation Interactions

Interactions of dislocations with interstitial atoms such as carbon and nitrogen have been well accepted as the origin of yield point phenomena in steels. The interaction energy of a hydrogen atom with the elastic field of an edge dislocation is expressed as [17]

$$W = \frac{Gb\,(1+v)\;\delta\mathrm{v}\;\sin\,\theta}{3\pi\,(1-v)\,r}, \tag{3.8}$$

where G is shear modulus, b is Burger's vector, v is Poisson's ratio, δv is internal volume change around a hydrogen atom, r and θ are cylindrical coordinates fixed on the dislocation line. The volume change δv is 1.2 ml/mol in iron and is related to the partial molar volume V_H by

$$\delta\mathrm{v} = \frac{\mathrm{V}_H(1+v)}{3\,(1-v)}. \tag{3.9}$$

Then, the value of W is 28 kJ/mol for a hydrogen atom located at $r = 0.4$ nm and $\theta = \pi/2$. The elastic field of edge dislocation attracts hydrogen atoms, and Hirth and Carnahan numerically calculated the integral amount of hydrogen atoms in both the Boltzmann and Fermi-Dirac distributions [18]. Results in the two distributions beyond a critical inner cutoff radius of 0.248 nm were similar, but the use of the Fermi-Dirac distribution was necessary in a near core region.

An atomistic calculation of the distribution and the trap energy of hydrogen around an edge dislocation in iron was conducted by Taketomi et al. [19] The model dislocation was a $\{112\} < 111 >$ edge dislocation on a $\{112\}$ plane and the crystalline-disordered region was denoted as the dislocation core. Two types, tetragonal (T) and octahedral (O), of hydrogen occupation sites were considered and the energy of the system was calculated using an embedded atom method (EAM) potential. The hydrogen-trap energy is sensitive to both hydrostatic and shear stresses, and strong trap sites are distributed on the slip plane around the dislocation core. The calculated hydrogen-trap energy varies by the type of site and region around the dislocation core. The maximum trap energy in the core was about 42 kJ/mol. In outside of the core, the maximum trap energy was about 12 kJ/mol at a T-site below the slip plane, while O-sites showed much stronger trap energy in a region along the slip plane.

On the other hand, a straight screw dislocation has no long-range hydrostatic stress field. Elastic interaction with hydrogen appears in regions near wiggles on a flexible screw dislocation, leading to relatively weak and short-range elastic interactions. The origin of the high potential barrier has been attributed to core structures of screw dislocations [20]. Atomistic simulations with different methods have been conducted on the core structures and kink-pair formation [21–24].

Screw components of dislocations determine the mobility of dislocations in body-centered cubic metals at low temperatures, and thermal activation of kink pairs mediates the motion of screw dislocation. Wen et al. calculated the energy of a 1/2[111] screw dislocation introduced into a supercell in bcc iron using an EAM [25]. One hydrogen atom was placed at various sites in the core, and the binding energy of hydrogen was defined as the difference in energies between the states with and without hydrogen atom. The binding energies of hydrogen at thirteen sites available to hydrogen atom in the core were in the range between 43 and 4.3 kJ/mol.

On the other hand, Itakura et al. calculated the energy of screw dislocation using the density functional theory (DFT), placing a hydrogen atom at each *T*-site near the core [26]. The binding energy E_b of a specific site was defined as the hydrogen solution energy E_s referred to the bulk *T*-site. The expression of E_s was in the form

$$E_s = E_{d+H} - E_d - E_{H_2}/2, \tag{3.10}$$

where E_{d+H}, E_d and E_{H2} denote energies of a dislocation with a hydrogen atom, a reference dislocation configuration and a hydrogen molecule, respectively. Calculated values of E_b varied by the core configuration and site of hydrogen atom. The maximum values of E_b in the stable and unstable core configurations were 25 kJ/mol and 38 kJ/mol, respectively. The authors deduced that a hydrogen atom can lower the Peierls barrier by about 12.5 kJ/mol. Softening and hardening effects of hydrogen are expected by the reduction of either kink nucleation enthalpy or kink trapping, respectively. The calculations on the mobility of screw dislocations are further described in Sect. 5.5.2.

First-principles calculations of the electron structure affected by interstitial atoms in fcc iron were conducted by Gavriljuk et al. [27, 28]. The results were applied to the analysis of the interactions between dislocations and interstitial atoms. The calculations were for cases of fairly high hydrogen concentrations, 3 ~ 5 at% in atomic ratio [27] or 0.25 or 1.0 in an elementary cell [28]. The results are that hydrogen increases the density of conduction electrons in the vicinity of hydrogen atoms and lowers the shear modulus, the stress for the activation of dislocation sources, the line tension of dislocations and the distance between dislocations in the pileups. Similar effects as hydrogen are expected for nitrogen, but opposite for carbon because carbon decreases the density of conduction electrons around dislocations [27].

Interactions of hydrogen with dislocations strongly depend on structures of dislocations. Model structures of dislocations employed for theoretical estimations cited above are simplified for the convenience of calculation. Actually, densities of dislocations in steels that exhibit hydrogen embrittlement are very high and inhomogeneous segments on dislocation lines such as kinks, jogs, tangles and cell configurations induce complex stress and displacement fields.

Alternatively, Kirchheim developed an extensive theory on the stabilization of lattice defects by hydrogen in a thermodynamic scheme [29, 30]. By analogy with the Gibbs adsorption isotherm for a change in the surface energy by the adsorption of molecules, the total free energy of the system is reduced when solute atoms segregate at lattice defect. The reduction is ascribed to the decrease in the formation energy $d\gamma$ of the defect. The expression of $d\gamma$ in terms of the excess of solute at defect, Γ, and the change of the chemical potential on segregation, $d\mu$, for a solute A is in the form of

$$d\gamma = -\Gamma_A d\mu_A . \tag{3.11}$$

For dislocation, Γ_A was defined under constant temperature, volume and chemical potentials of A and the solvent as

$$\Gamma_A = \left.\frac{\partial n_A}{\partial l}\right|_{T,\,V,\mu_A,\mu}, \tag{3.12}$$

where l is the dislocation length and n_{A} is the number of A atoms under open system.

The decrease in the formation energy in the presence of hydrogen activates dislocation sources. Then, it was supposed that newly generated dislocations push former dislocations together with the ease of kink-pair formation and that the sequence appears as the observed enhanced mobility of dislocations by hydrogen [31]. This defect acting agent (DEFACTANT) mechanism is general and can be applied to formation energies of various defects such as dislocations, vacancies, grain boundaries and crack surfaces [31].

3.2 Vacancies

Vacancies play a crucial role in creep failure of metallic materials at high temperatures, but their role in hydrogen embrittlement has not been paid so much attention. Then, in order to understand interactions between hydrogen and vacancies, this section starts from some general attributes of vacancies.

3.2.1 Density

(a) Thermal equilibrium

The density of a single vacancy C_{V} in thermal equilibrium is given as [32, 33],

$$C_{\mathrm{V}} = A\exp\left(-\frac{H_f}{RT}\right), \tag{3.13}$$

where A is the entropy factor of $1 \sim 10$ in most metals and H_f is the formation enthalpy of mono-vacancy. The magnitude of C_{V} is obtained directly from measured thermal dilatations subtracting the change of lattice constants, and the temperature dependence of C_{V} gives H_f. Reported values of C_{V} are very small, 2.4×10^{-11}, 1.3×10^{-21} and 7.6×10^{-27}, respectively, for Al, Cu and α-Fe at room temperatures with $\mathrm{A} = 5$. It is to be noticed that observed C_{V} involves clustered vacancies [32]. The values of H_f are 65, 124 and 154 kJ/mol for Al, Cu and α-Fe, respectively.

Positron annihilation spectroscopy (PAS) is another powerful tool for measuring vacancy concentrations [32, 34]. Positrons injected into metal crystals migrate through the lattice before annihilation with electrons, and the lifetime depends on the diffusional path. Vacancies effectively trap positron because of its relatively long lifetimes owing to low electron densities. The positron lifetime in vacancies is enhanced by 20 ~ 80 % to that in the perfect lattice. The positron-trapping probability in vacancies is proportional to the vacancy concentration. The trapping rate κ_{v} is expressed as

$$\kappa_v = \mu_v C_V , \tag{3.14}$$

where μ_{v} is the specific trapping rate for mono-vacancy and is estimated to be $(1.1 \pm 0.2) \times 10^{15}$/s [35]. The value of κ_{v} is determined from observed positron lifetime.

Positron annihilation is detected by measuring γ-ray emitted at the time of annihilation. Doppler broadening of annihilation γ-rays is utilized to distinguish annihilations with core and conduction electrons. The formation enthalpy H_f is calculated from observed Doppler broadening by using a trapping model. The obtained values of H_f for pure iron are 173 and 193 kJ/mol in the paramagnetic and ferromagnetic state, respectively [36]. Applications of PAS to hydrogen effects on lattice defects are presented in following Sects. 3.2.2 and 3.2.3(b).

(b) Generation associated with plastic deformation

The density of vacancies substantially increases associated with plastic deformation. The density of point defects amounting to 4×10^{-5} was estimated from electrical resistivity measurements on annealing iron strained to 20 % [37]. The observed density of point defects is ascribed mostly to vacancies because of the lower formation energy of vacancy than that of interstitial.

Generation of vacancies by mutual interactions of moving dislocations is well accepted. Van Bueren considered randomly distributed dislocations that form a spatial network [38]. Each element of the network can act as dislocation sources, and a generated dislocation loop crosses dislocations and forms jogs. The density of point defects left behind in the wake of moving jogs on the dislocation was estimated as $1.3 \times 10^{21} \varepsilon^2/\mathrm{cm}^3$ in the case of multiple glide in copper. Cuttiño and Ortiz considered the motion of jogged screw segments formed by dislocation intersection and by double cross slip [39]. Computed vacancy concentrations in a uniaxial tension test on copper single crystal oriented for single slip are shown in Fig. 3.3 [39]. Quadratic dependence on strain appears in the multiple glide region, and the expected C_{v} is as high as 10^{-4} at strain of 30 %. An alternative mechanism of generating a high density of vacancies is mutual annihilation of dislocations of opposite signs approaching on closely neighboring glide planes [40]. The density of point defects depends on the density of dislocations, and a high concentration ~ 10^{-3} is expected for vacancies in the dislocation-rich walls of persistent slip bands in fatigued copper [40].

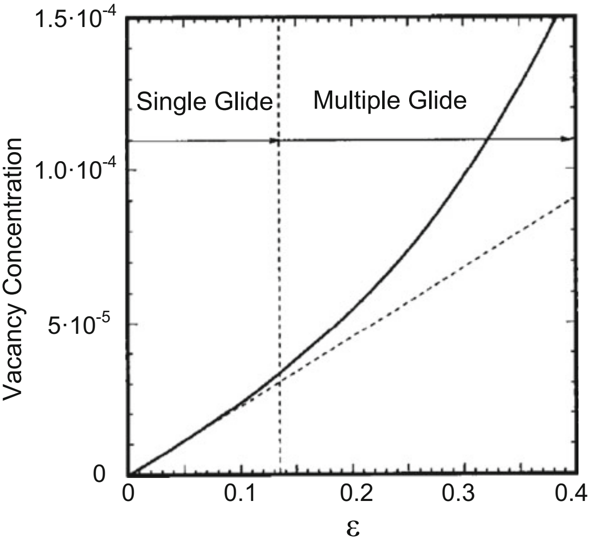

Fig. 3.3 Vacancy generation by the motion of jogged dislocations vs. axial strain (Cuttiño et al. [39])

3.2.2 Vacancy Clusters and Migration

Vacancy clusters and vacancy-impurity complexes are formed during migration, and the energies of vacancies are reduced by forming clusters. The formation enthalpy of a vacancy cluster of order n, $H_{f,,nv}$, is defined as

$$H_{f,\,nv} = nH_{f.1\,v} - H_{b,nv}\ , \tag{3.15}$$

where $H_{b,nv}$ is the binding enthalpy of a n-cluster. The $H_{b,nv}$ depends on the configuration of the vacancy cluster and a first-principles calculation of $H_{b,nv}$ was conducted for various configurations in α-iron [41]. The most stable configurations of n-vacancies in bcc structures are compact clusters, followed in order of decreasing stability by double layers, linear chains, tetravacancies, single layers, trivacancies and divacancies. Calculated dissociation energies of vacancy clusters of $V_n \rightarrow V_{n\text{-}1} + V_1$ increase with increasing cluster size, i.e., 85, 94, 117,140 kJ/mol for $n = 2$, 3, 4, 6, respectively, and almost constant for $n > 6$.

Positron annihilation spectroscopy is a useful tool for detecting vacancy clusters, and positron states thereof have been calculated using the density functional theory (DFT) [42]. Calculated positron binding energies and lifetimes for vacancy clusters shown in Fig. 3.4 [42] are listed in Table 3.2 [42]. When multiple traps are present, the observed positron lifetime τ is a weighted mean of lifetime components τ_i in each trap, i.e.,

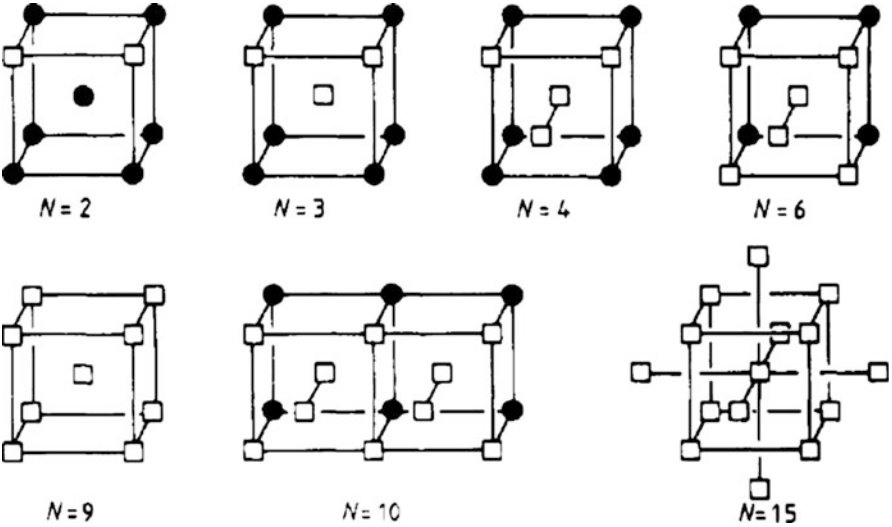

Fig. 3.4 Vacancy agglomerates in bcc structures. N is the number of vacancies (open square) in the agglomerate. *Filled circles* denote lattice sites (Puska et al. [42], Reprinted with permission from IOP Publishing)

Table 3.2 Calculated positron lifetime τ and binding energy E_b in vacancy clusters in Fe and Ni

Number of vacancies		1	2	3	4	6	10(Fe) 13(Ni)
Fe	τ(ps)	190	197	232	262	304	334
	E_b(eV)	3.0	4.0	5.6	6.6	7.7	8.6
Ni	τ(ps)	184	203		263	288	376
	E_b(eV)	2.6	3.8		5.9	6.8	9.2

Puska et al. [42], Reprinted with permission from IOP Publishing

$$\tau = \sum_{i=1}^{N} I_i \tau_i . \tag{3.16}$$

On isochronal annealing from 77 K for high-dose electron-irradiated pure ion, two-step decrease at about 220 and 350 K appeared as shown in Fig. 3.5 [35] for the short positron lifetime component τ_1 in a two-components analysis of τ. Alternatively, a long-lifetime component τ_2 appeared at 220 K, extended its value gradually on increasing the annealing temperature and finally disappeared at about 500 K. The decrease in τ_1 and the appearance of the τ_2 component at 220 K were ascribed to the thermally activated mobilization of mono-vacancies introduced by irradiation and the formation of small clusters. Successive increase in τ_2 was likely due to the increasing cluster size as shown in Table 3.2. The disappearance of τ_2 component at 500 K was ascribed to full annealing out of vacancy clusters and annihilation of dissociated vacancies [35].

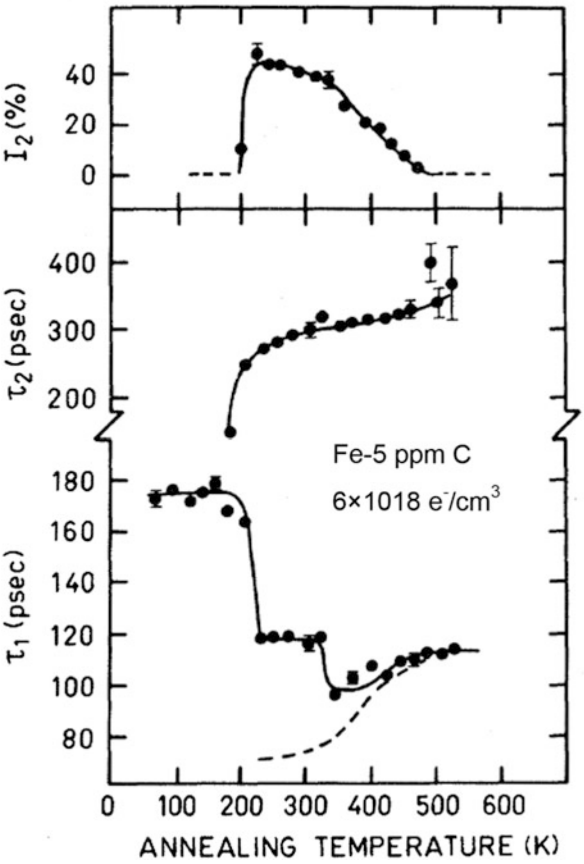

Fig. 3.5 Positron lifetime parameters vs. isochronal annealing temperature in the high-dose electron-irradiated pure iron (Vehanen et al. [35], Reprinted with permission from American Physical Society)

Interstitial impurities trap migrating vacancies and free carbon atoms form carbon-vacancy pairs or complexes [35]. For iron carbon-doped by 50 and 750 ppm, the decrease in τ_1 at 220 K indicated that the tendency of vacancies to form clusters decreased with carbon addition. For iron carbon-doped by 750 ppm, the short positron lifetime τ_1 after the drop at 220 K kept a higher level than that in pure iron [35]. The phenomenon was ascribed to the capture of migrating vacancies by carbon atoms, forming immobile carbon-vacancy pairs at the expense of forming vacancy clusters. The positron lifetime of the carbon-vacancy pair was estimated to be about 130 ps, much less than 190 ps for mono-vacancy. It was also suggested that the onset of free migration of carbon at 350 K caused further decoration of carbon-vacancy pairs that no longer had positron-trapping capability. The capability of positron capture of carbon-vacancy complexes is likely less than vacancy clusters, but it still remains on isochronal annealing above 350 K and disappears at 500 k due to the dissociation of the complexes [35].

Vacancies are mobile even at temperatures as low as 220 K in α-iron, but large three-dimensional clusters are immobile. The smallest immobile cluster is the tetravacancy. From the growth rate of interstitial-type dislocation loops introduced by electron irradiation, the estimated activation energy of migration of a single vacancy in iron was 120 kJ/mol [43]. On the other hand, calculated migration energies of mono-, di- and trivacancies in α-iron are in the range of 63.7–65.6 kJ/mol [41]. It is to be noticed that vacancy clusters must dissociate in order that the migration of vacancies takes place. In fcc metals such as Au, Al and Pt, calculated migration energies are in decreasing order from mono- to trivacancies [44]. A possible reason is that relatively loosely bound trivacancy is more mobile than divacancy which in turn is more mobile than mono-vacancy [44]. The disappearance of positron capture at 500 K implies that the dissociation of vacancy clusters takes place and that migrating vacancies annihilate in sites such as dislocations, grain boundaries and surfaces.

Electrical resistivity measurement is also used to detect lattice defects. Resistivity of pure iron increases by cold-work, and the strain-induced resistivity recovers on isochronal annealing. The recovery that took place from room temperature to 673 K was rather gradual, and then two stages appeared, the one centered around 753 K and the other distinctly at 823 K [37]. The continuous recovery up to 713 K was ascribed to the annihilation of point defects that amounted to the density of 10^{-5}. The further recovery was ascribed to the reduction in the density of dislocations that amounted to 10^{10} cm^{-2}. Annealing out of vacancy clusters at about 600 K and of dislocations at above 800 K was also detected by means of PAS for pure iron plastically deformed by 60 % [35].

It is to be noticed that the temperature at which recovery takes place on isochronal annealing varies not only by the presence of impurities but also by the concentration of vacancies. Decrease in the recovery temperature associated with increased quenching temperatures was observed in Au and Al corresponding to increased concentrations of quenched in vacancies [44].

3.2.3 Interaction of Hydrogen with Vacancies

(a) Binding energy and trapping configuration

Measurements of the binding energy of hydrogen with vacancies in metals were conducted extensively by Myers et al. by means of deuterium implantation methods [45–50]. Deuterium was ion-implanted at 15 keV into pure iron and formed a deuterium-rich zone close to the surface accompanying irradiation-induced defects [45]. Subsequent temperature ramp caused diffusion of deuterium. The concentration of deuterium in the implanted zone was detected using a 0.7 MeV^{3}He ion beam that yielded counting protons by the D(^{3}He, p) ^{4}He nuclear reaction on the impingement. The release of deuterium from the implanted zone took place in two stages on the temperature ramp, and each stage was modeled mathematically using diffusion

Table 3.3 Binding energies of deuterium with vacancies produced by ion implantation

Material	$E_{\text{V-H}}$ (kJ/mol)	Type of vacancies	Ref.
Fe	46	Monovacancy	[45]
Fe	51	Monovacancy	[46]
Fe	68	Cluster	[46]
Fcc stainless steels	22	Cluster	[47]
Ni	23	Monovacancy	[48]
Ni	41	Multi-Vacancy	[48]
Cu	41	Monovacancy Small cluster	[49]
Mo	111	Cluster	[50]
Mo	99	Monovacancy (Low occupancy)	[50]
Mo	77	Monovacancy (High occupancy)	[50]

equations of the McNabb-Foster type, Eqs. (2.21 and 2.22), which included trapping terms. Trapping parameters were determined numerically so as to fit the theoretical calculation to experimental data. A sharp release stage centered around 260 K was ascribed to the migration of detrapped deuterium from deuterium-monovacancy pairs of 46 kJ/mok in the binding enthalpy. The successive stage in 350–450 K was ascribed to detrapping from a small vacancy cluster with the binding enthalpy of about 78 kJ/mol [45]. The figures were corrected later to 51 and 69 kJ/mol, respectively, in a modified experiment that suppressed the loss of deuterium from the surface [46].

Binding enthalpies of hydrogen with vacancies in various metals obtained by ion-implantation methods are listed in Table 3.3. In austenitic stainless steels, all release data of deuterium are approximately consistent with trapping at a single binding enthalpy of ~22 kJ/mol [47]. It is also to be noticed that the binding energy with vacancies alters by multiple trapping of hydrogen as described shortly.

Experimentally obtained binding enthalpies were theoretically rationalized referring to the location of hydrogen atom neighboring vacancies. Experimentally, a ^{3}He ion-channeling measurement for deuterium in an iron single crystal with the binding energy of 46 kJ/mol revealed that the deuterium atom displaced by 0.04 nm from the octahedral position along a $<100>$ direction toward a nearest-neighbor vacancy site [45]. The reason for the displacement is that a deuterium atom seeks the optimum electron density so as to minimize its energy. The binding energy of hydrogen atom calculated using an effective medium theory (EMT) was consistent with the observed one when a displacement of 0.05 nm was assumed [51].

There are 6 O-sites and 8 or 24 T-sites in fcc or bcc structure, respectively, around a vacant lattice site. Multiple occupations by hydrogen were deduced experimentally from ion-implantation experiments of deuterium with different fluencies. Figure 3.6 [52] shows effects of deuterium fluence on retained concentrations of deuterium in the implanted zone in iron after a linear temperature ramp. A decrease in the deuterium concentration appeared at 220 K, and the decrease was

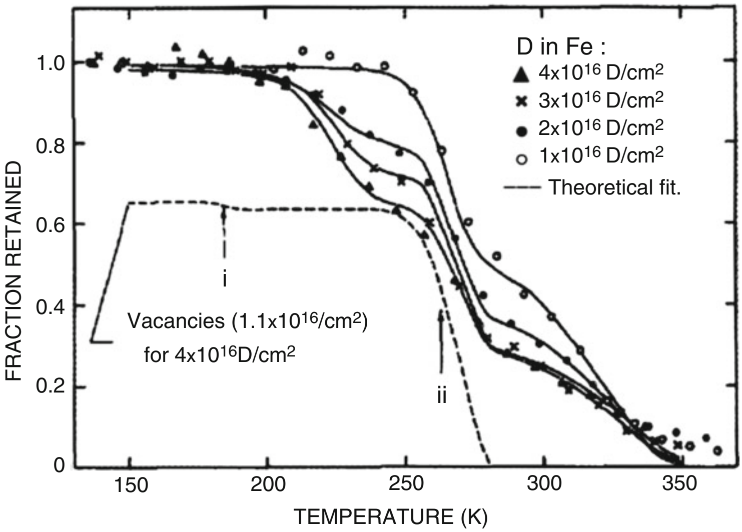

Fig. 3.6 D retention vs. temperature profile of 15-keV D in Fe. Strong He traps at 1.2 μm act as sinks for the released D (Besenbacher et al. [52], Reprinted with permission from AIP Publishing LLC)

enhanced with increasing deuterium fluence. The shift of the start of deuterium migration to lower temperatures associated with higher fluences was ascribed to the release of deuterium from multi-trapped states at mono-vacancy when the binding energy decreased with the increasing number of trapped deuterium atoms.

Binding enthalpies were also calculated using EMT for occupancy of 1–6 deuterium atoms for a vacancy in transition metals [53]. In EMT, the binding energy is defined as the energy required to embed a hydrogen atom into the host metal, and the hydrogen trapping energy in multiple occupancy is defined for the last hydrogen atom in VH_N complex as

$$\Delta E(N) = E(N) - E(N-1) - E^{\text{sol}}, \tag{3.17}$$

where E^{sol} denotes the interstitial binding energy [53]. The observed profiles in Fig. 3.6 were in agreement with the ones calculated using trapping enthalpies of 61 kJ/mol for $N = 1$–2 and 41 kJ/mol for $N = 3$–6 [52]. The results implied decreasing trapping strength with increasing occupancy. Trapping energies calculated afterward using a modified EMT are included in Fig. 3.7 [54] with open circles.

Trapping energies for multiple hydrogen occupancy for a mono-vacancy were also calculated for iron using the density functional theory (DFT) [54, 55]. Calculated trapping energies of VH_N complexes in iron are shown in Fig. 3.7 together with the previous results of EMT calculations [53]. The DFT calculation shows that trapping energies of VH_1 and VH_2 are about 60 kJ/mol and that VH_6 is unstable. The calculation also shows that up to three hydrogen atoms are exothermically bound to mono-vacancy. Thus, very high site-occupancies of hydrogen are

Fig. 3.7 Hydrogen trapping energy in α-Fe calculated using DFT (*filled circle*) and EMT (*open circle*) (Tateyama et al. [54], Reprinted with permission from American Physical Society)

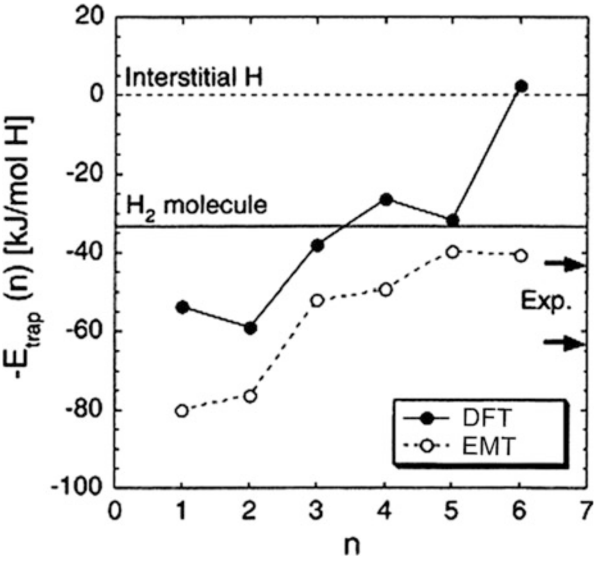

expected for VH and VH_2 and most vacancies may exist in the form of VH_2 [55]. Another atomistic calculation using DFT combined with molecular dynamics and Monte Carlo methods [56] showed that a three-dimensional tetrahedral configuration has the lowest energy for VH_4 and the binding was exothermic.

An explanation of the stability deduced by the DFT analysis was that Fe3*d*-H1*s* hybridization causes charge transfer to the region around the hydrogen atom from neighboring iron atoms. Resulting negatively charged hydrogen atoms might repel each other, and distances between hydrogen atoms and the corresponding *O*-sites in the VH_N complexes were calculated to decrease with the increasing number of trapped hydrogen atoms *N* [54].

(b) Enhanced generation of vacancies

The increase in the hydrogen absorption capacity by plastic straining was revealed by means of hydrogen thermal desorption analysis (TDA) as shown in Fig. 3.2 for low-carbon ferritic steel. TDA profiles corresponding to the increase are shown in Fig. 2.4 for cold-drawn eutectoid steel. The increase in the hydrogen absorption capacity associated with plastic straining is enhanced when hydrogen is present at the time of straining. Figure 3.8 [57] shows the amount of hydrogen introduced to specimens of pure iron and Inconel 625 alloy as the tracer of defects. In Fig. 3.8, the tracer-hydrogen introduced to saturation into specimens is denoted as [strain], [H + strain] and [H + strain + 200 °C], each respectively indicating specimens "strained," "strained after hydrogen precharging" and "annealed at 200 °C after hydrogen precharging and straining." The enhanced increase by hydrogen precharging is generally observed for various steels and is in accord with the notion that hydrogen enhances the formation of strain-induced vacancies and their clustering, i.e., hydrogen-enhanced creation of strain-induced vacancies (HESIV).

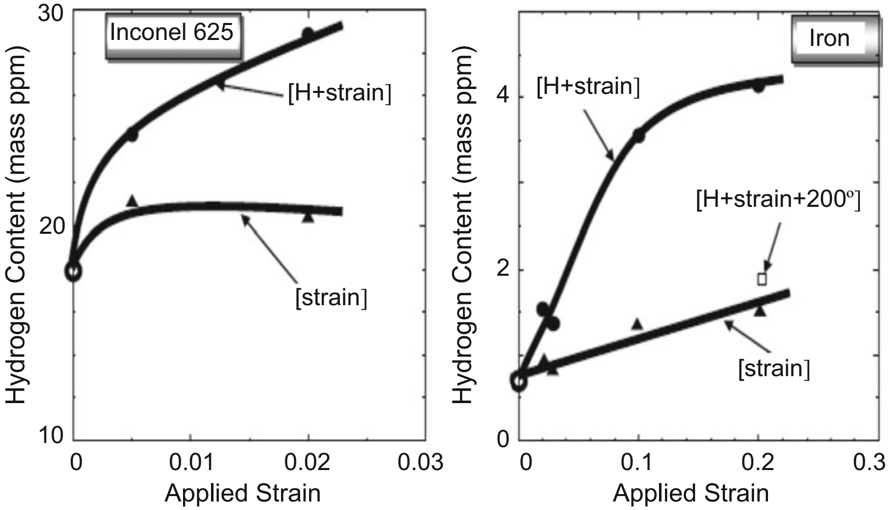

Fig. 3.8 The amounts of the tracer-hydrogen introduced to iron and Inconel 625 specimens after straining [strain], strained after hydrogen-precharging [H + strain] and further annealing at 200 °C [H + strain + 200 °C] (Takai et al. [57])

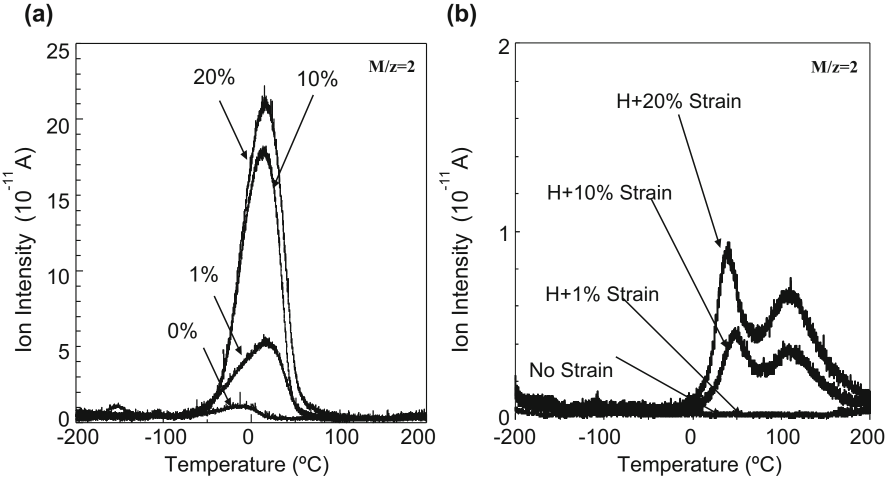

Fig. 3.9 LTDS profiles of hydrogen introduced into iron specimens given strain up to 40 % (**a**) without and (**b**) with hydrogen precharging. The thickness of specimen and the concentration of NH_4SCN are 0.3 mm and 20 % at 50 °C for (**a**) and 0.4 mm and 0.05 % at 30 °C for (**b**), respectively (Sato et al. [58], Abe et al. [59], Reprinted with permission from The Iron & Steel Inst. Japan)

The nature of strain-induced defects that interact with hydrogen has been examined by means of TDA and PAS. The low temperature thermal desorption spectroscopy (LTDS) described in Sect. 2.1.2(d) could firstly separate different strain-induced traps of diffusive hydrogen. Figure 3.9 [58, 59] shows LTDS profiles

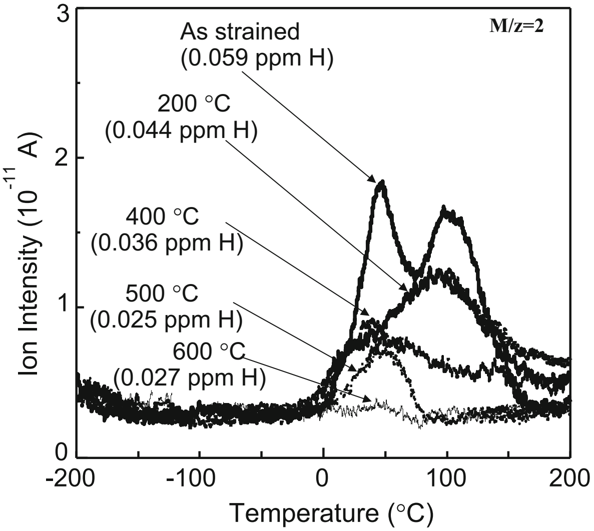

Fig. 3.10 LTDS profiles of hydrogen introduced into iron specimens given straining of 20 % and subsequent annealing at different temperatures. Hydrogen charging is by immersing specimens of 0.4 mm in thickness in a 0.05 mass % NH_4SCN aq at 30 °C for 6 h. Hydrogen contents are shown in brackets (Takai [60], By courtesy of Prof. K. Takai before publication)

of hydrogen introduced as the tracer of defects into specimens of pure iron given tensile strain up to 40 % with and without hydrogen precharging. Tracer-hydrogen was introduced by immersing specimens in aqueous solution of NH_4SCN. The amount of the tracer-hydrogen increases with strain, and effects of hydrogen precharging are characterized by a subpeak that appears at the higher-temperature side.

The strained specimens were then subjected to annealing at various temperatures, and hydrogen was again introduced as the tracer of defects.

Figure 3.10 [60] shows the change of LTDS profiles of the tracer-hydrogen with elevated annealing temperatures. The desorption at around 100 °C was substantially reduced by annealing at temperatures higher than 400 °C, while the lower temperature peak centered around 50 °C showed a two-step decrease firstly by annealing at 200 °C and completely at about 600 °C. The peak around 100 °C corresponds to the annihilation of vacancy clusters. The origin of the 50 °C peak is not definite. The changes in TDA profiles caused by annealing are due to not only the binding energy with traps but also to changes in the structure of trapping defects. As described in Sect. 3.2.3(a), deuterium implantation experiments revealed detrapping of deuterium from small vacancy clusters at 350–450 K. A possible origin of the substantial reduction of the low temperature peak by 200 °C annealing is reconfiguration of vacancy clusters associated with annealing and the resulted decrease in the affinity with tracer-hydrogen. A small further decrease in the 50 °C peak by annealing at 600 °C may be ascribed to the annihilation of dislocations trapping in which has been unable to detect by conventional TDA technique.

Positron annihilation spectroscopy (PAS) is a more direct method to reveal the nature of lattice defects as described in Sects. 3.2.1 and 3.2.2. Figure 3.11 [61] shows mean positron lifetimes τ_m in pure iron on isochronal annealing after tensile

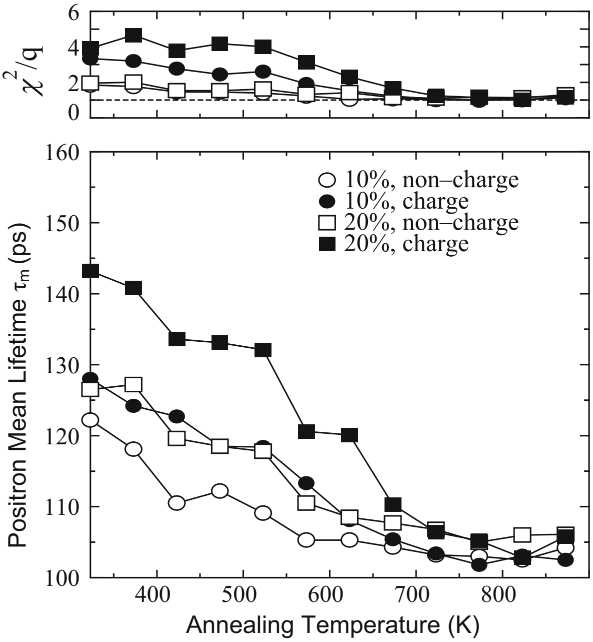

Fig. 3.11 Positron mean lifetime during isochronal annealing of iron deformed with and without hydrogen precharging. Filled marks denote hydrogen-precharged specimens (Sakaki et al. [61])

straining at room temperature with and without hydrogen precharging. The increase in τ_m by straining is enhanced by the presence of hydrogen at the time of straining. Annealing at 900 K reduced τ_m to 100 ± 2 ps which is coincident to the calculated τ in the α-Fe lattice [42]. The variances, χ^2/q, larger than 2.0 for τ_m in deformed iron indicate that τ_m is composed of multicomponents.

Significant recoveries of τ_m that appear at about 400 K, 550 K and 650 K were analyzed to components. Figure 3.12 [61] shows results for specimens deformed by 20 % (a) without and (b) with hydrogen precharging. In the annealing temperature range from 400 K to 625 K, the longer lifetime in two-component analyses was 150 ps that is coincident with a calculated τ in dislocations [62]. At temperatures lower than 375 K for (a) and 575 K for (b), three-component analyses gave the longest components τ_3 over 400 ps. The recovery stage corresponds to the annihilation of vacancies and τ_3 indicates positron lifetime likely in large vacancy clusters.

Figures 3.11 and 3.12 exhibit hydrogen effects that increase τ_m and retain the longest lifetime component τ_3 at high temperatures. The relative intensity of the τ_i component is related to the positron-trapping probability κ_i in Eq. (3.14) and κ_i is proportional to the concentration of the i-th defect C_i [35, 62]. The estimated densities of dislocations and vacancies are listed in Table 3.4 [61]. The density of dislocations increases with the amount of plastic strain as expected, but no effects of hydrogen appeared on the increase. On the other hand, a substantial enhancement by hydrogen is evident for the strain-induced generation of vacancies. This HESIV is consistent with the TDA results shown in Figs. 3.8 and 3.9 and manifests the preferential effect of hydrogen on strain-induced generation of vacancies rather than dislocations.

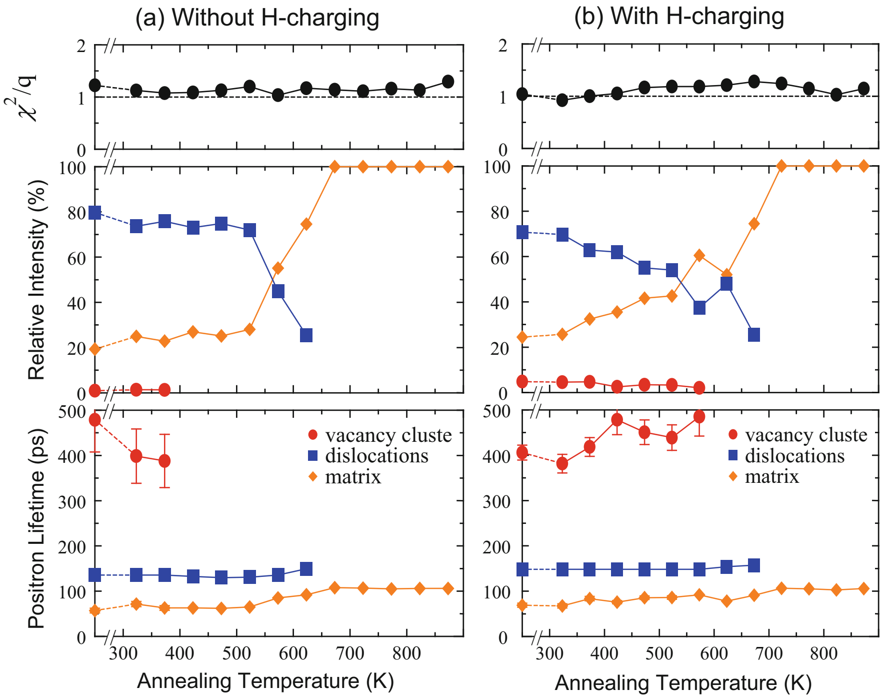

Fig. 3.12 Components of mean positron lifetimes shown in Fig. 3.11 and their relative intensities (Sakaki et al. [61])

Table 3.4 Densities of dislocations (C_d) and vacancies (C_V) in iron deformed with/without hydrogen precharging. Measurements by positron annihilation spectroscopy

Strain (%)	Hydrogen	C_d ($10^{10}/cm^2$)	C_V (10^{-7})
10	None	1	Not-detected
	Charged	0.9	1.7
20	None	2.2	1.7
	Charged	1.9	8.2

Sakaki et al. [60]

The thermal equilibrium density of vacancies increases with the decrease in the formation enthalpy of vacancies as Eq. (3.13) states. When the DEFACTANT mechanism by Kirchheim described in Sect. 3.1.2 is applied to vacancies with which hydrogen combines, the formation enthalpy of vacancies H_f is related to the logarithm of hydrogen activity as expressed in the form

$$\frac{\partial H_f}{\partial \ln a} = -\mathrm{RTZ}\,, \tag{3.18}$$

where Z is the average number of hydrogen atoms per vacancy [30]. A DFT calculation of the total energy of vacancy-hydrogen complex by Tateyama and

Ohno [54] showed a substantial decrease in H_f of VH_N, occasionally to negative values, under high hydrogen pressures of $1 \sim 2$ GPa and Z of 5 or 6. However, expected densities of vacancies are still very low in thermal equilibrium in most situations where hydrogen embrittlement appears.

Another mechanism of realizing high densities of vacancies is kinetic effects. Excess vacancies generated by mutual interactions of dislocations are unstable and tend to annihilate at various sinks such as dislocations, grain boundaries and surfaces. Migration of vacancies is requisite for this process, but the formation of immobile clusters and of complexes with impurity atoms impede the migration as described in Sect. 3.2.2. Such states of vacancies retard annihilation and help to keep high densities before reaching thermal equilibrium.

The mobility of single vacancy in bcc iron under a hydrogen environment has been calculated using the DFT and the nudged elastic band method to find the diffusion path of the minimum energy [55]. A configuration, two hydrogen atoms trapped at opposite O-sites across a vacancy, has the highest binding energy, and the fraction of VH_2 complex is predominant at room temperature. In that configuration, the activation energy of diffusion of vacancy increases from 60 to 103 kJ/mol, and the frequency decreases from 1.71×10^{-2} to 1.62×10^{-8} s^{-1}, showing that the vacancy is almost immobile. As a consequence, in the case of vacancy generation by jog dragging of screw dislocations, high densities of vacancies are expected to remain behind moving screw dislocations [55].

3.3 Precipitates

Fine carbides or nitrides are widely utilized for grain refinement and precipitation hardening of steels. Interactions of hydrogen with such precipitates are important for hydrogen embrittlement of high strength steels, and many studies have been reported. Experiments to obtain binding energies mostly address diffusion or permeation processes in which hydrogen trapping and detrapping take place, as described in Sects. 2.1.2(b) and 3.1.1(b).

TiC is the most extensively studied precipitate. Asaoka et al. visualized the distribution of tritium introduced into a Fe-0.15%Ti alloy by means of tritium autoradiography and examined the thermal desorption and associated changes of the distribution of tritium [63]. Release of tritium from incoherent TiC/matrix interface took place at 600 °C, and the trapping enthalpy calculated using Oriani's diffusion equation [12] was 71–79 kJ/mol. The calculation, however, neglected the entropy term, and higher enthalpy values ~130 kJ/mol was estimated when the entropy term was taken into account.

Hydrogen thermal desorption analysis was applied by Lee and Lee to Fe-Ti-C alloys in which the amounts of Ti and C were varied in a wide range while fixing the Ti/C mass ratio at 4:1 [64]. Hydrogen was charged at 673 K under 0.1 MPa hydrogen gas, and the diffusive part of hydrogen was successively released at room temperature. TDA of remained hydrogen showed three desorption peaks at

473, 773 and 996 K at a heating rate of 3 K/min, and the 996 K peak was assigned to detrapping from the incoherent TiC/matrix. The activation energy of detrapping obtained from Kissinger's equation, Eq. (2.7), was 86.9 kJ/mol. The binding energy of hydrogen with TiC was calculated using the relation between the TDA peak area and the hydrogen-charging temperature T_{H} of the form

$$C_x = N_x C_0 \exp\left(\frac{E_b - E_0}{RT_H}\right), \tag{3.19}$$

where C_x and C_0 are respectively concentrations of hydrogen trapped at TiC and in solid solution, N_{x} is the trap density and E_0 is the heat of solution [64]. The estimated binding energy $E_{\mathrm{b}}^{\mathrm{TiC}}$ and N_{x} are 28.1 kJ/mol and 10^{23}/cm^3-Fe, respectively.

Alternatively, TDA was conducted for specimens with controlled TiC/matrix interfaces [65]. Hydrogen introduced to a ferritic Fe-Ti-C alloy heat-treated at different austenitizing temperatures showed four desorption peaks at 383, 473, 748 and 880 K at a heating rate of 3 K/min. Two peaks at 748 K and 800 K were assigned to detrapping from semi-coherent and incoherent interfaces, respectively. It implies that the trapping strength of TiC increases associated with the loss of particle/interface coherency. It is to be noticed that the hydrogen trapping energy at the incoherent interface is not always unique. The peak temperature assigned to incoherent interface shifted to higher temperatures when specimens were further heat-treated to increase the TiC particle size.

In ferritic Fe-Ti-C alloys, incoherent TiC particles and Ti atoms in solution act as irreversible and reversible traps, respectively. The apparent diffusion coefficient obtained by permeation transient is often used to estimate the binding energy of hydrogen with traps as described in Sect. 3.1.1(b). A sequential permeation method was devised to separate trapping parameters of reversible and irreversible traps [66]. Both types of trapping take place in the first permeation, but reversible trapping dominates diffusivity in the second transient after irreversible traps have been filled. Irreversible trapping parameters were obtained from the difference between the first and the second transients. The obtained binding energies were 94.6 kJ/mol for incoherent TiC and 26 kJ/mol for reversible trap assigned to solute Ti atom [66]. Precipitation of TiC on tempering of martensitic steels brings about a substantial increase in hydrogen absorption capacity, but the distinction between coherent and incoherent precipitation for the increase is not definite [67].

NbC and VC that take NaCl-type structures are also common precipitates in high strength low alloy steels, and their precipitation increases hydrogen absorption capacities of steels. Desorption peak temperatures on TDA relevant to NbC and VC are generally lower than the peak temperature due to TiC [68, 69] but are often in the same range as desorption from other traps. Determination of specific trapping parameters is difficult, but lower peak temperatures imply lower binding energies of hydrogen with NbC and VC than that with TiC. Figure 3.13 [70] shows TDA profiles of hydrogen introduced to 0.37C-1.0Mo-0.54 V martensitic steel tempered at different temperatures. The precipitation of fine VC particles causes a prominent

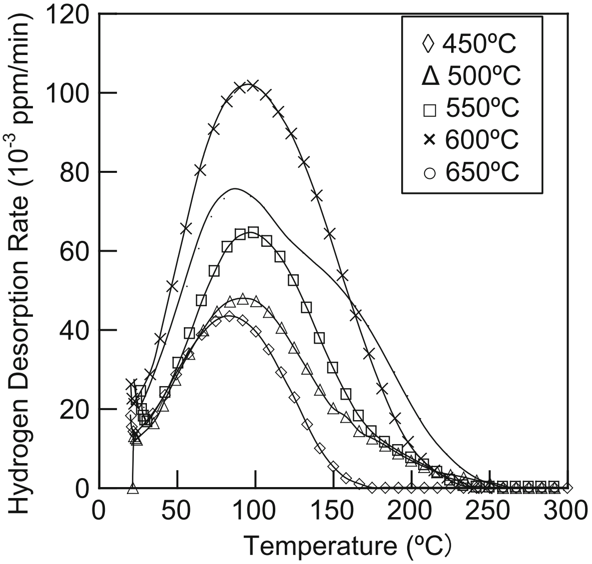

Fig. 3.13 TDA profiles of hydrogen introduced to 0.37C-1.0Mo-0.54 V martensitic steel tempered at temperatures shown in the insert (Nagumo et al. [70])

secondary hardening of martensite. Separately conducted hardness measurements and transmission electron microscopy revealed that the increase in the hydrogen absorption capacity was associated with secondary hardening [69]. A distinct shoulder in the high-temperature side of the desorption peak for 650 °C tempering is ascribed to trapping at fine VC precipitates.

An important subject on interactions of hydrogen with precipitates is effects of applied stress or plastic strain. In previous sections, the hydrogen-enhanced creation of strain-induced vacancies is presented, where vacancies act as traps of diffusive hydrogen. Interactions of hydrogen with fine VC precipitates were examined under applied stress for Mo-V steel [70]. Figure 3.14 [70] shows TDA profiles of hydrogen introduced to specimens under simultaneous loading. The specimens were tempered at 550 °C and 650 °C, and the applied stress was 0.4 of the ultimate tensile strength. In Fig. 3.14, the filled marks indicate TDA profiles after degassing at room temperature for 24 h. The difference between the open and filled marks is the amount of diffusive hydrogen. TDA curves exhibit a single peak, but the peak widths are fairly wide. Room temperature degassing showed that hydrogen composing the higher-temperature side of the peak is nondiffusive. A separately conducted measurement showed that the applied stress increased densities of trap sites of both diffusive and nondiffusive hydrogen [70], and that the increase was more prominent for nondiffusive one.

The results indicate that applied stress enhances strong hydrogen trapping by VC. The number of precipitates, i.e., of the hydrogen trapping sites, is much higher and their distribution is more uniform by tempering at 650 °C than at 550 °C. On the other hand, weakly trapped diffusive hydrogen is crucial to degradation. It should be noticed that the overall or average information from a specimen does not always

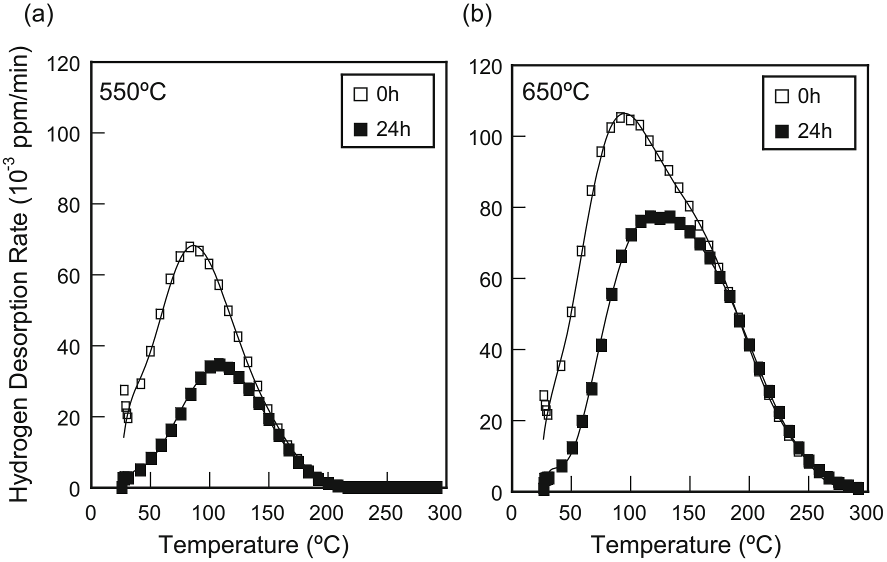

Fig. 3.14 TDA profiles of hydrogen introduced to 0.37C-1.0Mo-0.54 V martensitic steel tempered at (**a**) 550 °C and (**b**) 650 °C. Hydrogen charging is conducted under applied stress of 0.4 tensile strength. Filled marks denote specimens kept for 24 h at 30 °C to remove diffusive hydrogen (Nagumo et al. [70])

represent local situations crucial to fracture events. Details of hydrogen trapping behaviors concerning hydrogen embrittlement are described in Sect. 8.1(b).

Precipitation of fine Fe_3C hardly affects the hydrogen absorption capacity on tempering of 0.42 % C martensitic steel [67]. TDA profiles of hydrogen in eutectoid steel does not show trapping of hydrogen to pearlitic Fe_3C when cold-working is not applied as shown in Fig. 2.4. It suggests that Fe_3C and its interface are not strong trap sites. On the other hand, two TDA peaks appeared by cold-drawing originated in fine lamellar Fe_3C. The appearance of higher-temperature peak and its increase by cold-drawing are surely due to the strain-induced formation of irreversible traps in the interface or within Fe_3C. A noteworthy fact is that such irreversibly trapped hydrogen or trapping defects are almost immune to hydrogen embrittlement.

3.4 Grain Boundaries

Accumulation of hydrogen along grain boundaries has been revealed directly by means of tritium autoradiography as shown in Fig. 2.12 for ferritic steel. However, types and structures of grain boundaries are diverse, and quite different values have been reported for binding energies of hydrogen with grain boundaries. Thermal desorption kinetics and tritium autoradiography for ferritic Fe-Ti-C alloys showed that the release of tritium from grain boundaries took place below 300 °C and the calculated trapping energy was 59 kJ/mol, neglecting the entropy term in the free energy change [63].

The binding energy of hydrogen with ferrite grain boundaries in iron was also reported from TDA measurements [14]. The grain size of cold-worked iron was widely controlled from two to nine in the ASTM numbers by recrystallization. A TDA peak that appeared around 373 K preceding the evolution of a large desorption peak was assigned to grain boundaries. The activation energy of desorption obtained using Kissinger's equation was 17.2 kJ/mol, giving 9.6 kJ/mol for the binding energy after subtracting the saddle point energy of 7.6 kJ/mol. However, Kissinger's equation implicitly addresses the dissociation-controlled desorption of hydrogen, and the value of 9.6 kJ/mol is too small to apply the analysis. For the experiment, the specimen was 8 mm in diameter and degassing at room temperature for 6 h was given, but excess solute hydrogen might have remained. Alternatively, modeling of TDA profiles of hydrogen from pure iron with different grain size was conducted assuming diffusion-controlled desorption [15] as described in Sect. 2.1.2 (b). The desorption-rate peak at 415 K was assigned to grain boundaries, and the binding energy of 49 kJ/mol gave the best fit between simulated and experimental TDA profiles.

Prior austenite grain boundaries in martensitic steels are often decorated with impurity segregation and precipitates. However, observed accumulation of hydrogen along grain boundaries does not necessarily induce intergranular fracture. The role of grain boundaries in hydrogen embrittlement is to be considered taking into account various factors, not only cohesive strength of boundaries and its modifications by segregated impurities or precipitates but also concentrated plastic deformation in adjacent areas.

3.5 Voids and Surfaces

Formation of small voids or cracks is feasible in deformed metallic materials, and such defects are activated by the precipitation of molecular hydrogen under high hydrogen fugacity. Detrapping of deuterium from helium bubbles formed by ion implantation of 15-keV ^{4}He into iron and austenitic stainless steels was investigated by measuring the release of deuterium [46, 47]. The size of bubbles was about 1 nm in diameter, and the thermal release of deuterium from the implanted zone was analyzed in the same way as described in Sect. 3.2.3(a). For iron, three types of traps were assumed, and the strongest trap with the binding enthalpy of 75 kJ/mol was assigned to detrapping from He bubbles [46]. Similarly in a Type 304 stainless steel, the corresponding value was 41 kJ/mol assuming two types of traps [47].

When molecular hydrogen in voids diffuses out, adsorption on the void surface is requisite as an intermediate step, and the binding of deuterium with He bubble is considered as chemisorption-like interaction. The binding energy of hydrogen with the bubble surface E_T is the lowering of the hydrogen energy relative to lattice site as illustrated in Fig. 3.15 [71]. It is written as

Fig. 3.15 Schematic illustration of hydrogen energies. E_T is the lowering of hydrogen energy by moving from solutionized bulk to surface site (Picraux [71])

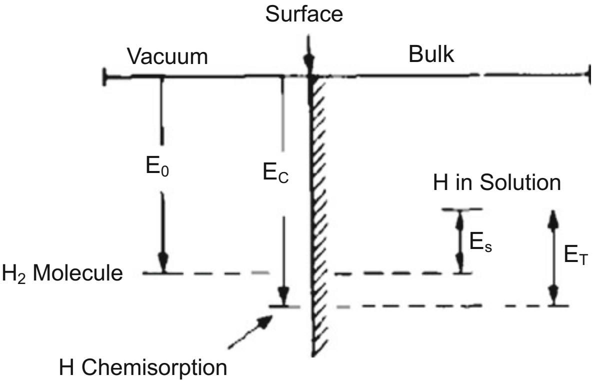

$$E_T = E_{\text{chem}} + E_s - \frac{1}{2} E_{H_2} \,, \tag{3.20}$$

where E_{chem} is the chemisorption binding energy of hydrogen referred to the free hydrogen atom in vacuum, E_s is the heat of solution and E_{H2} is the energy of hydrogen molecule. Using experimental values of $E_{\text{chem}} = 259$ kJ/mol and $E_s = 28$ kJ/mol together with $E_0 = 222$ kJ/mol for α-Fe, a calculated E_T is 77 kJ/mol [71]. The calculated value of E_T is consistent with the value obtained from the deuterium implantation experiment [46].

References

1. R. Gibara, A.J. Kumnick, in *Hydrogen Embrittlement and Stress Corrosion Cracking*, ed. by R. Gibara, R.F. Hehemann (ASM, Metals Park, 1984), pp. 61–77
2. T.S. Kê, Scr. Metall. **16**, 225–231 (1982)
3. V. Hivert, P. Groh, W. Frank, I. Ritchie, P. Moser, Phys. Status Solidi (a), **46**, 89–98 (1978)
4. G.M. Sturges, A.P. Miodownik, Acta Metall. **17**, 1197–1207 (1969)
5. J.P. Hirth, Metall. Trans. A **11A**, 861–890 (1980)
6. G. Schoek, Scr. Metall. **16**, 233–239 (1982)
7. A. Seeger, Scr. Metall. **16**, 241–247 (1982)
8. J.P. Hirth, Scr. Metall. **16**, 221–223 (1982)
9. A. Zielinski, E. Lunarska, M. Smialowski, Acta Metall. **25**, 551–556 (1977)
10. R. Gibara, Trans. Metall. Soc. AIME **239**, 1574–1585 (1967)
11. S. Asano, M. Shibata, Scr. Metall. **16**, 1171–1174 (1982)
12. R.A. Oriani, Acta Metall. **18**, 147–157 (1970)
13. A.J. Kumnick, H.H. Johnson, Acta Metall. **28**, 33–39 (1980)
14. W.Y. Choo, J.Y. Lee, Metall. Trans. A **13A**, 135–140 (1982)
15. K. Ono, M. Meshii, Acta Metall. **40**, 1357–1364 (1992)
16. M. Nagumo, K. Ohta, H. Saitoh, Scr. Mater. **40**, 313–319 (1999)
17. J.P. Hirth, in *Hydrogen Degradation of Ferrous Alloys*, ed. by R.A. Oriani, J.P. Hirth, M. Smialowski (Noyes Pub., Park Ridge, 1985), pp. 131–139
18. J.P. Hirth, B. Carnahan, Acta Metall. **26**, 1795–1803 (1978)
19. S. Taketomi, R. Matsumoto, N. Miyazaki, Acta Mater. **56**, 3761–3769 (2008)

20. J.W. Christian, Metall. Trans. A **14A**, 1237–1256 (1983)
21. M.S. Duesbery, V. Vitek, Acta Mater. **46**, 1481–1492 (1998)
22. M. Wen, A.H.W. Ngan, Acta Mater. **48**, 4255–4265 (2000)
23. S.L. Frederiksen, K.W. Jacobsen, Philos. Mag. **83**, 365–375 (2003)
24. M. Itakura, H. Kaburaki, M. Yamaguchi, Acta Mater. **60**, 3698–3710 (2012)
25. M. Wen, S. Fukuyama, K. Yokogawa, Acta Mater. **51**, 1767–1773 (2003)
26. M. Itakura, H. Kaburaki, M. Yamaguchi, T. Okita, Acta Mater. **61**, 6857–6867 (2013)
27. V.G. Gavriljuk, V.N. Shivanyuk, B.D. Shanina, Acta Mater. **53**, 5017–5034 (2005)
28. V.G. Gavriljuk, B.D. Shanina, V.N. Shivanyuk, S.M. Teus, J. Appl. Phys. **108**, 083723 (2010)
29. R. Kirchheim, Acta Mater. **55**, 5129–5138 (2007)
30. R. Kirchheim, Acta Mater. **55**, 5139–5148 (2007)
31. R. Kirchheim, Scr. Mater. **62**, 67–70 (2010)
32. H.J. Wollenberger, in *Physical Metallurgy*, ed. by R.W. Cahn, P. Hansen, vol. II, 4th edn. (North-Holland, Amsterdam, 1996), Chapter 18
33. R.W. Siegel, J. Nucl. Mater. **69&79**, 117–146 (1978)
34. P. Hautojä, in *Characterization of Defects in Materials*, ed.. by R.W. Siegel, J.R. Weertman, R. Sinclair, Materials Research Society Proceedings, vol. 82 (MRS, 1987), pp. 3–21
35. A. Vehanen, P. Hautojärvi, J. Johansson, J. Yl-Kauppila, P. Moster, Phys. Rev. B **25**, 762–780 (1982)
36. L. De Schepper, D. Segers, L. Dorikens-Vanpraet, M. Dorikens, G. Knuyt, L.M. Stals, P. Moser, Phys. Rev. B **27**, 5257–5269 (1983)
37. J. Takamura, I. Takahashi, M. Amano, Trans. ISIJ **9**, 216–221 (1969)
38. H.G. van Bueren, Acta Metall. **3**, 519–524 (1955)
39. A.M. Cuttiño, M. Ortiz, Acta Mater. **44**, 427–436 (1996)
40. U. Essmann, H. Mughrabi, Philos. Mag. A **40**, 731–756 (1979)
41. J.R. Beeler Jr., R.A. Johnson, Phys. Rev. **156**, 677–684 (1967)
42. M.J. Puska, R.M. Nieminen, J. Phys. F: Met. Phys. **13**, 333–346 (1983)
43. M. Kiritani, H. Takata, K. Moriyama, F.E. Fujita, Philos. Mag. A **40**, 779–802 (1979)
44. R.W. Balluffi, J. Nucl. Mater. **69&70**, 240–263 (1978) (Overview)
45. S.M. Myers, S.T. Picraux, R.E. Stolts, J. Appl. Phys. **50**, 5710–5719 (1979)
46. S.M. Myers, D.M. Follstaedt, F. Besenbacher, J. Bøttiger, J. Appl. Phys. **53**, 8734–8744 (1982)
47. S.M. Myers, W.R. Wampler, F. Besenbacher, J. Appl. Phys. **56**, 1561–1571 (1984)
48. F. Besenbacher, J. Bøttiger, S.M. Myers, J. Appl. Phys. **53**, 3536–3546 (1982)
49. F. Besenbacher, B.B. Nielson, S.M. Myers, J. Appl. Phys. **56**, 3384–3393 (1984)
50. S.M. Myers, F. Besenbacher, J. Appl. Phys. **60**, 3499–3507 (1986)
51. F. Besenbacher, J. Bøttiger, B.B. Nielson, A.A. Pisarew, Phys. Rev. Lett. **49**, 1420–1422 (1982)
52. F. Besenbacher, S.M. Myers, P. Nordlander, J.K. Nørskov, J. Appl. Phys. **61**, 1788–1794 (1987)
53. P. Nordlander, J.K. Nørskov, F. Besenbacher, S.M. Myers, Phys. Rev. B **40**, 1990–1992 (1989)
54. Y. Tateyama, T. Ohno, Phys. Rev. B **67**, 174105 (2003)
55. R. Matsumoto, N. Nishiguchi, S. Taketomi, N. Miyazaki, J. Soc. Mater. Sci. Jpn. **63**, 182–187 (2014)
56. E. Hayward, B. Beeler, C. Deo, Philos. Mag. Lett. **82**, 217–225 (2012)
57. K. Takai, H. Shoda, H. Suzuki, M. Nagumo, Acta Mater. **56**, 5158–5167 (2008)
58. Y. Sato, T. Doshida, H. Suzuki, K. Takai, Y. Hagiwara, CAMP-ISIJ **23**, 1292 (2010)
59. N. Abe, H. Suzuki, K. Takai, N. Ishikawa, H. Sueyoshi, in *Environmentally Assisted Cracking of Materials*, Proceedings MS&T 2011 (2011), pp. 1277–1284
60. By courtesy of Prof. K. Takai for results before publication
61. K. Sakaki, T. Kawase, M. Hirano, M. Mizuno, H. Araki, Y. Shirai, M. Nagumo, Scr. Mater. **55**, 1031–1034 (2006)
62. C. Hidalgo, G. González-Doncel, S. Linderoth, J. San Juan, Phys. Rev. B **45**, 7017–7021 (1992)

63. T. Asaoka, C. Dagbert, M. Autocouturier, J. Galland, Scr. Metall. **11**, 467–472 (1977)
64. H.G. Lee, J.Y. Lee, Acta Metall. **32**, 131–136 (1984)
65. S.M. Lee, J.Y. Lee, Acta Metall. **35**, 2695–2700 (1987)
66. G.M. Pressouyre, I.M. Bernstein, Metall. Trans. A **9A**, 1571–1580 (1978)
67. F.-G. Wei, T. Hara, T. Tsuchida, K. Tsuzaki, ISIJ Int. **43**, 539–547 (2003)
68. T. Omura, T. Kushida, K. Miyata, Y. Komizo, Tetsu-to-Hagané **90**, 106–112 (2004)
69. T. Tsuchida, T. Hara, K. Tsuzaki, Tetsu-to-Hagané **88**, 771–778 (2002)
70. M. Nagumo, T. Tamaoki, T. Sugawara, in *Hydrogen Effects on Materials Behavior and Corrosion Deformation Interactions*, ed. by N.R. Moody, A.W. Thompson, R.E. Ricker, G.W. Was, R.E. Jones (TMS, Warrendale, 2003), pp. 999–1008
71. S.T. Picraux, Nucl. Inst. Methods **182/183**, 413–437 (1981)

Chapter 4
Diffusion and Transport of Hydrogen

The diffusion of hydrogen is a subject described in Sect. 2.1.2(b), (c) about the thermal desorption analysis of hydrogen and in Sect. 3.1.1(b) about the hydrogen permeation in defected metals. In this section, the general features of hydrogen diffusion and transport in metals are briefly presented.

4.1 Determination of Diffusion Coefficient

The diffusion coefficient in Fick's first law, Eq. (2.1), is a function of temperature. Published data of hydrogen diffusion in metals are collected in a book [1], and the range of data for iron and steels are shown in Fig. 4.1 according to the original compilation by McNabb and Foster [2]. A reported value of the hydrogen diffusion coefficient in a 99.99 % purity iron specimen which is almost free from dislocation trapping is [3]

$$D\left(m^2/s\right) = 5.8 \times 10^{-8} \exp\left(-4.5(\mathrm{kJ/mol})/RT\right). \tag{4.1}$$

A wide spread over three orders of magnitude of D_{eff} at low temperatures in Fig. 4.1 corresponds to the scatter in the solid solubility shown in Fig. 2.1 resulting from trapping of hydrogen in various lattice defects.

Hydrogen atoms migrating in crystalline lattice tolerate various energy barriers. The diffusivity of hydrogen in close-packed fcc γ-iron is lower than that in bcc α-iron as a result of the higher activation energy of diffusion in fcc structures. Figure 4.2 [5] shows hydrogen diffusion coefficients from the literature in various austenitic stainless steels. It is to be noticed that the effects of alloying elements are substantial on diffusion coefficients in addition to those of crystal structures. The hydrogen diffusion coefficient reported for Type 304 stainless steel in the temperature range 311–332 K is [5]

M. Nagumo, *Fundamentals of Hydrogen Embrittlement*,
DOI 10.1007/978-981-10-0161-1_4

Fig. 4.1 Literature data range of effective diffusion coefficient of hydrogen in iron and steels (Data lines are shown in [2])

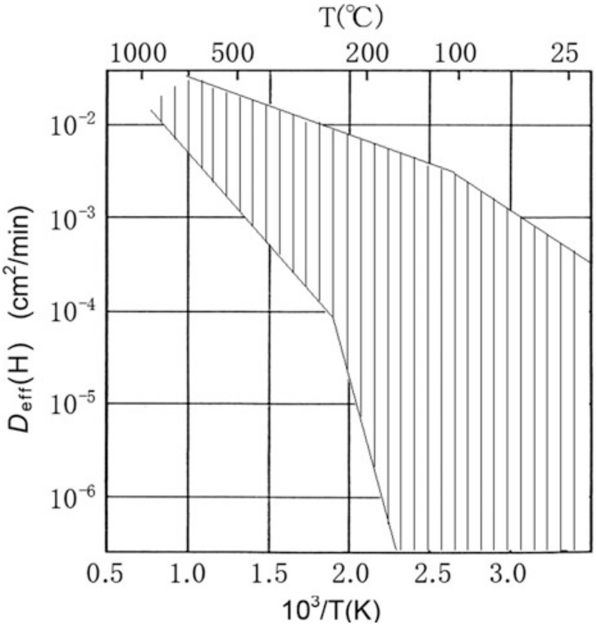

Fig. 4.2 Hydrogen diffusion coefficients in austenitic stainless steels (Caskey [4])

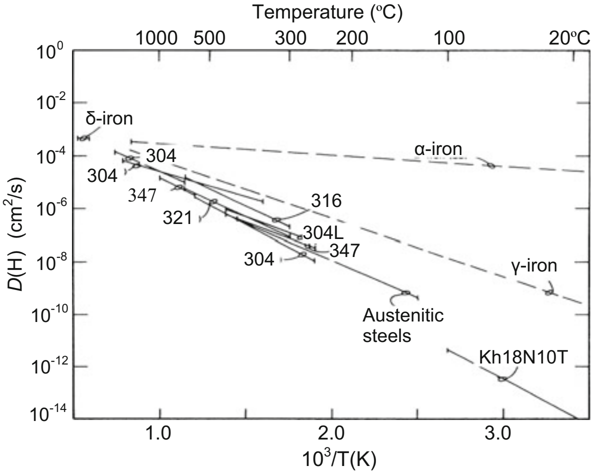

$$D\left(m^2/s\right) = 4.41 \times 10^{-7} \exp\ \left(-53.5\ (\text{kJ/mol})/RT\right). \tag{4.2}$$

Migration distances of hydrogen in terms of $\sqrt{Dt}$ calculated using Eqs. (4.1) and (4.2) at room temperature are drastically different between α-iron and austenitic stainless steels, roughly 100 μm and 20 nm per second respectively.

The hydrogen diffusivity has been measured by various methods [6], and gas or electrochemical permeation techniques have been widely employed. The electrical circuit for the electrochemical cell employed by Devanathan and Stachurski is shown in Fig. 4.3 [7]. The specimen is sandwiched between two individual electrolyte cells and hydrogen generated electrochemically on one side of the specimen by cathodic polarization is absorbed into the bulk. Then, hydrogen diffusing through the specimen is oxidized at constant potential. Zero coverage on the opposite side is maintained by anodic polarization, and the oxidation current is proportional to the amount of hydrogen penetrating through the specimen with time. The continuous record of the current in the anodic potentiostatic circuit represents the instantaneous rate of hydrogen permeation.

Figure 4.4 [8] illustrates schematically the permeation transient and its integration with time after switch-on of galvanostatic cathodic potential. The diffusion coefficient of hydrogen is obtained in various ways from the transient curves, but somewhat different quantities are used according to experimental conditions. In the non-steady-state galvanostatic time-lag method, a constant hydrogen flux is

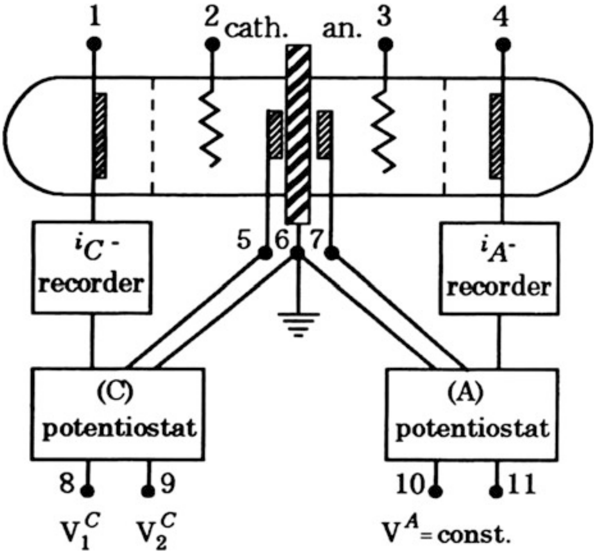

Fig. 4.3 Schematic diagram of the electrical circuit for hydrogen permeation experiment (Devanathan et al. [7]. Reprinted with permission from The Royal Society)

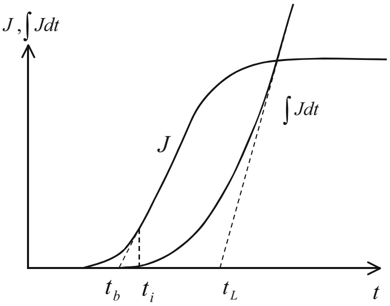

Fig. 4.4 Permeation current density or hydrogen flux J permeating with time after starting galvanostatic cathodic polarization (Boes et al. [8])

established at the entrance side by a constant cathodic current. Time lag t_i shown in Fig. 4.4 is expressed from the solution of Fick's second law as [8],

$$t_i = \frac{3\ln 3}{2}\frac{L^2}{\pi^2 D} \approx \frac{L^2}{6D}\,, \tag{4.3}$$

where L is the thickness of the specimen.

The integral of the current with time, $\int J\mathrm{d}t$, becomes linear when a stationary linear concentration gradient is established in the specimen. Another time lag t_L is the time required to obtain a steady-state flow after a sudden change of the boundary condition and is defined as the intercept on the t-axis of the extrapolation of the straight line [8],

$$t_L = \frac{L^2}{2D}\,. \tag{4.4}$$

Further, the breakthrough time t_b is defined as the intersection of the tangent at the inflection point with the initial level $J = 0$,

$$t_b = 0.76\frac{L^2}{\pi^2 D} \approx 0.077\frac{L^2}{D}\,. \tag{4.5}$$

In the case of the non-steady-state potentiostatic method with a constant hydrogen concentration at the entrance side, expressions for time lag are

$$t_i = \frac{\ln 16}{3}\frac{L^2}{\pi^2 D} \approx 0.091\frac{L^2}{D}\,, \tag{4.6}$$

$$t_L = \frac{L^2}{6D}\,, \tag{4.7}$$

$$t_b = 0.5\frac{L^2}{\pi^2 D} \approx 0.05\frac{L^2}{D}\,. \tag{4.8}$$

In this condition, t_L is simply obtained as the time at which the rate of permeation is 0.63 of the steady-state value [7].

4.2 Diffusion Process

The driving force of diffusion is the concentration gradient, and the hydrogen flux in metals is expressed by Fick's first law, Eq. (2.1). Fick's second law, Eq. (2.20), for non-steady flow describes the change of hydrogen concentration in a volume element. The diffusion coefficient in the equations is a quantity resulting from the jumping frequency of atoms in crystalline lattice, but macroscopically observed diffusion coefficients are mostly averaged ones over diffusion paths. Migrating hydrogen atoms encounter trapping and detrapping in various lattice defects, and Fick's laws must be modified to include discrete processes.

The McNabb and Foster equation, Eqs. (2.21) and (2.22), is a general formulation of diffusion accompanying trapping and detrapping. The equation complements Fick's law taking into account the elementary process of atomic jumping at trap site. Approximate solutions of the McNabb-Foster equation for thick and thin specimens were presented in their original work [2]. The case of thick specimens is described in Sect. 2.1.2(c), and the effective diffusivity is derived in the form of Eq. (2.25) using trapping parameters k and p. McNabb and Foster applied their equations to hydrogen permeation through a plate of thickness L under boundary conditions of constant C_0 and zero hydrogen concentrations on the input and output surfaces, respectively. In the permeation transient in the presence of traps, the time lag t_L required to obtain a steady-state flow was derived in a modified form of Eq. (4.7) as

$$t_L = \frac{L^2}{6D}(1+\alpha)\left\{1 - \frac{1}{2}\alpha\beta/(1+\alpha) + O\left(\beta^2\right)\right\}, \tag{4.9}$$

where $\alpha = N_\mathrm{x}k/p$, $\beta = C_0 k/p$ [2]. Equations (3.6) and (3.7) are approximated forms of Eq. (4.9). Equation (4.9) is the same form as Eq. (4.7) when the notation of D is replaced by D_eff defined as

$$D_\mathrm{eff} = D(1+\alpha)^{-1} = D_L\left(1 + N_x\frac{k}{p}\right)^{-1}, \tag{4.10}$$

where N_x denotes the number of trap-site per unit volume. Equation (4.10) is the same as Eq. (2.25).

From the definitions of p and k, the time required for one trapping or detrapping event is expressed as $1/C_\mathrm{L}k$ or $1/p$, while the time to pass through a specimen of the thickness a is a^2/D. "Thick" specimen means that frequent trapping and detrapping events happen during diffusion through the specimen, *i.e.* $D/a^2 \ll p$, $C_\mathrm{L}k$. On the other hand, in "thin" specimen in which $D/a^2 \gg p$, $C_\mathrm{L}k$, lattice hydrogen diffuses out readily and trapping and detrapping events take place independently. The desorption of hydrogen from a thin specimen then indicates the decrease in the amount of trapped hydrogen being controlled by detrapping, *i.e.*

$$\frac{\partial C_x}{\partial t} = -pC_x\,. \tag{4.11}$$

When thermal equilibrium is established at $t = 0$, the numbers of trapping and detrapping hydrogen atoms are the same, *i.e.*

$$k\,C_L^0 N_x\left(1-\theta^0\right)=p\,\theta^0 N_{xsss}, \tag{4.12}$$

where θ denotes the fractional occupancy of the trap. Then, the decrease in trapped hydrogen that approximates the amount of remained hydrogen is expressed in terms of trapping parameters as [2],

$$C_x=C_x^0\exp\left(-pt\right)=\theta^0 N_x\exp\left(-pt\right)=\frac{C_L^0 N_x k/p}{1+C_L^0 k/p}\exp\left(-pt\right). \tag{4.13}$$

Diffusion coefficient has been derived in a more general way from stochastic viewpoints on the movement of atoms. The mean square displacement of particles is proportional to Dt in Brownian motion according to Einstein's relation [9]. From the viewpoint of random walk, Koiwa assumed that the mean square displacement of a diffusing species after the same number of atomic jumps is the same irrespective of the presence of traps [10]. Since the time of stay at a trap may differ from that at a normal lattice site, the relation between apparent and normal lattice diffusion coefficients is expressed as [10]

$$D_{\mathrm{eff}}\,t'_U=D_L t_U\,, \tag{4.14}$$

where t'_{U} and t_{U} denote the times required for a diffusing atom to make the same number of jumps with and without traps, respectively. When the change in the saddle point energy, ΔE, is zero in the energy diagram shown in Fig. 2.8, interstitial atoms visit all sites with an equal probability. In this case, t'_{U} is the weighted mean of the mean times of stays at a normal lattice site, t_{L}, and at a trap site, t_{T}. Assuming that trap sites for interstitials in the bcc lattice are substitutional foreign atoms of c in atomic ratio, Eq. (4.14) is written for O-occupancy of hydrogen in bcc metals as

$$t'_U=(1-2c)t_L+2ct_T\,. \tag{4.15}$$

For T-occupancy of hydrogen, $2c$ in Eq. (4.15) is replaced by $4c$.

The jump frequency v between nearest neighbor sites with the activation energy E_{a} is given as

$$v=v_0\exp\left(-E_a/RT\right). \tag{4.16}$$

Since the time of stay is the inverse of v, D_{eff} is derived from Eqs. (4.14), (4.15) and (4.16) in the form

$$D_{\mathrm{eff}}=D\left[1-2c+2c(v_L/v_T)\exp\left(E_b/RT\right)\right]^{-1}, \tag{4.17}$$

where v_L and v_{T} are frequency factors of the jump from the normal lattice site and trap site, respectively. Equation (4.17) corresponds to Eq. (2.19) derived by Oriani for the case of local equilibrium. Koiwa further considered the case in which the

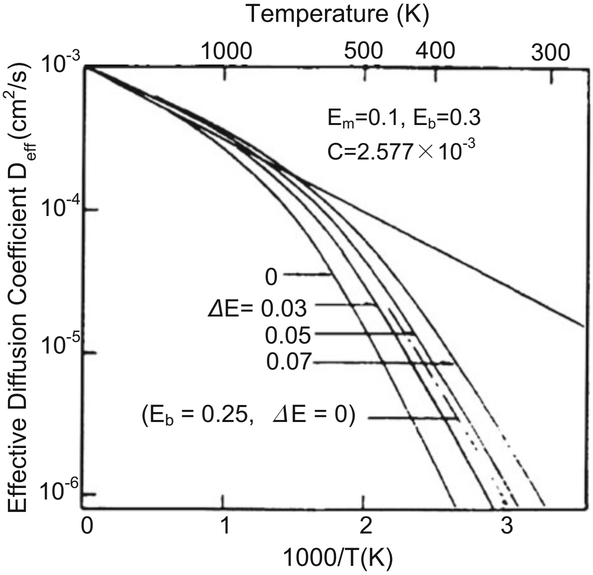

Fig. 4.5 Effects of the change in saddle point energy ΔE on effective diffusion coefficient of interstitial atoms in the bcc lattice. The *straight line* shows the normal diffusion coefficient (Koiwa [10])

interaction between trapping centers and hydrogen atoms is extended to nearest neighboring sites. In this case, a more general form of D_{eff} was derived taking into account a high probability of reverse trapping at the original trap center immediately after the release.

Equation (4.17) is for the case of $\Delta E = 0$ in Fig. 2.8, but it is to be noticed that the saddle point energy substantially affects D_{eff} as shown in Fig. 4.5 [10]. Increase in ΔE, *i.e.* decrease in the saddle point energy, increases D_{eff} substantially at low temperatures in negative curvature range. Surroundings of a defect, like networks, tangles and cell structures for dislocations, may affect the saddle point energy. In this case, even for traps of the same E_{b}, the diffusivity of hydrogen affected by dislocations may differ from that in the lattice of low dislocation densities. It is also to be noticed that the assumption of an equal probability for visiting all sites is not valid when $\Delta E \neq 0$.

Another stochastic approach to hydrogen diffusion was made by Kirchheim using Monte-Carlo methods [11, 12]. The procedure is that interstitial atoms P in number are initially distributed randomly in metal lattice, and each atom is given energy E which is generated as a random number by the computer. The probability p(E) that an atom has energy E is

$$p\,(E) = \exp\left(-E/RT\right). \tag{4.18}$$

If the energy E is larger than at least one of the surrounding energy barriers, a jump to a neighboring site is possible and this step is repeated for a definite numbers (100P or 1000P) of jumps. In the first run during time ^{1}t, the diffusion coefficient for i-th interstitial atom is calculated in terms of the position vectors $\boldsymbol{R}_{\mathrm{i}}$ and $\boldsymbol{R}_{\mathrm{i0}}$ for the final and the initial positions of the i-th atom, respectively, as

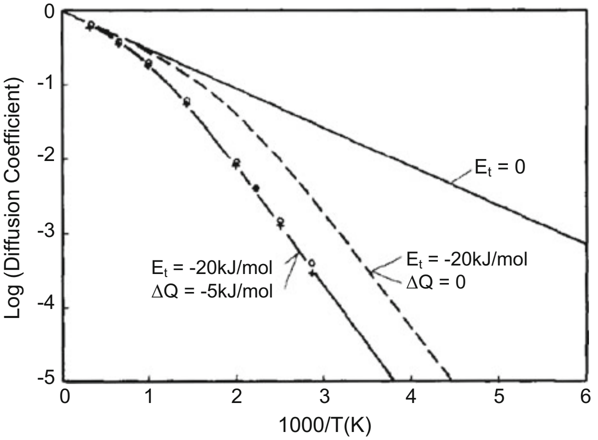

Fig. 4.6 Calculated diffusion coefficient in the fcc lattice with traps (trap concentration = 1 %, $E_t = -20$ kJ/mol) having lower saddle point energies ($\Delta Q = -5$ kJ/mol). The *broken line* is calculated with $\Delta Q = 0$ (Kirchheim [11])

$$^1D_i = \frac{(\boldsymbol{R}_i - \boldsymbol{R}_{i0})^2}{2d\,^1t}, \tag{4.19}$$

where d is the dimension of the lattice considered. The ^1D_i is averaged over all P interstitial atoms, and then the whole procedure is repeated after the time ^kt with the atom starting from the final position of the previous run until the average of ^1D_i over all n runs,

$$D = \sum_{k=1}^{n} \frac{^kD\,^kt}{t}, \tag{4.20}$$

is constant.

The effects of the site and the saddle point energies on diffusion coefficient and site occupancy were examined numerically for fcc lattice. Results of the calculation for the effects of the saddle point energy on diffusion coefficient are shown in Fig. 4.6 [11] for dilute solutions, *i.e.* for low occupancy of trap. Decreases in both the free energy of a trap site and the saddle point energy reduce the diffusion coefficient compared to the normal lattice, in contrast to Fig. 4.5. It was also shown that the occupancy of a site by an interstitial atom is determined not only by the binding energy in the equilibrium position but also by the heights of surrounding barriers.

4.3 Hydrogen Transport by Dislocations

Hydrogen embrittlement premises the presence of hydrogen and hydrogen transport to critical sites is a matter not to be overlooked in examining effects of microstructures on fracture. The mechanism of hydrogen transport in addition to diffusion through lattice is important especially for fcc and hcp metals in which intrinsic hydrogen diffusivity is low.

4.3.1 Release of Internal Hydrogen

Promoted evolutions of precharged tritium were observed during tensile straining for various metals and alloys such as iron, Type 304 stainless steel, nickel, Inconel 718 and 5086 aluminum alloys [13]. In all cases, the release rate increased rapidly at the proportional limit or yield point, reached a maximum as the strain was raised, then fell with additional strain, and finally showed a large release at fracture. For iron the release rate was constant during Lüder's extension and the rate was a function of temperature and strain-rate. Activation energies for the release were about 8 kJ/ and 40 kJ/mol for iron and Type 304 stainless steel, respectively, but the corresponding thermally activated process was not definite.

Similar deformation-enhanced desorption of hydrogen was observed for iron and Inconel 625 alloy [14]. Hydrogen released during tensile tests of iron specimens was detected by a quadrupole mass spectrometer. Hydrogen was precharged to saturation by cathodic electrolysis, and the test was conducted in a vacuum chamber at room temperature. Figure 4.7 [14] shows (a) the hydrogen desorption rate and (b) the stress-time curve for iron. Extraneous hydrogen coming from the dissociation of water or molecular hydrogen on the specimen surface was subtracted from the total amount of desorbed hydrogen. Cyclic stressing applied in the elastic range increased only slightly the desorption rate, but a rapid increase in the early stage of plastic deformation and the following decrease were consistent with previously reported results [13]. The ratio of released hydrogen during tensile straining to the initial content differs by the strain rate. For iron, the ratios were not monotonic

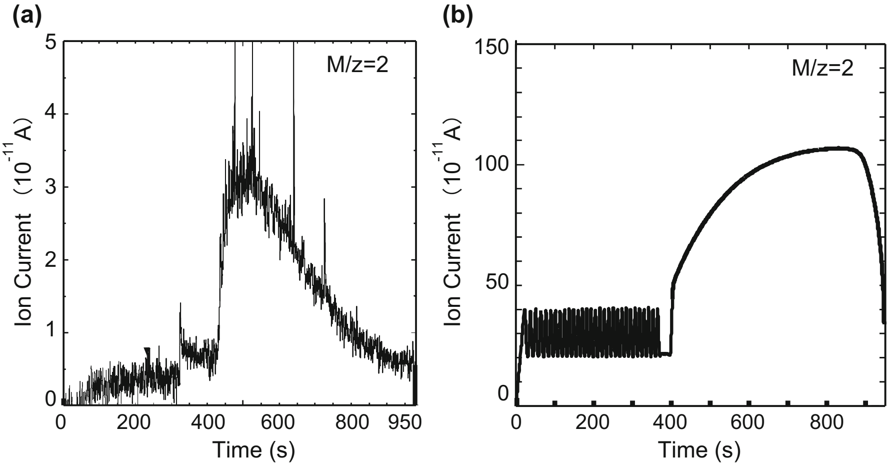

Fig. 4.7 (**a**) Hydrogen desorption during elastic cyclic stressing and subsequent tensile straining until failure of a pure iron specimen. Hydrogen is precharged by cathodic electrolysis in poisoned H_2SO_4 aq of pH 2.5 at a current density of 50 A/m^2. The tensile strain rate is 4.2×10^{-4}/s. The stress-time curve is shown in (**b**) (Shoda et al. [14]. Reprinted with permission from The Iron & Steel Inst. Japan)

against the strain rates in the range from 4.2×10^{-3}/s to 4.2×10^{-5}/s, and the maximum release was 16 % at 4.2×10^{-4}/s. On the other hand for Inconel 625, a monotonic increase in the fraction of released hydrogen appeared with decreasing strain rate from almost 0 % at 4.2×10^{-3}/s to 9 % at 4.2×10^{-6}/s [14].

The direct observations of the hydrogen release from the surface during tensile deformation was conducted for pure aluminum at different temperatures by means of hydrogen microprint technique [15], described in Sect. 2.3. The emission of residual impurity hydrogen during tensile straining to 5 % prominently took place along coarse slip bands at room temperature, but the emission along grain boundaries rather than slip bands was preferential at 82 °C. The emission along slip bands was also reduced at – 70 °C. The results were ascribed to the transport of hydrogen by moving dislocations at room temperature and to thermal dissociation of accumulated hydrogen along grain boundaries at 82 °C.

The diffusivities of hydrogen in fcc and hcp metals and alloys are very low at room temperature. A substantial desorption of hydrogen implies that desorption is not simply due to the diffusion of hydrogen but is likely associated with the movement of dislocations. However, the possibility cannot be ruled out that fresh metal surface and/or surface steps formed by slip-off of dislocations act as active sites for desorption by reducing the barrier energy for the emission.

4.3.2 Electrochemical Permeation

Anodic current at the steady state of the electrochemical permeation changes when straining is applied to the electrode. Figure 4.8 [16] is a schematic illustration of anodic current as a function of time when straining is applied to the polycrystalline nickel electrode. The magnitude and even the sign of the change of the total anodic

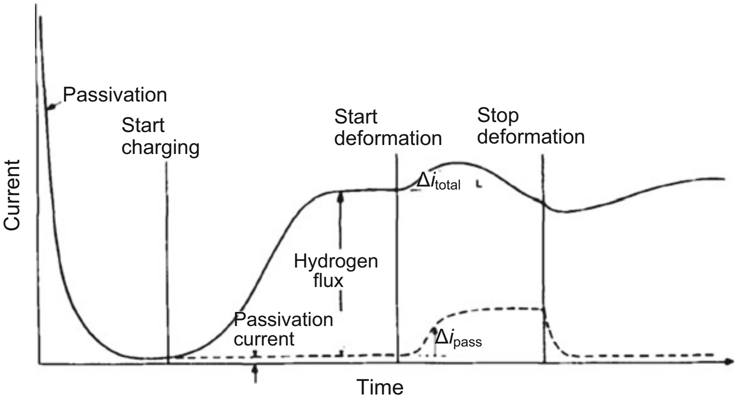

Fig. 4.8 Schematic representation of anodic current for electrochemical permeation through nickel specimen measured as a function of time, illustrating experimental procedure (Frankel et al. [16])

current Δi_{tot} differ by materials and experimental conditions. The observed changes of anodic current are affected by various factors. Hydrogen transport by moving dislocations expects an increase in anodic current, but a large portion of Δi_{tot} is the background current to passivate the newly formed surface of the electrode by straining. The net current Δi_{net} after subtracting the passivation current from Δi_{tot} still includes currents of various origins other than the transport by dislocations, such as dynamic trapping by newly created dislocations, associated depletion of the lattice hydrogen concentration, the decrease in the thickness of the specimen and the increase in the input hydrogen concentration by the fresh metal surface enhancing hydrogen entry. Further, the concentration gradient at the output surface of the specimen is critical to the release of hydrogen diffusing through lattice. It is also to be noticed that the concentration gradient is not constant at dynamic trapping within the specimen [16].

For tensile straining of polycrystalline nickel, observed Δi_{tot} was complicated according to experimental conditions. Positive Δi_{tot} was observed at a strain rate as low as 1×10^{-6}/s and increased with the amount of strain, but it was negative at strain rates higher than 1×10^{-5}/s [16]. The estimation of various factors in Δi_{net} was sophisticated. In polycrystalline nickel, dislocation transport of hydrogen to great depths was unlikely, but a contribution of the dislocation transport in the easy glide region of deformation was concluded for a thin (~100 μm) single crystal slices [16]. However, the passivation current occupied about 90 % of the total permeation current [17].

Hydrogen transport by dislocation at electrochemical permeation was examined for iron single crystals with respect to effects of the type of dislocation [18]. Specimens of 2 mm in thickness were sliced to prepare three combinations of the surface orientation and the tensile axis so as to selectively give the primary slip system for edge, screw and mixed dislocations, respectively. The application of tensile straining during the steady state permeation did not affect anodic current in the elastic range, but anodic current fell discontinuously at the onset of plastic deformation and reached nearly constant levels in easy glide regimes for all three orientations. In the strain range of less than 1 %, small distinct peaks of anodic current appeared for the screw orientation, but the current fluctuated irregularly around a constant level without showing peaks for edge or mixed orientations.

The main decrease in anodic current associated with plastic deformation was reasonably ascribed to trapping of lattice hydrogen by newly generated defects. It was then assumed that hydrogen transport by dislocations gave rise to small discontinuous peaks for the screw orientation. Hydrogen transport rate per unit strain was strongly dependent on strain rate, increasing with decreasing strain rates. The longer time spent per unit strain at the lower strain rate is consistent with the notion that lattice diffusion of hydrogen plays the dominating role in anodic current. Hydrogen transport by moving dislocations was discussed about the hydrogen-carrying capacity which was dependent on types of dislocations [18].

For polycrystalline iron, electrochemical permeation experiments were conducted using cylindrical specimens of 0.3 mm in the wall thickness

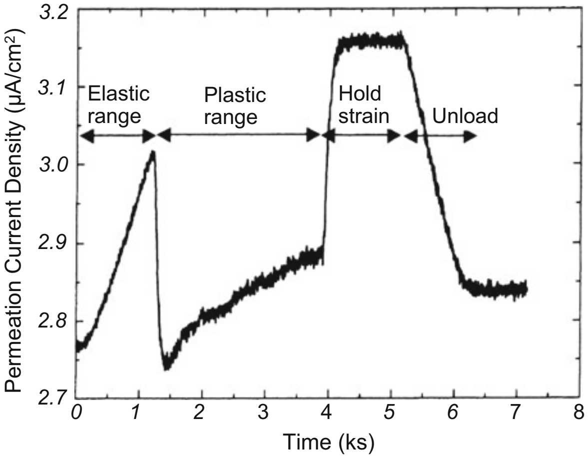

Fig. 4.9 Change in hydrogen permeation current with elastic and plastic deformation for pure iron (Huang et al. [19]. Reprinted with permission from The Iron & Steel Inst. Japan)

[19]. Permeation current after subtracting the passivation current is shown in Fig. 4.9 [19] as a function of time from the start of tensile straining during the steady state permeation stage. The permeation current increased linearly in the elastic range, decreased discontinuously at the onset of plastic deformation, increased gradually and increased rapidly by stopping the load-increase. The discontinuous drop of the permeation current is consistent with a previous study for a single crystal [18] as a result of trapping of lattice hydrogen by newly generated defects. Refilling of depleted hydrogen is likely the reason of the following gradual increase and of the rapid increase at stopping the load rise. Geometrical thinning of the specimen also caused an increase of permeation current in elastic and also in plastic ranges.

References

1. D.J. Fisher (ed.), *Hydrogen Diffusion in Metals – A 30-Year Retrospective* (Scitec Pub., Zürich-Uetikon, Switzerland, 1999)
2. A. McNabb, P.K. Foster, Trans. Metall. Soc. AIME **227**, 618–627 (1963)
3. H. Hagi, Mater. Trans. **35**, 112–117 (1995)
4. G.R. Caskey Jr., in *Hydrogen Degradation of Ferrous Alloys*, ed. by A. Oriani, J.P. Hirth, M. Smialowski (Noyes Pub., Park Ridge, 1985), pp. 822–862
5. Y. Sakamoto, H. Katayama, J. Jpn. Inst. Metals **46**, 805–814 (1982)
6. P. Kedzierzwawski, in *Hydrogen Degradation of Ferrous Alloys*, ed. by A. Oriani, J.P. Hirth, M. Smialowski (Noyes Pub., Park Ridge, 1985), pp. 251–270
7. M.A.V. Devanathan, Z. Stachurski, Proc. Roy. Soc. A **270**, 90–103 (1962)
8. N. Boes, H. Züchner, J. Less Common Met **49**, 223–240 (1976)
9. J.L. Bocquet, G. Brebec, Y. Limoge, in *Physical Metallurgy*, ed. by R.W. Cahn, P. Haasen, vol. 1, 4th edn. (Elsevier Sci., Amsterdam, 1996), pp. 536–668
10. M. Koiwa, Acta Metall. **22**, 1259–1268 (1974)
11. R. Kirchheim, Acta Metall. **35**, 271–280 (1987)

12. R. Kirchheim, Prog. Mater. Sci. **32**, 261–325 (1988)
13. J.A. Donovan, Metall. Trans. A. **7A**, 1677–1683 (1976)
14. H. Shoda, H. Suzuki, K. Takai, Y. Hagiwara, ISIJ Int. **50**, 115–123 (2010)
15. K. Koyama, G. Itoh, M. Kanno, J. Jpn. Inst. Metals **42**, 790–795 (1998)
16. G.S. Frankel, R.M. Latanision, Metall. Trans. A **17A**, 861–867 (1986)
17. G.S. Frankel, R.M. Latanision, Metall. Trans. A **17A**, 869–875 (1986)
18. C. Hwang, I.M. Bernstein, Acta Metall. **34**, 1001–1010 (1986)
19. Y. Huang, A. Nakajima, A. Nishikata, T. Tsuru, ISIJ Int. **43**, 548–554 (2003)

Chapter 5
Deformation Behaviors

5.1 Elastic Moduli

Elastic moduli that characterize the linear relationship between stress and strain express the shape of the potential energy of an atom-pair in materials. If solute hydrogen alters the distance or the cohesive force between neighboring host atoms, its effects are expected to appear in elastic moduli. The effects of hydrogen on Young's modulus of polycrystalline bcc tantalum, niobium and vanadium were measured from the velocity of 100 kHz elastic wave in wire specimens [1]. Hydrogen was cathodically charged in 4 % sulfuric electrolyte with small amounts of CS_2 and As_2O_3. Numerical values of hydrogen contents were not shown, but a linear increase in Young's modulus E with hydrogen content was reported for each metal. The increases in terms of $\Delta E/E$ were 0.07, 0.58 and 0.48 % for Ta, Nb and V, respectively, per 1 at % of hydrogen. On the contrary, a linear decrease in Young's modulus against the square root of the hydrogen concentration up to 2.5×10^{-3} was reported for a Ti-Mo alloy accompanying solution softening and expansion of lattice parameter [2].

The solid solubility of hydrogen in α-iron at room temperature is normally very low as described in Chap. 1, and the expected changes of moduli, if any, are also very small. The measurements of shear modulus of hydrogen-charged polycrystalline α-iron by means of a torsion pendulum method showed a decrease of about 0.3 % of the pendulum frequency at temperatures lower than 200 K [3]. For the experiment, hydrogen was introduced by electric discharge of wet hydrogen gas. The hydrogen concentration was not exact, but an estimated decrease in the shear modulus of iron by 1 at % hydrogen was about 8 % at 100 K.

M. Nagumo, *Fundamentals of Hydrogen Embrittlement*,
DOI 10.1007/978-981-10-0161-1_5

5.2 Flow Stress

Lattice distortion around solute hydrogen atoms and resulted interactions between dislocations and hydrogen, described in Sect. 3.1, may cause solid solution hardening or softening. However, the low concentrations of hydrogen and trapping in various lattice defects often make precise arguments difficult. For a Ti-Mo alloy cited above [2], the proportional limit and 0.2 % proof stress decreased linearly against the square root of hydrogen concentration. For iron and steels, hydrogen effects are fairly complicated depending on materials, deformation stages and testing conditions. Hydrogen effects on the flow stress of iron are not yet conclusive, and Table 5.1 summarizes reported results in the literature [4–15].

(a) Hardening

Hardening by hydrogen is more general than softening for commercially pure iron, low-alloyed and stainless steels tested for bulky specimens at room temperature. For iron single crystal containing about 50 ppm or less of carbon, the critical resolved shear stress for yielding increased on $\{110\} < 111 >$ slip system in a hydrogen precharged specimen, while it was almost immune on $\{112\} < 111 >$ slip system [4]. The tensile straining was conducted at room temperature at strain rates of about 10^{-4}–10^{-5}/s using specimens of 2 mm in thickness. The effects of hydrogen on hardening behaviors vary by carbon contents. For carbon-doped iron single crystals, flow stress increased by 165 ppm carbon but decreased by 10 ppm on tensile straining in the presence of hydrogen [7]. For an intermediate 90 ppm carbon, the flow stress was higher or lower than that of the hydrogen-free specimen according to strain ranges less or larger than about 30 %, respectively. For the experiments, tensile straining was conducted setting the tensile axis near $<001>$ at room temperature under cathodic electrolysis.

For polycrystalline iron containing 10 ppm carbon and ~30 μm in grain size, the yield and flow stress increased by hydrogen on tensile straining of specimens of 2 mm in thickness [8]. For the experiments, hydrogen of ~2 ppm was precharged in 0.1 MPa hydrogen gas at 850 °C and tensile tests were conducted at 0 °C and −80 °C. A noteworthy fact was that hydrogen enhanced the increase in the flow stress by strain aging at low strains less than 5 %.

The grain size dependence of hydrogen effects was also examined in terms of the Hall–Petch relation for the grain size range of 10 ~ 150 μm with commercial pure iron [9]. Tensile tests were conducted at room temperature under cathodic hydrogen-charging to 2–7 ppm in the average hydrogen concentration. The 0.5 % offset stress decreased by hydrogen for coarse grain sizes over ~30 μm but increased for finer grain sizes. However, for iron in which interstitial impurities were reduced by adding 0.15 % titanium as a getter, reductions of the strength by hydrogen were observed for all grain sizes.

The effects of specimen thickness on flow stress at room temperature were examined with a decarbulized rimmed steel containing ~40 ppm of carbon [10]. The flow stress always increased for specimens of 0.8 mm in thickness

Table 5.1 Effects of hydrogen on the flow stress of iron

	Specimen			H-Charging	Strain Rate (s^{-1})	Temperature	Hydrogen Effects	Ref.
	Purity	Grain Size	Size (t × w)					
1	Decaborized Armco iron (C: 30 ~ 50 ppm)	single crystal	2 × 2 mm	1 N HCl aq + hydrazine 30 A/m^2	3.3×10^{-4}, 3.3×10^{-5}	RT	Hardening for: {110} < 111>, Small change for {112} < 111>	[4]
2	Zone-refined pure iron	single crystal	1.5 mmφ	1 N H_2SO_4+ As_2O_3 40 A/m^2	4×10^{-4}	RT	Softening	[5]
3	Zone-refined pure iron (Resistance ratio 4700)	single crystal	0.4φ or 0.1 × 1.4	0.1 N CH_3OH $- H_2O - H_2SO_4$ 20 or 40 A/m^2	8.3×10^{-4}	200 K	Softening, but hardening in the 3rd work-hardening stage	[6]
4	Zone-refined pure iron (Varied C contents)	single crystal	– TA //<001>	1 N H_2SO_4+ As_2O_3	–	RT	Softening in the 1st and 2nd work hardening stages. Hardening when C is added	[7]
5	Vacuum melt electrolytic iron	30 μm	2 × 5 mm	1 atm H_2, 850 °C × 1 h → liq. N_2	6×10^{-4}	0 °C ~ -80 °C	Hardening, prominently at $\varepsilon < 8$ %	[8]
6	Decarbolized Ferrovac E	10 ~ 150 μm	-	1 N H_2SO_4+ As 10 A/m^2	6.5×10^{-3}	RT	Enhanced grain-size dependence of proof stress. Hardening for fine grain size less than 30 μm	[9]
7	Remelt Plasitron (added 0.15%Ti)	10 ~ 150 μm	–	1 N H_2SO_4+ As 10 A/m^2	6.5×10^{-3}	RT	Softening	[9]

(continued)

Table 5.1 (continued)

	Specimen			H-Charging	Strain Rate (s^{-1})	Temperature	Hydrogen Effects	Ref.
	Purity	Grain Size	Size (t × w)					
8	Vacuum melt mild steel and pure iron	20 μm	0.06 ~ 0.8 × 6 mm	1 N $H_2SO_4 + As_2O_3$ 10 A/m^2	3.3×10^{-5}	RT	Hardening, but softening for fine specimen size less than 0.19 mm	[10]
9	Zone-refined pure iron (Resistance Ratio 3500 ~ 6000)	0.3 mm (RRR 3600) 1.0 mm (RRR 5000)	0. 4 mmφ	0.1 N NaOH + Na_2AsO_2 100 or 300 A/m^2	8.3×10^{-5}	170 ~ 297 K	Softening, but hardening even at 200 k for low purity iron. Enhanced softening at lower strain rate	[11]
10	Zone-refined pure iron (Resistance Ratio 1800 ~ 5000)	0.1 mm (RRR 1800) 0.3 mm (RRR 3600) 1.0 mm (RRR 5000)	0. 4 mmφ	0.1 N CH_3OH - H_2O - H_2SO_4 20 or 40 A/m^2	8.3×10^{-5}	170 ~ 297 K	Softening reduced at elevating temperatures. Hardening at room temperature for low purity iron	[12]
11	Zone-refined pure iron +0.6 at %Ti Zone-refined pure iron +0.2 at%Mo	60 ~ 100 μm	0. 5 mmφ	*ibid*	3.3×10^{-5}	200 ~ RT	Hardening for Fe-T. Hardening at RT but softening at below 0 °C for Fe-Mo	[13]
12	Zone-refined pure iron (Resistance Ratio 3600 ~ 5200)	0.4, 1.0, 2.0 mm	0. 4 mmφ	*ibid*	$1.7 \times 10^{-3} \sim 8.3 \times 10^{-5}$	170 ~ 297 K	Softening reduced by increasing strain rate and current density	[14]
13	Remelt electrolytic iron	Single crystal	TA // <110 > (0.1–1.0) × 5 mm	C_2H_5OH + H_2SO_4 50 A/m^2	5×10^{-5}	195 K	Enhanced softening for smaller specimen size	[15]

The residual resistance ratio (RRR) is a measure of the purity of material defined as the ratio of electric resistivity at room temperature and that at 4.2 K when the cathodic current for hydrogen-charging was switched on during tensile straining. However, the flow stress turned to decrease with strain by reducing specimen thickness and softening appeared for the thickness less than 0.20 mm. On the other hand, hardening was always the case for 17Cr steel.

Hardening by hydrogen was also observed for a commercial quenched and tempered steel [8] and a Fe-0.5%Ti alloy [13] on tensile straining at temperatures below room temperature. Another demonstration of hardening was that two-stage Lüders deformation appeared on tensile straining of commercial 1045 steels [16]. For the experiment, hydrogen was introduced into one half of the gauge section, and the second stage Lüders deformation was deduced to arise from the yielding of the hydrogen-charged portion.

(b) Softening

On the other hand, softening by hydrogen generally appears for thin specimens of high purity iron at temperatures below room temperatures. Figure 5.1 [12] shows tensile stress–strain curves of zone-refined high purity iron specimens of 0.4 mm in diameter tested at low temperatures. Upward and downward arrows indicate, respectively, switching on and off of cathodic current for hydrogen charging. While only hardening by hydrogen was observed at room temperature, a gradual decrease of flow stress after a small hump or a prompt decrease appeared at lower test temperatures. It is to be noticed that the decrease in the flow stress at the start of hydrogen charging was temporal at temperatures lower than 180 K and the flow

Fig. 5.1 Effects of cathodic polarization on tensile curves of pure iron specimens at different temperatures (Matsui et al. [12])

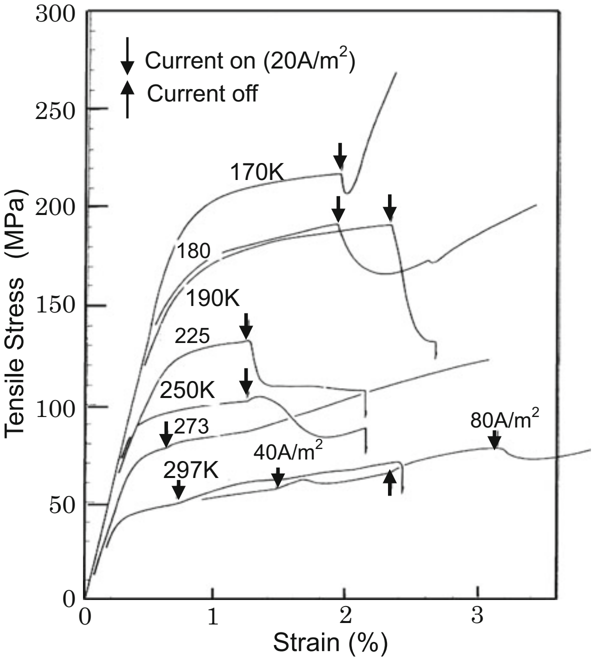

stress tended to increase again at 170 K. The decrease in the flow stress on hydrogen charging at low temperatures was more prominent for higher purity iron. The amount of softening depends on test conditions. The difference in the flow stresses between the final steady level and before charging increased with the higher charging current density, the lower strain rate and the smaller specimen size [14]. It is to be noted that microstructures of the coarse-grain specimens were bamboo-like.

Softening by hydrogen was also observed for tensile straining of single crystal iron specimens as thick as 3 mm in diameter at room temperature and within the easy glide region under continuous hydrogen charging [17]. Slip markings on the specimen surface were finer for hydrogen-charged specimens than those of the hydrogen-free ones. According to the shear stress *vs.* shear strain curve, work-hardening rate soon after yielding increased in the presence of hydrogen and shear stress exceeded that of hydrogen-free specimens, *i.e.* softening turned to hardening. The critical resolved shear stress for yielding was, however, almost the same for specimens with/without hydrogen charging. Softening was also observed over a wide range of strain at 200 K for a single crystal iron specimen of 2 mm in thickness, but a polycrystalline iron showed hardening in small strains less than 5 % [18].

Softening by hydrogen is more prominent for lower strain rates. Figure 5.2 [11] shows the temperature dependence of the yield stress of high purity iron tested at different strain rates. For the experiments, the specimens of 0.4 mm in diameter were prestrained to 1–2 % and hydrogen-precharged by cathodic electrolysis. The

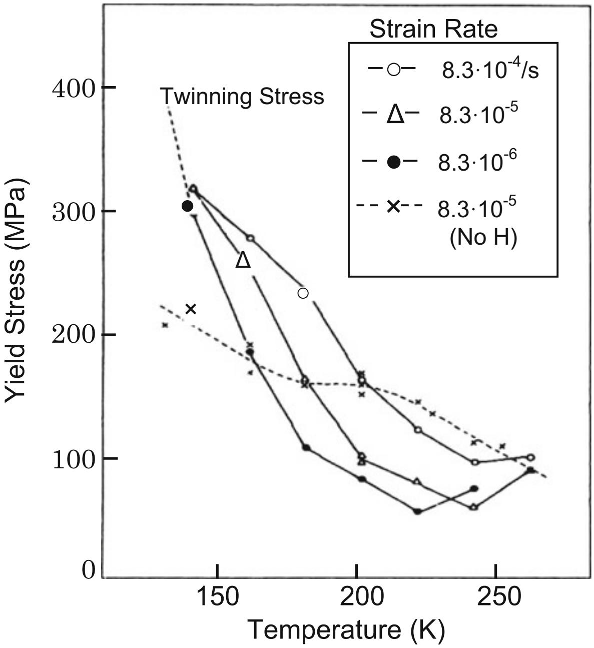

Fig. 5.2 Yield stress of prestrained and hydrogen-precharged iron at different strain rates and temperatures. The broken line is for specimens without hydrogen (Moriya et al. [11])

yield stress increased with decreasing temperature and exceeded the yield stress of the hydrogen-free specimens, *i.e*. turned to hardening by hydrogen. It is noticed that prestraining introduces fresh dislocations in specimens. Aging of prestrained and hydrogen precharged specimens at room temperature diminished hydrogen effects on the yield stress or rather showed hardening at 200 K even at the strain rate of 8×10^{-5}/s [11].

Softening by hydrogen was reported earlier as a pronounced decrease of torque in torsion tests of mild steel tubes [19]. The specimen was a tube of 2 mm in wall thickness and 20 mm in outer diameter. The test was conducted at room temperature, and hydrogen was introduced by immersing the specimen in 5 % H_2SO_4 with small additions of poisons. The observed softening and fractographic features described in Sect. 7.1(f) are the basis of the hydrogen-assisted cracking (HAC) model for the mechanism of hydrogen embrittlement described in Sect. 10.2.

(c) Explanations of experimental results

Observed changes of flow stress induced by hydrogen charging are complicated as described above, depending on the purity, grain size, specimen size, testing temperature, strain rate and fugacity of hydrogen. Hydrogen effects for softening have been discussed so far with respect to (1) interactions of hydrogen with dislocations, (2) the increase in the density of mobile dislocations or (3) the formation of damage in near-surface areas. In many experiments, hydrogen was introduced into specimen using cathodic electrolysis under fairly high fugacity of hydrogen as shown in Table 1.1. It is to be noticed, however, that direct evidences for supposed mechanisms are scarce and quantitative theoretical estimations are difficult.

The motion of screw dislocations dominates plastic deformation after pre-yield strain for iron single crystal at low temperatures. The Peierls potential for screw dislocations in bcc metals is high and strain rate is controlled by the formation of kink-pairs and the side-way movement of kinks. To explain softening observed for high purity iron, Matsui et al. postulated that hydrogen enters the dislocation core and modifies the core structure to increase the double kink nucleation rate [12]. A prompt response of the flow stress to cathodic polarization was ascribed to the transportation of hydrogen by moving dislocations. Experimental conditions employed by Matsui et al. were characterized by high hydrogen fugacity, extremely high purity, and also coarse-grain thin specimens. High concentrations of hydrogen far exceeding equilibrium may exhibit solid solution hardening or softening in similar ways as carbon and nitrogen play their roles. However, Matsui et al. ruled out this possibility for tests at temperatures at which hydrogen was mobile together with dislocations. They assumed that interactions between hydrogen and impurities cause hardening at and above 273 K in impure specimens containing dissolved impurities comparable in concentrations to hydrogen. First-principles calculations for interactions of hydrogen with the core of screw dislocations and for their role on the mobility of dislocations are presented in Sects. 3.1.2 and 5.5, respectively.

On the other hand, Lunarska et al. suggested that softening by hydrogen in the easy glide region at room temperature was due to long-range internal stress rather than double kink formation, because the critical resolved shear stress for yielding was unaffected by hydrogen charging [17]. The proposed mechanism was that the segregation of hydrogen around dislocations lowered elastic interactions between dislocations. On the other hand, hydrogen effects were featured by fine slip markings and higher work-hardening rate leading to hardening in Stage III. Lunarska et al. also suggested the formation of some obstacles against dislocation motion. Hydrogen effects on enhancing the mobility of dislocations are also discussed with respect to shielding of elastic fields by hydrogen as described in Sect. 5.5.1 concerning direct observations by transmission electron microscopy. Hydrogen-enhanced strain localization (HELP) associated with the formation of defects is described in Sect. 7.2.1.

High hydrogen fugacity eventually induces surface damage and actually some blisters appear on the surface of hydrogen-charged specimens [12]. Oriani and Josephic noticed that the generation of blisters or microvoids themselves causes softening by reducing localized stress at the sites and thus increasing the effective stress [16]. They also noticed that the surface of microvoids might facilitate deformation by serving as additional source and sinks of dislocations, increasing the number of mobile dislocations and reducing the number of dislocation pile-up. On the other hand for hardening effects by hydrogen, Oriani and Josephic proposed that hydrogen reduces stacking fault energy that impedes cross slipping. Suppression of the dislocation nucleation from grain boundaries and their ledges was another mechanism Oriani and Josephic proposed for hardening.

The specimen size dependence of softening [10] is a support for surface effects originating in flaw induced by hydrogen charging. However, softening appeared even under mild hydrogen-charging conditions by which the formation of blisters is unlikely [11]. Changes of stress–strain curves associated with switching on and off of charging current are too complicated to simply ascribe to the formation of blisters or voids. An important viewpoint not so much paid attention so far on the flow stress under concurrent electrolysis is the decrease in surface energy due to adsorption of hydrogen on the surface. Surface effects are viable for experiments using thin specimens. As shortly described in following sections, surface effects likely operate in stress relaxation, creep and dislocation mobility under *in situ* transmission electron microscopy. Generation of dislocations from the surface and associated changes of internal dislocation structures should be considered.

An important aspect to be not disregarded on functions of hydrogen associated with the movement of dislocations is the creation of point defects. Moving dislocations multiply dislocations, and screw dislocations gliding on a slip plane generate jogs by intersecting screw dislocations on other slip planes. Transmission electron microscopy applied to deformation microstructures revealed large jogs forming dipoles of edge dislocations for a single crystal of 3 % Si iron [20], and the formation of tangles and cells of dislocations in iron single crystals as a result of mutual interactions of dislocations [21]. The interactions of dislocations with other lattice defects are important factors controlling the flow stress. The interactions of hydrogen with lattice defects created by moving dislocations besides with dislocations are important particularly in areas when the density of dislocations is substantial. The interactions of hydrogen with vacancies created by dragging of jog are described in Sect. 3.2.3.

5.3 Stress Relaxation and Creep

5.3.1 Stress Relaxation

Stress relaxation is a partial release of external stress under a constant strain. An example of stress relaxation in engineering practice is the loss of compacting stress in prestressed steel structures. Stress relaxation eventually leads to fracture. The delayed fracture of steel components stressed at constant displacement in corrosive environments is a case associated with hydrogen-assisted stress relaxation.

Dislocation configurations forming under rising stress turn towards stable structures on stopping the stress increase. At a constant-strain state, the macroscopic strain-rate is zero, *i.e.*

$$\varepsilon = \varepsilon_{\mathrm{e}} + \varepsilon_{\mathrm{p}} = \mathrm{const}, \tag{5.1}$$

then

$$\dot{\varepsilon}_p = -\dot{\varepsilon}_e = -\frac{\dot{\sigma}_e}{E}, \tag{5.2}$$

where suffixes e and p denote elastic and plastic, respectively, and E is Young's modulus. Equation (5.2) implies that plastic strain-rate associated with the rearrangement of dislocations appears as a decrease of elastic stress-rate. Stress relaxation originates in microplasticity and is a measure of the stability of microstructures, particularly of configurations of dislocations. The relaxation rate is very susceptible to temperature variation and its measurement must be conducted under a careful temperature control.

According to dislocation theory of plasticity, the plastic strain-rate is expressed as

$$\dot{\varepsilon}_p = \varphi\rho b\overline{\upsilon}, \tag{5.3}$$

where φ is a geometric factor, ρ is the density of mobile dislocations, b is their Burgers vector and $\overline{\upsilon}$ is the average velocity of dislocations. When the viscous flow model of dislocations [22] is employed, $\overline{\upsilon}$ is expressed as

$$\overline{\upsilon} = A(\tau - \tau_i)^m, \tag{5.4}$$

where A is the average velocity at unit effective stress, τ is the applied shear stress, τ_{i} is the internal shear stress and m is the dislocation velocity-stress exponent. Equation (5.2) is written using Eqs. (5.3) and (5.4) as

$$\dot{\varepsilon}_p = -K\rho(\tau - \tau_i)^m, \tag{5.5}$$

where K is a constant [23]. Then, hydrogen effects in stress relaxation are related to the density of mobile dislocations, the magnitude of internal stress and m.

Hydrogen enhances stress relaxation. Stress relaxation of a zone-refined pure iron in the uniform elongation region shows a substantially enhanced load drop when cathodic hydrogen charging is applied [24]. Figure 5.3 [24] shows hydrogen effects on deformation parameters in Eq. (5.4) obtained by stress relaxation experiments for coarse-grain pure iron at room temperature. Stress relaxation was started at different initial tensile strains ε_0 and hydrogen charging was applied some 1.5–5 min after the start of stress relaxation using cathodic electrolysis in poisoned 1 N H_2SO_4 at a current density of 20–170 A/m^2. The results of Fig. 5.3 indicate that hydrogen reduces internal stress and the dislocation velocity-stress exponent m in Eq. (5.4). Hydrogen fugacity in that experiment was fairly high while data were collected before the formation of blisters.

Reduction of the current density or interruption of charging resulted in an increase of load, and the restart of the cross-head motion showed a jump-like increase in load. Similar hydrogen effects in stress relaxation were observed for many types of iron and steels. Figure 5.4 [10] shows effects of charging current on

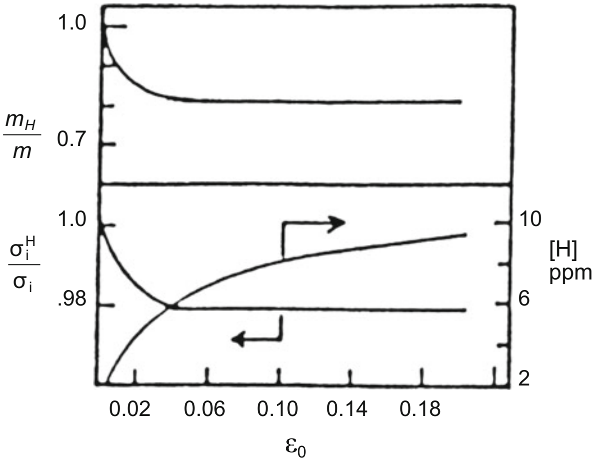

Fig. 5.3 Deformation parameters in Eq. (5.4) for coarse-grain pure iron at stress relaxation tests from different initial strains ε_0 with and without hydrogen-charging. Hydrogen-charging current is 3.8 mA/cm^2 (Lunarska [24])

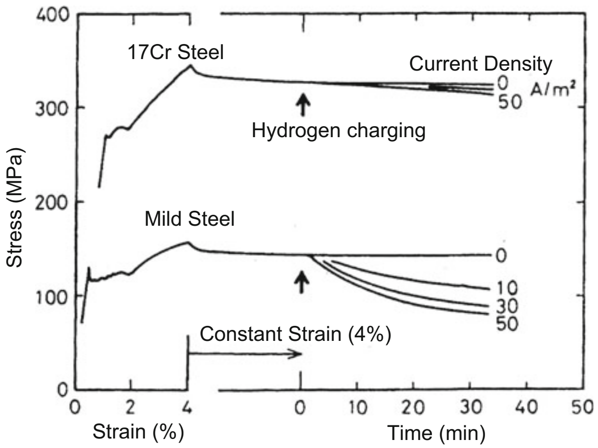

Fig. 5.4 Stress relaxation curves of mild steel and 17Cr steel specimens started at constant strain of 4 %. Cathodic electrolysis was applied in the course of stress relaxation (Asano et al. [10]. Reprinted with permission from Japan Inst. Metals)

enhancing stress relaxation for decarbulized rimmed steel and 17Cr steel. Cathodic polarization was applied during stress relaxation at a constant strain of 4 %. The thickness of the specimen in Fig. 5.4 was 0.8 mm, but the enhancement was more prominent for thinner specimens [10], similarly to the flow stress on tensile straining.

The magnitude of the charging current density is related to hydrogen fugacity that determines solid solubility of hydrogen (Sect. 2.1.1). Oriani and Josephic showed a threshold of the input hydrogen fugacity, *i.e.* some critical hydrogen charging current density, for inducing an abrupt increase in the relaxation rate [25]. The threshold fugacity was higher for higher initial plastic strain to start stress relaxation. On the other hand, a well-defined effect by hydrogen was not discernible on the slope of the relaxation curve at initial strain below a certain amount. The experiments were conducted for AISI 1045 steels 0.25 mm in thickness at room temperature under a careful temperature control. Preceding experiments for flow stress and stress relaxation mostly employed hydrogen charging under fairly high fugacity, but Oriani and Josephic used poisoned 0.1 N NaOH for electrolyte at very low current density and the estimated threshold fugacity was several MPa. The mechanism was discussed in terms of hydrogen-assisted nucleation and growth of microvoids due to decohesion of atomic bonds.

The enhancement of stress relaxation appears not only at simultaneous hydrogen charging during stress relaxation but also by precharged hydrogen. Figure 5.5 [26] shows stress relaxation curves of a 0.37%C-0.6%Si-1.0%Mo-0.5%Cr-0.54 V martensitic steel tempered at 550 °C and 650 °C. Secondary hardening due to the precipitation of fine vanadium carbides by tempering at 650 °C coupled with advanced recovery of martensite gave the same tensile strength of 1470 MPa as that for specimens tempered at 550 °C. Hydrogen precharging was conducted in a mild condition using cathodic electrolysis in a 3 % NaCl + 3 g/*l* NH_4SCN solution at a current density of 5 A/m^2. The specimens were 2 mm in thickness and stress relaxation at 28 ± 0.5 °C was started by stopping tensile straining at 60 % of the

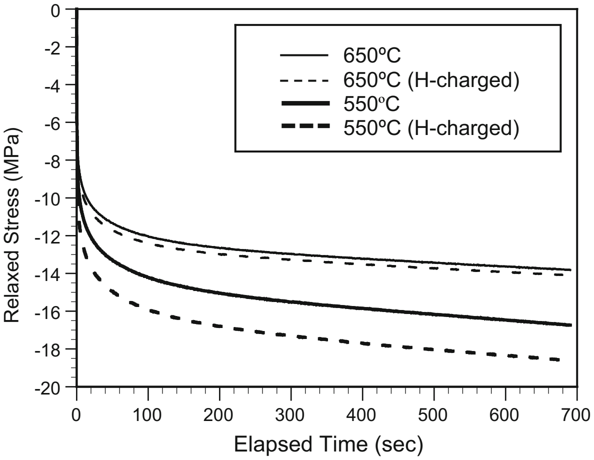

Fig. 5.5 Effects of hydrogen-precharging on stress relaxation curves of Mo-V martensitic steel specimens tempered at 550 and 650 °C. The initial stress is 0.6 of the tensile strength and the test temperature is 28 ± 0.5 °C (Nagumo et al. [26])

ultimate tensile strength. Enhancement of stress relaxation by hydrogen was observed for both tempering temperatures, but tempering at 650 °C substantially reduced the extent of relaxation. It is likely that more stable microstructures of martensite formed by the higher tempering temperature coupled with homogeneous distributions of vanadium carbides suppress strain localization and reduce associated plastic strain rates.

A noteworthy fact concerning the relevance of stress relaxation to hydrogen embrittlement was that tempering of the Mo-V steel at 650 °C improved the resistance to delayed fracture compared with tempering at 550 °C [26]. Relevance of stress-relaxation rates to the susceptibilities to delayed fracture is likely a general feature for steels of similar strength levels or chemical compositions. Early studies revealed a high resistance to delayed fracture and a very small stress relaxation in an 18Ni maraging steel [27]. A correlation between stress relaxation rate and the time to fracture in delayed fracture tests was found for low carbon martensitic steels [28]. Relevance of stress relaxation to hydrogen embrittlement for the Mo-V steel is described in Sects. 6.4.2 and 8.1(b).

5.3.2 Creep

Creep is time-dependent plasticity under constant load or stress and is particularly important for the high-temperature engineering life of materials. At elevated temperatures, sliding of grain boundaries or diffusion of vacancies are primary origins of creep failure. Creep strain is normally very small at room temperature, but delayed fracture under constant stress is a phenomenon accompanying creep. Various mechanisms operate according to types of materials, applied stress and temperatures [29]. Motion of dislocations induced by external stress is opposed by internal stress and obstacles. However, thermal energy gives rise to activation of dislocations or other elements that have been equilibrated under an applied stress and causes microplasticity.

The general form of creep curve is schematically shown in Fig. 5.6, and it depends on temperature and applied stress. The creep curve is generally composed

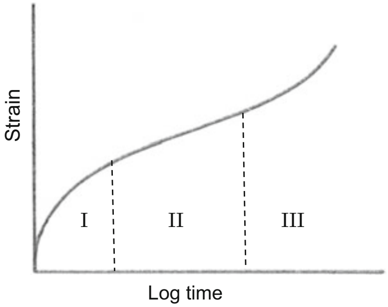

Fig. 5.6 Schematic illustration of three stages in creep curve

of three stages, the transient creep stage of decelerating flow, the steady-state creep of a constant minimum rate and eventually at high temperatures the stage of accelerating flow that ends in fracture. The exhaustion theory of transient creep is that each element is thermally activated only once by a characteristic activation stress and contributes to plastic strain [29]. The creep rate in the transient and steady-state stages is expressed as

$$\dot{\varepsilon} = At^{-n}, \tag{5.6}$$

where A and n are constants and $0 < n < 1$. The steady-state creep rate increases strongly with temperature. The rate over a small range of stress is expressed in terms of the activation energy of dislocation movement in the form of

$$\dot{\varepsilon} = K\exp\left(-\frac{U - b\sigma}{RT}\right), \tag{5.7}$$

where K, U and b are constants. A refined form of the activation energy was derived by Cottrell considering dislocation movement passing through closely spaced obstacles, like dislocation forests [30]. Preceding studies about hydrogen effects descried below, however, were developed before this consideration was presented.

Hydrogen effects on the density, mobility and barriers to movement of mobile dislocations are to appear on creep behaviors while experiments on this matter are not many. Creep rates are higher for higher hydrogen concentrations, similarly to the stress relaxation test shown in Fig. 5.4. During creep deformation of a single crystal specimen of pure iron at 200 K, a sudden application of cathodic potential was insignificant to the creep rate when the potential was low. At a higher applied potential, acceleration of creep rate appeared initially gradually then rapidly and finally to a nearly steady state [18]. In the experiments by Park et al., the thickness of the specimens was 0.8 mm and the applied stress was 60 % of the yield stress. Hydrogen effects were more prominent at higher current densities and stress levels, but the acceleration decreased with increasing temperature and was insignificant at room temperature. When the potential was turned off, the creep rate returned in a few minutes to the initial value before cathodic charging. Such temperature dependence of the accelerated creep rate is similar to softening of the flow stress shown in Fig. 5.1.

The threshold fugacity for accelerating creep rate was also found by Oriani and Josephic with spheroidized AISI 1040 steel [31] by a similar method as used for stress relaxation [25]. The wire specimen was 0.12 mm in diameter and hydrogen charging was conducted by cathodic electrolysis in poisoned 0.1 N NaOH aqueous solution at room temperature. The creep rate at room temperature increased abruptly on applying cathodic potential above a critical value. The increase then decelerated following the form of

$$\varepsilon - \varepsilon_0 = k\ln(t - t_0). \tag{5.8}$$

Shut off of the charging current raised markedly the creep rate to a maximum and then the rate decreased. Oriani and Josephic considered the function of hydrogen similar to that in stress relaxation [25], *i.e.* the reduction in internal stress by the nucleation and growth of microvoids induced by the reduced cohesive strength by hydrogen.

Contribution of vacancies to creep becomes significant with elevating temperatures. If hydrogen increased the density of vacancies as described in Sect. 3.2.3, hydrogen might increase creep rate. Actually, the creep rate at 736 ~ 1200 K of a Pd wire of 0.1 mm in diameter was about six times higher in a 0.1 MPa H_2 atmosphere than that in an Ar atmosphere of the same pressure [32]. Hydrogen reduced the creep activation energy from 38.6 ± 1.9 kJ/mol in Ar gas to 30.0 ± 1.5 kJ/mol in H_2 gas. However, the mechanism of the observed creep was ascribed to grain boundary diffusion of Pd atoms and the effect of hydrogen on the diffusion of Pd atoms was not discussed.

5.3.3 Implications of Surface Effects

The effects of hydrogen on stress relaxation and creep have been discussed mostly with respect to interactions of hydrogen with moving dislocations in specimens and also to surface damage induced by a high hydrogen fugacity. Cathodic polarization introduces hydrogen into metals, but anodic polarization also increases creep rate. Figure 5.7 [33] compares creep curves of a thin copper wire for (a) anodic and

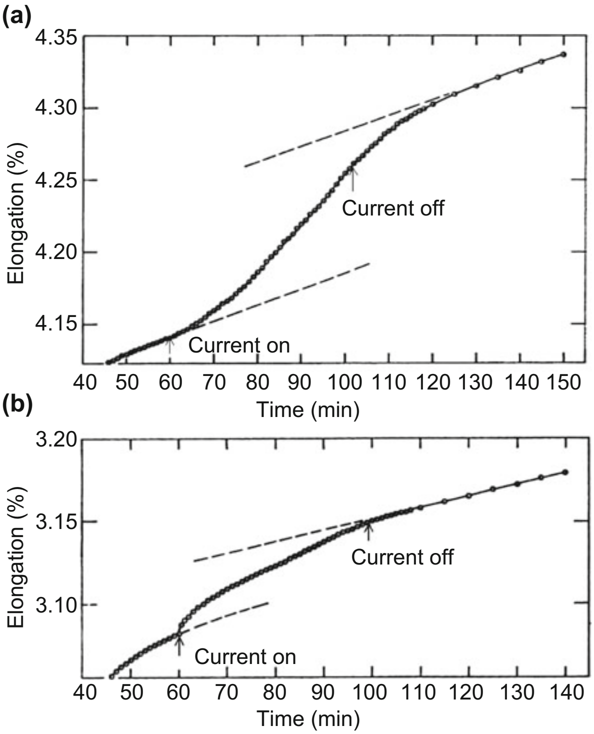

Fig. 5.7 Effects of polarization on creep curves of Cu wire at room temperature. The diameter of wires is 0.27 mm, and the applied stress is 90 MPa. (**a**) anodic polarization, and (**b**) cathodic polarization (Revie et al. [33])

(b) cathodic polarizations. The average grain size was about 20 μm and the diameter of the wire was 0.27 mm. The electrolyte was an aqueous acetate buffer solution of pH 3.7 at 25 ± 0.5 °C and the current density was 9 A/m^2. Both cathodic and anodic polarizations increased creep rate. Anodic polarization increased the creep rate gradually and shutting-off of the current decreased the rate to a level similar to that before the application of polarization. On the other hand, cathodic polarization also increased the creep rate to the same order as anodic polarization, but the increase in creep rate was abrupt on the application of polarization.

The increase in creep rate by both anodic and cathodic polarizations implies that some factors other than hydrogen affect creep rate associated with chemical reactions on the specimen surface. On anodic polarization estimated thinning of the wire was not significant. Revie and Uhlig [33] ascribed the observed lag in the creep response to diffusional process of vacancies that were created very near the metal surface associated with metal dissolution [34]. Divacancies diffusing from the surface were assumed to interact with sessile dislocations causing climb under applied stress.

On the other hand, cathodic polarization is characterized by an abrupt increase in creep rate and a very small current density of 0.1 A/m^2 resulted in a marked increase of creep rate compared with anodic polarization. Revie and Uhlig ascribed the effect to the reduction of surface energy. Hydrogen generated by cathodic electrolysis adsorbs on the specimen surface preceding the entry into the bulk. The change in surface energy, $d\gamma$, of metals caused by a change of the chemical potential, $d\mu$, of an adsorbed phase is given by the Gibbs adsorption isotherm. If the adsorption takes place at temperature T and pressure p,

$$\begin{aligned} d\gamma &= -\Gamma d\mu \\ &= -\Gamma k_B T \ln p, \end{aligned} \tag{5.9}$$

where Γ is the number of molecules adsorbed per unit area and k_B is the Boltzmann constant [35]. For the Langmuir adsorption, *i.e.* monolayer adsorption, of dissociated atoms of diatomic molecules, γ is expressed as

$$\gamma = \gamma_0 - 2\Gamma_s k_B T \ln\left[1 + (Ap)^{1/2}\right], \tag{5.10}$$

where γ_0 is the surface energy without adsorption, Γ_s is the saturation value of Γ and A is a constant. Petch calculated the reduction of γ of α-iron by the adsorption of hydrogen on the crack surface at room temperature, and the results are shown in Fig. 5.8 [35]. The idea and assumptions for the calculation are described in Sect. 9.2 concerning mechanisms of hydrogen embrttlement. The magnitude of γ_0 is about 2 J/m^2 and the fractional reduction of γ shown in Fig. 5.8 is substantial even for very low hydrogen concentrations. Revie and Uhlig postulated that the reduction in surface energy facilitated slip step formations at the metal surface [36]. Since the ease of the slip step formation operates in grains facing the surface, the idea is consistent with the higher acceleration of creep rate for the larger grain size. The

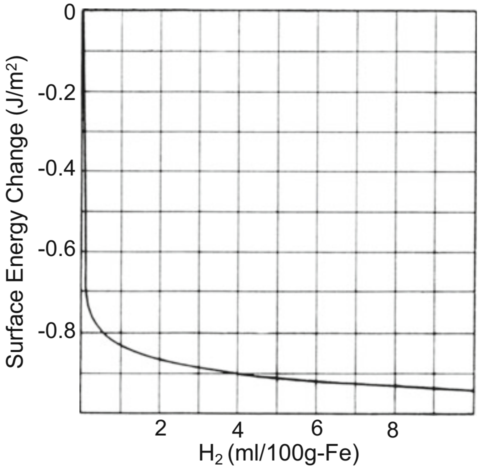

Fig. 5.8 Decrease in the surface energy of iron by adsorption of hydrogen (Petch [35])

idea is also consistent with the fact that the application of cathodic polarization causes a sudden response of creep rate.

If the reduction in surface energy due to adsorbed hydrogen affected creep rate, it also should play a role in stress relaxation. Change of stress states at the surface should alter the balance of internal stress states and induce auxiliary plastic strain. From this notion, the additional plasticity is not a consequence of some direct interactions between hydrogen and dislocations within the bulk phase. In the context, the abrupt drop of the flow stress associated with cathodic polarization on tensile straining, shown in Fig. 5.1, might be ascribed to a decrease in surface energy.

However, Fig. 5.5 that demonstrates the effects of internal hydrogen on stress relaxation implies that surface effects, if any, are not the sole origin of hydrogen effects on creep and stress relaxation. Another candidate mechanism is interactions between hydrogen and strain-induced vacancies. Vacancy formation associated with cathodic electrolysis or dissociation of water molecule at the surface of pure aluminum was observed by Birnbaum et al. [36]. Small angle X-ray scattering and measurements of lattice parameters showed the formation of hydrogen-vacancy complexes clustered into platelets lying on the {111} planes. Candidate origins of vacancies are interactions of moving dislocations as well as possible products on the surface in the case of anodic polarization.

5.4 Direct Observation of Dislocation Activity

The decrease in flow stress shown in Fig. 5.1 and the enhanced stress relaxation shown in Figs. 5.4 and 5.5 lead to the notion of hydrogen-enhanced plasticity. Strong supports of the notion have been obtained by means of in situ environmental cell transmission electron microscopy. The first observation was for iron foils stretched to a constant displacement initially in vacuum and successively in hydrogen gas introduced into the environmental cell [37]. Increase in the hydrogen gas pressure up to 35 kPa increased the velocity of screw dislocations and the removal of the gas rapidly decreased dislocation velocity to the initial value in vacuum. Similar results were observed for a variety of metals and alloys of bcc, fcc and hcp structures [38]. For high purity aluminum, the introduction of hydrogen increased the length of screw components at the intersection of two slip planes and decreased the length of mostly edge components [39]. It was deduced then that pinning by hydrogen stabilized edge segments of dislocations and decreased the tendency to cross-slipping [39]. For nickel, detailed observations showed that hydrogen increased the dislocation velocity and the generation rate of both isolated and tangled dislocations [40]. Increases in dislocation velocity observed for dislocations lying in tangles and for dislocations emanating from crack tips were ascribed to a volumetric rather than a surface phenomenon. It is to be noticed, however, that the stress balance in the specimen may transmit alteration of surface states to that of internal dislocation structures without the entry of hydrogen.

Enhanced strain localization is another feature of hydrogen effects. In situ observations revealed the crack propagation associated with the emission of dislocations from the crack tips [41]. Generation of dislocations in the vicinity of dislocation cell walls ahead of the crack tip was also observed. Initially formed and arrested cracks in iron foil in vacuum restarted by introducing hydrogen gas into the environmental cell at a stress lower than that in vacuum. Deformation was highly localized near the crack tip and resulted in the formation of small voids. The observations have served as an experimental basis of the hydrogen enhanced localized plasticity (HELP) mechanism of hydrogen embrittlement described in Sects. 5.5 and 10.2.

Hydrogen fugacity expected in environment cell is much lower than the threshold fugacity for stress relaxation observed for a carbon steel [25]. Concentrations of solute hydrogen estimated from Sieverts' law are very low compared with other alloying elements or impurities that alter deformation behaviors of steels. It is to be noticed that most dislocations arrays observed by transmission electron microscopy are initially pinned at the surface of the foil specimen. It is feasible that a substantial decrease in surface energy caused by the adsorption of very small amount of hydrogen, as shown in Fig. 5.8, alters the mechanical balance and induces movements of unpinned dislocations.

5.5 Elastic and Atomistic Calculations

5.5.1 Elastic Shielding of Stress Centers

The elastic interaction energy between a hydrogen atom and an edge dislocation originating in the volumetric effect is described in Sect. 3.1.2. The enhancement of dislocation mobility by hydrogen, revealed by in situ transmission electron microscopy, is quite general for fcc, bcc and hcp crystal structures and also for both edge and screw types of dislocations. Some qualitative explanations of experimental observations are described in Sect. 5.2(c), and a quantitative estimation has been made about the reduction of barriers against dislocation motion.

The mobility of dislocations is affected by elastic interactions between dislocations and between dislocations and other stress centers such as solute atoms and precipitates. Hydrogen atmospheres are formed in the dilatational fields so as to make the energy of the system minimum. Sofronis and Birnbaum calculated effects of hydrogen on the dislocation mobility taking into account both the first order dilatational interaction energy expressed by Eq. (3.8) for an edge dislocation and a second order interaction energy that arises from the change in the elastic moduli caused by the presence of hydrogen in solid solution [38, 42].

Calculations were conducted for various configurations and types of elastic centers. Figure 5.9 [38, 42] is a schematic illustration of the coordinates of interacting two edge dislocations of the same sign and hydrogen atmosphere. The shear stress due to hydrogen atmosphere in the area dS is denoted as $d\tau_H$. The net shear stress, τ_H, acting at the core of the dislocation #2 due to the hydrogen atmosphere of the local concentration $C(r, \varphi)$ is given regarding to the hydrogen volumetric effect as

$$\tau_H = -\frac{\mu}{2\pi(1-\nu)}\frac{V_H}{N_A}\int_0^{2\pi}\int_{r_2}^{R} C(r,\varphi)\frac{\sin 2\varphi}{r}\,drd\varphi, \tag{5.11}$$

where μ is the shear modulus, ν is Poisson's ratio, V_H is the partial molar volume of hydrogen, N_A is Avogadro's number, r_2 is the inner cut-off radius of the dislocation 2 and R is the outer cut-off radius of the atmosphere centered at the dislocation #2. It is to be noticed that $C(r, \varphi)$ is the hydrogen distribution in equilibrium with an applied stress field and also with stress fields due to the dislocations #1 and #2. The shear stress τ_D resolved along the slip plane and exerted by the dislocation #1 at the core of the dislocation #2 is

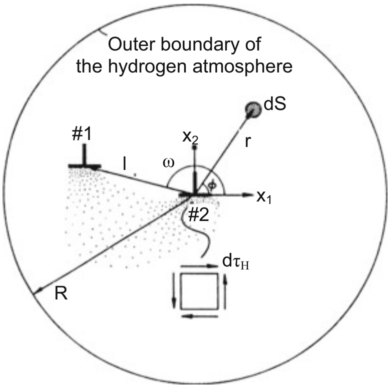

Fig. 5.9 Schematic model for the shear stress acting at the core of dislocation #2 by the hydrogen dilatation lines of an infinitesimal area dS at the position (r, φ) (Birnbaum et al. [38])

$$\tau_D = -\frac{b_1}{2\pi(1-\nu)} \frac{\cos\omega \cos 2\omega}{l}, \tag{5.12}$$

where b_1 is the Burgers vector of the dislocation 1. The net shear stress exerted on the dislocation #2 is equal to $\tau_D + \tau_H$.

Figure 5.10 [38, 42] plots calculated normalized shear stresses, τ_H/μ, τ_D/μ and $(\tau_D + \tau_H)/\mu$, *vs.* normalized distance, l/b, and nominal hydrogen concentrations of H/M = 0.1 and 0.01 for bcc niobium at 300 K. Figure 5.10 indicates that hydrogen atmosphere reduces the repulsive interaction between parallel edge dislocations of the same sign. Very similar results were also obtained for two dislocations of opposite signs. Calculated elastic energies of edge dislocations with and without hydrogen atmospheres are shown in Fig. 5.11 [39] for aluminum as a function of nominal hydrogen concentration. The energies are expressed as the energy per atomic distance along the dislocations. In both Figs. 5.10 and 5.11, fairly high

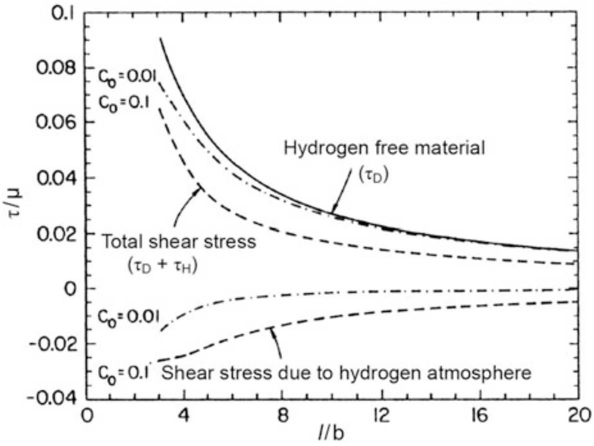

Fig. 5.10 The normalized shear stress due to hydrogen, τ_H/μ, and due to dislocation #1, τ_D/μ, and net shear stress, $(\tau_D + \tau_H)/\mu$, at the core of dislocation #2 at 200 K and nominal hydrogen concentrations of H/M = 0.1, 0.01 in Nb (Sofronis et al. [42])

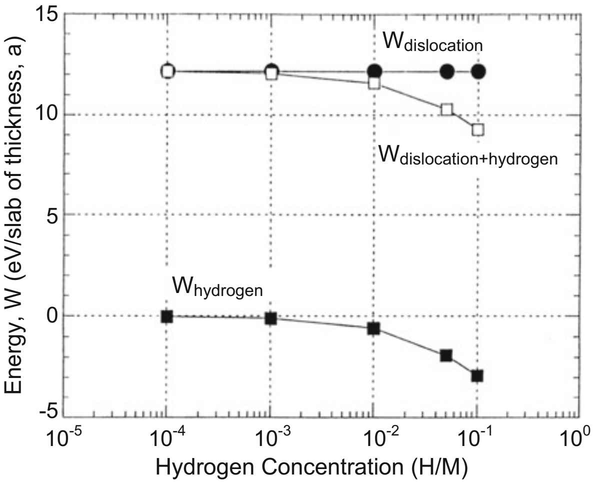

Fig. 5.11 Calculated elastic energies of edge dislocations with and without hydrogen atmospheres as a function of hydrogen concentrations. The energies are given as energy per atomic distance along the dislocation (Ferreira et al. [39])

hydrogen concentrations over 0.01 are necessary to exhibit the shielding effects by hydrogen. Ferreira et al. postulated that the formation of hydrogen atmosphere around edge components of dislocations decreased the energy of the system and disturbed cross-slipping [39]. However, low hydrogen gas pressure in the environmental cell is unlikely to realize such a high hydrogen concentration.

For screw dislocations, direct interactions with hydrogen are very weak because of a cubic symmetry of the deformation field around a hydrogen atom. Sofronis and Birnbaum showed that hydrogen shielding operates also in elastic interactions between dislocations and carbon atom. Screw dislocations interact with carbon atoms. Then, the stress acting on screw dislocations as well as edge dislocations are affected by hydrogen as a result of interactions between hydrogen and carbon atoms [38, 42]. Sofronis and Birnbaum calculated the interaction energy between a dislocation and a carbon atom in the presence of hydrogen atmosphere. A finite element method calculation was conducted taking into account the modulus change of the carbon atom by hydrogen atmosphere as shown in Eq. (5.13) using data for niobium [43],

$$E = E_0(1 + 0.34c), v = v_0 - 0.025c, \mu = \mu_0 \frac{1 + 0.34c}{1 - 0.0177c}. \tag{5.13}$$

The results are complicated, either increase or decrease in the interaction energy depending on the locations and tetragonal axes of the carbon atom. The modulus effect is a weak second order interaction operating in a short range. Hydrogen effects were prominent when the carbon atom locates very close, within one Burgers vector, to the dislocation core. Also, the calculations were for the case of a very high nominal hydrogen concentration of H/M = 0.1.

On the other hand, atomistic modellings for the edge dislocation mobility and pile-ups showed hydrogen effects against shielding of elastic fields [44]. Large-scale molecular dynamics simulations were conducted by applying shear stress to a cell composed of bcc iron and three edge dislocations with/without hydrogen precharging. The formation of the Cottrell atmosphere of hydrogen around moving dislocations was derived, and the pile-up structures were not affected by hydrogen. The results imply that the mobility of edge dislocation is reduced by the drag of hydrogen and that the hydrogen atmosphere provides no measurable shielding of dislocation interactions.

5.5.2 Mobility of Screw Dislocations – Atomistic Calculations

First-principles calculations on interactions between hydrogen and screw dislocation core are described in Sect. 3.1.2. The nucleation of kink-pair and its expansion control the movement of screw dislocation. Wen et al. calculated the effects of hydrogen on the nucleation and the sideward movement energies of kink-pairs in bcc iron [45]. Assuming the kink nucleation on 1/2[111] screw dislocation to take place at a hydrogen atom, binding energies of hydrogen were calculated for various sites of hydrogen in the core. Kinking processes were determined so as to take the minimum energy path during the expansion along the dislocation meeting and overcoming another hydrogen atom. The activation energy of kinking was expressed in terms of the maximum of the increased energy of the dislocation during kinking process.

Softening by hydrogen, *i.e.* reduction in the activation energy, appeared in the sideward movement rather than in the nucleation of a kink pair when the hydrogen state changed from a weaker trapped site to a stronger one. The maximum reduction by hydrogen was about 20 % of about 100 kJ/mol of the overall increase in the dislocation energy in the kinking process. However, softening was not always the case in the kinking process. Hardening was expected when the transition was from a stronger to a weaker trapped site. When hydrogen sites before and after kinking were of the same binding energy, hydrogen effects did not appear in kinking. The sideward motion of a kink pair is impeded when the kink pair meets hydrogen thus inducing hardening.

Itakura et al. conducted a density functional theory calculation of the kink pair nucleation enthalpy H_k in bcc iron using a line tension model of a curved dislocation with/without hydrogen [46]. Two types of the core configuration, stable or unstable, were assumed for screw dislocation and hydrogen atoms were placed at various T-sites near the core. Movement of a screw dislocation required alternation of the two core configurations with the saddle point of the migration path close to the unstable configuration. The enthalpy of a curved dislocation incorporated the position energy of the core, the Peierls barrier, the contributions of external stress and the interaction energy between the dislocation line and hydrogen atoms.

Hydrogen enhances the kink nucleation rate by reducing H_k. The calculated H_k was a function of applied stress, decreasing from 700 kJ/mol to zero as shear stress up to 1000 MPa was applied [46]. The effect of hydrogen in reducing H_k was about 11 kJ/mol for all levels of applied stress. The velocity of screw dislocation was determined by the kink nucleation rate. In order that softening takes place, a sufficient trapping of hydrogen must occur at moving kinks. Itakura et al. showed a region in the temperature-stress diagram where the screw dislocation velocity was increased by hydrogen in bcc iron [46]. Figure 5.12 [46] shows the region for 0.1 at.

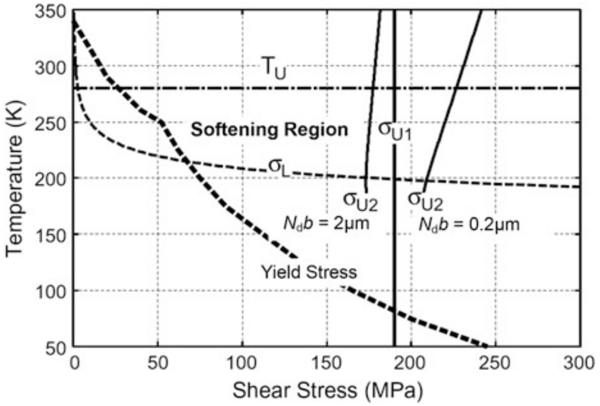

Fig. 5.12 A region in the temperature-stress diagram where an increase in the screw dislocation velocity by solute hydrogen is possible. Calculation for 0.1 at. ppm of hydrogen and two dislocation lengths of 2.0 and 0.2 μm (Itakura et al. [46])

ppm of hydrogen in solid solution. The region is bounded by the upper critical temperature T_U, the lower critical stress σ_L, the yield stress and two kinds of upper critical stress σ_{U1} and $\sigma_{U2.}$ Two upper critical stresses limit the movements of the dislocation and the kink so as to keep the hydrogen concentration together with. The activation of screw dislocations against trapping of kink by hydrogen required large applied shear stress. Values of σ_{U2} were calculated for two typical dislocation lengths denoted as N_d in unit of the Burgers vector b. Also, the upper critical temperature was determined to keep the hydrogen concentration at the promotion sites. The temperature ranges are almost consistent with experimental flow stress behaviors shown in Sect. 5.2, while exact hydrogen concentrations are not definite.

In Sect. 3.2, the generation of vacancies associated with dragging of jogs on screw dislocations and its enhancement by hydrogen is described. The velocity of jog under applied stress is a function of the sum of the formation and the migration energies of vacancies. Matsumoto et al. noticed that hydrogen effects on the two energies almost cancel and the velocity of jogs is not affected by the presence of hydrogen [47]. Hydrogen effects on jog dragging are to increase the density of created vacancies by suppressing the diffusion of vacancies.

References

1. H.A. Wriedt, R.A. Oriani, Scr. Metall. **8**, 203–208 (1974)
2. N.E. Paton, O. Buck, J.C. Williams, Scr. Metall. **9**, 687–691 (1975)
3. E. Lunarska, A. Zielinski, M. Smialowski, Acta Metall. **25**, 305–308 (1977)
4. S. Matsuyama, in *Report of Studies on the Mechanism of Delayed Fracture* (Iron and Steel Institute of Japan, Tokyo, 1975), pp. 113–124
5. A. Goumelon, Mem. Sci. Rev. Mét. **72**, 475–489 (1975)
6. A. Kimura, H. Matsui, H. Kimura, in *Hydrogen in Metals*, Suppl. Trans. JIM **21**, 541–544 (1980)
7. M. Cornet, S. Talbot-Besnard, in *Hydrogen in Metals*, Suppl. Trans. JIM **21**, 545–548 (1980)
8. Y. Tobe, W.R. Tyson, Scr. Metall. **11**, 849–852 (1977)
9. I.M. Bernstein, Scr. Metall. **11**, 343–350 (1977)
10. S. Asano, Y. Nishino, M. Otsuka, J. Jpn. Inst. Metals **43**, 241–248 (1979)
11. S. Moriya, H. Matsui, H. Kimura, Mater. Sci. Eng. **40**, 217–225 (1979)
12. H. Matsui, H. Kimura, S. Moriya, Mater. Sci. Eng. **40**, 207–216 (1979)
13. H. Kimura, H. Matsui, A. Kimura, in *Hydrogen in Metals*, Suppl. Trans. JIM **21**, 533–540 (1980)
14. H. Matsui, H. Kimura, A. Kimura, Mater. Sci. Eng. **40**, 227–234 (1979)
15. H. Wada, S. Sakamoto, in *Hydrogen in Metals*, Suppl. Trans. JIM **21**, 553–556 (1980)
16. R.A. Oriani, P.H. Josephic, Metall. Trans. A **11A**, 1809–1820 (1980)
17. E. Lunarska, V. Novak, N. Zarubova, S. Kadeckova, Scr. Metall. **17**, 705–710 (1983)
18. C.G. Park, K.S. Shin, J. Nakagawa, M. Meshii, Scr. Metall. **14**, 279–284 (1980)
19. C.D. Beachem, Metall. Trans. **3**, 437–451 (1972)
20. E. Furubayashi, J. Phys. Soc. Jpn. **27**, 130–140 (1969)
21. A.S. Keh, Philos. Mag. **12**, 9–30 (1965)
22. W.G. Johnston, J.J. Gilman, J. Appl. Phys. **30**, 129–144 (1959)
23. I. Gupta, J.C.M. Li, Metall. Trans. **1**, 2323–2330 (1970)
24. E. Lunarska, Scr. Metall. **11**, 283–287 (1977)

25. R.A. Oriani, P.H. Josephic, Acta Metall. **27**, 997–1005 (1979)
26. M. Nagumo, T. Tamaoki, T. Sugawara, in *Hydrogen Effects on Materials Behavior and Corrosion Deformation Interactions*, ed. by N.R. Moody, A.W. Thompson, R.E. Ricker, C.W. Was, K.H. Jones (TMS, Warrendale, 2003), pp. 999–1008
27. T. Fujita, T. Sakai, in *Report of Studies on the Mechanism of Delayed Fracture* (Iron and Steel Institute of Japan, Tokyo, 1975), pp. 189–199
28. M. Nagumo, Y. Monden, in *Report of Studies on the Mechanism of Delayed Fracture* (Iron and Steel Institute of Japan, Tokyo, 1975), pp. 149–164
29. A.H. Cottrell, *Dislocations and Plastic Flow in Crystals*, Chap. 16 (Oxford University Press, London, 1956)
30. A.H. Cottrell, Philos. Mag. Lett. **82**, 65–70 (2002)
31. R.A. Oriani, P.H. Josephic, Acta Metall. **29**, 669–674 (1981)
32. Z.R. Xu, R.B. McLellan, Acta Mater. **46**, 4543–4547 (1998)
33. R.W. Revie, H.H. Uhlig, Acta Metall. **22**, 619–627 (1974)
34. D.A. Jones, Metall. Trans. A **16A**, 1133–1141 (1985)
35. N.J. Petch, Philos. Mag. **1**, 331–337 (1956)
36. H.K. Birnbaum, C. Buckley, F. Zeides, E. Sirois, P. Rozenak, S. Spooner, J.S. Lin, J. Alloys Compds. **253-254**, 260–264 (1997)
37. T. Tabata, H.K. Birnbaum, Scr. Metall. **17**, 947–950 (1983)
38. H.K. Birnbaum, P. Sofronis, Mater. Sci. Eng. **A176**, 191–202 (1994)
39. P.J. Ferreira, I.M. Robertson, H.K. Birnbaum, Acta Mater. **47**, 2991–2998 (1999)
40. I.M. Robertson, H.K. Birnbaum, Acta Metall. **34**, 353–366 (1986)
41. T. Tabata, H.K. Birnbaum, Scr. Metall. **18**, 231–236 (1984)
42. P. Sofronis, H.K. Birnbaum, J. Mech. Phys. Solids **43**, 49–90 (1995)
43. F.M. Mozzolai, H.K. Birnbaum, J. Phys. F: Met. Phys. **15**, 507–523 (1985)
44. J. Song, W.A. Curtin, Acta Mater. **68**, 61–69 (2014)
45. M. Wen, S. Fukuyama, K. Yokogawa, Acta Mater. **51**, 1767–1773 (2003)
46. M. Itakura, H. Kaburaki, M. Yamaguchi, T. Okita, Acta Mater. **61**, 6857–6867 (2013)
47. R. Matsumoto, N. Nishiguchi, S. Taketomi, N. Miyazaki, J. Soc. Mater. Sci. Jpn. **63**, 182–187 (2014)

Chapter 6
Manifestations of Hydrogen Embrittlement

Internal cracking such as blistering is, historically and still in the present, a typical hydrogen problem for structural steel components. Blistering is induced under high hydrogen fugacity even without external stress, but degradation or eventually failure of structural steel components emerges in use under mild atmospheric environments. It is to be noticed that the function of hydrogen in the degradation is coupled with applied stress and plastic strain. In this section, mostly phenomenological manifestations of hydrogen effects in various mechanical testing of steels are presented.

6.1 Tensile Tests

(a) Phenomenological features

At tensile tests using bulky specimens, hydrogen degradation appears as premature fracture after or eventually before necking in the apparently elastic region close to the yield stress according to materials, hydrogen concentrations and testing conditions. The degradation is expressed in terms of the fracture stress, the elongation to fracture and the reduction in area. Figure 6.1 [1] shows stress–strain curves of high strength steel bar specimens of 3 mm in diameter with and without hydrogen precharging. The microstructure of the steel (0.84C-0.19Si-0.76Mn in %) was lower bainite of 1517 MPa in tensile strength and was hydrogen precharged by immersing specimens in a 20 % aqueous solution of NH_4SCN at 50 °C for various periods to control hydrogen concentrations. The tensile tests were conducted at room temperature with the strain rate of 5×10^{-7}/s.

The hydrogen concentration increased with the immersion time and tended to saturate at about 3 mass ppm after 10 h. Thermal desorption analysis (TDA) profiles of hydrogen exhibited a single desorption-rate peak at around 120 °C, suggesting that hydrogen is weakly trapped in lattice defects as described in Sect. 2.1.2.

M. Nagumo, *Fundamentals of Hydrogen Embrittlement*,
DOI 10.1007/978-981-10-0161-1_6

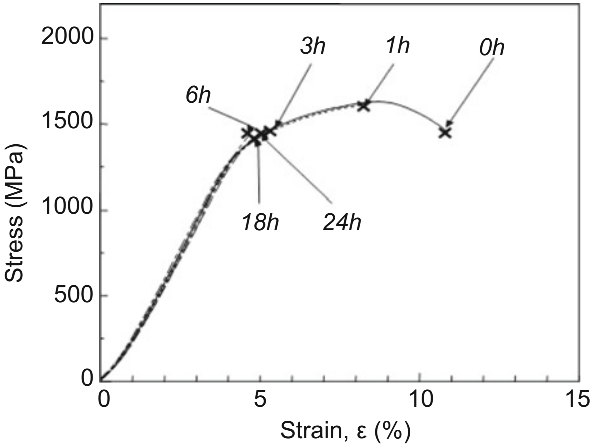

Fig. 6.1 Tensile stress–strain curve of a high-strength lower-bainitic steel with/without hydrogen precharging by immersion in 20 % NH_4SCN solution at 50 °C for various periods. Test at room temperature at a strain rate of 5×10^{-7}/s (Takai et al. [1]. Reprinted with permission from The Iron & Steel Inst. Japan)

Actually hydrogen almost totally diffused out at room temperature in 800 h. A good correlation was revealed between the increase in hydrogen concentrations and the degradation in tensile properties shown in Fig. 6.1.

Alternatively, the steel of the same compositions was isothermally transformed at 550 °C to eutectoid structure and was given cold-drawing to 85 % reduction in area [1]. Hydrogen precharging was conducted in the same way as for the lower bainite steel in Fig. 6.1. TDA profiles of hydrogen exhibited two peaks at around 120 °C (Peak$^{\#1}$) and 350 °C (Peak$^{\#2}$) similarly to Fig. 2.4, and each peak increased with the immersion time. Specimens containing only Peak$^{\#2}$ hydrogen were prepared by annealing cold-drawn and hydrogen-charged specimens at 200 °C. It indicates that hydrogen composing Peak$^{\#2}$ is strongly trapped and non-diffusive even at 200 °C. As shown shortly in Fig. 6.4, tensile tests of thus annealed specimens revealed that hydrogen composing Peak$^{\#2}$ is immune to degradations. It implies that the total hydrogen content does not serve as a parameter for the degradation of tensile properties.

For hydrogen embrittlement of steels, the stage in which the onset of fracture takes place is important for considering the function of hydrogen. Figure 6.2(a) [2] is an example of tensile stress–strain curves of Type 304 and Type 316 L austenitic stainless steels at room temperature with and without hydrogen precharging. Hydrogen was uniformly precharged in 10 MPa hydrogen gas at 400 °C to about 35 mass ppm. Hydrogen degradation appeared for Type 304 steel and fracture took place apparently discontinuous in the uniform elongation stage. However, careful examination revealed that the load drop was rather continuous as shown in Fig. 6.2(b). Since the strain rate was 8.3×10^{-4}/s, elongation of 0.5 % spent about 1 min. The finding suggests that hydrogen promotes the onset of plastic instability, but the diffusion of hydrogen is not likely to cause the instability since diffusion of hydrogen in austenitic stainless steels is almost negligible during the test at room temperature. Related descriptions on the event are made in Sects. 7.2.1(b) and 8.4.4 about strain localization and in Sect. 10.5 about its role in the mechanism of hydrogen embrittlement.

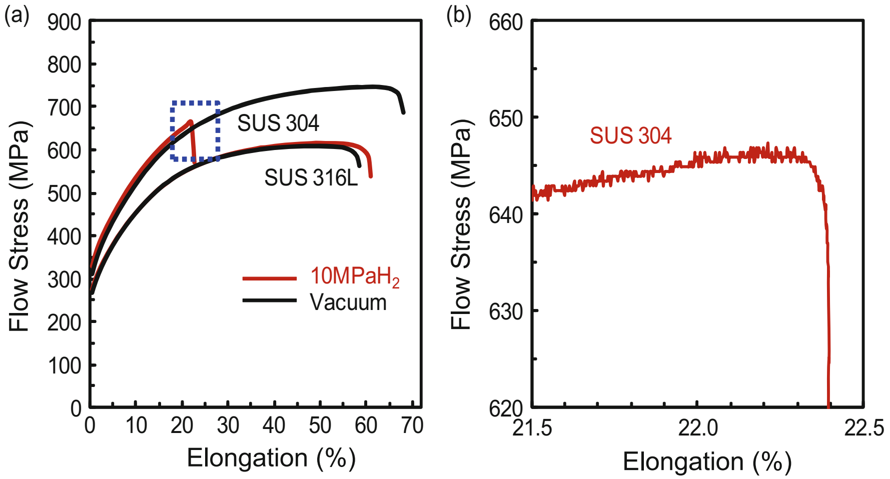

Fig. 6.2 (**a**) Stress–strain curves of Type 304 and Type 316 L stainless steels with/without hydrogen pre-charging. (**b**) A magnified view of the curve near the load-drop of hydrogen-charged Type 304 (Hatano et al. [2])

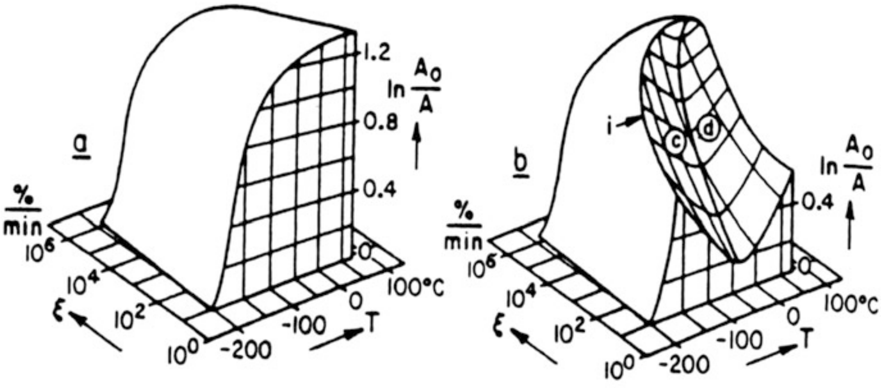

(a) Uncharged (b) Charged

Fig. 6.3 Schematic diagram for the effects of strain rate and temperature on tensile properties of mild steel with and without hydrogen (Bernstein [3]. Reprinted with permission from TMS)

(b) Involvement of strain-induced vacancies in degradation

Strain rate and testing temperature dependencies characterize the susceptibility to hydrogen embrittlement of steels in tensile tests. Figure 6.3 [3] schematically illustrates the dependencies of fracture strain in terms of the reduction in area at fracture for mild steel. The degradation is the most prominent at around room temperature and with decreasing strain rates. A common understanding so far on the origin is the rate of buildup of local hydrogen concentration through diffusion.

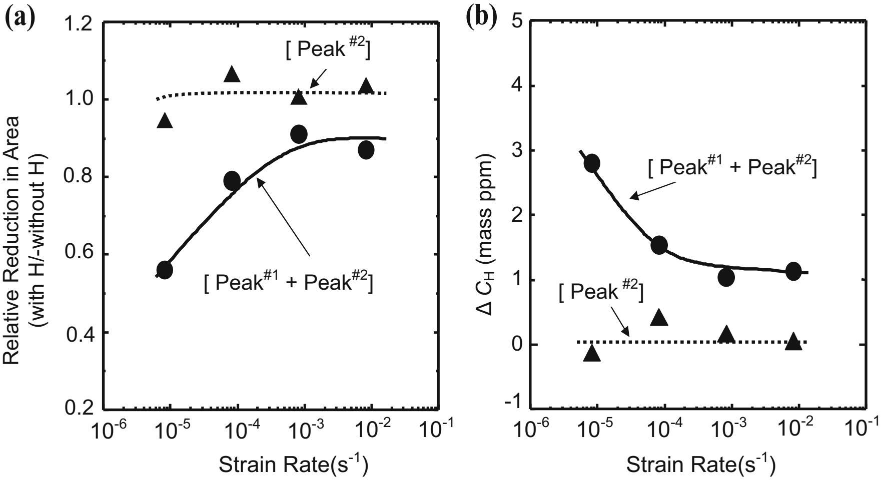

Fig. 6.4 Strain rate dependencies of (**a**) relative reduction in area at tensile tests for specimens containing [Peak$^{\#1}$ + Peak$^{\#2}$] hydrogen and only [Peak$^{\#2}$] hydrogen, (**b**) difference of Peak$^{\#1}$ hydrogen, ΔC_H, between specimens strained to 0.08 with and without hydrogen for [Peak$^{\#1}$ + Peak$^{\#2}$] and [Peak$^{\#2}$] series (Doshida et al. [4])

On the other hand, the origin of the dependencies was studied by means of TDA that gave information on the states of hydrogen in materials [4].

As described in the preceding Sect. 6.1(a), hydrogen introduced into cold-drawn eutectoid steel bars exhibit two thermal desorption-rate peaks, Peak$^{\#1}$ and Peak$^{\#2}$. Tensile test results for the two series of specimens, one containing both Peak$^{\#1}$ and Peak$^{\#2}$ and the other containing only Peak$^{\#2}$, are shown in Fig. 6.4(a) [4] at various strain rates. The ordinate denotes the ratio of reduction in area at tensile tests of steels with and without hydrogen precharging. Hydrogen degradation and a strong strain rate dependence of tensile ductility appeared for specimens containing Peak$^{\#1}$ hydrogen while specimens containing only Peak$^{\#2}$ were almost immune.

The amounts of lattice defects newly created during tensile straining were evaluated in terms of the amount of tracer-hydrogen introduced to saturation into specimens after tensile straining. Since Peak$^{\#1}$ hydrogen was crucial to embrittlement, the amounts of tracer-hydrogen in strained specimens initially containing [Peak$^{\#1}$ + Peak$^{\#2}$] or only [Peak$^{\#2}$] were measured by TDA. The enhancement by hydrogen of strain-induced creation of defects was expressed in terms of ΔC_H defined as the difference in Peak$^{\#1}$ tracer-hydrogen between specimens strained to 0.08 with and without hydrogen. Figure 6.4(b) [4] shows ΔC_H for [Peak$^{\#1}$ + Peak$^{\#2}$] and only [Peak$^{\#2}$] series at different strain rates. The ΔC_H for [Peak$^{\#1}$ + Peak$^{\#2}$] series increased at lower strain rates, but it was independent of strain rates for [Peak$^{\#2}$] series. The results correspond well to the degradation of tensile ductility shown in Fig. 6.4(a). Hydrogen effects are relevant to the enhanced creation of strain-induced defects composing Peak$^{\#1}$, and the strain rate dependence of degradation is associated with the amount of strain-induced defects. The strain rate dependence is also shown in Figs. 7.18 and 7.19 in Sect. 7.3.2 for effects of cyclic prestressing. The vacancy-type entity of lattice defects relevant to the strain-induced increase in Peak$^{\#1}$ hydrogen is described for Fig. 3.10 in Sec. 3.2.3(b) about low temperature thermal desorption spectroscopy.

Similar experiments were conducted for the temperature dependence of tensile ductility [4]. The hydrogen-enhanced loss of ductility appeared significantly with increasing test temperatures from −50 °C to 75 °C for specimens containing Peak$^{\#1}$ hydrogen, while the ductility of specimens containing only Peak$^{\#2}$ were almost immune to hydrogen. The temperature range in which the increase in ΔC_{H} appeared for [Peak$^{\#1}$ + Peak$^{\#2}$] series was coincident with that for the loss of ductility.

Positron annihilation spectroscopy was further successfully applied to discriminate lattice defects involved in the strain rate effect [5, 6]. Positron lifetime in strained pure iron exhibited a long lifetime component exceeding 250 ps when hydrogen was precharged. The component corresponded to vacancy clusters and its relative intensity increased with decreasing strain rates in accord with the behavior of ΔC_{H}. It is a complementary and more direct support for the notion that the strain rate dependence of the susceptibility to hydrogen embrittlement is closely related to the strain-induced creation of vacancies and their clusters.

Discussion on the function of hydrogen in embrittlement has addressed mostly the initiation and growth of cracks in late stages of deformation. However, it was demonstrated for iron and Inconel 625 that hydrogen is not necessarily requisite for embrittlement in the late stage of deformation [7]. The experiments were to interpose unloading and reloading during tensile tests of hydrogen-precharged specimens as schematically shown in Fig. 6.5 [7]. Unloading was applied at

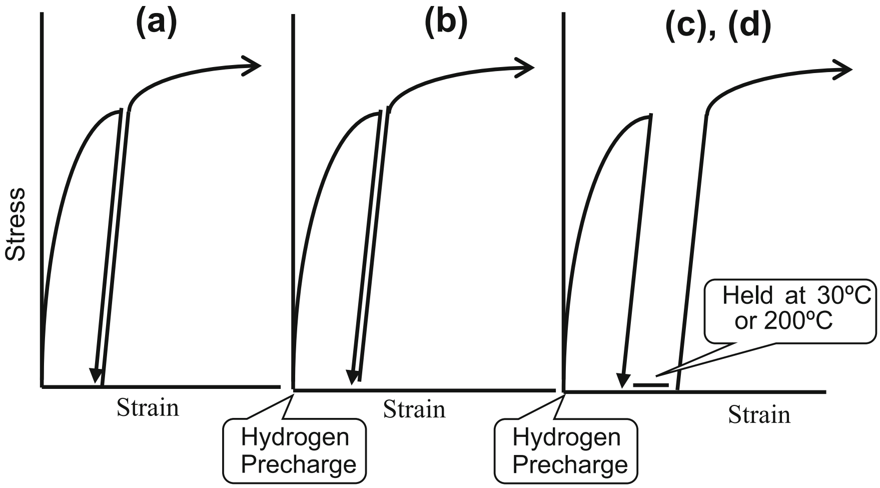

Fig. 6.5 Procedures of interposed unloading and reloading during tensile test. (**a**) Immediate reloading after unloading without hydrogen precharging. (**b**) Hydrogen precharged and immediate reloading after unloading. (**c**) Hydrogen precharged and aged at 30 °C or (**d**) at 200 °C after unloading (Takai et al. [7])

Fig. 6.6 Stress–strain curves of Inconel 625 at tensile tests with interposed unloading shown in Fig. 6.5 (Takai et al. [7])

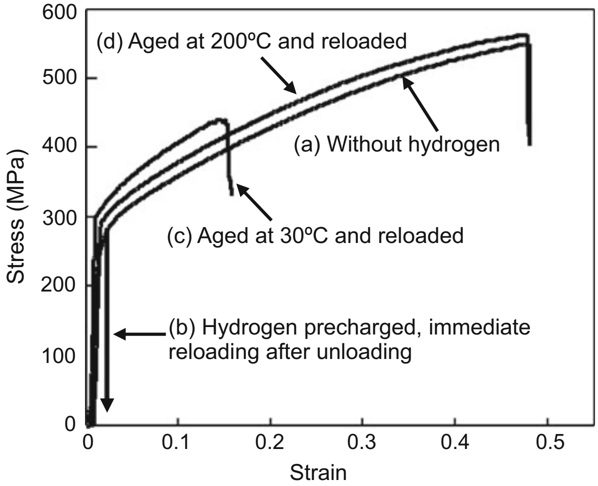

about a half of or close to the fracture strain for iron or Inconel 625, respectively, and degassing at 30 °C or annealing at 200 °C was conducted at the unloaded stage.

Figure 6.6 [7] shows tensile curves of Inconel 625 after reloading. Hydrogen precharging degraded substantially tensile properties and the interposed unloading did not affect the degradation in the hydrogen-charged specimen when reloaded immediately. On the other hand, a substantial degradation remained while hydrogen was removed at the unloaded stage and complete recovery of the degradation appeared by annealing at 200 °C at the unloaded stage. The result demonstrates that the hydrogen-enhanced creation of strain-induced vacancies (HESIV), rather than hydrogen itself, plays the essential role in the degradation.

6.2 Fracture Mechanics Tests

Fracture toughness of materials is evaluated by means of various fracture mechanics test methods using notched or precracked specimens. Charpy impact tests are not appropriate for evaluating hydrogen embrittlement because of involved high strain rate. Fracture toughness is expressed in terms of various quantities such as stress intensity factor (K), crack-opening displacement (COD), and J-integral [8, 9]. In hydrogen or hydrogen-producing environments, the macroscopic crack initiates at the notch-root or the tip of the precrack. The initiation and slow growth rates of cracks are schematically shown in Fig. 6.7 as a function of applied K. Below a threshold stress intensity K_{TH}, crack growth is negligible and K_{TH} is usually denoted as K_{ISCC} for stress corrosion cracking under plane strain condition. Crack growth rates generally exhibit three stages. The growth rate in Stage II is much lower than in Stage I or insensitive to K. Stage III corresponds to final fracture when K reaches the fracture toughness K_c of the material. In sustained-load testing at a

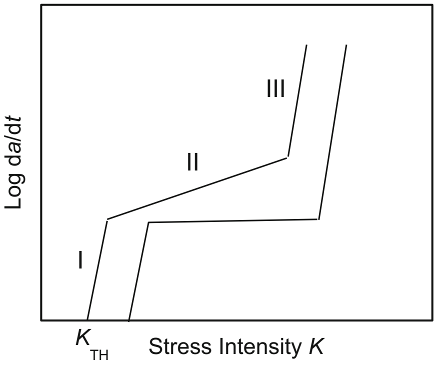

Fig. 6.7 Schematic diagram of three stages of slow crack growth rates with increasing stress intensity

constant applied stress, K increases with the crack growth. On the other hand, K decreases with the crack growth in constant displacement loading. Another threshold stress intensity for crack arrest K_{th} is the value at which the crack growth ceases. Fracture mechanics tests normally need bulky specimens, and inhomogeneous distribution of hydrogen makes the exact estimation of the hydrogen concentration difficult at active sites in the specimen for fracture.

6.2.1 Crack Initiation

The initiation and growth of a crack are detected for fatigue-precracked wedge-opening-load (WOL), compact tension (CT) and double cantilever beam (DCB) specimens under controlled environments [10–14]. The crack growth rate is measured directly [12, 13] or is calculated from the time record of compliance of the specimen [10–14]. Crack growth kinetics varies with the strength level, hydrogen concentration and temperature. Data of threshold stress intensities for the crack initiation in hydrogen gas were compiled by Moody and Robinson as shown in Fig. 6.8 [15] for AISI steels of different yield strengths. The K_{TH} values are strongly dependent on the yield strength and decrease to some limiting values with elevated hydrogen gas pressure. An observed relationship between K_{TH} and P_{H2} at room temperature for an AISI 4340 steel of 1240 MPa in yield strength was [10]

$$\begin{gathered} K_{TH} = 151 - 60\log P_{H_2} \\ (15 < P_{H_2} < 115), \end{gathered} \tag{6.1}$$

where P_{H2} was in unit of 6.89 kPa and K_{TH} was in unit of 1.1 MPa·m$^{1/2}$. However, a lower limit existed for K_{TH} at high hydrogen gas pressures above about 690 kPa. The pressure dependence of K_{TH} is strongly dependent on the yield stress of steels, and the dependence is also sensitive to the magnitude of K_{TH} as shown in Fig. 6.8.

The value of K_{TH} increases with the rise of temperature [10, 15]. Low K_{TH} values at room temperature correspond to Fig. 6.3 for tensile ductility. The

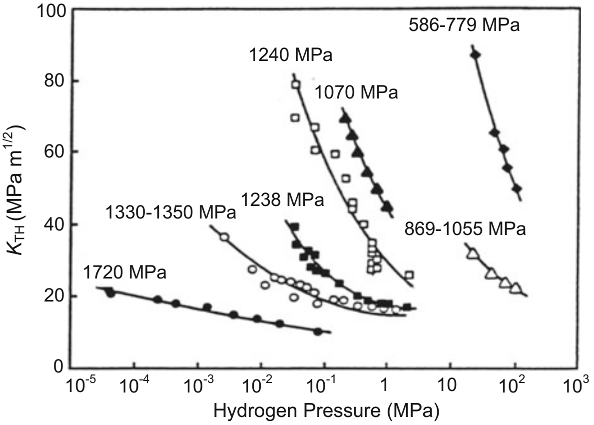

Fig. 6.8 Effects of hydrogen pressure on the threshold stress intensity K_{TH} for crack initiation for AISI 4340 steel (yield strength in MPa) (Moody et al. [15])

dependence differs by steels and magnitudes of K_{TH}. An Arrhenius relationship that indicates a thermally activated process for the same steel as used for Eq. (6.1) in 551 kPa hydrogen was [10],

$$K_{TH} = 3631\exp\left(-1471/T\right) \quad (298 < T(K) < 480)\,, \tag{6.2}$$

where K_{TH} was in unit of 1.1 MPa·m$^{1/2}$.

The K_{TH} values are lower for higher strength steels at a given hydrogen gas pressure. The yield strengths of the steels shown in Fig. 6.8 were controlled through microstructural alterations by tempering temperatures. Micro-plasticity at the crack front should play the role in the degradation, but the intrinsic factor or microscopic process that controls such dependencies is not simple.

The values of K_{TH} were determined by modified WOL tests from the stationary value of the load reached after decreasing with time from the load at which a load drop took place on step loading [16]. Takeda and McMahon noticed with measurements for a 5 % Ni HY 130 steel in hydrogen gas that a subtle crack initiation actually took place along the periphery of plastic hinge or slip lines well below the detectable K_{TH} on loading [16]. Related descriptions concerning impurity effects are in Sect. 8.2(a).

Stress and strain fields in front of the crack tip are expressed in terms of the stress intensity, but the method has limitations when crack-tip plasticity extends. The quantities COD and J-integral are then employed to properly evaluate fracture toughness for medium strength steels. The J-integral is a path-independent integral along an arbitrary counterclockwise path Γ around the tip of crack and is defined as

$$J = \int_{\Gamma} \left(w dy - T_i \frac{\partial u_i}{\partial x} ds \right), \tag{6.3}$$

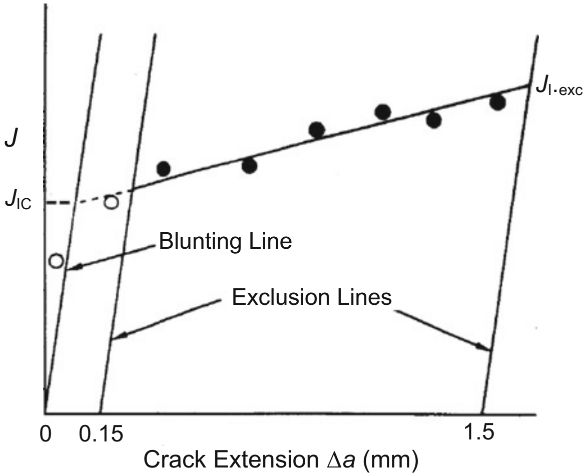

Fig. 6.9 A typical Mode I *J*-resistant curve for a pure mode I test (Gordon et al. [17])

where w is the strain energy density, T_i is the i-th component of the traction vector, u_i is the i-th component of displacement vector and ds is the length increment along the contour Γ. The *J*-integral is a measure of the energy dissipated per unit length of crack tip per unit distance of crack advance and is experimentally obtained from the specimen geometries and the area of the load *vs.* load-point displacement curve.

The *J*-integral value at the onset of a stable crack growth, J_{TC}, is determined as the intersection of the crack blunting line with the *J vs.* Δa curve. For pure mode I loading, J_{TC} is denoted as J_{IC} as shown in Fig. 6.9 [17]. In many practical situations, multiple loading modes superpose, and mode III loading causes localized shear ahead of the crack tip, and an empirical correlation which relates the mixed-mode fracture toughness to the process zone size was proposed [18]. Hydrogen effects on mixed mode I/III fracture toughness were examined for a high purity Ni-Cr-Mo-V steel of tempered lower bainitic structure and 855 MPa in tensile strength [17]. Hydrogen was precharged in 13.8 MPa hydrogen gas at 100 °C to a hydrogen concentration of 2 at. ppm equivalent to a hydrogen fugacity of 1.26 GPa at room temperature. In order to adjust the shear stress component, CT specimens with a slant notch of varied angle Φ were used. Figure 6.10 [17] shows that the increasing mode III component decreases J_{TC} in both hydrogen-charged and uncharged conditions and that hydrogen enhances the degradation additionally by about 30 %. The fracture surface exhibited smaller and more uniform dimples with the increase in the mode III loading component. The findings imply that plasticity plays a role in the crack initiation and that hydrogen is incorporated in the degradation through plasticity. The mechanistic explanation of the finding is described in Sect. 10.4.

Experimental determination of the crack initiation from the precrack is often not precise for medium strength steels. A method for detecting the onset of a stable crack growth from the precrack tip was devised [19] by recording the progress of crack-tip opening displacement δ according to the theory by Needleman and

Fig. 6.10 A plot of J_{TC}*vs.* tilting angle Φ showing J_{TC} decreasing with increasing mode III loading (Gordon et al. [17])

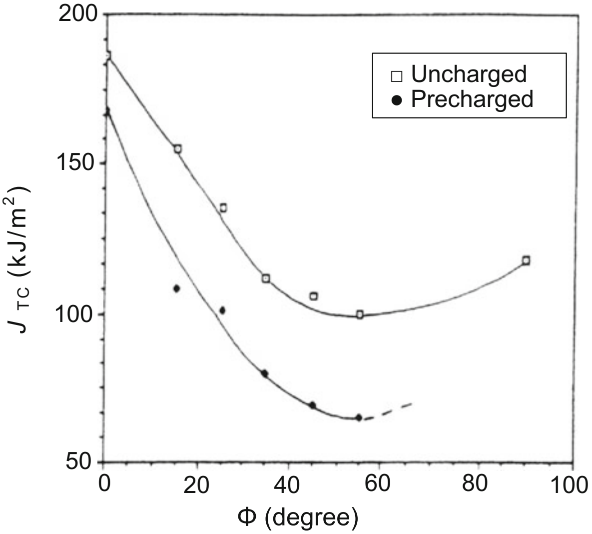

Fig. 6.11 Schematic illustration of the appearance of a “jog” on crack opening displacement δ *vs.* J-integral normalized by yield stress

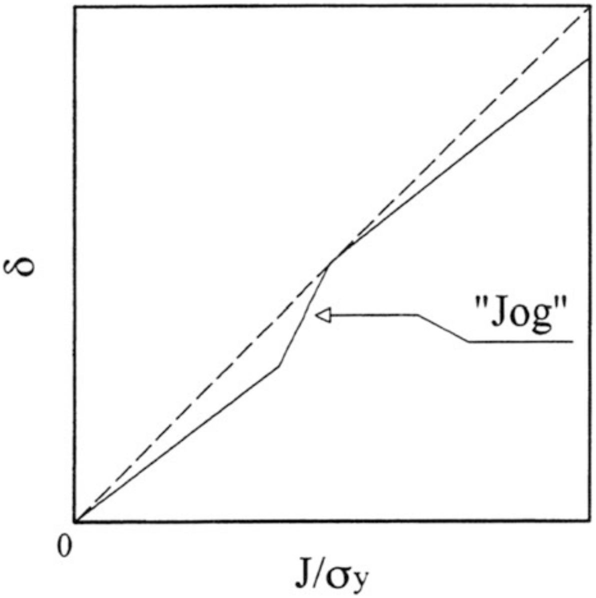

Tvergaard [20] described in Sect. 10.1.3. The onset of the stable crack growth expects a discontinuous increase in δ accompanying a jog to appear on the δ vs J-integral curve. However, the jog will be too small to be detected directly. Alternatively, the gradient of the curve is more sensitive to the appearance of a jog as schematically shown in Fig. 6.11. The method was applied to a three-point bending test of notched specimens of a low carbon steel of 450 MPa in tensile strength. The

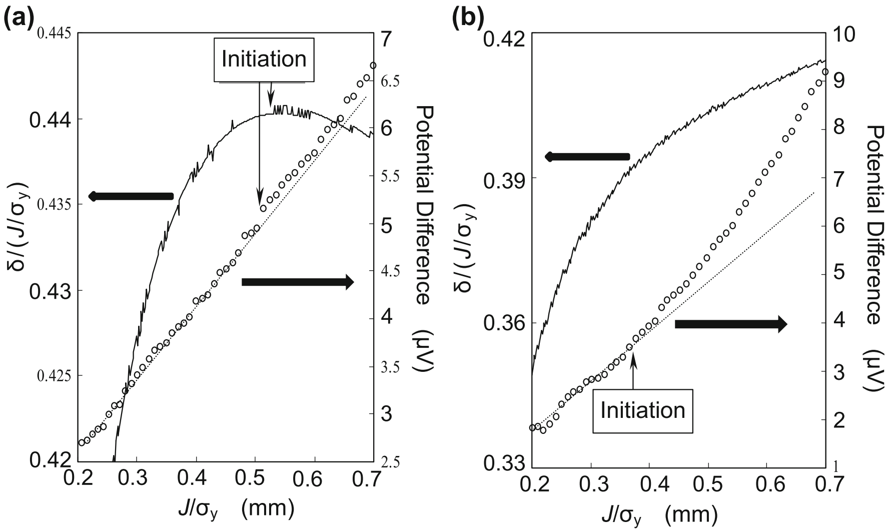

Fig. 6.12 The ratio of crack opening displacement, δ, to J/σ_y*vs.* increasing J/σ_y at a three-point bending test of notched specimen of a low carbon steel. Concurrently observed electric potential drop across the notch is also shown: (**a**) without and (**b**) with hydrogen precharging (Shimomura et al. [21])

result is shown in Fig. 6.12(a) [21] in which J-integral is normalized by the yield strength σ_y. The maximum on the $\delta/(J/\sigma_y)$ *vs.* J/σ_y curve corresponds to the appearance of a jog on the δ *vs.* J/σ_y curve. The crack initiation was confirmed by a simultaneous measurement of electric resistance across the ligament in front of the precrack, shown also in the figure. The crack initiation points detected by the two methods were quite consistent. The result reproduced a previous result by the method applied to a low-carbon low-alloyed steel of 6000 MPa in tensile strength [19].

Subsequently, the above method was applied to hydrogen effects on the crack initiation. The same steel used for Fig. 6.12(a) was hydrogen precharged to 0.82 mass ppm under a fairly mild fugacity using cathodic electrolysis in an aqueous solution of 3 % NaCl + 3 g/l NH_4SCN at a current density of 5 A/m^2 for 24 h. Promoted crack initiation by hydrogen was revealed by means of the electric resistance method as shown in Fig. 6.12(b), but $\delta/(J/\sigma_y)$ increased continuously with J/σ_y without showing a maximum. It implies that the opening of the precrack proceeds gradually without a large step-wise advance. The theory by Needleman and Tvergaard [20], described in Sect. 10.1.3, assumed that a discontinuous advance of the crack at a critical amount of void volume fraction is caused by the loss of stress-carrying capacity in the area adjacent to the crack. The observed rather gradual growth suggests that hydrogen coupled with strain-induced defects continuously and incrementally reduces the stress carrying capacity. The function of hydrogen originating in the enhanced creation of strain-induced vacancies is described in Sect. 10.5.

6.2.2 Crack Growth

(a) Growth rate ~ Gaseous hydrogen environment

Crack growth rate is important for kinetics of hydrogen embrittlement, and it has been examined mostly for Stage II in the three stages shown in Fig. 6.7. The steady crack growth rate at Stage II is little affected by the magnitude of stress intensity and is likely rate-controlled by some factors other than mechanical driving force.

The temperature dependence of the growth rate gives information on the controlling process. Temperature dependencies of the growth rate of AISI 4130 steel in 98 kPa hydrogen gas and at applied stress of 39 $\text{MPa}\cdot\text{m}^{1/2}$ are opposite in sign according to temperature regions as shown in Fig. 6.13 [22]. Activation energies obtained from each Arrhenius relationship were 16 and −23 kJ/mol in Region 3 and Region 1, respectively. Similar opposite temperature dependencies of the Stage II crack growth rate were observed in 133 kPa dry hydrogen gas for AISI 4340 steel of 2082 MPa in tensile strength [12]. The activation energy of Stage II crack growth in Region 3 was 14.7 kJ/mol, close to 16 kJ/mol for AISI 4130 steel.

The crack growth in dry hydrogen gas proceeds with adsorption and following migration of hydrogen on the specimen surface. Williams and Nelson ascribed the rate-controlling process of the crack growth to adsorption of hydrogen on the steel surface taking into account the fractional coverage of initial adsorption sites [22]. Simmons et al. noticed that fractographic features at tests in hydrogen gas and in water are similar and deduced that surface reactions of water with steel controlled the crack growth rate in water [12].

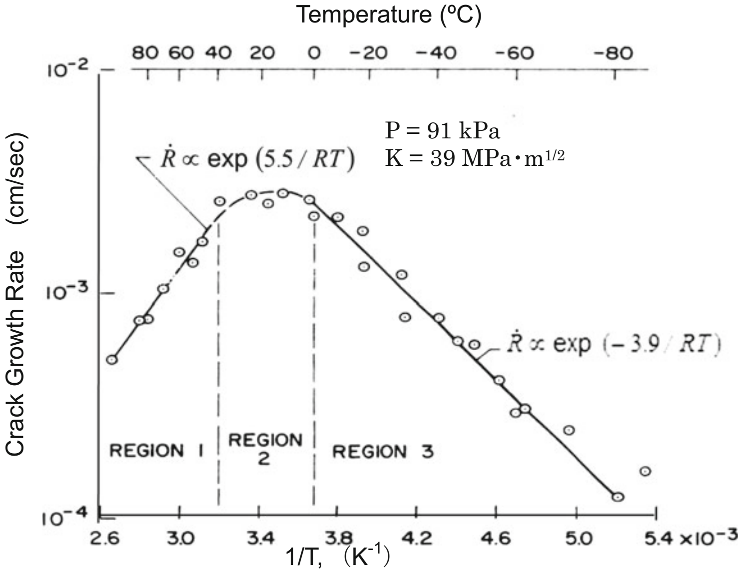

Fig. 6.13 Temperature dependence of the crack growth rate for AISI 4130 steel in low pressure hydrogen gas (Williams et al. [22])

The temperature dependence of Stage II crack growth rate varies by microstructures. For experiments with 18Ni maraging steels, tensile strength levels were controlled to 1330 MPa and 1720 MPa by tempering at 200 °C and 250 °C, respectively [23]. The temperature dependence of Stage II crack growth rate in dry hydrogen was similar to Fig. 6.13, but the slope in Region 1 was very steep. The transition temperatures from Region 1 to Region 3 in 133 kPa hydrogen gas were about 20 °C and −20 °C, respectively, for steels tempered at 250 °C and at 200 °C, respectively. Magnitudes of the crack growth rate at the transition temperature were also fairly different between the two steels, about 5×10^{-5} m/s and 5×10^{-6} m/s for tempering at 250 °C and 200 °C, respectively. The crack growth rate increased proportionately to $\sqrt{P_{H2}}$ in Region 3 with the activation energy of 18.4 kJ/mol irrespective of tempering temperatures and hydrogen gas pressures. Gangloff and Wei suggested that some reactions in a near surface region operated associated with hydrogen transport by diffusion, but the process controlling Region 1 was not definite [23].

Vehoff and Rothe found that the crack-tip opening angle (CTOA) α is constant during the stable crack growth at tensile loading of notched Fe-2.6%Si single crystals in low pressure hydrogen gas [24]. The value of α characterizes the amount of ductility accompanying crack growth. The fracture surface showed a very fine mixture of plastic shearing off and cleavage-like facets on a scale of 0.1 μm or less. The value of α was a function of temperature, hydrogen pressure or activities and crack growth rate. The temperature dependence of α in the intermediate temperature range $293 \text{ K} < T < 390 \text{ K}$ showed an Arrhenius-type relation with an apparent activation energy of 49 kJ/mol. Vehoff and Rothe deduced that isolated microcracks were initiated along the crack front and that the embrittlement was related to the fractional hydrogen coverage of special sites right at the tip of a stressed crack with the binding energy of 49 kJ/mol [24].

Similar results were obtained with low cycle fatigue of nickel single crystals in electrolytes at different cathodic potentials. The fracture mode was a mixture of alternate slip and local brittle fracture [25]. The apparent binding energy obtained from the temperature dependence of CTOA was 32 kJ/mol.

(b) Crack growth rate ~ Internal hydrogen

Crack growth in gaseous hydrogen likely involves surface reactions, but the effects of internal hydrogen have been also examined. Three stages of crack growth rate of the type shown in Fig. 6.7 were observed at sustained-loading tests of hydrogen precharged AISI 4340 steels [13, 26]. Hydrogen precharging was conducted by cathodic electrolysis in poisoned 5 % H_2SO_4 aqueous solution at a current density of 20 A/m^2 and hydrogen was enclosed within the specimens by cadmium plating [26]. The crack growth in hydrogen-precharged specimens exhibited an incubation time and a transient stage before establishing the steady state Stage II. The growth rate at room temperature was at least one order of magnitude faster for specimens of 1620 MPa in yield strength by tempering at 230 °C than for 1340 MPa specimens by tempering at 450 °C. Stage II crack growth rates were also dependent on temperature with Arrhenius relations. A theoretical model for the crack growth rate was proposed assuming that the build-up of local hydrogen concentration by diffusion to a critical value in the crack tip region triggered fracture there and induces the crack advance [26]. Using numerical values of parameters obtained from the literature, experiments and also as adjustable variable, crack growth rates were calculated to fit fairly well with the observed temperature dependence for 230 °C tempering. The estimated binding energies of hydrogen with the critical trap sites for the crack initiation were 75 kJ/mol and 27 kJ/mol for 230 °C and 450 °C tempering, respectively. Fractographic features were mixtures of IG and QC for specimens tempered at 230 °C. For tempering at 450 °C, alternate IG and MVC regions were assigned to intermittent slow and fast crack growth. Details of fractographic features are described in Sect. 7.1(e).

In the model proposed by Gerberich et al. [26], crucial assumptions are (i) the fracture stress decreasing in proportion to hydrogen concentration, and (ii) high local hydrogen concentrations due to both the dilatational stress field and trap-binding effects. Plastic constraint was also taken into account for computing the triaxial stress at the critical site. Critical trap sites to cause sequential fracture were assigned from fractographic observations to martensite lath boundaries intersecting the prior austenite grain boundaries for 230 °C tempering and to oxysulfides located at the edge of plastic zone for tempering at 450 °C. However, the critical hydrogen concentrations that the model estimated at the trap sites were very high, more than 10^6 times of hydrogen in solution. The problems are further described in Sect. 8.1 (a) about fractographic features and in Sect. 9.3 about the mechanism.

(c) Crack growth resistance

The resistance against rack growth rate is a direct measure of intrinsic degradation of materials. Crack growth resistance curve (*R*-curve) plots the total energy dissipation rate as a function of the crack length in slow stable crack growth. The total energy dissipation rate is expressed in terms of the *J*-integral in the elastic–plastic regime. Figure 6.14 [27] compares *R*-curves of notched specimens of low

Fig. 6.14 R-curves of low carbon ferrite-pearlite steel with and without hydrogen precharging. ○, ● : observed values; Δ, ▲ : calculated values using a finite element method (Nagumo et al. [27])

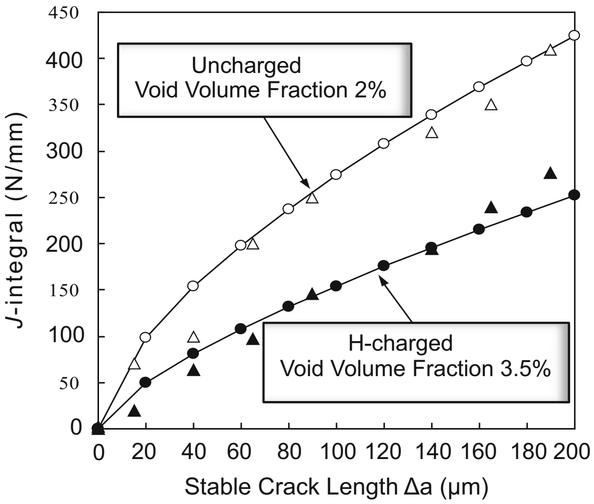

carbon ferrite-pearlite steel subjected to three-point bending tests with and without hydrogen precharging. Hydrogen charging was conducted in a mild condition by cathodic electrolysis in 3 % NaCl + 3 g/*l* NH_4SCN aqueous solution at a current density of 5 A/m^2 for 24 h. A substantial decrease in the crack growth resistance appeared for hydrogen-charged specimens. The marks Δ and ▲ in the figure for specimens without and with hydrogen precharging, respectively, denote calculated *J*-integral values from the stress and strain fields near the crack. A constitutive relation for porous materials was used for the calculation, and the decrease in the *J*-integral by hydrogen was ascribed to an increase in nucleation void densities. The method of modelling *R*-curve in Fig. 6.14 is described in Sect. 10.5.3. *R*-curve is closely related to strain-induced lattice defects and analyses of microscopic origins are described in Sect. 10.5.2.

Effects of hydrogen on *R*-curve were also shown for disc-shaped compact tension specimens of 21Cr-6Ni-9Mn austenitic stainless steel [28]. Hydrogen was thermally precharged to 210–230 mass ppm in high pressure hydrogen gas. The fracture initiation toughness J_{Q} was defined as the *J* value at the intersection of the 0.2 mm offset blunting line with the *R*-curve. Alternatively, initial damage at the precrack tip was detected as a subtle deviation from linearity of the COD *vs*. crack length measured using the direct current potential difference according to ASTM E1737. The deviation point was denoted as J_i and J_Q according to the choice of the initial blunting line. Hydrogen reduced both J_i and J_{Q} by more than 80 % from the values for hydrogen-free specimens. Crack growth resistance denoted by d*J*/d*a* also decreased nearly 50 % by hydrogen. Nibur et al. carefully examined deformation microstructures that exhibited enhanced strain localization. The features are described in Sect. 7.3.1.

The *R*-curve is strongly dependent on microstructures of steels. It was revealed for ferrite-pearlite steels that carbides precipitated along grain boundaries acted as barriers against slip extension across grain boundaries and affect *R*-curves prominently [29]. The functions of the slip constraint in *R*-curve for that case are described in Sect. 10.5.2 about the strain-induced creation of vacancies.

6.3 Fatigue

Fatigue failure is the most common type of failure of metallic structural components in practical services. Not only under high pressure hydrogen gas environments, hydrogen comes from humid or corrosive environments, during cathodic protection of off-shore structures, or at electroplating, and plays a crucial role in fatigue failure. Corrosion fatigue is often caused by hydrogen produced by corrosion reactions on the metal surface.

Fatigue properties of materials are commonly expressed in terms of fatigue life and fatigue limit determined from the plot of the stress amplitude *vs*. the number of cycles to failure (*S*-*N* curve). The fatigue limit $\Delta\sigma_{\mathrm{c}}$ and the threshold stress intensity range for no detectable crack growth ΔK_{th} are design parameters for the safety against fatigue failure [30]. Fatigue failure proceeds through the crack nucleation and growth. Measurements of fatigue-crack growth in laboratories are conducted commonly using notched specimens. Fatigue tests consume a substantial time for one run, and hydrogen contents in specimens are often not constant during a test-run due to the entry and loss of hydrogen and/or internal changes of materials.

Fatigue failure is affected by many factors and their effects are not similar among different expressions of fatigue properties. Early works for hydrogen effects on metal fatigue were reviewed by Gerberich with respect to different approaches such as total life, threshold and crack growth [31].

(a) *S*-*N* curve

Hydrogen generally reduces fatigue life and fatigue limit. Figure 6.15 [32] plots tension-compression fatigue test data of two lots of surface-hardened 0.36C-Cr-Mo martensitic steel with/without hydrogen. Hydrogen was initially charged by immersing specimens in 20 % NH_4SCN aqueous solution at 50 °C, and hydrogen contents were controlled to 10, 0.8 and 0.3 mass ppm by partial degassing at room temperature. Fatigue specimens contained a small hole of 100 μm in both diameter and depth on the specimen surface as the crack starter. Fatigue tests were conducted at a stress ratio R ($= \sigma_{max}/\sigma_{min}$) of -1 and with different frequencies up to 1000 Hz. Hydrogen was recharged to specimens every 8×10^6 fatigue cycles so as to keep the same content during the test. The control of hydrogen content was by partial degassing, and the reductions in fatigue life and fatigue limit by hydrogen were reversible against the entry of hydrogen. A small amount, ~ 0.3 mass ppm, of hydrogen remaineded in as-heat-treated specimens, and thermal desorption analysis

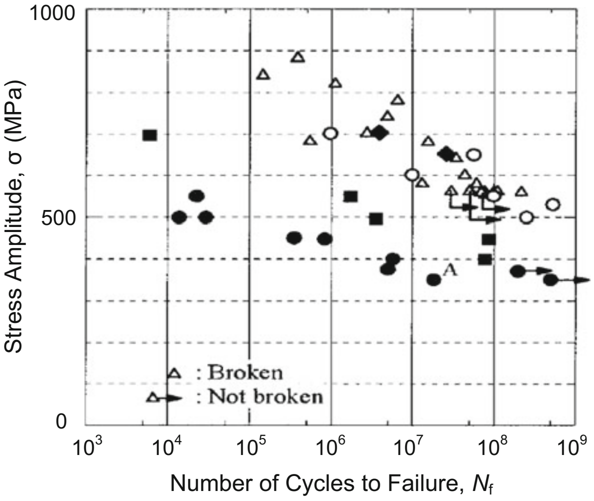

Fig. 6.15 Effects of hydrogen on *S*-*N* diagram of two lots of SCN 435 steel. Open marks, as-heat-treated (0.3 ppm H); Solid marks, H-charged. Initial hydrogen contents are controlled by partially degassing at room temperature after hydrogen charging: ● (10 ppm), ■ (100 h after hydrogen charging, 0.8 ppm), ♦ (4300 h after hydrogen charging, 0.3 ppm) (Murakami et al. [32])

(TDA) showed a small peak at 300 °C indicating strongly trapped non-diffusive nature of residual hydrogen as described in Sect. 2.1.2. On the other hand, artificially charged hydrogen diffused out at room temperature exposure and the thermal desorption ceased by 300 °C. The observations imply that the degradation is caused by diffusive hydrogen. Murakami et al. revealed the fatigue-crack initiation from non-metallic inclusions [32]. Non-metallic inclusions are possible trap sites of non-diffusive hydrogen, but non-diffusive hydrogen is generally immune to degradation. Alternatively, diffusive hydrogen might interact with non-metallic inclusions and/or with plastic deformation around inclusions, but the changes of trapped states during fatigue cycles were not examined.

Hydrogen effects to decrease fatigue life and fatigue limit at rotational bending tests are shown in Fig. 6.16 [33] for unnotched round bar specimens. The steel was a high strength Si-Cr martensitic steel hydrogen precharged under a fairly mild condition by cathodic electrolysis in a 3 % NaCl + 3gl^{-1} NH_4SCN aqueous solution at a current density of 7.5 A/m^2. Lattice defects produced during fatigue were detected by introducing hydrogen as the tracer of defects into fatigued specimens after removing precharged hydrogen at room temperature. The tracer hydrogen exhibited a single peak at about 120 °C on TDA, indicating weakly trapped states. The amounts of the tracer-hydrogen in fatigue-fractured specimens at two applied stress levels are shown in Fig. 6.17 [33]. The stress amplitude of 580 MPa was close to the fatigue limit. The amounts of the tracer hydrogen were larger in hydrogen-precharged specimens than in uncharged ones in spite of shorter fatigue cycles for hydrogen-precharged specimens. The results suggest that the promoted failure by hydrogen is due to the enhanced creation of defects during fatigue cycles. Vacancy-type nature of defects created during fatigue cycles is described in Sect. 7.3.1.

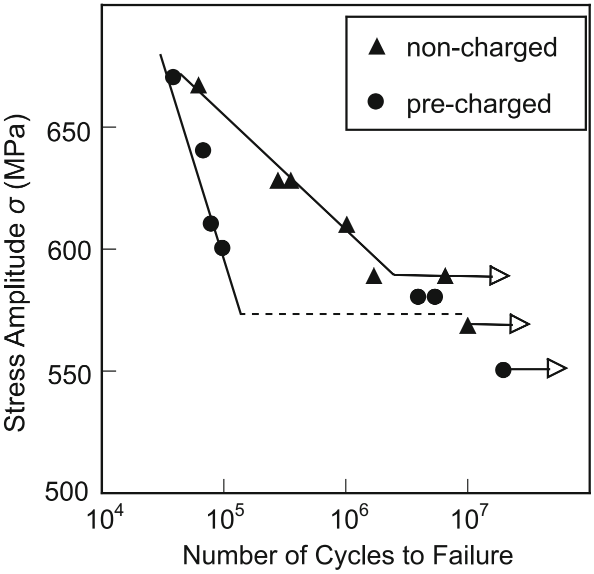

Fig. 6.16 *S*-*N* diagrams at rotational bending fatigue for Si-Cr martensitic steel with and without hydrogen precharging. The arrows indicate no failure (Nagumo et al. [33])

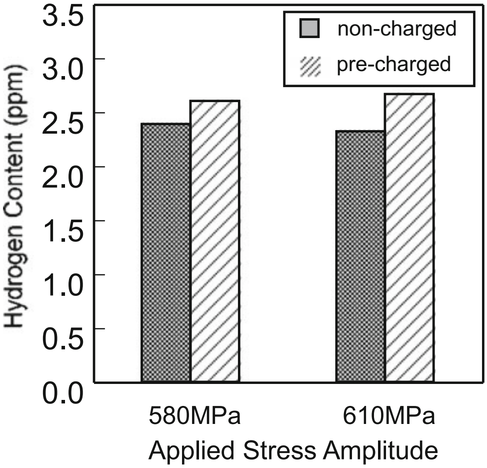

Fig. 6.17 The amounts of tracer-hydrogen in Si-Cr steel specimens fatigue-fractured at two applied stress amplitudes with and without hydrogen precharging. Fatigue cycles applied to the non-charged and pre-charged specimens were respectively 6×10^6 and 5.5×10^6 at the stress amplitude of 580 MPa, and 2×10^5 and 8×10^4 at the stress amplitude of 610 MPa (Nagumo et al. [33])

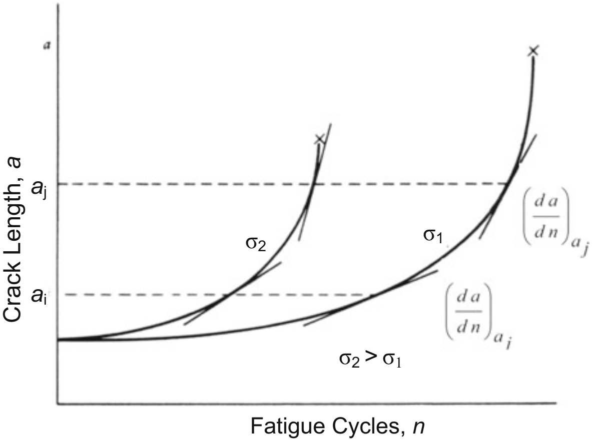

Fig. 6.18 Schematic illustration of applied stress dependence of fatigue crack growth (Hertzberg [30])

(b) Fatigue-crack growth

The growth of a fatigue-crack starting from the surface notch is schematically shown in Fig. 6.18 [30] against fatigue cycles for two applied stresses. The crack growth rate is computed from the observed crack length record. It should be noticed, particularly at the regime of crack growth rates as low as 1×10^{-9} m/cycle, that the computed growth rate does not necessarily mean the actual crack advance at every cycle. Environments often complicate the morphology of the notch root, and the effects of corrosion or oxidation overlap hydrogen embrittlement.

Environmental effects on fatigue crack growth of high strength steels are complicated according to ΔK level and stress ratio. Accelerated fatigue crack growth in hydrogen gas compared to that in air was reported for 2¼ Cr-1Mo steels at two growth rate regimes, *i.e*. at near threshold levels and at higher growth rates typically $>10^{-8}$ m/cycle above a critical $K_{\max}$ value [34]. The hydrogen effect in the latter regime appeared at frequencies below a critical value (*e.g*. 5 Hz at the stress ratio of 0.05) associated with a fracture mode change to predominately intergranular cracking, consistently with general features of hydrogen embrittlement.

On the other hand, at near threshold levels below 10^{-9} m/cycle, the accelerated growth rate in dry hydrogen compared to moist air appeared only at low load ratios [34]. Suresh et al. ascribed the influence of environment on near-threshold fatigue crack growth to the oxide-induced crack closure mechanism. An earlier contact between the facture surfaces during the closure portion raises the closure load and reduces ΔK_{eff} as

$$\Delta K_{eff} = K_{max} - K_{cl}, \tag{6.4}$$

where K_{cl} is the stress intensity to close the crack. Thus reduced ΔK_{eff} decelerates crack growth rates at low load ratios. The deceleration of fatigue-crack growth due to crack closure is prominent when the crack opening is small at low ΔK levels and low stress ratios in corrosive environments. The magnitude of mechanical wedging action is a function of the thickness and location of the debris [35]. Suresh et al. noted that pulsating crack-tip opening displacements were of a size comparable to fracture surface roughness and the thickness of corrosion debris within the crack [34].

The initiation and the early stage growth of fatigue crack, especially in the range of very small ΔK under corrosive environments, have been extensively studied [31, 36]. Fatigue crack growth rates of high strength steels under the same applied stress intensity increased in 3 % NaCl aqueous solution and water compared to those in air. The increase was much higher for short than for long cracks [31]. An expression of short crack effects is to use ΔK_{eff} by adding an effective crack length l_0 to the actual crack length l [36, 37], *i.e.*

$$\Delta K_{eff} = A\,\Delta\sigma\sqrt{\pi\,(l + l_0)}, \tag{6.5}$$

where A is the elastic stress concentration factor and $\Delta\sigma$ is the applied nominal stress range. The magnitude of ΔK_{eff} is larger than the apparent ΔK, and the contribution of l_0 to ΔK_{eff} is significant when l is small. Environmental effects are ascribed to large l_0 in the presence of corrosive environment. However, the physical meaning of l_0 is not definite while an intrinsic defect size such as a microfracture process zone size has been proposed.

The fatigue crack growth rate is often expressed by Paris' law as a function of ΔK,

$$\frac{da}{dN} = A\Delta K^{m}, \tag{6.6}$$

where A and m are constants that vary with material, environment and testing conditions [30]. Fatigue tests in high pressure hydrogen gas of Ni-Cr-Mo

Table 6.1 Fatigue crack growth parameters in Eq. (6.6) for as-quenched and tempered martensitic steels in Ar and hydrogen environments

Steel	Quenched (TS:1344 MPa)			Quenched-Tempered (TS: 1274 MPA		
Atmosphere	Ar	1.1 MPa H_2	4 MPa H_2	Ar	1.1 MPa H_2	4 MPa H_2
m	4.1	6.5	7.1	4.7	12.1	15.6
K_Q (MPa $m^{1/2}$)	59	23	17	72	27	21

Fukuyama et al. [38]. Reprinted with permission from The Society of Materials Science, Japan

martensitic steel subjected to two types of heat-treatment, *i.e.* as quenched and quenched-tempered, showed increased crack growth rates with increasing hydrogen gas pressure at a given ΔK [38]. The growth rate at a given ΔK was much higher for the as-quenched martensite than for the tempered one, but the susceptibility of the growth rate to hydrogen expressed in terms of *m*-value in Paris' law was higher for the tempered martensite than for the as-quenched one as shown in Table 6.1 [38]. The fatigue tests were conducted using DCB specimens at $R = 0.1$ and a sinusoidal frequency of 5 Hz. The as-quenched martensite exhibited significant hydrogen effects at small ΔK near the threshold, while the effects were almost insignificant for tempered martensite at 573 K. The reason is not definite. Closure effects due to oxides or debris are not likely since all the tests were conducted under dry environments. The susceptibility to hydrogen embrittlement in terms of fracture toughness K_Q is included in Table 6.1, and the reductions by hydrogen in terms of the ratio to the fracture toughness in argon gas were of similar levels for the two heat-treatments.

Enhanced crack growth rate by internal hydrogen at near-threshold region was deduced by Esaklul et al. separating from any crack closure effects [39]. The steel was AISI 4340 steel of 1800 MPa in tensile strength, and hydrogen was precharged under a fairly high fugacity by cathodic electrolysis in poisoned 5 % H_2SO_4 at a current density of 20 A/m^2 followed by cadmium plating. Fatigue tests were conducted using CT specimens at $R = 0.1$ and 30 Hz. Plots of log d*a*/d*N* *vs*. nominal ΔK showed enhanced crack growth rates by hydrogen at ΔK above 7 MPa-$m^{1/2}$ or in d*a*/d*N* above 5×10^{-9} m/cycle. However, crack growth rates were almost identical for hydrogen-charged and uncharged specimens in the lower ΔK range. Fractographic features showed oxide buildup, and geometrical asperities for hydrogen-charged specimens and the load *vs*. crack-opening-displacement curves exhibited closure of the crack surface. Then, the nominal ΔK was converted to ΔK_{eff} in Eq. (6.5) using the estimated contact area and contact point on the observed fracture surface. Then, the plots of log d*a*/d*N* against ΔK_{eff} revealed hydrogen-enhanced crack growth rates even in the ΔK_{eff} range below 5 MPa-$m^{1/2}$ or in d*a*/d*N* below 1×10^{-9} m/cycle.

Hydrogen generally promotes the crack initiation and growth in fatigue, but unexpected "decrease", rather than increase, in fatigue crack growth rates was reported for a tension-compression fatigue test of Type 304 and Type 316 L austenitic stainless steels containing more than about 70 wt. ppm hydrogen [40]. The specimens were round bars of 7 mm in diameter, and hydrogen was precharged in a high pressure hydrogen gas at high temperatures. A small hole, 100 μm both in depth and diameter, was drilled on the surface after hydrogen charging as the starter of fatigue crack. Fatigue tests were conducted at 1 Hz and a stress ratio of -1, and the advancing crack length was measured on the surface using a replica method.

On the contrary, a stress-controlled fatigue test using compact tension specimens of Type 304 and Type 316 L containing 70 ppm of hydrogen showed accelerated fatigue crack growth by hydrogen more pronouncedly for Type 304 than for Type 316 L [41]. The tests were conducted at the stress ratio of 0.1 and the frequency of 1, 0.1 and 0.01 Hz. Also, cyclic-pressurization fatigue tests using tubular specimens without a notch in high pressure hydrogen gas showed a decrease in the fatigue life for Type 304 steel [42]. The maximum and the lowest internal hydrogen gas pressures were 88 MPa and 0 MPa, respectively, and the cycle time was 20s per cycle. Type 316 L showed no degradation in this type of tests even for tubular specimens notched on the internal surface. A precipitation-hardened austenitic stainless steel A285 and a low alloy Si-Cr-Mo high strength steel showed a substantial degradation in fatigue life by hydrogen [42]. The characteristics of hydrogen embrittlement of austenitic steels are described in Sect. 8.4.

(c) High cycle fatigue near threshold

Fatigue crack growth behaviors near the threshold stress intensity range are of practical importance for structural components under long-term service. Threshold, below which the crack growth rate becomes diminishingly small, was not found for ultrasonic tension-compression fatigue tests near the ΔK_{th} ranges of mild steel, Type 304 stainless steel and copper in 3.5 % NaCl aqueous solution, but a distinct threshold existed in non-corrosive silicon oil [43]. The fracture mode of samples fatigued in corrosive environment changed from ductile transgranular to intergranular fracture.

Involvement of a very small amount of hydrogen in extremely high cycle fatigue limits was presented by Murakami et al. [44] for a surface-hardened Cr-Mo steel quenched and tempered in a reductive atmosphere (QT) or in a vacuum (VQ). Hydrogen entered into specimens during the fabrication process and the concentrations were 0.7–0.9 and 0.01 mass ppm for QT and VQ, respectively. Fatigue tests were tension-compression at $R = -1$ with cyclic frequency of 20–80 Hz. For extremely high cycle fatigue in the regime of $N > 10^7$, the *S-N* plots showed a substantial scatter but fatigue lives and fatigue limit were lower for QT than VQ. Murakami et al. pointed out the importance of non-metallic inclusions. Crack initiation sites were subsurface non-metallic inclusions located at centers of fish-eye associated with optically dark area (ODA) characterized by rough and irregular surface morphology. The size of ODA in QT was about twice as large as that of non-metallic inclusions and was larger than ODA in VQ. Secondary ion mass spectroscopy detected hydrogen at near non-metallic inclusions in QT but not in VQ. Murakami et al. deduced that hydrogen assists the formation of ODA and determines fatigue lives at low stress levels near the fatigue limit [44]. At an extremely slow crack growth stage of 1×10^{-10} m/cycle, more than thousands of cycles were applied in order that a detectable crack advance took place. Effects of some structural damages might be expected.

6.4 Delayed Fracture

Eventual failure in a long-term use under mild corrosive environments is a crucial problem for the structural components of high strength steels. Periods of service until fracture range to years. For laboratory tests, delayed fracture characteristics are expressed by the applied stress *vs.* time to fracture diagram similar to the *S*-*N* curve for fatigue tests. Accordingly, an alternate terminology for sustained-loading delayed fracture is "static fatigue". Fracture mechanics test under sustained loading is a type of delayed fracture. The threshold stress intensity for the crack initiation K_{TH} described in Sect. 6.2.1 for fracture mechanics tests corresponds to the lower limit of the applied stress below which delayed fracture does not occur, but notches are not requisite to induce delayed fracture. Delayed fracture diagrams vary by testing temperature, environment or hydrogen concentration, and specimen geometry. A long exposure time to fracture in practical services inevitably necessitates some accelerated tests in laboratories. The correspondence between practical and laboratory test results is a matter that needs careful examination.

6.4.1 *Factors Affecting Delayed Fracture*

Early works intended to disclose the role of hydrogen in delayed fracture. Figure 6.19 [45] for AISI 4340 steel of 1600 MPa in tensile strength might be historically the first diagram obtained by laboratory tests under constant-stress tensile loading. The specimens were circumferentially notched bars, and hydrogen was precharged under a fairly high fugacity by cathodic electrolysis in 4 % H_2SO_4 at a current density of 30 A/m^2. Hydrogen was enclosed in specimens by cadmium-electroplating, and the Cd-plated specimens were then baked at 150 °C (=300 °F) to homogenize the distribution of hydrogen. Partial degassing took place during baking, but hydrogen concentrations were not measured. Instead, baking times at 150 °C were used as the parameter of hydrogen concentration. As-received specimens contained about 1.5 mass ppm of hydrogen exceeding electrolytically introduced hydrogen, but the as-received hydrogen was immune to the embrittlement. It suggests that apparent hydrogen concentrations do not always serve as a measure for causing degradation.

Another diagram for the effects of hydrogen concentrations on delayed fracture is the plot of diffusive hydrogen concentrations *vs.* the time to fracture under a given applied stress [46, 47]. For martensitic steels, hydrogen was precharged without [46] or with [47] cadmium plating and most fracture took place within 24 h. Hydrogen concentrations were measured by means of thermal desorption

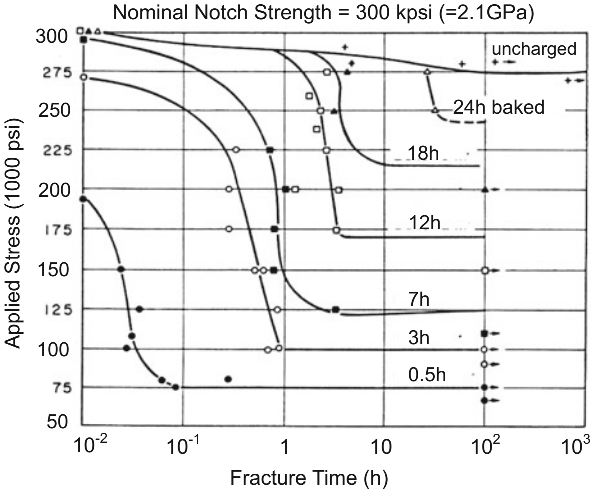

Fig. 6.19 Delayed fracture diagram of AISI 4340 steel. Hydrogen-charged specimens are Cd-plated and baked at 150 °C for various periods (Johnson et al. [45])

analysis, and the amounts hydrogen desorbed below 500 K were employed as the amount of diffusive hydrogen. Delayed fracture is sensitive to specimen geometries. The notch radius on specimens used for Fig. 6.19 was 25 μm, but the notch sharpness affects delayed fracture diagrams [45] in a similar form as the effects of baking times shown in Fig. 6.19. Delayed fracture test methods using specimens without an artificial notch were also presented for the assessment of stress corrosion cracking of prestressing steel bars [48].

The susceptibility to delayed fracture is generally higher for steels of higher strength levels. Figure 6.20 [49] compiles threshold stresses of various commercial steels subjected to delayed fracture tests in water for 100 h. The threshold stress turns to decrease for steels of the tensile strength higher than 1200 MPa, which corresponds to the strength level of high strength fasteners that exhibit delayed fracture in service under atmospheric environments. It is to be noticed that the critical tensile strength above which the threshold stress turns to decrease differs by steel types. Maraging steels have higher resistance than low-alloyed steels, and the mechanism is an important subject for designs of hydrogen-resistant steels. Testing temperature also substantially affects the time to fracture. For sustained tensile-loading delayed fracture tests in water for a martensitic steel of 1510 MPa in tensile strength, elevation of water temperature from 25 °C to 80 °C reduced the time to fracture more than one order of magnitude [49] .

For fracture mechanics tests, the critical stress intensity K_{TH} below which no cracking occurs is affected by stress states operating on the specimen. The stress state in the vicinity of crack-tip changes from plane strain to plane stress as the thickness and/or the yield strength of the specimen decreases. Gerberich and Chen showed that the transition from a plane strain to a plane stress state increases K_{TH} [50], but conceivable mechanisms of the effect of stress states are not simple. Triaxial stress enhances the buildup of local hydrogen concentration, but it also promotes the void nucleation and growth rates as microstructural effects.

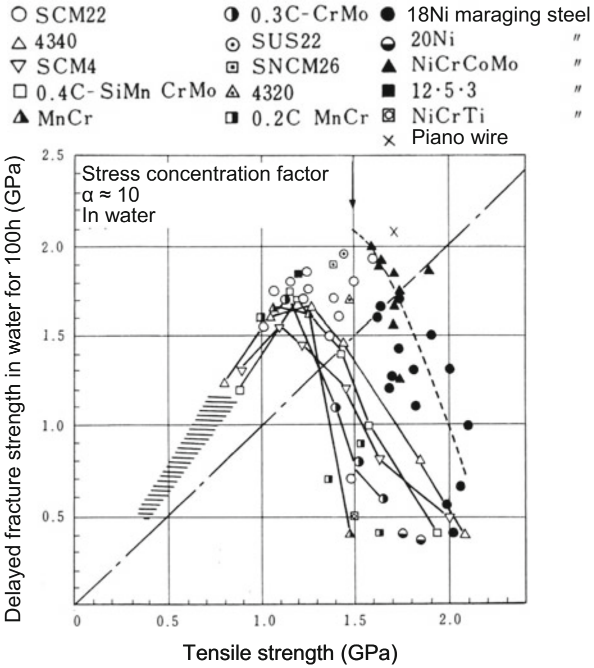

Fig. 6.20 Threshold stresses at 100 h for delayed fracture of various high strength steels in water (Yamamoto et al. [49])

6.4.2 Incubation Period

The initiation of an incipient crack and its growth take place substantially prior to the onset of final fracture at delayed fracture tests. The initiation and discontinuous growth were detected by means of electric resistance techniques [45, 50]. The incubation period before the crack initiation was prolonged by decreasing hydrogen concentration, but it was almost independent of the applied stress for a given hydrogen concentration [51]. The incubation period covers a major part of the time to fracture at high applied stresses. Assuming a diffusion-controlled process in the incubation period, Steigerwald et al. obtained the activation energy of 38 kJ/mol from an Arrhenius relationship for the logarithm of the ratio of the incubation time to the absolute temperature [51]. The value is fairly higher than reported activation energies for hydrogen diffusion in iron and steels and some other controlling processes are not ruled out. A noteworthy result was that the true fracture stress, *i.e.* applied stress divided by the uncracked area determined on the fracture surface, was constant over a wide range of applied stress and of hydrogen concentration. It suggests that the fracture stress in the central portion of specimens is irrelevant to hydrogen concentrations. If the true fracture stress represented the critical degradation of the material during the delayed fracture test, the observation might suggest that hydrogen functions in some kinetics during the incubation period rather than at the final fracture stage before reacing a critical state.

Events that happen in the incubation period of delayed fracture tests were detected by means of acoustic emission (AE) technique for high strength steels of

1300 MPa in tensile strength [52]. The delayed fracture tests were conducted using V-notched specimens subjected to a constant load cantilever bending in 0.1 N HCl solution. Acoustic emissions were observed in the incubation period prior to the onset of the crack initiation that was detected by a concurrently conducted electric resistance measurement. The number of AE signals increased with time and their wave forms in the incubation period and the crack growth stage are compared in Fig. 6.21 [52]. The wave form in the incubation period was packet-like similar to that emitted associated with plastic deformation, while that in the crack growth stage was irregular with higher amplitudes.

Interactions of hydrogen with strain-induced lattice defects are possible functions of hydrogen in the incubation period. Mechanistic behaviors in delayed fracture tests are essentially the same as stress relaxation and creep that involve plastic deformation as described in Sect. 5.3. Hydrogen enhanced stress relaxation shown in Fig. 5.5 for a 0.37%C-0.6%Si-1.0%Mo-0.5%Cr-0.54 V martensitic steel indicates that the precipitation of fine VC reduces both the stress relaxation rate and its enhancement by hydrogen. Delayed fracture test results of the same steel are shown in Fig. 6.22 [53]. Two tempering temperatures of 550 °C and 650 °C were

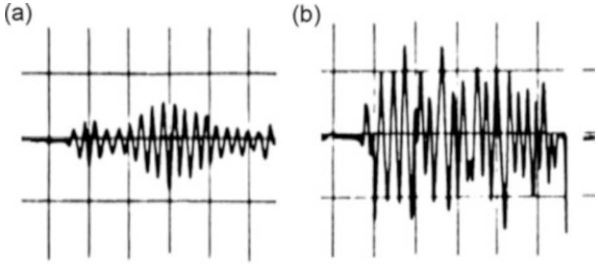

Fig. 6.21 Wave forms of acoustic emission generated during delayed fracture tests of high strength martensitic steel. (**a**) Incubation time, (**b**) During crack extension (Nagumo [52])

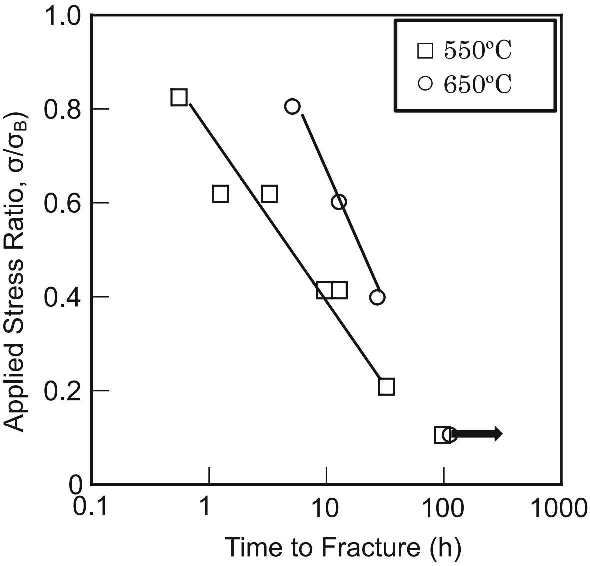

Fig. 6.22 Delayed fracture diagrams for medium carbon Mo-V martensitic steels tempered at 550 °C and 650 °C. The arrow indicates unfailed specimens (Nagumo et al. [53])

employed to give the same tensile strength of 1470 MPa for both with and without VC precipitation. Sustained loading tests were conducted at room temperature using flat specimens hydrogen-precharged under a mild hydrogen fugacity by cathodic electrolysis in a 3 % NaCl + 3gl^{-1} NH_4SCN solution at a current density of 5 A/m^2. Precipitation of fine VC brought about a substantial improvement of the time to fracture. The correspondence between the stress relaxation rates and hydrogen effects implies involvements of plasticity and associated hydrogen effects in delayed fracture.

A further issue is microstructural alterations associated with plastic deformation in the incubation period. A common notion so far assumed for the origin of delayed fracture is buildup of hydrogen concentration to some critical values, and it has been widely adopted as the mechanism of delayed fracture. However, reported data of hydrogen concentration in structural components exposed to environments for long terms are few. Figure 6.23 [54] shows hydrogen contents in high strength steel specimens exposed to atmospheric environments at various sites in Japan for four years. The specimens were 1500 MPa in tensile strength and flat plates of 3 mm in thickness were U-shape bent. Hydrogen contents were measured by means of TDA as the amounts of hydrogen desorbed below 200 °C at which the desorption almost ceased. Hydrogen contents increased with time, as expected, in initial six months, but tended to decrease to a constant level on further exposure. Data showed a substantial scatter, but systematic effects of local climates were not discernible. The facts are against the common notion and imply that hydrogen contents are not always the decisive factor to cause delayed fracture.

The enhanced creation of strain-induced vacancies by hydrogen is described in Sect. 3.2.3(b). Changes of hydrogen contents during immersion in 20 % NH_4SCN

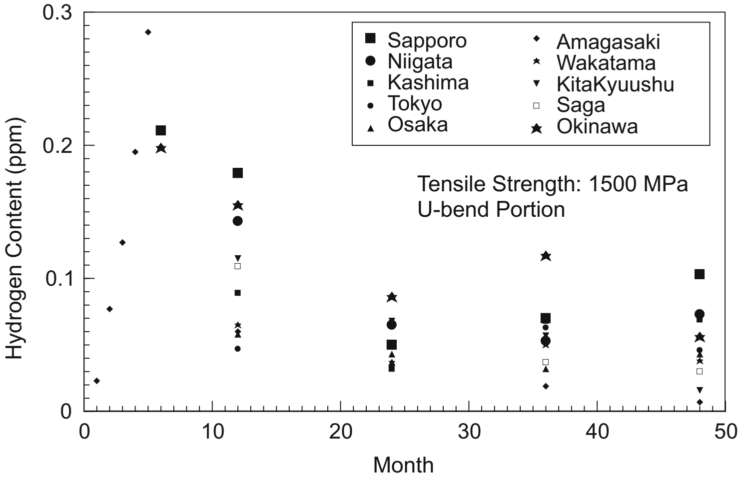

Fig. 6.23 Hydrogen contents in U-bend loaded high strength steel sheets of 1500 MPa in tensile strength after exposure at various sites in Japan (Kushida [54], Reprinted with permission from The Iron & Steel Inst. Japan)

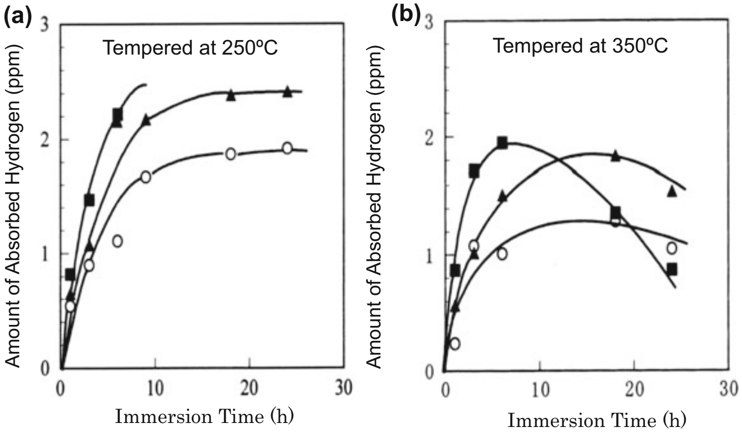

Fig. 6.24 Amounts of absorbed hydrogen in medium carbon tempered martensitic steels during immersion in 20 % NH_4SCN aqueous solution at 50 °C. ○, unloaded; ▲, prestressed to 80 % of the tensile strength; ■, concurrently loaded to 80 % of the tensile strength. (**a**) tempered at 250 °C, (**b**) tempered at 350 °C (Nagumo et al. [55])

aqueous solution at 50 °C are shown in Fig. 6.24(a) [55] for 0.33 % C martensitic steel bars of 5 mm in diameter. The order of the increase in hydrogen content among three conditions, *i.e.* (○) unstressed, (▲) prestressed at 80 % of the tensile strength and (■) under sustained-loading at 80 % of the tensile strength, corresponds to the order of strain-induced creation of lattice defects and its enhancement by hydrogen. However, unexpectedly, the increase in the hydrogen content was not monotonic in the steel tempered at 350 °C as shown in Fig. 6.24(b). The hydrogen content turned to decrease with the increasing loading time. The TDA profile of absorbed hydrogen for each condition showed a single broad peak between 50 °C and 200 °C. Comparisons of TDA profiles for the three conditions revealed that the higher temperature side of the TDA peak was associated with the increase in hydrogen contents. It implies, as described in Sect. 2.1.2, that traps with high binding energies with hydrogen are formed during the immersion. Alterations of strain-induced defects during delayed fracture tests have been discussed with respect clustering of vacancies [55].

The initial increase and subsequent decrease in hydrogen contents during sustained-loading delayed fracture tests were reproduced for another martensitic steel in a separate study [56]. Hydrogen contents represent densities of lattice defects that trap hydrogen, but hydrogen contents in Fig. 6.24 are the amount of hydrogen that entered into specimen through electrochemical reactions on the metal surface during the tets. Then, alteration in lattice defects during delayed fracture tests was separately evaluated in terms of tracer-hydrogen which was re-introduced into specimens after testing. Tracer-hydrogen was introduced into specimens interrupting loading and degassing at 30 °C for 168 h at the unloaded state. Figure 6.25 [56] shows the amounts of tracer-hydrogen introduced to fine-grained 0.32 % C martensitic steel specimens subjected to sustained-loading in 20 %

Fig. 6.25 Amounts of tracer-hydrogen introduced to martensitic steel bar specimens subjected to sustained-loading at 0.6 or 0.8 of the tensile strength in 20 % NH_4SCN aqueous solution at 50 °C. Δ and ▲ denote fractured specimens (Doshida et al. [56]. Reprinted with permission from The Iron & Steel Inst. Japan)

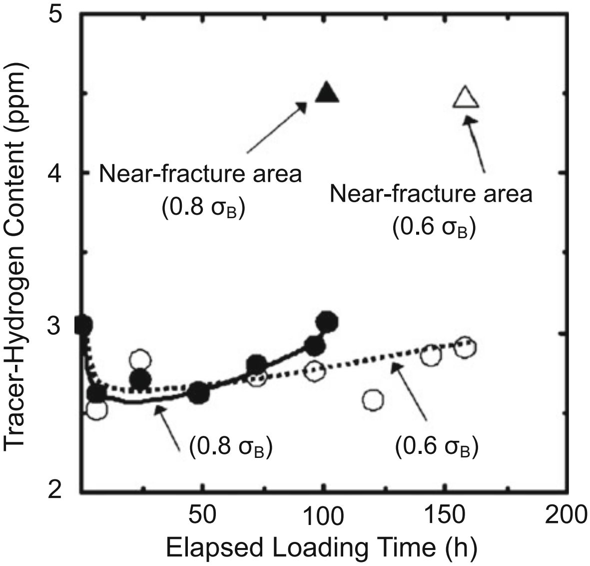

NH_4SCN aqueous solution at 50 °C. The applied stress was 60 % or 80 % of the tensile strength and both levels were apparently within the elastic range.

The amount of tracer-hydrogen, *i.e.* hydrogen absorption capacity, initially decreased but then gradually increased with increasing loading time. In fractured specimens, the portions near the fracture surface showed substantially high tracer-hydrogen contents as indicated by Δ and ▲ marks. The high values are due to concentrated strain near the fracture surface, and the findings are consistent with the strain-induced creation of vacancies and its concern with fracture. The initial decrease may be due to reconfigurations of dislocations associated with hydrogen-entry and loading. A similar initial decrease followed by a gradual increase in tracer-hydrogen content was also observed for a rotational bending fatigue test of high strength steel [33]. Alterations of TDA profiles with increasing sustained-loading time [55] are consistent with the formation of vacancy clusters as described in Sects. 2.1.2 and 3.2. Positron annihilation spectroscopy is a more direct method to identify vacancies. Concurrently conducted positron probe microanalysis (PPMA) revealed the formation of a high density of vacancy clusters near the fracture surface corresponding to TDA results [56].

6.4.3 Effects of Environmental Variations

Structural components tolerate more or less variations of applied stress and environmental condition even in apparently stationary usages. Alternating hydrogen entry due to daily changes of humidity in ambient atmosphere is demonstrated in

Fig. 2.3 in Sect. 2.1.1. Delayed fracture is normally assigned as the fracture under static loading, but the effects of mechanical and electrochemical variations must be considered.

(a) Stress variations

Superposition of small amplitude stress oscillation on sustained-loading promotes the macroscopic crack initiation and decreases the lower limit stress in delayed fracture tests [57]. The used material was Ni-Cr-Mo steel of 1800 MPa in tensile strength and sinusoidal oscillation of 15 or 400 cpm was superposed on U-notched static bending at various constant stresses. The promotion of the crack initiation by the superposed oscillating stress was prominent when water was dropped at the U-notch. The degradation appeared for stress amplitude as low as 50 MPa at the constant stress of 1260 MPa, and the degradation was more prominent with higher stress amplitudes and oscillating frequencies. Results for various steels are shown in Fig. 6.26 [58] at the oscillating frequency of 15 cpm and the stress amplitude of 50 MPa. Superposition of oscillating stress on sustained-loading delayed fracture tests may induce interactive functions of hydrogen operating alternately in delayed fracture and fatigue.

For experiments shown in Fig. 6.26, the maximum applied stress was raised by the superposition of the oscillatory stress. In order to separate effects of the cyclic variation and the level of the applied stress, another method to keep the maximum stress constant during the test was used. For sustained–loading delayed fracture tests of martensitic steel, the load was cyclically reduced by up to 10 % at a frequency of 5 or 10 cpm [59]. The steel was 1300 MPa in tensile strength and specimens of 5 or 7 mm in diameter were immersed in 20 % NH_4SCN aqueous

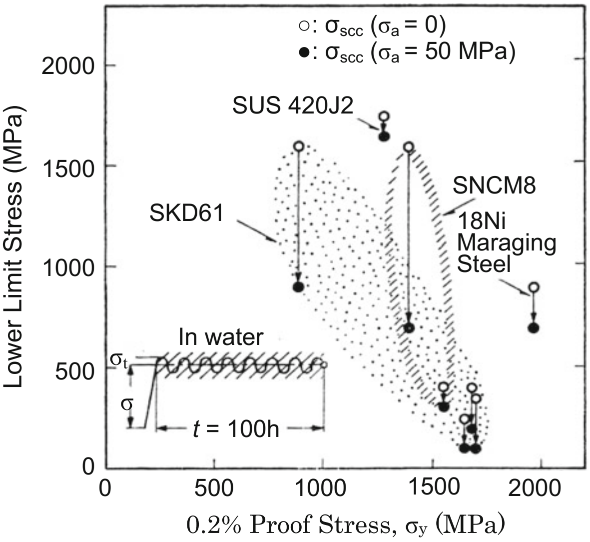

Fig. 6.26 Decrease in the lower limit stress by superposing cyclic variations of applied stress at sustained loading delayed fracture tests for various high strength steels (Kido et al. [58]. Reprinted with permission from The Iron & Steel Inst. Japan)

Fig. 6.27 Accelerated fracture by superposing cyclic stress variations at delayed fracture test of high strength steel. The maximum stress is constant (Izutsu et al. [59])

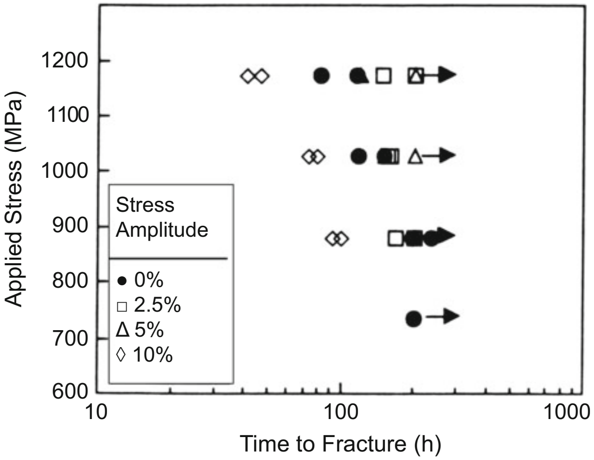

solution at 50 °C. Figure 6.27 [59] shows delayed fracture diagrams for various stress amplitudes. Promotion of fracture was evident at the stress amplitude of 10 % while the mean stress was lower than the constant stress level. A noteworthy finding was that hydrogen concentrations in tested specimens were uniquely determined by the immersion time in the solution irrespective of constant or cyclic stressing [59]. It implies that total hydrogen content is not the controlling factor for promoting fracture. The amount of lattice defects measured in terms of the amount of tracer-hydrogen introduced after the tests decreased when tested specimens were annealed at 200 °C. The decrease was larger for cyclic-stressed specimens than for sustained-loaded specimens. It indicates that cyclic stressing enhances creations of vacancies during the tests. Further studies on the effects of cyclic prestressing on tensile test and on interactions of fatigue and delayed fracture are presented in Sect. 7.3.2 concerning accumulation of damage.

(b) Environmental variations

Another factor to be examined for delayed fracture of structural components in service is variations of hydrogen fugacity associated with changes of weather. A laboratory method to examine effects of environmental variations on delayed fracture was to cyclically vary the hydrogen-charging current density [60]. Experiments were conducted for high strength martensitic steel of 1390 MPa in tensile strength in sustained-loading tests under concurrent hydrogen-charging. The specimens were round bars of 5 mm in diameter and hydrogen charging was conducted by a fairly mild cathodic electrolysis in a 3 % NaCl + 3 g/l NH_4SCN aqueous solution. The applied tensile stress was 70 % of the tensile strength, and the current density was cyclically varied from 0.1 to 100 cpm in a rectangular form keeping the maximum current density constant.

The time to fracture as a function of the frequency of cyclic currents is shown in Fig. 6.28 [60], where the maximum current density was 7.5 A/m^2 and the relative amplitude of the current variations was 10 %. Promoted failure by higher

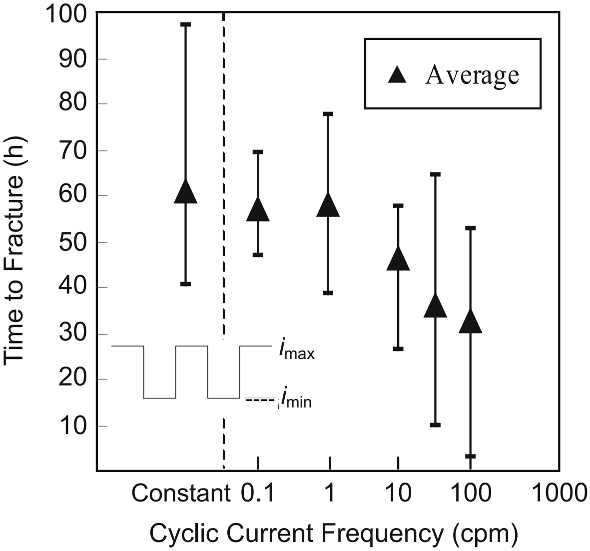

Fig. 6.28 Effects of cyclic variation of hydrogen-charging current density on the time to fracture at delayed fracture tests of high strength steel. The maximum current density is not varied (Nagumo et al. [60])

frequencies is evident. Hydrogen contents in unstressed specimens were uniquely determined by the total supplied electric charge irrespective of cyclic variations of the current density [60]. Subsequent analyses of trapped states of hydrogen by means of TDA revealed that TDA profiles changed with elapsed time of the test. The TDA profile showed a single broad peak centered at around 80 °C, but the higher temperature side of the peak showed a more pronounced increase with time. Similarly to the case of cyclic stress variation [59], alteration of TDA profiles with time appeared earlier for the cyclic current conditions than for the constant current test. The TDA results indicate the creation of trap sites of high binding energies. The low temperature thermal desorption spectroscopy (LTDS) shown in Figs. 3.9 and 3.10 ascribed the origin of such TDA profiles to vacancy clustering. The effects of environmental variations are consistently understood from the viewpoints of promoted vacancy clustering.

References

1. K. Takai, R. Watanuki, ISIJ Int. **43**, 520–526 (2003)
2. M. Hatano, M. Fujinami, K. Arai, H. Fujii, M. Nagumo, Acta Mater. **67**, 342–353 (2014)
3. I.M. Bernstein, in *Hydrogen Effects in Materials*, ed. by A.W. Thompson, N.R. Moody (TMS, Warrendale, 1996), pp. 3–11
4. T. Doshida, K. Takai, Acta Mater. **79**, 93–107 (2014)
5. K. Takai, H. Suzuki, M. Fujinami, *Reports on Construction of Fundamentals of Hydrogen Embrittlement* (Iron and Steel Inst., Japan, 2013), pp. 129–134
6. T. Nakamoto, T. Doshida, K. Takai, Y. Kubo, M. Fujinami, CAMP ISIJ **25**, 1210 (2012)
7. K. Takai, H. Shoda, H. Suzuki, M. Nagumo, Acta Mater. **56**, 5158–5167 (2008)

8. J.F. Knott, *Fundamentals of Fracture Mechanics* (Butterworth, London, 1973)
9. T.L. Anderson, *Fracture Mechanics*, 3rd edn. (Taylor & Francis, Boca Raton, 2005)
10. W.G. Clark Jr., J. Mater. Energy Syst **1**, 34–40 (1979)
11. R.A. Oriani, P.H. Josephic, Acta Metall. **22**, 1065–1074 (1974)
12. G.W. Simmons, P.S. Pao, R.P. Wei, Metall. Trans. A **9A**, 1147–1158 (1978)
13. W.W. Gerberich, Y.T. Chen, C. St John, Metall. Trans. A **6A**, 1485–1498 (1975)
14. J.F. Lessar, W.W. Gerberich, Metall. Trans. A **7A**, 953–960 (1976)
15. N.R. Moody, S.L. Robinson, W.M. Garrison, Res Mechanica **30**, 143–206 (1990)
16. Y. Takeda, C.J. McMahon Jr., Metall. Trans. A **12A**, 1255–1266 (1981)
17. J.A. Gordon, J.P. Hirth, A.M. Kumar, N.E. Moody Jr., Metall. Trans. A **23A**, 1013–1020 (1992)
18. S.V. Kamat, J.P. Hirth, Scr. Metal. Mater. **30**, 145–148 (1994)
19. Y. Fujii, A. Kikuchi, M. Nagumo, Metall. Mater. Trans. A **27A**, 469–471 (1996)
20. A. Needleman, W. Tvergaard, J. Mech. Phys. Solds **35**, 151–183 (1987)
21. Y. Shimomura, M. Nagumo, in *Environment-Induced Cracking of Materials: Chemistry, Mechanics and Mechanisms*, ed. by S.A. Shipilov, R.H. Jones, J.M. Olive, R.B. Rebak (Elsevier, Oxford, 2007), pp. 285–294
22. D.P. Williams, H.G. Nelson, Metall. Trans. **1**, 63–68 (1970)
23. R.P. Gangloff, R.P. Wei, Metall. Trans. A **8A**, 1043–1053 (1977)
24. H. Vehoff, W. Rothe, Acta Metall. **31**, 1781–1793 (1983)
25. H. Vehoff, H.-K. Llameth, Acta Metall. **33**, 955–962 (1985)
26. W.W. Gerberich, T. Livne, X.-F. Chen, M. Kaczorowski, Metall. Trans. A **19A**, 1319–1334 (1988)
27. M. Nagumo, H. Yoshida, Y. Shimomura, T. Kadokura, Mater. Trans. **42**, 132–137 (2001)
28. K.A. Nibur, B.P. Somerday, D.K. Balch, C. San Marchi, Acta Mater. **57**, 3795–3809 (2009)
29. M. Nagumo, T. Yagi, H. Saitoh, Acta Mater. **48**, 943–951 (2000)
30. R.W. Hertzberg, *Deformation and Fracture Mechanics of Engineering Materials*, 3rd edn. (Wiley, New York, 1989), Chapters 12, 13
31. W.W. Gerberich, in *Hydrogen Degradation of Ferrous Alloys*, ed. by R.A. Oriani, J.P. Hirth, M. Smialowski (Noyes Pub, Park Ridge, 1985), pp. 366–413
32. Y. Murakami, H. Matsunaga, Int. J. Fatigue **28**, 1509–1520 (2006)
33. M. Nagumo, H. Shimura, T. Chaya, H. Hayashi, I. Ochiai, Mater. Sci. Eng. **A348**, 192–200 (2003)
34. S. Suresh, G.F. Zamiski, R.O. Ritchie, Metall. Trans. A **12A**, 1435–1443 (1981)
35. S. Suresh, R.O. Ritchie, Scr. Metall. **17**, 575–580 (1983)
36. S.J. Hudak Jr., Trans. ASME J. Eng. Mater. Tech. **103**, 26–35 (1981)
37. M.H. Haddad, N.E. Dowling, T.H. Topper, K.N. Smith, Int. J. Fracture. **16**, 15–30 (1980)
38. S. Fukuyama, K. Yokogawa, M. Araki, J. Soc. Mater. Sci. Jpn. **34**, 709–714 (1985)
39. K.A. Esaklul, A.G. Wright, W.W. Gerberich, Scr. Metall. **17**, 1073–1078 (1983)
40. Y. Murakami, T. Kanezaki, Y. Mine, Metall. Mater. Trans. A **41A**, 2548–2562 (2010)
41. S. Ohmiya, H. Fujii, M. Nagumo, CAMP Iron Steel Inst. Jpn **25**, 1207 (2012)
42. J. Nakamura, M. Miyahara, T. Omura, H. Semba, M. Wakita, J. Soc. Mater. Sci. **60**, 1123–1129 (2011)
43. S. Stanzl, E. Tschegg, Acta Metall. **29**, 21–32 (1981)
44. Y. Murakami, H. Konishi, K. Takai, Y. Murakami, Tetsu-to-Hagané **86**, 777–783 (2000)
45. H.H. Johnson, J.G. Morlet, A.R. Troiano, Trans. Metall. Soc. AIME **212**, 528–536 (1958)
46. N. Suzuki, N. Ishii, T. Miyagawa, H. Harada, Tetsu-to-Hagané **79**, 227–232 (1993)
47. S. Yamazaki, T. Takahashi, Tetsu-to-Hagané **83**, 454–459 (1997)
48. Technical Report on Prestressing Steel 5: Fédération Int. Précontrainte (1980)
49. S. Yamamoto, T. Fujita, Kobe Steel Tech. Rep. **18**, 93–108 (1968)
50. W.W. Gerberich, Y.T. Chen, Metall. Trans. A **6A**, 271–278 (1975)
51. E.A. Steigerwald, F.W. Schaller, A.R. Troiano, Trans. Metall. Soc. AIME **215**, 1048–1052 (1959)

52. M. Nagumo, in *Fracture 1977, Proceedings of the 4th International Conference Fracture*, ed. by D.M.R. Taplin, vol. 3 (Univ. Waterloo Press, Waterloo, 1977), pp. 757–764
53. M. Nagumo, T. Tamaoki, T. Sugawara, in *Hydrogen Effects on Materials Behavior and Corrosion Deformation Interactions*, ed. by N.R. Moody, A.W. Thompson, R.E. Ricker, C.W. Was, K.H. Jones (TMS, Warrendale, 2003), pp. 999–1008
54. T. Kushida, ISIJ Int. **43**, 470–474 (2003)
55. M. Nagumo, M. Nakamura, K. Takai, Metall. Mater. Trans. A **32A**, 339–346 (2001)
56. T. Doshida, H. Suzuki, K. Takai, N. Oshima, T. Hirade, ISIJ Int. **52**, 198–207 (2012)
57. K. Nakasa, M. Kido, H. Takei, J. Jpn. Inst. Metals **40**, 744–751 (1976)
58. M. Kido, K. Nakasa, H. Takei, Tetsu-to-Hagané **65**, 535–541 (1979)
59. K. Izutsu, K. Takai, M. Nagumo, Tetsu-to-Hagané **83**, 371–376 (1997)
60. M. Nagumo, H. Uyama, M. Yoshizawa, Scr. Mater. **44**, 947–952 (2001)

Chapter 7
Characteristic Features of Deformation and Fracture in Hydrogen Embrittlement

In Chap. 6, the degradation of mechanical properties that appear at various testing methods in the presence of hydrogen is described. An issue to be followed is features that characterize deformation and fracture behaviors common to various testing methods originating in functions of hydrogen. Fracture of materials proceeds macroscopically starting from the nucleation and growth of crack, and each stage exhibits features varying by materials and situations such as stress states and environments. The features are diverse but are closely related to underlying mechanisms of deformation and fracture. The comprehensive understanding of commonness in hydrogen effects is useful for revealing intrinsic mechanism and also to judge the origins of service failure.

7.1 Fractographic Features

Fracture surface exhibits the crack propagation path. Since plastic deformation dissipates the major part of the energy needed for crack propagation, the concern of plasticity is an important aspect in examining fracture surfaces. Fracture surfaces of metallic materials are diverse depending on situations but are classified into a few basic modes: cleavage, interface separation and microvoid coalescence. Fracture surfaces of hydrogen-degraded steels exhibit some characteristic features depending on microstructures, hydrogen concentration or fugacity, and stress states. However, the basic classification of fracture modes is not exceptional for hydrogen embrittlement, and characteristic features due to hydrogen are to be examined in the framework of the basic modes of fracture und their underlying mechanisms.

(a) Cleavage

Cleavage fracture is typical for brittle fracture of body-centered-cubic steels and is characterized by the transgranular crack propagation along {100} planes

M. Nagumo, *Fundamentals of Hydrogen Embrittlement*,
DOI 10.1007/978-981-10-0161-1_7

associated with river markings. For hydrogen embrittlement of steels, cleavage fracture is exceptional and appears when an incipient crack is formed by the precipitation of molecular hydrogen of a high fugacity that satisfies the Griffith condition for unstable crack extension. Cleavage fracture was observed for Fe-3% Si single crystals which were severely hydrogen-charged either by cathodic electrolysis in a 4 vol.% $H_2SO_4 + CS_2 + As_2O_3$ solution at a current density of 160 A/m^2 or by quenching from a hydrogen atmosphere of 0.125 MPa at 700 ~ 1200 °C [1]. While the specimens were not externally loaded, the arrays of decorated dislocations in the vicinity of cracks indicated plastic deformation associated with discontinuous growth of cracks. On the other hand, under combined static loading and hydrogen charging, *i.e.* in sustained-loading delayed fracture tests, fracture surfaces exhibited a large number of curved steps different from cleavage steps [2].

Cleavage fracture in hydrogen embrittlement was also observed on the tensile test of 0.014%C iron single crystal at room temperature under simultaneous hydrogen charging [3]. The tensile axis was along [001] axis, and hydrogen was charged by cathodic electrolysis in poisoned 0.05 N H_2SO_4 at a current density of over 30 A/m^2. In that case, cleavage fracture with river markings took place after the crack advance with striation-like appearance. Details of striation-like appearance are described in Sect. 7.1(c).

(b) Dimple patterns

Dimple patterns typically characterize ductile fracture that proceeds with the so-called microvoid coalescence (MVC). The size and shape of dimples are not uniform and are roughly classified into relatively large primary dimples and fine secondary ones. Second phase particles are often observed accompanying primary dimples, but fine secondary dimples without any particles are commonly observed.

Dimple patterns appear on hydrogen-assisted fracture surfaces of steels in cases where a substantial ductility still remains in degradation. An increase in dimple size by hydrogen precharging was reported for tensile fracture of spheroidized near-eutectoid steels [4]. In that case, diameters and spacing of carbides were less than or comparable to dimple size. Hydrogen precharging was conducted under a fairly high fugacity using cathodic electrolysis in 1 N H_2SO_4 poisoned by arsenic at a current density as large as 300 A/m^2. High hydrogen fugacity of precipitated hydrogen should have promoted void formation by causing separation of the interface between carbides and surrounding matrix. On the other hand, hydrogen generally reduces the size of secondary dimples. On a mixed mode I/III loading fracture toughness test of a high purity Ni-Cr-Mo-V steel of lower bainitic structure of 855 MPa in tensile strength, hydrogen precharging at an equivalent hydrogen fugacity of 1.26 MPa at room temperature degraded the fracture toughness associated with reduced dimple sizes compared with those of uncharged specimens [5].

The fracture surface at a three-point bending test of a mildly hydrogen-precharged low-carbon medium strength steel exhibited patterns consisting of mostly primary and secondary dimples [6]. Hydrogen precharging caused rather enlargement of primary dimples while secondary dimples were refined. The area fractions of dimples with different depth (h)/width (w) ratio are shown

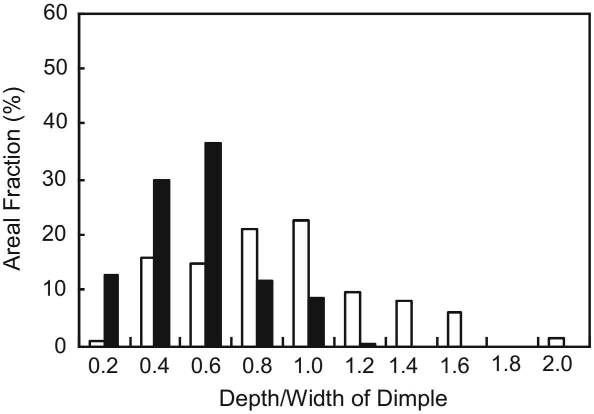

Fig. 7.1 Area fractions of dimples with different depth/width ratio on fracture surfaces of a low-carbon medium strength steel subjected to a three-point bending test with/without hydrogen precharging. The open and filled bars indicate non-charged and hydrogen-charged specimens, respectively (Nagumo et al. [6])

in Fig. 7.1 [6] for hydrogen precharged and uncharged specimens. The area fraction of shallow dimples ($h/w < 0.5$) increased by hydrogen precharging. It implies that hydrogen reduces the extent of plastic deformation on dimple formation and thus the energy dissipated during ductile crack propagation.

Shallow dimples are generally observed in cases of moderate degradation as a characteristic feature of hydrogen embrittlement. Examples are found for low alloy steel in three-point bending test [7] and Type 304 austenitic stainless steel in tensile test [8]. For as-quenched low carbon martensitic steel subjected to tensile tests, an orientation relationship of the fracture surface that exhibited dimple patterns was parallel to $\{011\}_M$ planes which are also parallel to block and lath boundaries of martensite [9]. In that case, microcracks along prior austenite grain boundaries were observed in areas far from the fracture surface. Hydrogen precharging was conducted by cathodic electrolysis in 1 N H_2SO_4 with As_2O_3 at a current density of 100 A/m^2.

(c) Striations

Striations have been observed mostly for single crystal and coarse-grain specimens. Striations on the tensile fracture surface are shown in Fig. 7.2 [3] for hydrogenated 0.001 % C iron single crystal. The crack growth as a whole was in the [010] direction macroscopically on the (001) plane, but the actual growth of the crack front was in <110> directions. Striations parallel to the crack front were coincident with traces of {112} slip planes. Examinations of fine details by means of scanning tunneling microscopy (STM) and mating of opposite fracture surfaces revealed the formation of fine voids at intersections of striations as shown schematically in the lower part of Fig. 7.2. Crystallographic relations are consistent with the void formation originating in interactions of dislocations that move on intersecting slip planes.

Fine striations of about 1 μm spacing along {112} slip planes were reported formerly associated with the slow crack growth macroscopically on {001} and in <110> directions for Fe-3%Si single crystal specimens [10]. Fatigue-prenotched

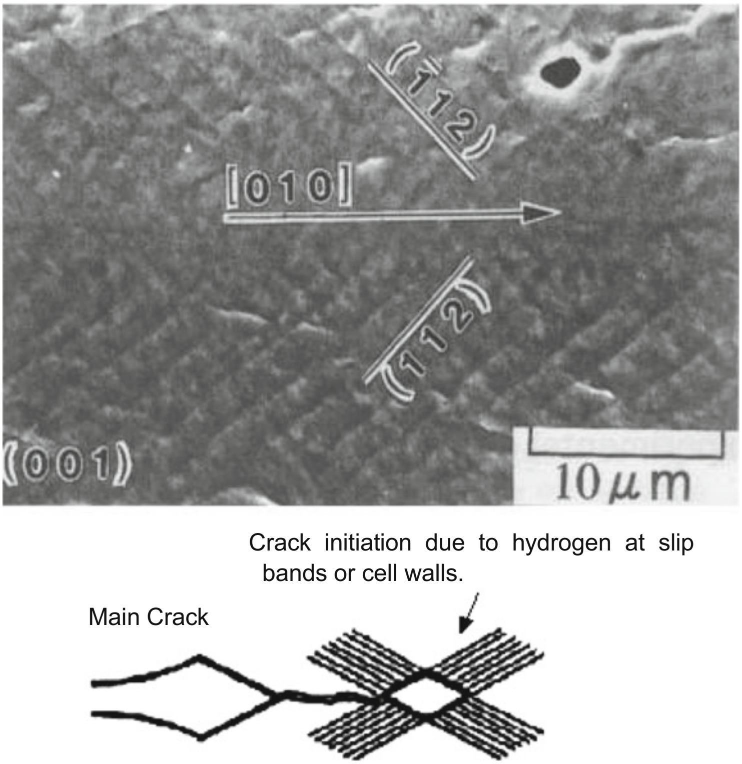

Fig. 7.2 Striations on the tensile-fracture surface of a hydrogen-charged iron single crystal specimen. The lower illustration is a schematic STM view showing a microcrack formed at the intersection of striations (Terasaki et al. [3])

disc-shaped miniature compact tension specimens were gaseous hydrogen charged and subjected to sustained-loading tests with the loading axis parallel to <110>. Simultaneously conducted acoustic emission (AE) measurements detected discontinuous crack growth. The discontinuous steps were ascribed to intermittent cleavage fracture, but direct evidences for cleavage were not presented from crystallographic measurements.

Fine structures of striations and associated plasticity were examined for the internal surface of hydrogen-induced cracks formed within coarse-grain polycrystalline Fe-3%Si specimens [11]. Internal cracks initiated at non-metallic inclusions and propagated macroscopically on {100} cleavage planes associated with striations of an average spacing of 300 nm. Finer striations with a spacing of around 30 nm and a height of 15 nm were also observed. Transmission electron microscopy (TEM) revealed planar slip with interplanar spacing of 15–30 nm that corresponded to the separation of fine striations. Electron backscatter diffraction (EBSD) patterns from regions within internal cracks were diffuse and indicated a substantial crystalline distortion.

Essentially the same and a more pronounced involvement of plasticity in hydrogen-induced crack growth was observed for pure iron [12]. Hydrogen-induced cracks in a bicrystalline pure iron specimen were formed under a high hydrogen fugacity without applying external stress. The cracks were parallel to variants of mostly {110} and partially to {112}, instead of {001} in the case of Fe-3%Si specimens. Fracture surfaces showing striations with planar segments and markings perpendicular to the advancing crack front were common to Fe-3%Si specimens. Planar segments perpendicular to primary striations were also parallel to variants of slip planes.

Above findings indicate that the growth of internal cracks induced by hydrogen is associated with a substantial plasticity even though the appearance is macroscopically brittle-like. A crucial problem is the role of striations in degradation. The effects of hydrogen will distinctly appear in cases where a substantial plastic deformation is present prior to the final stage of fracture. Figure 7.3 [13] shows a cross-section of a commercial pure iron specimen tensile fractured at room temperature under hydrogen charging by cathodic electrolysis in 3 % NaCl aqueous solution at a current density of 100 A/m^2. The specimens of 5 mm in diameter had a

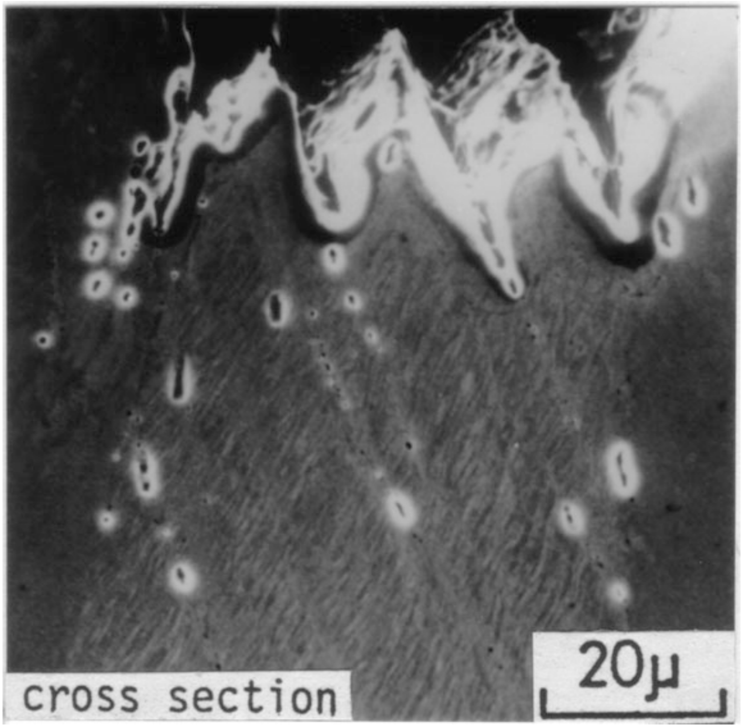

Fig. 7.3 Cross-sectional view of the area beneath the fracture surface of a coarse-grain iron specimen tensile-fractured under hydrogen charging. The surface striations correspond to internal slip bands and etch pits are formed along slip bands (Nagumo et al. [13])

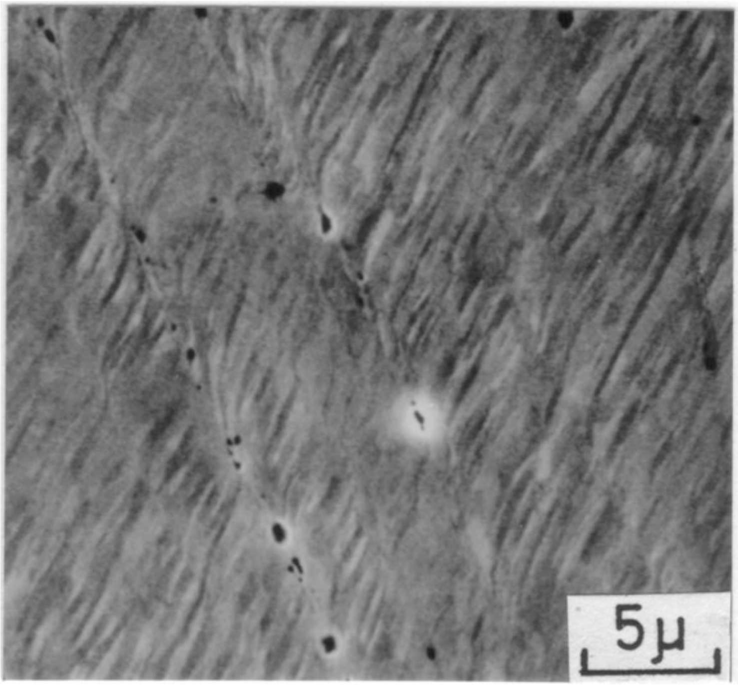

Fig. 7.4 Etch pits and microvoids formed in deformation bands in a coarse-grain iron specimen tensile-fractured under hydrogen charging (Nagumo et al. [13])

bamboo structure and fracture took place after the onset of necking. Striations on the fracture surface were coarse and corresponded to internal deformation structures. Striations were on the extension of deformation bands in which etch-pits and microvoids were formed as shown in Fig. 7.4 [13].

Trace analyses showed that lamellae in Fig. 7.4 are coincident with {110} and {112} slip planes. Deformation bands are regions where slip on the primary slip planes is hindered by the activation of secondary slip, thus causing there a high dislocation density resulting in mutual interactions of dislocations. TEM observations near the fracture surface revealed the formation of dislocation cell structures with cell walls coincident with {112} traces [13]. The formation of etch-pits implies deterioration of crystallinity at the sites. It is a natural consequence that the sites of intense strain localization act as void nucleation sites and that the voids link along deformation bands in the MVC process. The continuity of steps on the fracture surface to internal slip bands and the crack formation along active slip bands were also reported with hydrogen-charged austenitic stainless steels subjected to tensile fracture [14]. Hydrogen diffusivity in austenite is very low and the void formation is hardly ascribed to the precipitation of molecular hydrogen during the test. Fracture morphologies of austenitic stainless steels are described in Sect. 8.4.3.

(d) Quasi-cleavage

"Quasi-cleavage" is a term that broadly indicates fracture surfaces fairly flat and with irregular markings on planes not specified to cleavage planes. Quasi-cleavage (QC) is often observed for hydrogen embrittlement of steels and the morphology differs by microstructures, specimen geometries and also by hydrogen-charging conditions.

The fracture surface of a low carbon tempered martensitic steel (0.06C-5.9Ni-1.2Mn-0.7Cr-0.2Mo) subjected to three-point bending after hydrogen charging exhibited irregular flaky patterns of about 10 μm in size [15]. The specimens were a fatigue-notched standard Charpy type, and hydrogen precharging was conducted by cathodic electrolysis under a fairly high fugacity in poisoned 1 N H_2SO_4 at a current density of 10^3 A/m^2. Scanning electron micrograph revealed fine, lath-like features that correspond in dimension to martensite laths. The shape of etch-pits on the surface revealed their formation on {110} surfaces. The TEM observations also revealed that the fracture surface was along martensite lath boundaries almost over its whole length. The lath boundaries are sites of high dislocation density. The observations also revealed many fine secondary cracks immediately beneath the fracture surface and their initiation at irregularities in the lath boundary such as boundary intersections, steps or foreign particles.

Quasi-cleavage surfaces which are likely a premature dimple fracture are often observed for medium strength steels and for moderately embrittled high strength steels. Figure 7.5 [16] compares fracture surfaces of a low carbon ferrite-pearlite steel subjected to three-point bending tests with and without hydrogen-precharging. Hydrogen-charging under mild fugacity was conducted by cathodic electrolysis in

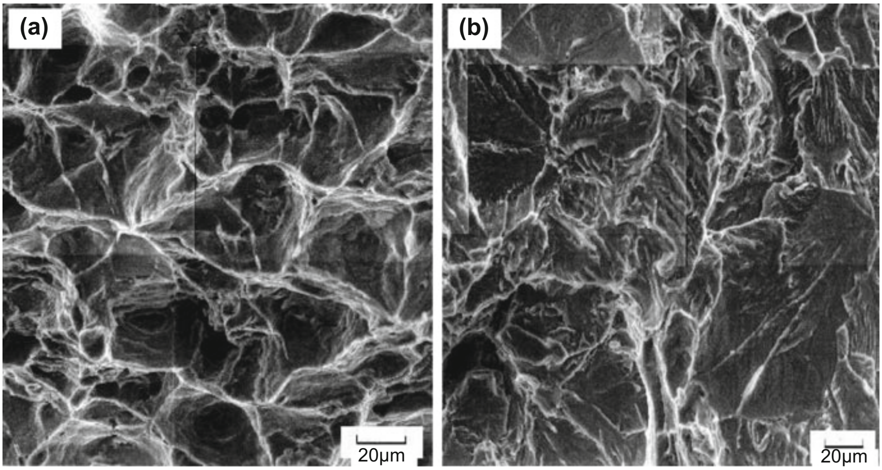

Fig. 7.5 Fracture surfaces of a low carbon ferrite-pearlite steel subjected to three-point bending tests (**a**) without and (**b**) with hydrogen precharging. (**a**) dimple and (**b**) quasi-cleavage patterns. Hydrogen charging is conducted by cathodic electrolysis in 3 % NaCl + 3 g/*l* NH_4SCN at a current density of 5 A/m^2 (Shimomura et al. [16])

3 % NaCl + 3 g/*l* NH_4SCN at a current density of 5 A/m^2. Detection of the onset of the stable crack in the steel is shown in Fig. 6.12. Dimple patterns observed for the uncharged specimen changed to QC with irregular morphologies for hydrogen-charged specimens. Fine striations also appeared in the latter. Effects of hydrogen are reasonably ascribed to cause premature fracture before a substantial growth of voids to form round dimples. The reduced roughness of the fracture surface by hydrogen shown in Fig. 7.5 is consistent with the decrease in the crack growth resistance by hydrogen shown in Fig. 6.14 for a low carbon ferrite-pearlite steel of similar compositions.

Microstructural changes that make up QC fracture surface were investigated by means of a focused ion beam (FIB) technique. Martin et al. examined correspondence between fine topographic features and underlying microstructures of API X60 and X80 pipeline steels subjected to compact tension tests in high pressure (5–100 MPa) hydrogen gas [17, 18]. The fracture surface exhibited some different morphologies and the surface with striations was referred as QC. A topographic surface map showed that striations running approximately parallel to the crack direction were in fact ridges. At low magnifications, ridges on quasi-cleavage [17] and fine undulations on flat featureless regions [18] were correlated with intense and highly localized shear bands. In high magnifications, the undulation was composed of small ~50 nm rounded mounds with a high density of dislocation lines and loops immediately beneath the surface [18].

Similarly, the fracture surface of a medium carbon high-strength martensitic steel which was gaseous hydrogen-charged and subjected to four-point bending tests showed “flat” and “quasi-cleavage” features [19]. The maximum nominal bending stress decreased by hydrogen from 2415 MPa to 501 MPa at room temperature. A high density of dislocations with localized slip bands was revealed beneath both “flat” and “quasi-cleavage” features, while flat one was along prior austenite grain boundaries with destructed lath boundaries.

Martin et al. postulated that undulations and mounds on the fracture surface were formed by either near-surface relaxation after fracture or the underlying dislocation structures [18]. However, Lynch objected that mounds were possibly small, shallow dimples resulting from nanovoid coalescence during fracture process [20]. Careful examinations of fracture surfaces were successively conducted by Neeraji et al. for hydrogen-precharged X65 and X80 line-pipe steels [21]. Evolution of a high dislocation density beneath quasi-cleavage facets was consistent with the observations by Martin et al., but mottled contrasts on the fracture surface were confirmed to be nanoscale dimples, 5 ~ 20 nm wide and 1 ~ 5 nm deep, of “valley-on-valley” type by mating halves of conjugate fracture surfaces. The findings indicate that nanovoid nucleation and linking, rather than the separation due to dislocation pileup, have taken place preceding the final fracture.

Quasi-cleavage and striations that characterize fractographic features of hydrogen embrittlement of steels originate in intense strain localization at shear bands. Shear localization promoting final fracture is described in Sects. 7.2.2 and 10.1.3 about the mechanism of hydrogen embrittlement.

(e) Intergranular fracture

Fracture surfaces of hydrogen-degraded high strength martensitic steels often exhibit morphologies that match prior austenite grains. The features have been assigned to intergranular (IG) crack propagation along prior austenite grain boundaries and have served as a basis of brittle fracture models of hydrogen embrittlement. The IG fracture is the typical mode for temper embrittlement of martensitic steels. As for hydrogen effects, a step-cooling heat-treatment of HY 130 (900 MPa in the yield stress) steel drastically reduced the threshold stress intensity for no failure at edge-notched cantilever bend tests in poisoned 0.1 N H_2SO_4 using precracked specimens [22]. The slow crack growth in unembrittled specimens started showing fractographic features with some IG mode. The features soon shifted to a mixture of cleavage and MVC and then to fully cleavage in the fast fracture region. On the other hand, embrittled specimens exhibited IG fracture from the point of the crack initiation through the slow and the fast growth regions. Related results for the effects of impurity segregation in prior austenite grain boundaries on hydrogen embrittlement are described in Sect. 8.2.

The IG fracture surfaces are not quite smooth, but usually exhibit fine markings associated with plastic deformation. Hydrogen precharged AISI 4340 steel subjected to sustained-loading tests using compact tension specimens exhibited fracture surfaces mixed of IG, QC and MVC regions [23]. Hydrogen pre-charging was conducted by cathodic electrolysis in poisoned 5 % H_2SO_4 at a current density of 20 A/m^2, and the crack growth behaviors at the test are described in Sect. 6.2.2 (b).

Main fractographic features of specimens tempered at 230 °C were IG and QC, and the fraction of IG increased by elevating test temperatures from −20 °C to 117 °C. On IG facets, "brittle" striations appeared perpendicularly to the local crack growth direction. The striations occasionally accompanied some small tear ridges, and the spacing of striations was nearly coincident with the average martensite lath spacing of 1 μm. Gerberich et al. assumed that brittle striations were intermittent arrest lines of advancing IG crack. The appearance of IG was less ductile than QC. However, the increase in the areal fraction of IG by elevating test temperatures was against an expected increase in ductility associated with thermal activation of dislocations. As the origin of IG at elevated temperatures, Gerberich et al. noticed a few oxysulfides revealed on IG surfaces. The particles were not associated with ductile tear and were assigned to the brittle fracture initiation sites.

On the other hand, fractographic features for 450 °C tempering showed intermittent slow and fast growth regions accompanying mixtures of IG and MVC ductile rupture regions. The fraction of IG *vs.* MVC was nearly 55 at room temperature. Ductile fingers or ligaments alternated in IG regions with the distance in between about 200 μm. A series of second phase particles was present on IG facets along ductile tearing striations. It was deduced that IG fracture proceeded from the particles in regions 100–200 μm in extent and then destabilized the ligaments to tear by MVC.

The IG fracture surfaces accompanying plasticity are not specific to steels and to the presence of hydrogen. Fracture surfaces of ultra-high strength 7075 aluminum alloys containing high Mg and Zn solutes were predominantly IG mode at fracture toughness tests, and fracture toughness decreased accompanying increasing amounts of IG fracture [24]. High magnifications of IG surfaces revealed very shallow dimples with fine particles (~0.1 μm). In situ observations for thin foil specimen revealed void initiation at grain boundary precipitates. It was postulated that the void initiation was induced by constraint against deformation near grain boundaries.

The prevalence of IG mode fracture was demonstrated for compositional effects in medium carbon martensitic steels at slow-elongation rate tensile tests under concurrent hydrogen charging [25]. The compositions of the steels were similar except manganese contents of 0.5, 1.0 and 1.5 %, and the specimens were plates of 2 mm in thickness and 10 mm in width without notch. Hydrogen charging was conducted by cathodic electrolysis in a 3 % NaCl aqueous solution containing 0.5 g/*l* 32# NH_4SCN at a current density of 5 A/m^2. Fracture surfaces are shown in Fig. 7.6 [25], and the tensile properties with and without hydrogen charging are shown in Fig. 8.8 in Sect. 8.2. It is to be noticed that enhanced degradation by higher manganese contents appeared only when hydrogen was present.

Fracture under hydrogen-charging always initiated near the corner of the specimen with IG fracture mode prevailing. Fine tear patterns were frequently observed on IG surfaces but the surface was smoother for higher manganese contents. Chemical etching of the IG surface with saturated picral revealed that tear took place along martensite lath boundaries. The average roughness of the fracture surface measured by means of scanning laser microscopy decreased with increasing Mn contents as shown in Fig. 7.7 [25]. The roughness corresponds to the dissipation of plastic energy on crack growth and the results of Fig. 7.7 are in accord with the

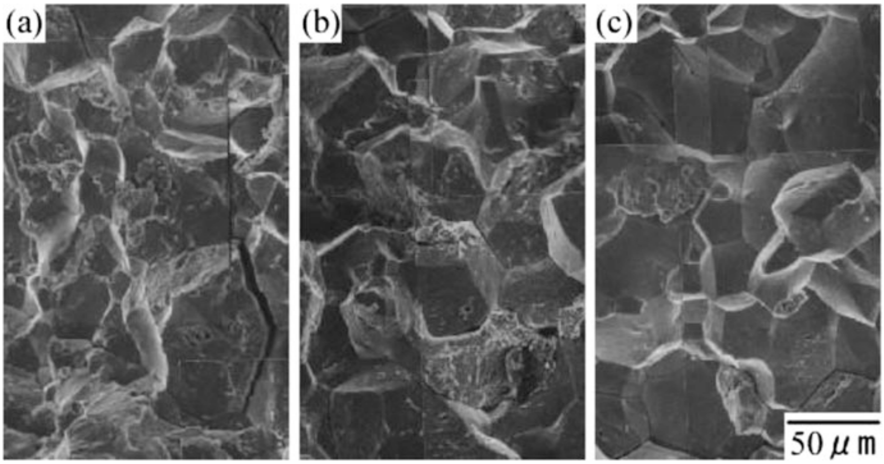

Fig. 7.6 Tensile-fracture surfaces of medium carbon martensitic steels under hydrogen charging. Manganese contents: (a) 0.5, (b) 1.0 and (c) 1.5 % (Nagumo et al. [25])

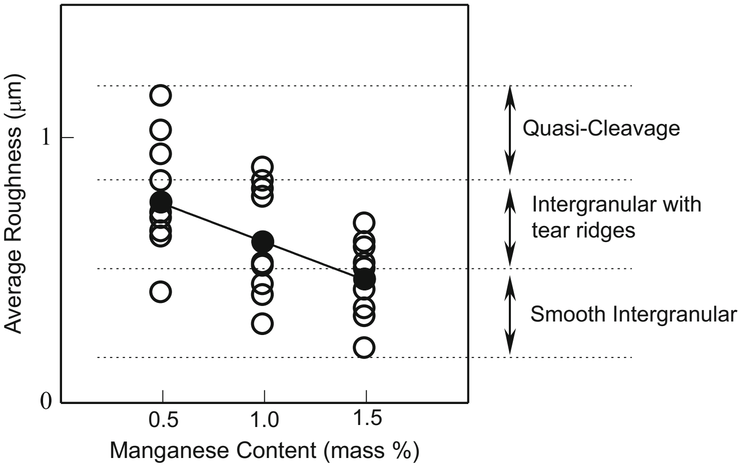

Fig. 7.7 Average roughness and patterns of fracture surfaces shown in Fig. 7.6 (Nagumo et al. [25])

Fig. 7.8 The amounts of hydrogen absorbed to saturation in specimens given various amounts of prestrain. The three martensitic steels with different Mn contents are used for Figs. 7.6 and 7.7 (Nagumo et al. [25])

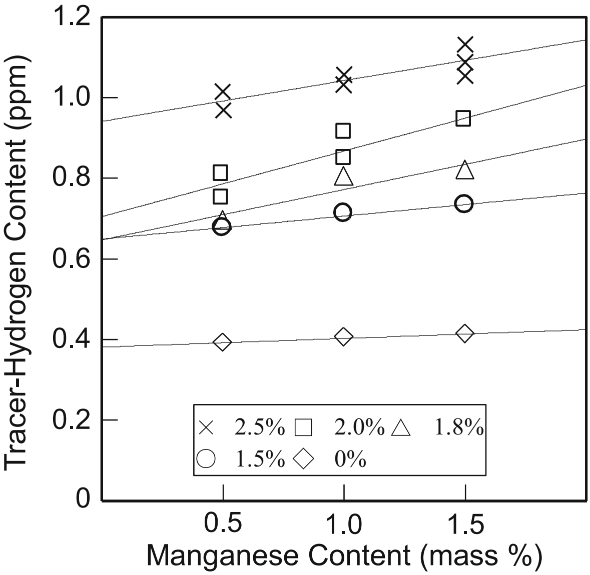

pronounced degradation of tensile properties shown in Fig. 8.8 with increasing Mn contents.

A crucial issue concerning IG fracture is the involvement of plasticity in embrittlement. A useful tool to detect lattice defects is to utilize tracer-hydrogen as shown in Figs. 3.2 and 6.25. Figure 7.8 [25] shows the amounts of hydrogen absorbed to saturation in specimens given various amounts of strain. The amount of absorbed tracer-hydrogen represents the densities of trap sites. The amounts for the

Fig. 7.9 Thermal desorption profiles of tracer-hydrogen introduced to the steel 1.5 % Mn steel specimens, unstrained, prestrained to 2 % and annealed at 250 °C for 1 h after straining (Nagumo et al. [25])

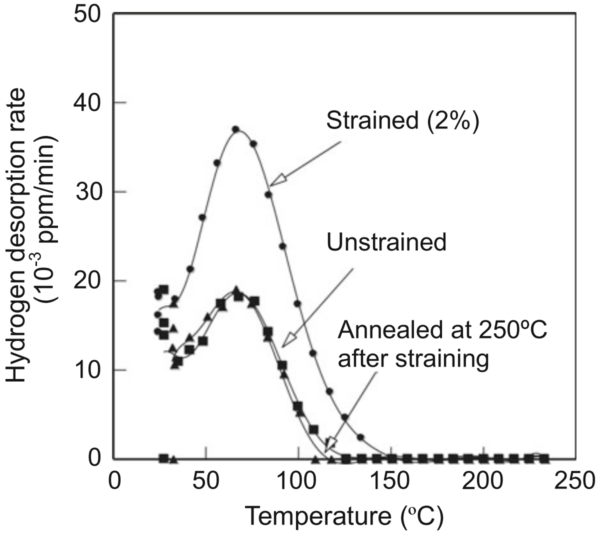

three steels are almost the same when straining was not given. On the other hand, a substantial increase by straining appeared more pronouncedly for higher manganese contents. As described for Figs. 3.2 and 3.10, TDA is a useful tool to examine the nature of strain-induced defects. Figure 7.9 [25] shows TDA curves of tracer-hydrogen introduced into three states of the 1.5 % Mn specimens, *i.e.* unstrained, prestrained to 2 % and annealed at 250 °C for 1 h after straining. The increase in the amounts of tracer-hydrogen totally disappeared by annealing the strained specimen at temperatures as low as 250 °C, indicating that lattice defects that interact with tracer-hydrogen are vacancies rather than dislocations. Thus, the origin of the effect of manganese contents is reasonably ascribed to the density of strain-induced vacancies. Precipitation of carbides along martensite boundaries was observed, but quantitative differences of microstructures that specify the three steels were not definite. Related degradations of tensile properties are described in Sect. 8.2.

Related information was reported from X-ray diffraction line broadening on IG fracture surfaces [26]. Fracture surfaces of compact tension test specimens of hydrogen-precharged 3.5 % Ni martensitic steel specimens showed IG fracture mode. Doping of phosphor and coarsening of prior austenite grain size reduced the threshold stress intensity and increased the crack growth rate. Rough and striped grain facets on fracture surfaces of undoped specimens became smoother and featureless by phosphor doping and grain coarsening. The {110} X-ray line was broader for the smooth surfaces than for the rough surfaces. It indicates the existence of a larger amount of residual strain beneath the fracture surface while plasticity is apparently less on the fracture surface. The relation between the fracture surface and X-ray line broadening is consistent with the findings in Figs. 7.7 and 7.8.

(f) Effects of stress and hydrogen concentration

Fractographic features are not uniform over the entire crack path. The propagation of a pop-in crack introduced by wedge-loading of AISI 4340 steel specimens in 3.5 % NaCl solution under a freely corroding (stress corrosion cracking, SCC) or attached to Mg anode (hydrogen assisted cracking, HAC) condition showed transitions of the fracture surface in a sequence of ductile dimple, QC, IG and fast fracture [27]. The test was a decreasing stress intensity (K) type during the crack growth. Beachem postulated that dissolved hydrogen enhanced deformation and that the crack path was determined by K, the dissolved hydrogen content c_H, and the microstructure. The combination of K and c_H at the crack tip varies with time. Beachem proposed a qualitative diagram of critical combinations of K and c_H for each fracture mode [27]. According to the diagram, the decrease in K at a constant c_H or in c_H at a constant K results in changes of the fracture modes as MVC → QC → IG. The diagram was an experimental one and microscopic origins of various fracture modes were not definite.

The change in the fracture mode of cracks from QC to IG was also observed for high strength AISI 4340 and ASTM A490 steels subjected to constant-stress delayed fracture tests [28]. The two steels were 1970 and 1700 MPa in tensile strength, respectively, and specimens were round and V-notched bars, respectively. Concurrent hydrogen charging was conducted by cathodic electrolysis in 1 N H_2SO_4 at a current density of 10–1000 A/m^2. The length of the QC region increased with decreasing notch sharpness and applied stress level. The results implied that QC triggered IG and that the crucial process for the start of delayed fracture was QC associated with plasticity even though the macroscopic fracture mode was brittle-like IG.

Alternatively, a highly disordered microstructure was revealed on the fracture surface of a hydrogen-charged iron [29]. Plate specimens of a 0.06%C ferritic steel of 310 MPa in tensile strength were tensile fractured under concurrent cathodic hydrogen-charging in 3 % NaCl + 3 g/l NH_4SCN aqueous solution at a current density of 10 A/m^2. The hydrogen charging condition was fairly mild and the elongation to fracture was still as large as 19 % in the presence of hydrogen. The fracture surface and the subsurface area were examined by TEM observations using a FIB technique for the sample preparation. The selected electron diffraction (SAD) from the fracture surface showed halo patterns and the lattice image of the surface layer showed disordered distributions of atoms. The thickness of the layer was less than 1 μm and the dislocation densities in neighboring areas were very high forming cell structures. Similarly disordered, amorphous-like layers of about 50 nm in thickness were also occasionally observed along dislocation cell walls at about 1 μm below the fracture surface.

In above experiments, many short cracks were present transverse to the tensile axis on the side surface of the fractured specimens. Similarly to the subsurface area, a featureless zone existed in the crack front as shown in Fig. 7.10 [29]. The SAD pattern in the insert showed halo rings similar to that at the subsurface, and dark

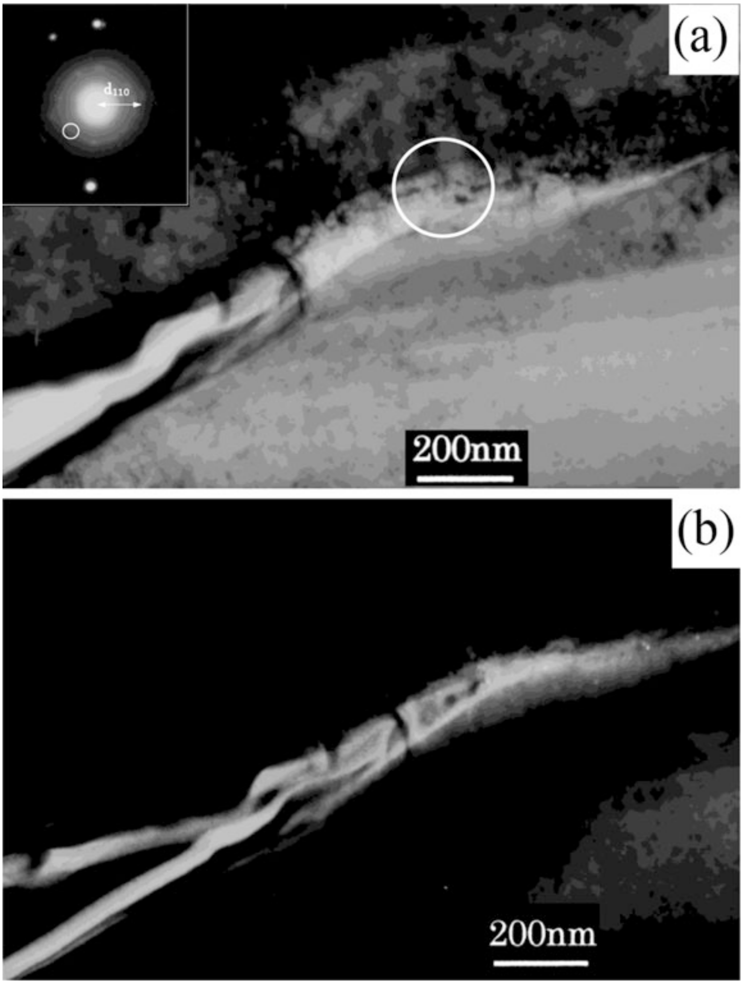

Fig. 7.10 (**a**) Featureless zone revealed by transmission electron microscopy in front of a small side crack formed on an iron specimen tensile-fractured under concurrent hydrogen-charging. (**b**) The dark field image of the encircled area in (**a**) from a hallo ring in selected electron diffraction (Nagumo et al. [29])

field image clearly showed the presence of amorphous-like structures in the crack front. The featureless zone of a few 100 nm in length was within the plastic zone.

Solid state amorphization induced by heavy plastic deformation has been known with mechanical alloying. The mechanical property of amorphous metallic alloys is characterized by low strain hardening that promotes strain localization and plastic instability. Hydrogen drastically reduces ductility of amorphous metals accompanying volume expansion [30]. Heavily disordered microstructures shown in Fig. 7.10 are in accord with high densities of vacancies suggested by the HESIV mechanism [8]. [25], and are viable as the origin of reduced ductility. However, only limited observations have been reported on the formation of amorphous phase at hydrogen embrittlement.

7.2 Strain Localization and Plastic Instability

7.2.1 Strain Localization

(a) Surface morphology

Fractographic features such as shallow dimples and QC in hydrogen embrittlement suggest that hydrogen suppresses the extension of plastic deformation on crack propagation. Hydrogen-enhanced strain localization has been reported often with slip morphology. Straightening, coarsening and increasing height of slip steps in the presence of hydrogen have been observed on fracture surfaces and side surfaces of tensile fractured austenitic stainless steel foil specimens [14, 31]. Confined surface reliefs along the advancing fatigue crack for a bulky specimen of hydrogen-precharged Type 304 stainless steel are shown in Fig. 7.11 [32]. Hydrogen was thermally precharged to about 90 mass ppm in high pressure hydrogen gas and the fatigue test was tension-compression at stress ratio of -0.1 and at frequency of 1.0 Hz. A small hole was drilled on the surface of specimens as the crack starter.

The features likely result from movements of dislocations taking different slip systems. For austenitic stainless steels, the primary factor that promotes the planarity of slip is stacking fault energy. For fcc metals and alloys, stacking fault energy plays a crucial role in plastic deformation associated with the ease of cross-slipping. Hydrogen reduces stacking fault energy and reported reductions are from 18 ~ 15 mJ/m^2 to 12 mJ/m^2 by 12 mass ppm of hydrogen and from 34.2 mJ/m^2 to 27.7 mJ/m^2 under 5.3 kPa of hydrogen gas for a Type 304 austenitic steel [33] and for a Type 310S austenitic steel [34], respectively. Effects of alloying elements on stacking fault energy in austenitic stainless steels were calculated by a first-principles calculation [35].

However, other types of steel also showed enhanced slip localization by hydrogen. Localized deformation around the advancing fatigue crack similar to Type 304 was observed for high strength Cr-Mo martensitic steel subjected to tension-compression fatigue tests [36]. Specimens were hydrogen-charged by immersion in 20 % NH_4SCN aqueous solution at 40 °C. Compared to hydrogen-uncharged specimens, the fatigue crack growth was straighter and slip bands were more concentrated near the crack front.

The effects of hydrogen on the morphology of slip bands were examined precisely for a 0.45 % C steel with ferrite and pearlite structures subjected to rotational bending fatigue tests at 45 Hz using shallow notched specimens hydrogen-precharged by immersing specimens in 20 % NH_4SCN aqueous solution at 40 °C [37]. Morphologies of slip bands at the notch root were examined using a

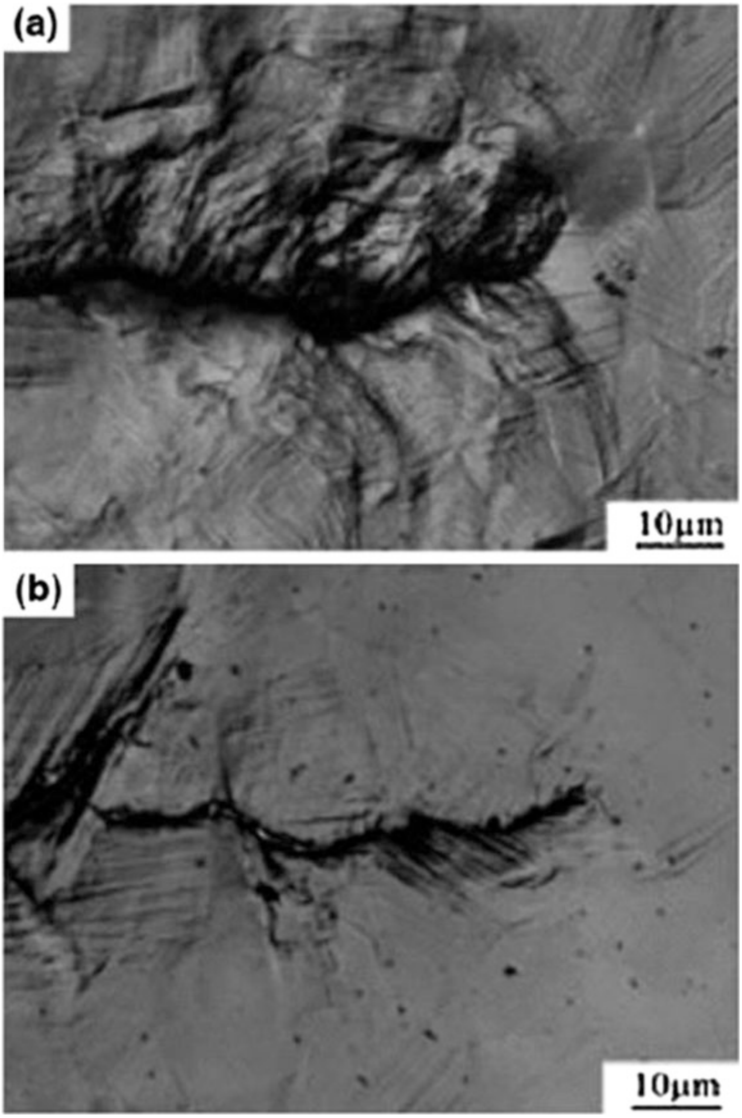

Fig. 7.11 Slip deformation behaviors near fatigue crack in Type 304. (**a**) Uncharged, $N = 13{,}200$, (**b**) Hydrogen-charged to 47.2 mass ppm, $N = 18.4000$ (Murakami et al. [32])

laser microscope for replicas of microstructures and were classified into three types as illustrated schematically in Fig. 7.12 [37]. The fraction of ferrite grains of Type C with discrete localized slip bands were 49 % in hydrogen-charged specimens after 6×10^5 fatigue cycles at 230 MPa, while Type C were not observed in uncharged specimens. Also, about 20 % of the crack initiation sites were along slip bands in hydrogen-charged specimens, while almost all were at grain boundaries in

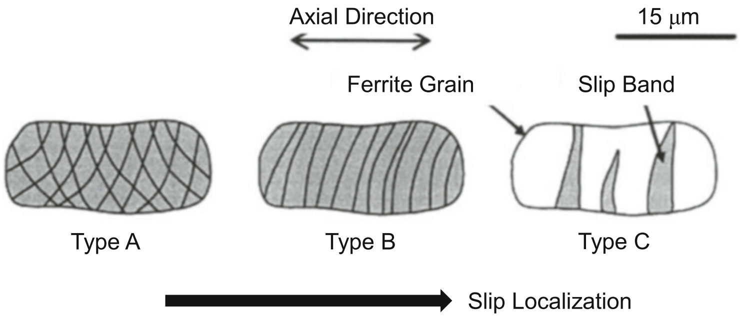

Fig. 7.12 Schematic illustrations of three types of slip bands at the notch root on 0.45 % carbon ferrite-pearlite steel specimens subjected to rotational bending fatigue (Uyama et al. [37]. Reprinted with permission from John Wiley & Sons)

uncharged ones. The results demonstrated hydrogen-enhanced slip localization and the crack nucleation therein. Degassing by aging hydrogen-charged specimens at room temperature for 270 h substantially reduced the fraction of Type C grains after fatigue tests.

Intense slip bands act as crack initiation sites as revealed in Fig. 7.3. Surface cracks at U-notch bend tests of spheroidized AISI 1090 steel specimens appeared at intense surface rumpling induced by slip bands [38]. The situations were essentially similar between hydrogen-charged and uncharged specimens, but a similar level of surface roughness or cracking was brought about for hydrogen-charged specimens by strain of about a factor of two lower than uncharged ones [38]. A similar U-notch bend test was conducted for quenched and tempered AISI 4340 steel of 1.35 MPa in tensile strength with and without hydrogen precharging under a high hydrogen fugacity estimated to be 1GPa [39]. Strain to fracture was markedly reduced by hydrogen-charging and cracks nucleated internally in a mode I manner. The crack extension to the surface was along the characteristic slip path. Concurrent hydrogen charging, instead of precharging, markedly promoted the crack nucleation reducing the plastic strain for the nucleation to essentially zero.

(b) Internal structures

Observations of deformation microstructures around fatigue crack by high-voltage electron microcopy (HVEM) were reported for Fe-2.6%Si single crystalline specimens [40]. The fatigue test was a sinusoidal tensile loading in hydrogen or helium gas of 0.58 MPa at stress ratio of 0.1 and 1 Hz in frequency. The crack propagation was along the $(1\ \bar{1}\ 0)$ plane in the [001] direction. Cross-sections of specimens exhibited remarkably different morphologies of slip and the crack outline between tests in hydrogen and helium gases. In hydrogen gas, the crack tip was sharp and the distribution of slip bands was concentrated within 5 μm from the crack, consistently with the surface relief observed for austenitic steels [32]. Also important is that the immediate vicinity of the crack was severely deformed while the crack outline was “brittle-like” straight. Slip bands were intermittently emitted from the crack tip, corresponding to the macroscopic crack growth rate.

The findings indicate that the crack advance is facilitated by extremely localized strain at the crack tip prior to the extension of the plastic region that accompanies the macroscopic crack opening. However, which of enhanced strain localization itself or associated creation of defects is the primary function of hydrogen in the crack advance is a matter to be examined further in Sect. 7.3.2.

Hydrogen-enhanced strain localization in internal microstructures was also revealed in addition to surface morphologies for austenitic stainless steels. Figure 7.13 [8] shows kernel average misorientation (KAM) maps obtained from electron backscatter diffraction (EBSD) for Type 304 austenitic stainless steels

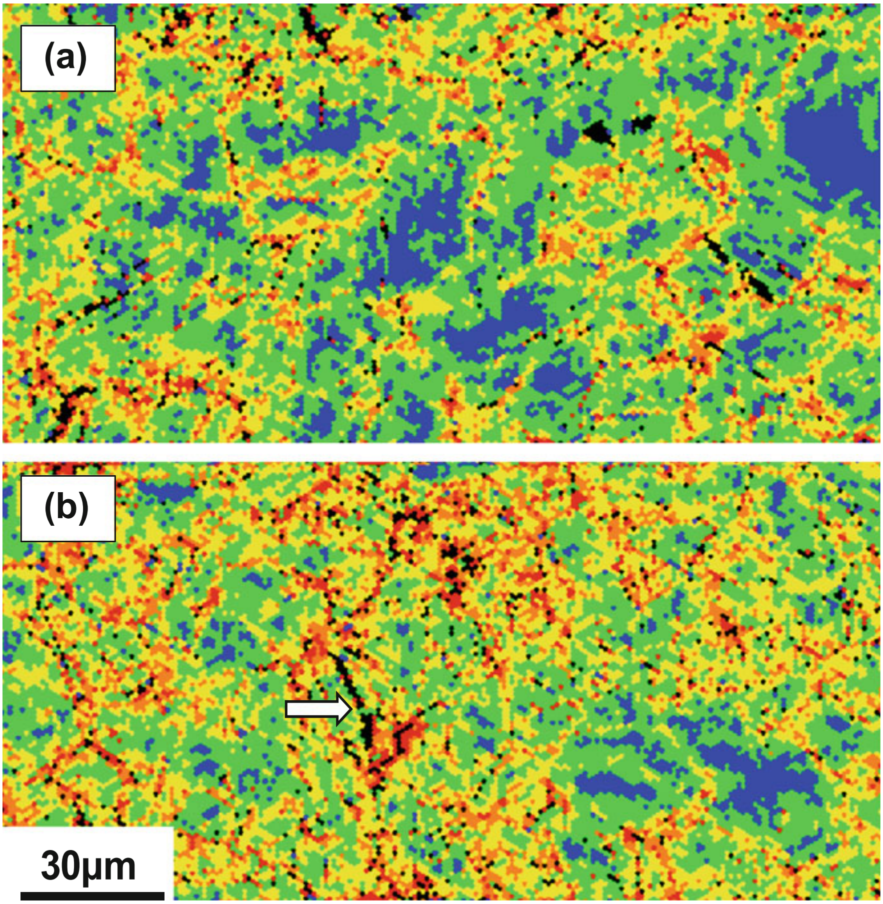

Fig. 7.13 Kernel average misorientation (KAM) maps of EBSD for Type 304 austenitic stainless steels tensile strained to 24 % (**a**) without and (**b**) with hydrogen precharging. Blue to red denotes higher misorientations between neighboring pixels. The *arrow* in (**b**) indicates annealing twin boundary (Hatano et al. [8])

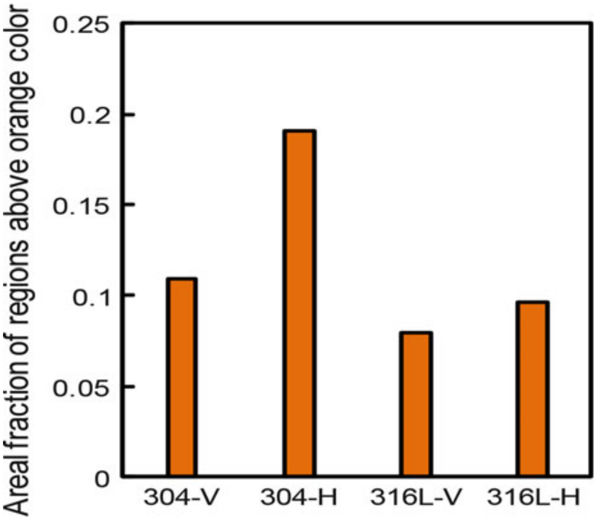

Fig. 7.14 Areal fractions of highly strained regions of orange and red colors in Fig. 7.13. Data for Type 316 L are also added. Suffixes "V" and "H" denote without and with hydrogen charging, respectively (Hatano et al. [8])

tensile strained to 24 % at room temperature with and without gaseous hydrogen precharging conducted under a high pressure at elevated temperature. The KAM map represents orientation differences between neighboring pixels and is a measure of the amount of strain. Blue to red colors in the KAM maps denote five levels from 0 to 5°.

The strain distribution is not uniform, and increased areal fractions of bright (orange and red) regions imply enhanced strain localization. A substantial decrease in tensile ductility by hydrogen appeared in Type 304, while Type 316 L was immune to hydrogen. Enhanced strain localization by hydrogen was observed also for Type 316 L, but it was to a less extent compared to Type 304. Figure 7.14 [8] shows a quantitative comparison of strain localization in terms of area fractions of orange and red color regions for Types 304 and 316 L steels strained to 24 % with and without hydrogen charging. Evidently the hydrogen effect to enhance strain localization is much more distinct in Type 304 than Type 316 L. The preferential strain localization in Type 304 is ascribed to stacking fault energy. The decrease in the stacking fault energy enhances strain-hardening and resultant phases such as stacking fault and ε-martensite act as barriers for the extension of slip. High densities of fine stacking faults and streaks of ε-martensite characterize microstructures of hydrogen-charged and deformed Type 304 austenitic steel [8]. Deterioration of crystallinity associated with strain localization is described in following Sect. 7.3.

Concurrently conducted positron annihilation spectroscopy (PAS) exhibited a more prominent increase in the mean positron lifetime associated with straining for Type 304 than for Type 316 L [8]. The utilization of PAS for identifying the type of hydrogen-enhanced strain-induced lattice defects is described in Sect. 3.2.3(b). For iron, isochronal annealing showed that the effect of hydrogen on increasing positron lifetime is due to the enhanced creation of vacancies. For austenitic stainless steels, vacancy clustering proceeded more prominently in Type 304 than in Type 316 L. The effects of enhanced strain localization on hydrogen embrittlement are related with enhanced creations of vacancies and their clusters. Other possibilities such as buildup of high local concentrations of hydrogen are not feasible because of very low diffusivity of hydrogen in austenitic stainless steels. Strain-induced transformation to martensite was not detected even in a region about 0.5 mm from the fracture surface of Type 304 [8].

7.2.2 Plastic Instability

Plastic instability is the localization of plastic flow departing from a homogeneous deformation during stressing process [41, 42]. Flow localization into a shear band appears as void sheet linking [43]. Plastic instability appears in uniaxial straining when the cross-section of a small portion of the length of the specimen differs from that of the remainder and the magnitude of the difference increases in the course of straining. Plastic instability is a crucial process in ductile fracture, and its mechanistic significance for ductile fracture is described in Sect. 10.1.3.

The appearance of rugged surface shear bands at U-notch bend tests of spheroidized AISI 1090 steel indicated the onset of flow localization or plastic instability [38]. Hydrogen promotes the evolution of surface rumpling and reduces the critical strain for the onset of plastic instability well before the profuse void formation in the bulk [38]. Internal small crack nucleation following surface rumpling was along characteristic slip traces as shown in Fig. 7.15 [38]. Criteria

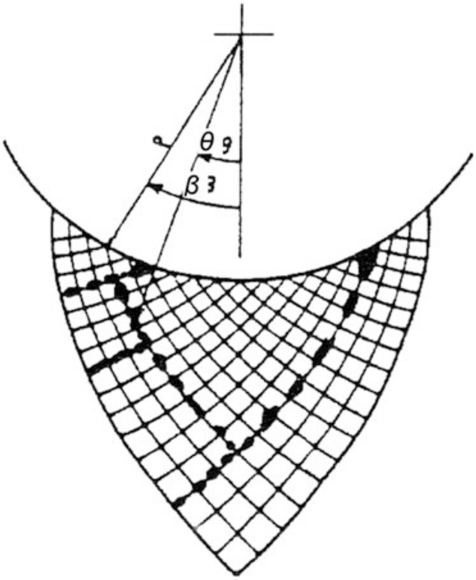

Fig. 7.15 Schematic show of logarithmic spiral slip traces for circular notch root and the formation microcracks (Onyewuenyi et al. [38])

of the onset of plastic instability are derived from material constitutive relations. The observed critical principal notch surface strain for the onset of plastic instability was in good agreement with the values calculated for a U-notched bend specimen [38]. For a U-notched bend test of AISI 4340 steel, the critical notch root strain at the crack initiation was nearly constant for three different notch-root radii of specimens [39]. It was deduced that hydrogen promoted plastic instability and that the crack nucleation within the plastic zone was induced by a combination of hydrogen concentration and total stress.

A crack initially formed in the central part of the specimen propagated stepwise following a "void sheet" path. Link-up of microcrack with a void situated at the tip of the microcrack by shear was reported for spheroidized AISI 1520 steel bar specimens subjected to axisymmetric tension after hydrogen precharging [43]. In that case, second phase particles were not ruled out as the crack initiation sites, but hydrogen promoted plastic instability and favored crack propagation.

The effects of hydrogen on the mixed mode I/III loading to fracture toughness tests, shown in Fig. 6.10, and the stable crack initiation from the precrack, shown in Fig. 6.13, are likely due to enhanced plastic instability as described in Sects. 10.4 and 10.5.

7.3 Precursory Damage to Crack Initiation

Hydrogen embrittlement draws attention when accidents such as delayed fracture of high strength fasteners or leak of sour oil/gas from pipes happen. Most studies so far conducted have remarked the onset and growth of cracks. However, the degradation of materials during the service practice is extremely important in stages preceding the onset of fracture, and the effects of hydrogen on the creation of damage in materials are critical subjects. The term "damage" in engineering often addresses flaws such as cracks or voids, but here it is used in a wide sense addressing crystalline deterioration far below visual scale.

7.3.1 Generation of Damage During Mechanical Tests

Local lattice distortion around hydrogen-induced cracks was detected for pure iron single crystal as smearing of X-ray Kossel lines [44]. Cathodic hydrogen-charging at a current density of 300 A/m^2 without external stress produced internal cracks of 50–75 μm in size accompanying lattice distortion localized within 100 μm of cracks. However, distorted absorption conics (Kossel lines) were also observed in regions where cracking had not yet occurred. Broadening of X-ray diffraction line width associated with hydrogen-charging was observed for mild steel specimens cathodically hydrogen-charged in poisoned 0.1 N H_2SO_4 at the current density of 10^3 A/m^2 [45]. The line broadening was unchanged during exposure of specimens at room temperature, but decreased about 25 % at 200 °C and almost totally disappeared at 400 °C. The aging behaviors imply that the line broadening was not due to elastic strain around hydrogen atoms but to plastic deformation induced at the time of hydrogen charging. The aging behaviors are quite consistent with Figs. 3.2(b) and 3.10 that imply vacancy-type defects created by plastic straining.

The effects of hydrogen on inducing lattice distortion are enhanced when plastic straining has been or is simultaneously applied to the specimen. The image quality (IQ) of EBSD analysis represents the crystallinity of the diffracting area and the dark contrast results from lattice distortion. Figure 7.16 [8] shows IQ maps of hydrogen-charged Type 304 austenitic stainless steel given tensile strain of 5 % or 24 %. The maps show more pronounced lattice distortion with increasing strain in regions close to grain-boundaries than in the bulk. The average strain obtained

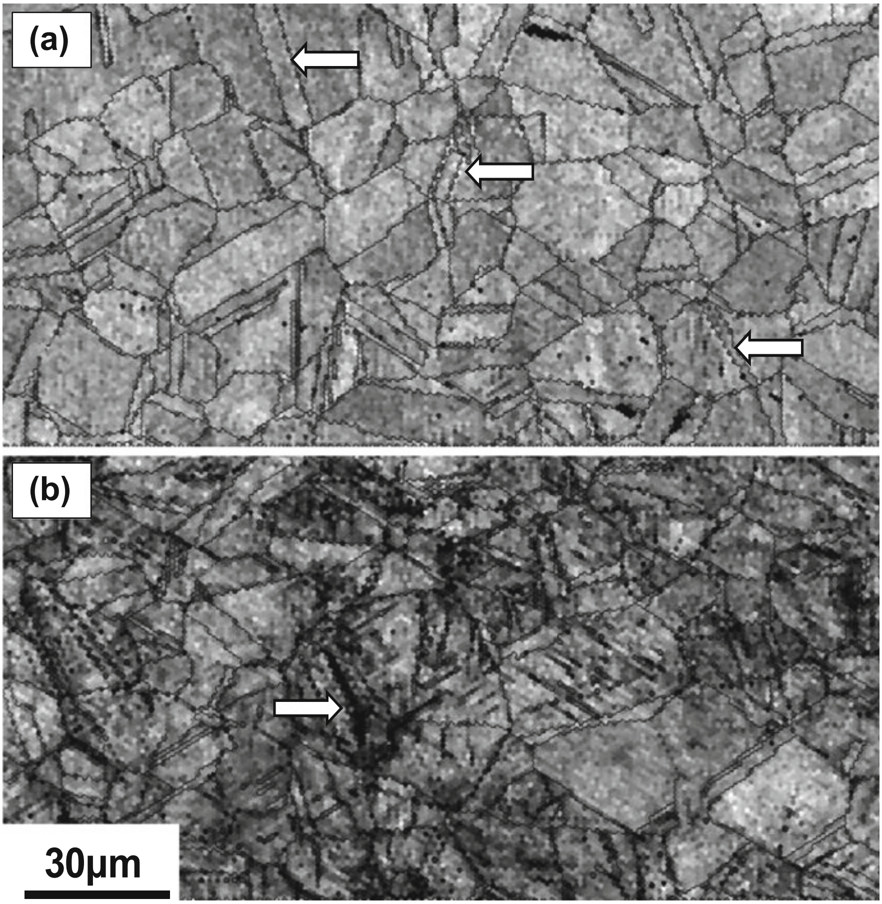

Fig. 7.16 Image quality (IQ) maps of EBSD for hydrogen-charged Type 304 austenitic stainless steels tensile strained to (**a**) 5 % and (**b**) 24 %. Arrows indicate annealing twin boundaries (Hatano et al. [8])

separately from KAM maps was reasonably lower for the specimen strained to 5 % than that for 24 %, but preferential strain localization appeared in hydrogen-charged Type 304 at strain as low as 5 % [8]. Annealing twins were often observed within grains, as indicated by arrows in Fig. 7.16, and twin boundaries tended to become blurred with increasing strain, implying distortion of areas near the interface of twin bands.

Nibur et al. examined fractographic features and deformation microstructures of 21Cr-6Ni-9Mn austenitic stainless steel specimens subjected to a compact tension test after thermal hydrogen precharging [46]. The features were somewhat dependent on included ferrite volume contents in the material, but the effects of hydrogen-precharging were characterized by shallow, non-equiaxed dimples and flat facets with limited plasticity. Examinations of cross-sections revealed the primary void nucleation at deformation band intersections. Relatively large facets were covered with fine, elongated dimples, and cross-sectional examinations revealed concentrations of microvoids along a continuous obstacle such as another deformation band. For the annealed material, microcracks were revealed along annealing twin boundaries at intersection points with deformation bands. The observations are consistent with the formation of a small crack at the intersection of slip bands shown in Fig. 7.2 for pure iron and the void nucleation in deformation bands shown in Figs. 7.3 and 7.4 for a ferritic steel. Nibur et al. postulated that hydrogen-enhanced localized plasticity (HELP) causes strain discontinuities at obstacles and void nucleation, but the deterioration of crystallinity along twin boundaries shown in Fig. 7.16 for Type 304 steel is also viable as the precursor of void nucleation. Fractographic features and deformation microstructures of austenitic stainless steels are further described in Sects. 8.4.3 and 8.4.4.

Koyama et al. prepared a 0.15 % C ferrite/martensite dual phase (DP) steel by water-quenching from the two-phase region and showed a substantial degradation by hydrogen-precharging on tensile straining [47]. Koyama et al. examined internal microstructures and used the term “damage” for flaws such as cracks and voids. The onset of necking and the evolution of the damage area during straining took place earlier for hydrogen precharged specimens than for uncharged specimens. An IQ map revealed the incipient crack nucleation in the incubation period before a substantial crack growth mostly inside of martensite. The grain-average KAM distributions associated with straining up to 7 % were unaffected by the presence of hydrogen in both ferrite and martensite phases, but incipient cracks grew into neighboring ferrite grains for hydrogen-charged specimens. Changes of the local orientation and high KAM values around the crack tip for hydrogen-charged specimens suggested a reduced crack-arresting ability by hydrogen. Related subjects on DP steels are described in Sect. 8.3.

The creation of lattice defects during incubation periods of fatigue and delayed fracture tests are shown in Figs. 6.17 and 6.25, respectively, detected by means of TDA of hydrogen used as the tracer of defects. The tracer-hydrogen contents in Fig. 6.17 are from the portions close to the fracture surfaces of high strength Si-Cr steel specimens subjected to rotational bending fatigue tests. Using the same test method, the fatigue-cycle dependence of the density of lattice defects was examined for two martensitic steels, a high strength Si-Cr steel bar designed for spring and a PC steel bar for pre-stressing tendom [48]. The amount of tracer-hydrogen increased in the latter half of fatigue lives for both steels, indicating accumulation of damage preceding the final fracture. The amounts of tracer-hydrogen in fatigued specimens decreased by annealing at 200 °C, indicating the vacancy-type nature of the lattice defects created before fracture. However, changes in the amount of tracer-hydrogen in the incubation stage were not simple depending on the tested steels. Preceding the increase in the late stage of fatigue, the amount of tracer hydrogen gradually decreased with fatigue cycles for PC steel while the decrease was very small for Si-Cr steel. The reason of the decrease and its dependence on steels is not definite, but reconfigurations or annihilation of dislocation structures during cyclic stressing were premised [48].

Positron annihilation spectroscopy (PAS) is another useful tool for detecting damage and was applied to tensile straining of Type 304 steel to identify types of lattice defects enhanced their creation by hydrogen. Figure 7.17 [8] shows mean positron lifetimes τ_m of Type 304 and Type 316 L steels given tensile straining with and without hydrogen-charging to 30 mass ppm. Hydrogen-charging prominently enhanced the increase in τ_m with increasing strain. The strain-induced increase in τ_m implies the creation of lattice effects that have longer positron lifetimes than that in the bulk. Successive isochronal annealing of strained materials showed monotonic reduced τ_m with increasing annealing temperatures [8]. The decrease in τ_m by annealing continued to temperatures as high as 1000 K, but the enhanced increase in τ_m by hydrogen disappeared by annealing at 300 °C. The annihilation temperature corresponds to that of vacancy clusters, and the difference of hydrogen effects between Type 304 and Type 316 L is ascribed to the creation and clustering of strain-induced vacancies. The results are consistent with PAS measurements for iron [49]. However, the observed τ_m is a weighted average of multiple lifetime components as described in Sect. 3.2.2. The contributions of dislocations and

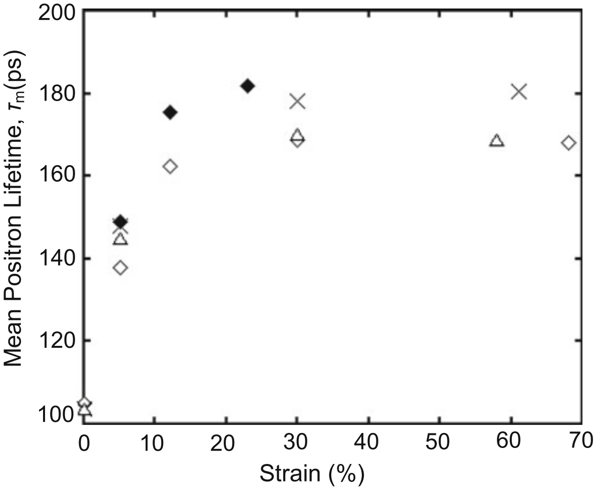

Fig. 7.17 Mean positron lifetimes of strained austenitic stainless steels: ◇, SUS304; ♦, H-charged SUS304; Δ, SUS316L; ×, H-charged SUS316L (Hatano et al. [8])

vacancies to τ_m for iron deformed with and without hydrogen-precharging are tabulated in Table 3.4. The deformation microstructures are further described in Sect. 8.4.4.

7.3.2 *Effects of Stress History*

Hydrogen degradation is evaluated under various types of loading. Controlling factors differ by the types, and operating mechanisms might not necessarily be identical. Structural components tolerate various stress histories during service, and damage produced in early stages is to be carried over to final fracture if hydrogen effects are common in each stage. In this section, some experiments about the effects of stress histories on hydrogen degradation are presented.

In Sect. 6.1(b), the essential role of vacancy-type lattice defects in hydrogen degradation in tensile tests is presented for iron, cold-drawn eutectoid steel and Inconel 625 alloy. Cyclic variations of applied stress promote failure at sustained-loading delayed fracture tests of martensitic steel as described in Sect. 6.4.3(a). Then, the effects of cyclic prestressing with and without hydrogen on tensile tests were examined for martensitic steel of 1433 MPa in tensile strength with respect to the creation of damage [50]. Initially, the applied stress was cyclically varied in the range of 0.7 ± 0.1 of the tensile strength with a triangular form. The strain rates and cycles were varied, and hydrogen-charging was conducted by immersing specimens in 20 % NH_4SCN solution at 50 °C. The specimens pre-stressed with and without hydrogen charging were denoted as [$\sigma + H$] and [σ], respectively. The degradation of tensile properties due to prestressing was expressed in terms of the hydrogen embrittlement susceptibility (*HES*) defined as the ratio of the fracture strain of [$\sigma + H$] to that of [σ] specimens at following tensile tests.

The effects of cyclic prestressing on *HES* are shown in Fig. 7.18 [50] for increasing the numbers of prestressing cycles at various strain rates. The degradation caused by hydrogen was enhanced by cyclic prestressing, more pronouncedly with increasing the number of cycles and reducing the strain rates. Damage introduced by cyclic prestressing was then examined using hydrogen as the tracer. Tracer-hydrogen was charged to saturation into cyclically prestressed specimens after exposing prestressed specimens at 30 °C for 168 h to degas hydrogen introduced at the prestressing stage. Tracer hydrogen was introduced without applying external stress under the same condition as the initial charging.

The amounts of tracer-hydrogen increased with the number of stressing cycles in both [σ] and [$\sigma + H$] specimens and their difference between [$\sigma + H$] and [σ] specimens was denoted as ΔC_H as a measure of the increase in damage due to hydrogen. The amount of ΔC_H represents hydrogen effects on the strain-induced creation of defects at cyclic prestressing. The magnitude of ΔC_H increased with cyclic stressing more pronouncedly with lower strain rates as shown in Fig. 7.19 [50]. The strain-rate dependence is consistent with that for tensile tests shown in Fig. 6.4 in Sect. 6.1(b). It indicates that cyclic stressing accumulates damage

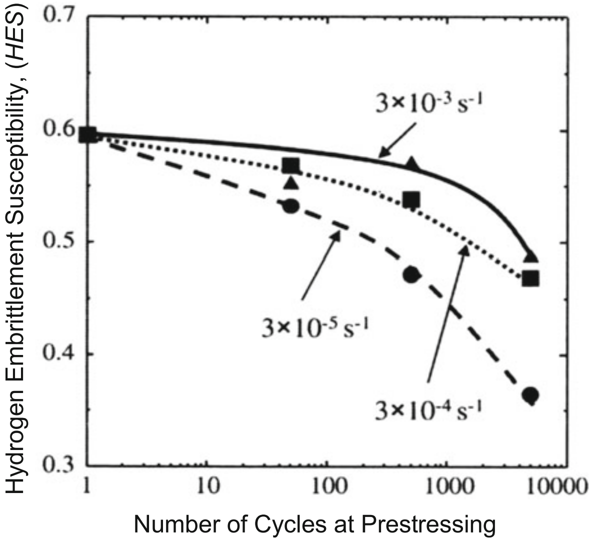

Fig. 7.18 Hydrogen embrittlement susceptibility (*HES*) on tensile tests of martensitic steel specimens applied cyclic prestressing at various strain rates (Doshida et al. [50])

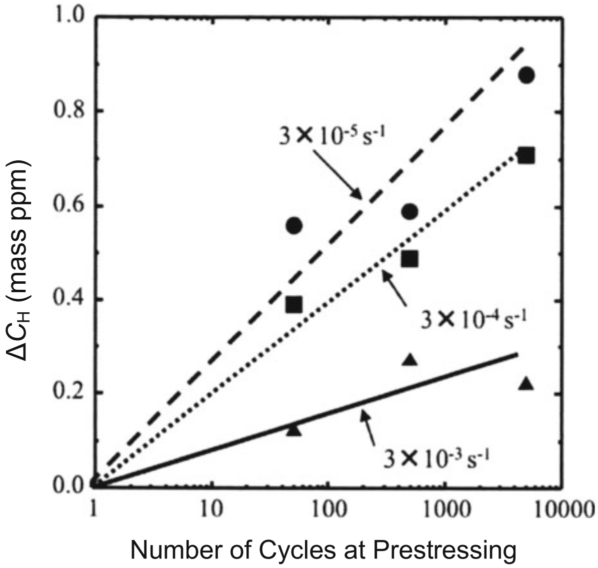

Fig. 7.19 Hydrogen enhancement of the strain-induced increase in the hydrogen absorption capacity, ΔC_H, on tensile tests of martensitic steel specimens after cyclic prestressing at various strain rates (Doshida et al. [50])

prior to the tensile tests. The thermal desorption profiles of tracer hydrogen showed a single peak centered at about 120 °C, and ΔC_H humped the higher temperature side of the TDA peak implying vacancy clusters as described in Sect. 3.2.3(b). An approximately linear correspondence exists between *HES* and ΔC_H [50]. It supports the notion that the hydrogen-enhanced creation of damage causes degradation through the whole stages of deformation.

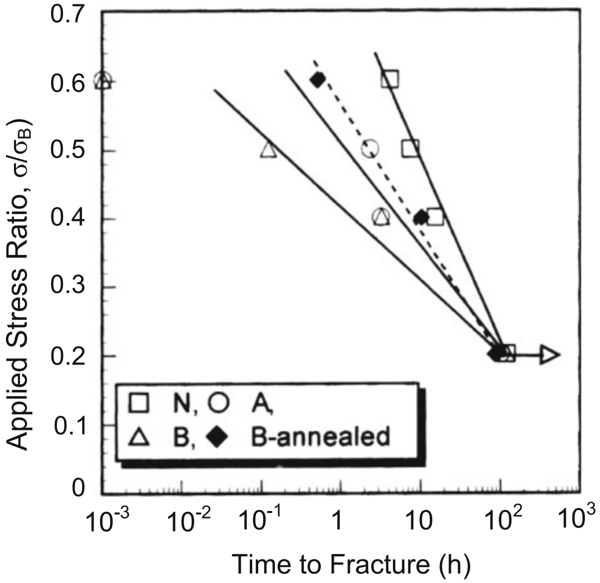

Fig. 7.20 Delayed fracture diagrams for prefatigued Si-Cr martensitic steel. □, N (without prefatigue); Δ, B (prefatigued close to failure); ◆, B (annealed at 200 °C for 1 h after prefatigue); ○, A (prefatigued to about one half of fatigue life) (Nagumo et al. [51])

In Sect. 6.3(a), promoted fracture by hydrogen at rotational bending fatigue tests of high strength Si-Cr steel is described, and defect creations in early stages of tests before final fracture are shown in Fig. 6.17 [51]. Similarly for delayed fracture, defects are accumulated in the incubation period as shown in Fig. 6.25 for high strength Si-Mn martensitic steel [52]. It leads to an expectation that stress histories play a role in hydrogen degradation.

Figure 7.20 [51] shows promoted delayed fracture by prefatigue for the Si-Cr martensitic steel used for Fig. 6.16. Prefatigue was applied by rotational bending for cycles about a half (Treat-A) of or close (Treat-B) to the fatigue life at the applied stress amplitude level of 640 MPa [51]. The two types of specimens were successively subjected to sustained-loading delayed fracture tests in 20 % NH_4SCN aqueous solution at 50 °C. Specimens without prefatigue (Treat-N) were also tested for comparison. Fracture of specimens given prefatigue for cycles close to the fatigue life, Treat-B, took place substantially earlier. However, annealing of the fatigued specimens at temperature as low as 200 °C for 1 h reduced the degradation caused by prefatigue. The results imply that damage accumulated during prefatigue plays a common function in failure as that created during delayed fracture test and that damage introduced by prefatigue is mostly vacancies without forming flaws such as voids and cracks.

Similar cumulative effects of damage were also shown between delayed fracture and tensile tests for high strength martensitic steel of 1433 MPa in tensile strength [52]. Specimens of 5 mm in diameter were initially sustained-loaded at a constant stress of 80 % of the tensile strength, apparently within the elastic range, for 96 h in 20 % NH_4SCN aqueous solution at 50 °C. After the sustained-loading, hydrogen was completely removed at 30 °C for 168 h and then some specimens were

Fig. 7.21 Tensile curves of high strength martensitic steel specimens. [H + stress (96)]: Initially sustained-loaded in 20 % NH_4SCN aqueous solution for 96 h at 50 °C; [H + stress(96) + 200 °C]: Annealed at 200 °C after sustained loading; [non-stressed + 200 °C]: Annealed at 200 °C without sustained-loading. All specimens are degassed at room temperature before tensile tests (Doshida et al. [52]. Reprinted with permission from The Iron & Steel Inst. Japan)

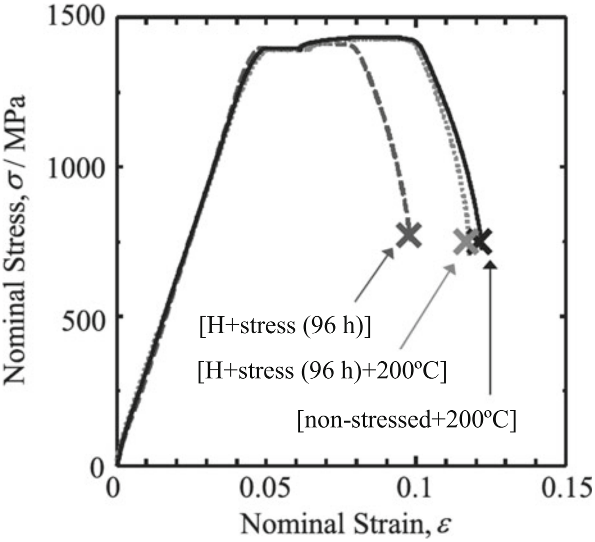

annealed at 200 °C for 2 h. The two series of specimens are denoted as [H + stress (96 h)] and [H + stress(96 h) + 200 °C], respectively. Also, specimens without sustained-loading but annealed at 200 °C were prepared with the notation of [non-stressed +200 °C]. Stress-strain curves at tensile tests are shown in Fig. 7.21 [52]. It is to be noticed that a substantial degradation appeared for the [H + stress (96 h)] series although hydrogen was absent at the time of tensile testing. The almost complete recovery for the [H + stress(96) + 200 °C] series indicates that the degradation is caused by vacancies created during sustained-loading without forming irreversible voids or cracks.

References

1. A.S. Tetelman, W.D. Robertson, Acta Metall. **11**, 415–426 (1963)
2. A.S. Tetelman, W.D. Robertson, Trans. Metall. Soc. AIME **224**, 775–783 (1962)
3. F. Terasaki, T. Kawakami, A. Yoshikawa, N. Takano, Rév. Métall-CIT/Sci. Génie Matér. **95**, 1519–1529 (1998)
4. R. Gerber, I.M. Bernstein, A.W. Thompson, Scr. Metall. **10**, 341–345 (1976)
5. J.A. Gordon, J.P. Hirth, A.M. Kumar, N.E. Moody Jr., Metall. Trans. A **23A**, 1013–1020 (1992)
6. M. Nagumo, H. Yoshida, Y. Shimomura, T. Kadokura, Mater. Trans. **42**, 132–137 (2001)
7. S.P. Lynch, Acta Metall. **32**, 79–90 (1984)
8. M. Hatano, M. Fujinami, K. Arai, H. Fujii, M. Nagumo, Acta Mater. **67**, 342–353 (2014)
9. A. Shibata, H. Takahashi, N. Tsuji, ISIJ Int. **52**, 208–212 (2012)
10. M.-J. Lii, X.-F. Chen, Y. Katz, W.W. Gerberich, Acta Metall. Mater. **38**, 2435–2453 (1990)
11. T.J. Marrow, M. Aindow, O. Prangnell, M. Strangwood, J.F. Knott, Acta Mater. **44**, 3125–3140 (1996)

12. F. Nakasato, I.M. Bernstein, Metall. Trans. A **9A**, 1317–1326 (1978)
13. M. Nagumo, K. Miyamoto, J. Jpn. Inst. Metals **45**, 1309–1317 (1981)
14. D.G. Ulmer, C.J. Altstetter, Acta Metall. Mater. **39**, 1237–1248 (1991)
15. Y.H. Kim, J.W. Morris Jr., Metall. Trans. A **14A**, 1883–1888 (1983)
16. Y. Shimomura, M. Nagumo, in *Environment-Induced Cracking of Materials: Chemistry, Mechanics and Mechanisms*", ed. by S.A. Shipilov, R.H. Jones, J.M. Olive, R.B. Rebak (Elsevier, Oxford, 2007), pp. 285–294
17. M.L. Martin, J.A. Fenske, G.S. Liu, P. Sofronis, I.M. Robertson, Acta Mater. **59**, 1601–1606 (2011)
18. M.L. Martin, I.M. Robertson, P. Sofronis, Acta Mater. **59**, 3680–3687 (2011)
19. A. Nagao, C.D. Smith, M. Dadfarnia, P. Sofronis, I.M. Robertson, Acta Mater. **60**, 5182–5189 (2012)
20. S.P. Lynch, Scr. Mater. **65**, 851–854 (2011)
21. T. Neeraj, R. Srinivasan, J. Srinivasan, Acta Mater. **60**, 5160–5171 (2012)
22. K. Yoshino, C.J. McMahon, Metall. Trans. **5**, 363–370 (1974)
23. W.W. Gerberich, T. Livne, X.-F. Chen, M. Kaczorowski, Metall. Trans. A **19A**, 1319–1334 (1988)
24. G.M. Ludtka, D.E. Laughlin, Metall. Trans. A **13A**, 411–425 (1982)
25. M. Nagumo, H. Matsuda, Philos. Mag. A **82**, 3415–3425 (2002)
26. J. Kameda, Acta Metall. **34**, 1721–1735 (1986)
27. C.D. Beachem, Metall. Trans. **3**, 437–451 (1972)
28. H. Yatabe, K. Yamada, E.R. de Los Rios, K.J. Miller, Fatigue Fract. Eng. Mater. Struct. **18**, 377–384 (1995)
29. M. Nagumo, T. Ishikawa, T. Endoh, Y. Inoue, Scr. Mater. **49**, 837–842 (2003)
30. M. Nagumo, T. Takahashi, Mater. Sci. Eng. **23**, 257–259 (1975)
31. D.P. Abraham, C.J. Altstetter, Metall. Mater. Trans. A **26A**, 2859–2871 (1995)
32. Y. Murakami, T. Kanezaki, Y. Mine, Metall. Mater. Trans. A **41**, 2548–2562 (2010)
33. A. Inoue, Y. Hosoya, T. Masumoto, Trans. ISIJ **19**, 170–178 (1979)
34. P.J. Ferreira, I.M. Robertson, H.K. Birnbaum, Mater. Sci. Forum **207–209**, 93–96 (1996)
35. L. Vitos, J.-O. Nilsson, B. Johansson, Acta Mater. **54**, 3821–3826 (2006)
36. H. Tanaka, N. Hommma, S. Matsunaga, Y. Murakami, Trans. Jpn. Soc. Mech. Eng. A **73**, 1358–1365 (2007)
37. H. Uyama, M. Nakashima, K. Morishige, Y. Mine, Y. Murakami, Fatigue Fract. Eng. Mater. Struct. **29**, 1066–1074 (2006)
38. O.A. Onyewuenyi, J.P. Hirth, Metall. Trans. A **14A**, 259–269 (1983)
39. T.D. Lee, T. Goldenberg, J.P. Hirth, Metall. Trans. A **10A**, 439–448 (1979)
40. Y. Takahashi, M. Tanaka, K. Higashida, H. Noguchi, Scr. Mater. **61**, 145–148 (2009)
41. F.A. Nichols, Acta Metall. **28**, 663–673 (1980)
42. O.A. Onyewuenyi, in *Hydrogen Degradation of Ferrous Alloys*, ed. by R.A. Oriani, J.P. Hirth, M. Smialowski (Noyes Pub., Park Ridge, 1985), pp. 414–453
43. I.-G. Park, A.W. Thompson, Metall. Trans. A **21A**, 465–477 (1990)
44. I.M. Bernstein, H.W. Wagenblast, J.L. Bomback, Metall. Trans. **2**, 2533–2534 (1972)
45. K. Kamachi, *Report of Research Team on the Mechanism of Delayed Fracture* (Iron and Steel Institute of Japan, Tokyo, 1975), pp. 93–111
46. K.A. Nibur, B.P. Somerday, D.K. Balch, C. San Marchi, Acta Mater. **57**, 3795–3809 (2009)
47. M. Koyama, C.C. Tasan, E. Akiyama, K. Tsuzaki, D. Raabe, Acta Mater. **70**, 174–187 (2014)
48. M. Nagumo, H. Shimura, T. Chaya, H. Hayashi, I. Ochiai, Mater. Sci. Eng. **A348**, 192–200 (2003)
49. K. Sakaki, T. Kawase, M. Hirano, M. Mizuno, H. Araki, Y. Shirai, M. Nagumo, Scr. Mater. **55**, 1031–1034 (2006)
50. T. Doshida, M. Nakamura, H. Saito, T. Sawada, K. Takai, Acta Mater. **61**, 7755–7766 (2013)
51. M. Nagumo, S. Sekiguchi, H. Hayashi, K. Takai, Mater. Sci. Eng. **344A**, 86–91 (2003)
52. T. Doshida, H. Suzuki, K. Takai, N. Oshima, T. Hirade, ISIJ Int. **52**, 198–207 (2012)

Chapter 8
Effects of Microstructural Factors on Hydrogen Embrittlement

Hydrogen embrittlement (HE) of steels is susceptible to microstructures, and understanding of functions of microstructural factors is indispensable to proper designs of steels against environmental degradation. Many studies have been conducted, and early works on material and environmental factors are in a review by Moody et al. for iron-base alloys [1]. Effects of alloying elements focusing on trapping of hydrogen were reviewed by Bernstein and Pressouyre [2]. It should be noticed that a procedure to control a specific type of microstructural factor occasionally alters other factors and the separation of contributions of each factor is not straightforward. For example, the grain refinement conducted by recrystallization of cold-worked iron accompanies recovery of substructures during annealing. Also, effects of material factors depend on environmental and mechanistic conditions. Comparisons of susceptibilities to HE of different materials must be made under proper conditions.

Characteristic features of fracture in HE are described in Chap. 7. Functions of microstructural factors in HE appear not only in resultant mechanical properties but also in features such as fracture morphology, strain localization, and damage accumulation. Interactions of hydrogen with lattice defects during processes preceding the final fracture exert influence on the final degradation.

Accordingly, functions of microstructural factors must be examined throughout the process leading to fracture. However, studies along the context are limited in the literature. In this section, the stability of substructures against external stress in the presence of hydrogen is paid particular attention for effects of microstructural factors.

M. Nagumo, *Fundamentals of Hydrogen Embrittlement*,
DOI 10.1007/978-981-10-0161-1_8

8.1 Dislocation and Slip Configurations

(a) Tempering of martensite and bainite

Tempered martensite is the most common microstructure of high-strength steels. On tempering, internal stress is relieved by rearrangement of a high density of dislocations to stable structures and by precipitation of supersaturated solute carbon to carbides. Then, effects of tempering are considered from two main aspects, the one is substructures and the other is carbide morphologies.

Effects of tempering temperatures on Stage II crack growth rates and on fractographic features are described in Sect. 6.2.2(b) and in Sect. 7.1(e), respectively, for hydrogen-precharged AISI 4340 steel. Increase in tempering temperatures from 230 °C to 450 °C reduced the yield strength from 1620 MPa to 1340 MPa and Stage II crack growth rates. Fractographic features changed from mixtures of IG and QC to alternate IG and MVC regions at 100–200 μm intervals. Gerberich et al. assumed that the different brittle fracture initiation sites between the two tempering conditions determine the Stage II crack growth rates [3]. Martensite lath intersections with prior austenite grain boundaries and oxysulfides are the proposed sites for the high and low strength steels, respectively.

Elevated tempering temperatures generally stabilize substructures and reduce the strength of martensite. Effects of tempering temperature are shown in Fig. 8.1 [4] for the threshold stress intensity, K_{ISCC}, at delayed fracture tests of 0.35C-Cr-Mo steels (SCM435 in Japanese Industrial Standard). The steels were additionally alloyed with (A) 0.04Nb, (B) 0.04Ti + 0.10 V, or (C) 0.10 V + 0.04Nb (mass %) to the base compositions in order to control strength levels at a given tempering temperature. The delayed fracture test was conducted with a cantilever beam bend test in 3 % NaCl aqueous solution using fatigue-notched specimens. Figure 8.1

Fig. 8.1 Dependence of K_{ISCC} on tempering temperatures for medium carbon Cr-Mo martensitic steels. (**a**) 0.04Nb, (**b**) 0.04Ti + 0.10 V or (**c**) 0.10 V + 0.04Nb (mass %) to the base compositions (Owada et al. [4]. Reprinted with permission from The Iron & Steel Inst. Japan)

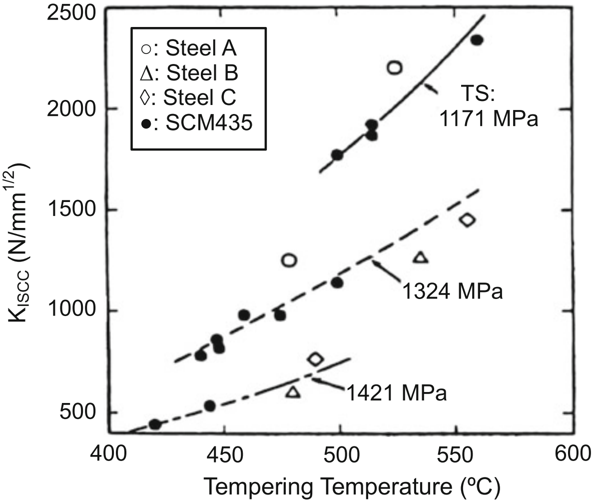

separates the effect of tempering temperature on K_{ISCC} from that of tensile strength by classifying K_{ISCC} data into three levels of tensile strength. Lower tensile strengths obtained by higher tempering temperatures generally elevate the level of K_{ISCC}, i.e., reduce the susceptibility to HE, but higher tempering temperatures increase K_{ISCC} even at a constant strength level. Separately conducted measurements of K_I exhibited that the ratio of K_{ISCC}/K_I at a given tensile strength differed by steels in a range of 0.45 ~ 0.15.

A proper alloy design makes possible to keep a high-strength level at high tempering temperatures, as shown for Mo-V martensitic steel in Sect. 5.3.1. Stabilized substructures by tempering reduce internal strain as observed by a linear decrease in broadening of X-ray diffraction line width with tempering temperatures [4]. Figure 8.2 [4] shows good correlations between K_{ISCC} and internal strain estimated from the half width of X-ray diffraction line for the steels in Fig. 8.1. The results strongly suggest that internal strain or associated dislocation arrangement is an important primary factor controlling the susceptibility to HE of martensitic steels.

Bainite is a generic term for microstructures obtained intermediately between pearlite and martensite reactions at the decomposition of austenite [5]. The apparent structures widely vary according to transformation temperatures. Lower bainite that forms in between 250 and 400 °C is composed of fine ferrite plates close in morphology to martensite plates. Carbides either Fe_3C or ε iron-carbide precipitate within the ferrite plates, and the density of dislocations is high. The strength of lower bainite is high, and the structures are more stable than as-quenched martensite.

Fig. 8.2 Relationship between K_{ISCC} and internal strain estimated from X-ray diffraction line broadening for the steels in Fig. 8.1 (The unit for strain may not be correct.) (Owada et al. [4]. Reprinted with permission from The Iron & Steel Inst. Japan)

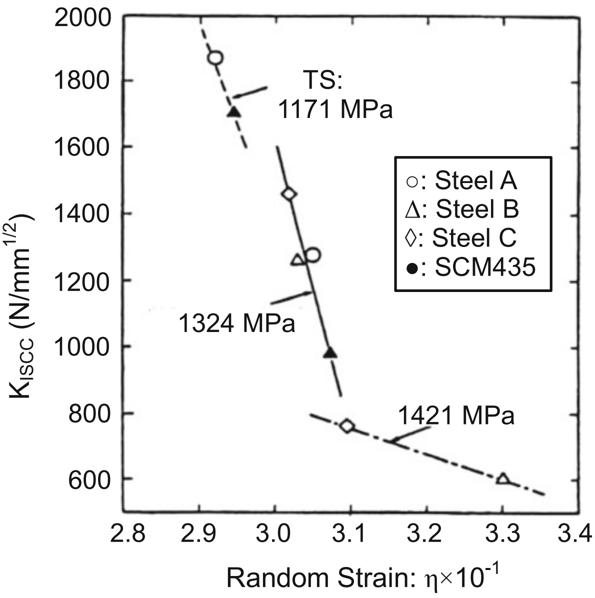

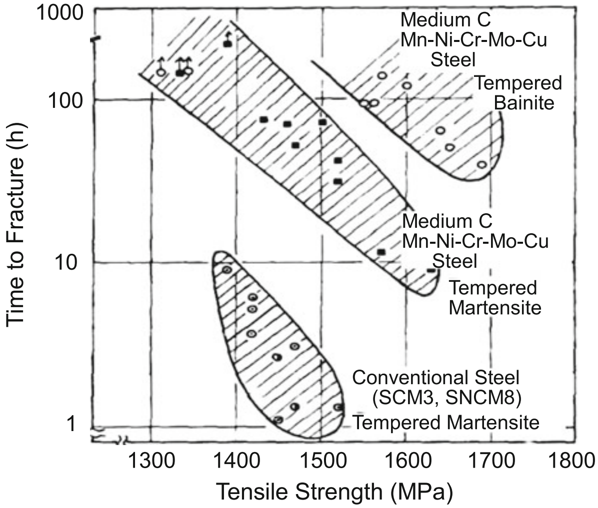

Fig. 8.3 Relationship between tensile strength and time to fracture at nominal bending stress of 1000 MPa in three-point bending delayed fracture test in 0.1 N HCl solution (Nakasato et al. [6])

Comparisons of the times to fracture at delayed fracture tests for tempered martensitic and lower bainitic steels are shown in Fig. 8.3 [6]. The steels are medium carbon low alloy steels of various compositions, and some are further micro-alloyed with V, Nb and Ti. Isothermal transformation at 320 °C or oil-quenching from austenitizing at 1000 °C was given to produce bainite or martensite structures, respectively. Tempering temperatures were 600 or 500 °C for both structures. Delayed fracture tests for Fig. 8.3 were conducted by three-point bending at a constant strain under an applied load of 1000 MPa in 0.1 N HCl at 12 °C using circumferentially V-notched round bar specimens of 10 mm in diameter. A superior resistance to delayed fracture of lower bainite compared with martensite is evident.

The crack growth was also measured by means of an electric potential method at a sustained-loading four-point bending test with U-notched rectangular bar shape specimens [6]. Specimens of the two structures were 1500 MPa in tensile strength, and the initial applied stress intensity was $1500\ \mathrm{N} \cdot \mathrm{m}^{-3/2}$ in 0.1 N HCl at 12 °C. The incubation time to initiate a crack was 105 and 55 min for bainite and martensite, respectively, and the crack growth rate was about one order of magnitude slower for bainite than for martensite. Further, K_{ISCC}, defined as the threshold stress intensity at which a growing crack was arrested, was measured by means of a constant-strain wedge opening loading test in 0.1 N HCl at 12 °C or in distilled water at 50 °C. In that test method, stress intensity decreased with the crack extension, and the values of K_{ISCC} of the two structures were almost the same irrespective of test solutions.

A highly supersaturated solute carbon precipitates as cementite on tempering, and cementites act as void nucleation sites on tensile deformation as observed for spheroidized carbon steels [7] even at low hydrogen fugacity [8]. In the experiment cited above [6], precipitation of cementite along prior austenite grain boundaries was substantial in martensitic structures, and intergranular fracture (IG) was dominant. On the other hand, the precipitation of cementite within lath was dominant in bainite structures, and the fracture surface showed quasi-cleavage (QC). The lower crack growth rate in bainitic structures might be ascribed to the cementite morphology. However, some fractions of IG existed for bainite according to the level of stress intensity. The IG fracture mode was dominant for bainitic structures at applied stress levels near K_{ISCC}. Effects of cementite morphology on delayed fracture may depend on stress states and deformation stages.

(b) Fine precipitates

Martensitic steels micro-alloyed with Ti, Nb, and V precipitate uniformly very fine carbides and/or nitrides on tempering. The precipitates are associated with coherent strain around the particles in the early stage of precipitation and act as obstacles for dislocation motion retarding decomposition of martensite and causing secondary hardening. Interactions of hydrogen with the precipitates increase the hydrogen absorption capacity of steels and reduce hydrogen diffusivity. Morphologies of precipitates are strongly dependent on tempering temperatures, and their functions in HE are complicated depending on situations.

Effects of V and Ti and additional Mo on sulfide stress cracking (SSC) were examined for 0.4C-1Cr-0.2Mo (mass %) martensitic steel at sustained-loading delayed fracture tests in the NACE solution (5 % NaCl + 0.5 % glacial acetic acid saturated with H_2S, pH =3) [9]. Two levels of tempering temperatures were chosen so as to give tensile strength of 900/950 and 1000/1050 MPa. Fine precipitates $\leq$ 20 nm in size were revealed by micro-autoradiogaphy. The SSC resistance in terms of the no-failure threshold stress was improved for all the modified steels compared with the reference steel without micro-alloying elements. Tempering temperatures for the two tensile strength levels were between 650 and 710 °C, and the best combination of alloying elements for the threshold stress was 0.1 V-0.1Ti-0.8Mo at the tensile strength of 1000 MPa. Concentrations of weakly trapped diffusive hydrogen and diffusivities of hydrogen were also measured, but their differences among various combinations were small, and no systematic correlations with the threshold stress were found. Charbonnier et al. postulated that a very strong trapping potentiality of fine carbides was beneficial for the SSC resistance [9]. In their experiments, measurements of hydrogen concentration and diffusivity were conducted by means of permeation and vacuum desorption experiments without applying external stress. Then, the trapped states of hydrogen might differ from those in stressed specimens under delayed fracture tests. The tensile strengths of specimens were the same at 1000 MPa, but different tempering temperatures, 700 °C for the 0.1 V-0.1Ti-0.8Mo steel and 660 °C for other steels, might have altered substructures other than precipitates and affected the susceptibility to SSC.

The superior resistance to delayed fracture in a long-term atmospheric exposure was reported for vanadium-bearing martensitic steels tempered at high temperatures [10]. Steels of various compositions ranging 1100–1630 MPa in tensile strength were exposed at seaside up to one year under external stressing. The specimens were circumferentially notched round bars and were applied external stress at yield strengths. The fracture ratio, i.e., the number of failed specimens against the total 60 specimens, was used as a measure of the susceptibility. No failure occurred for a 0.4C-1.2Cr-0.58Mo-0.35 V (mass %) steel tempered at 590 °C, giving 1450 MPa in tensile strength, but effects of vanadium were dependent on tempering temperatures. For a V-bearing steel of 0.3C-1Si-2Cr-0.4Mo-0.35 V (mass %), the fractions of failed specimens were 6.7 % and 63 % for the tensile strengths of 1537 and 1627 MPa by tempering at 510 and 430 °C, respectively. Delayed fracture did not occur for Al-treated 0.2C-0.76Mn-0.64Cr (mass %) martensitic steels tempered at 350 °C and 440 °C for 1303 MPa and 1078 MPa in tensile strength, respectively. A superior resistance to delayed fracture was obtained with a 0.4C-1.2Cr-0.58Mo-0.35 V (mass %) steel of 1450 MPa in tensile strength by tempering at 590 °C [10].

The objective of Yamazaki and Takahashi was to propose a test method to assess the susceptibility to delayed fracture in terms of the critical hydrogen concentration as the parameter. Specimens of the same geometries as those for the atmospheric exposure were hydrogen-precharged by cathodic electrolysis in a 3 % NaCl + 3 g/l CH_4N_2S solution at various current densities of 0.5–10 A/m^2 and Cd-plated so as to give different hydrogen contents. The time to fracture up to 100 h under an applied stress ratio of 0.9 of the tensile strength was measured as a function of the initial hydrogen contents. The critical hydrogen content H_C was defined as the maximum amount of diffusive hydrogen not to cause failure until 100 h. Also, the degree to absorb hydrogen from environments was evaluated in terms of the environmentally absorbed hydrogen content, H_E, defined as the diffusive hydrogen content measured after a cyclic corrosion test (CCT) under mist of 5 % NaCl water. The 1.2Cr-0.58Mo-0.35 V (mass %) steel tempered at 590 °C showed very high H_C and H_E compared with other steels, but a general correspondence between the fracture ratios at atmospheric exposure and H_C or H_E was poor. Instead, Yamazaki and Takahashi found a unique correlation of the fracture ratio with $(H_C - H_E)/H_C$. The 1.2Cr-0.58Mo-0.35 V steel tempered at 590 °C showed a high $(H_C - H_E)/H_C$ value. However, the comparison was made under different applied stresses since the stress ratio was the same for steels of different strength levels. Further, H_E was evaluated without applying external stress. The magnitude of H_E might be different from environmentally absorbed hydrogen in practical situations. Examinations for a wide range of steels and testing conditions are needed for the versatility of the proposed method.

Secondary hardening due to the precipitation of VC at tempering of vanadium-bearing martensitic steels enables to raise the tempering temperature, keeping the same strength. Improvement in the susceptibility to sustained-loading delayed fracture by the precipitation of VC is shown in Fig. 6.22 [11] for 0.37C-0.6Si-1.0Mo-0.5Cr-0.54 V (mass %) martensitic steels tempered at 550 and 650 °C. The precipitation of VC reduced the stress relaxation rate and its enhancement by hydrogen as shown in Fig. 5.5 [11]. It is likely that fine VC precipitates act as barriers to the motion of dislocations and their slip extension coupled with more stabilized structures of martensite by tempering at a higher temperature.

Fig. 8.4 The amounts of tracer-hydrogen introduced to three states of martensitic Mo-V steels tempered at 550 and 650 °C.
(1) Non-loaded,
(2) subjected to delayed fracture tests at 0.4 of the tensile strength,
(3) annealed at 200 °C after delayed fracture tests. □, measured after 15 min after H-charging; ■, measured after keeping at 30 °C for 24 h (Nagumo et al. [11])

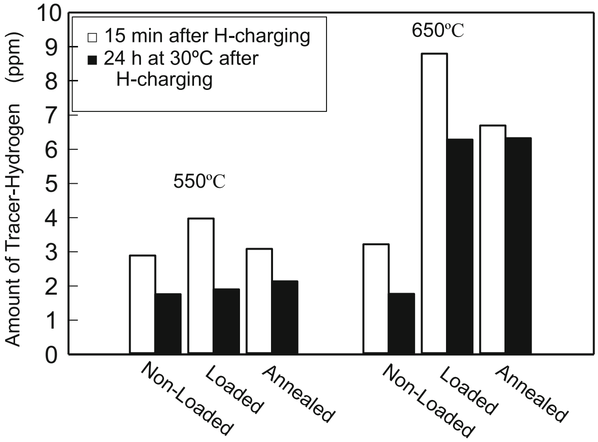

Thermal desorption profiles of hydrogen introduced to the Mo-V steel tempered at different temperatures are shown in Fig. 3.13 indicating that VC acts as strong trap sites. Hydrogen acted as the tracer of defects, and Fig. 8.4 [11] shows the amounts of tracer-hydrogen introduced to specimens subjected to delayed fracture tests. Three conditions of specimens, i.e., without loading, tested for 8 h at 0.4 of the tensile strength, and subsequently annealed at 200 °C, are compared. The open and filled bars in Fig. 8.4 denote measurements after 15 min and 24 h from hydrogen charging, respectively, and the difference between the open and filled bars corresponds to the amount of diffusive tracer-hydrogen.

Figure 8.4 indicates that external stress in the presence of VC enhances the creation of not only weak but also strong trap sites that remain at annealing at 200 °C. The amounts of diffusive hydrogen are similar between the two tempering temperatures, against the presumption that the susceptibility is related to the amount of diffusive hydrogen. Comparison of loaded and annealed conditions for specimens tempered at 650 °C implies that the trap sites of diffusive hydrogen are mostly vacancies, because the trap sites were almost totally lost by annealing. However, limitations of using hydrogen concentration for the assessment of hydrogen embrittlement are to be noticed. The observed total or the average hydrogen concentration per unit volume is not always a measure of the susceptibility to HE since local plastic deformation and thus local trapped states of hydrogen are critical for fracture. A uniform and dense distribution of VC particles should increase the total hydrogen absorption capacity, but strain localization and the local density of weak traps induced by mutual interactions of dislocations might be reduced.

Details of such structural alterations during straining associated with fine precipitates are not definite. Some stress-induced alterations of dislocation arrangements around the precipitates are possible origins of forming strong trap sites and also of stabilizing dislocation arrangements, reducing the stress relaxation rates. Transmission electron microscopic observations of martensitic vanadium-bearing steel during tempering were conducted by Tsuchida et al. referring to hydrogen absorption behaviors [12].

(c) Grain size effects

The term “grain size” of martensitic steels usually addresses prior austenite grain. The austenitizing temperature is often employed as a controlling variable of grain size, but it accompanies compositional alterations of solute elements including impurities in grain boundaries. Apparent effects of grain size on HE in the literature must be carefully examined with respect to alterations of substructures of martensite associated with experimental procedures.

Grain size effects evaluated by fracture mechanics tests have been examined about the crack growth rate and the threshold stress intensity. Hydrogen effects on crack growth are presented in Sect. 6.2. For AISI 4340 steel, the coarser grain size had the lower Stage I crack growth rate and the higher crack growth arrest threshold stress intensity K_{th} [13]. Stage II crack growth rate slightly decreased with increasing grain size. In the experiments, the prior austenite grain size was controlled from 20 μm to 140 μm by varying austenitizing temperatures and holding times. Austenitizations at 1173 K for 1 h and at 1373 K for 16 h also altered the tensile strength of the steel from 1460 MPa to 1230 MPa, whereas the tempering temperature was 300 °C for all specimens. The crack length and the applied stress intensity were calculated from the load *vs.* time record of V-notched double cantilever bend, DCB, specimens under constant displacement. Hydrogen was precharged by cathodic electrolysis in poisoned 4 wt% H_2SO_4 solution at a current density of 60 A/m^2 and was then enclosed by Cd-plating. Figure 8.5 [13] shows Stage I crack growth rates of steels of various grain sizes as a function of the applied stress intensity. The test was a *K*-decreasing type with the crack growth. The results were

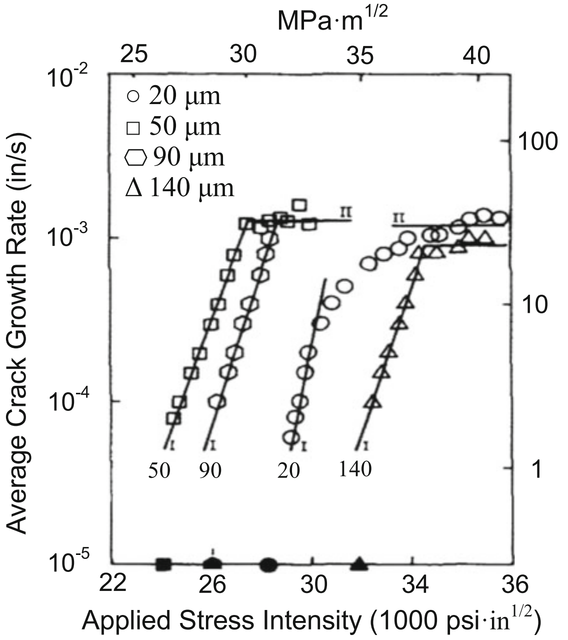

Fig. 8.5 Stage I crack growth rates at DCB tests for hydrogen-precharged AISI 4340 steels of various grain sizes (Lessar et al. [13])

rather complicated. The Stage I crack growth rates at constant applied K were inversely proportional to the square of the grain size. The primary failure mode for all grain sizes was intergranular, but the smaller grain sizes, in general, displayed a greater amount of failure by tear. The crack growth rate of larger grain size materials was lower, while the ductile rupture was less. Lessar and Gerbrich suggested that the crack growth kinetics were affected mostly by a diffusion-limiting process. Increasing grain size above 40 μm raised K_{th}, but the net increase in K_{th} was slight when the decreasing yield stress associated with grain coarsening was taken into account. Lessar and Gerbrich noticed that the primary effect of grain size was on the growth rate rather than K_{th} [13].

Effects of grain size were investigated for fcc superalloy IN903 of a constant yield strength [14]. Grain sizes ranging from 23 to 172 μm were obtained by varying solutionizing temperatures, and double aging was employed to control the yield strengths independent of grain size. Slow crack growth measurements were conducted using bolt-loaded wedge opening loading (WOL) specimens at 298 K in 207 MPa hydrogen gas. The crack growth threshold K_{TH} increased slightly but proportionately to the square root of the grain size. Comparing data for AISI 4340 and IN903, Moody et al. concluded that grain size effects on K_{TH} were the same for the two alloys when IG fracture prevailed [14].

For martensitic steels, impurities substantially affect fracture toughness. Effects of grain size and P-doping on the crack growth rate and the threshold stress intensity K_{TH} for the crack initiation were examined for 0.3C-3.5Ni-1.7Cr (mass %) martensitic steels of the same yield strength of 1275 MPa independent of P-doping and grain size [15]. Austenite grain sizes were varied in the range of 35–450 μm by adjusting austenitizing temperatures. Compact tension (CT) tests were conducted using specimens hydrogen-precharged in hydrogen gas at 300 °C, giving the hydrogen concentration of 1.2×10^{-4} in atomic ratio. Effects of grain size on Stage II crack growth rate were opposite between the P-doped and undoped steels at the same yield strength. For the undoped steel, the larger grain size brought about the lower growth rate and nearly the same K_{TH}. On the contrary for the 0.06 % P-doped steel, the larger grain size brought about the higher Stage II crack growth rate and the lower K_{TH}.

A high purity AISI 4340-type steel ($\mathrm{P} = 0.003$ %) exhibited a substantial reduction in K_{th} with increasing prior austenite grain size when tested in hydrogen gas using bolt-loaded modified WOL specimens at fixed displacement [16]. Hydrogen gas pressure was about 0.1 MPa at room temperature. The magnitudes of K_{th} in the high purity steels were five to six times as large as that for commercial steels tested under the same condition, and the fracture mode was mostly transgranular. Banerji et al. considered that high K_{th} with transgranular fracture mode represented intrinsic effects of hydrogen in this steel and that the low K_{th} with IG fracture mode was the effect of impurity such as P. Banerji et al. then suggested that the austenite grain refinement should be useful as a means to increase the resistance to hydrogen-assisted cracking for high purity steels.

Improvement of the resistance against sulfide stress cracking (SSC) by the refinement of the prior austenite grain size was reported for martensitic steels of 600 to 850 MPa in yield strength [17]. At constant-load delayed fracture tests in a

0.5 % CH_3COOH + 5 % NaCl solution saturated with H_2S at pH of 3.2, the threshold stress for no-failure increased with the yield strength but turned to decrease when the yield strength exceeded a critical value σ_c, indicating involvement of plastic deformation in the effects. Grain refinements shifted σ_c to higher values.

Examinations of grain size effects on tensile properties with respect to strain-induced lattice defects were conducted for martensitic steels in a very fine-grain size range [18]. Plate specimens of 2 mm in thickness and 10 mm in width of a steel 0.36C-0.97Si-0.20Mn-1.0Mo-0.2Cu (mass %) in compositions were repeatedly induction-heated and water-spray quenched to refine the prior austenite grain size in the range of 24 to 4.2 μm and then were followed by tempering at 550 °C to the tensile strength of 1350 MPa. Detection of lattice defects in specimens was conducted by using hydrogen as the tracer. The hydrogen absorption capacity was evaluated by means of TDA of tracer-hydrogen for three states of specimens: as-heat-treated, plastically deformed to 5 % and annealed at 250 °C for 1 h after straining.

Figure 8.6 [18] shows the amounts of tracer-hydrogen in specimens of various grain sizes at the three states. The amounts in the as heat-treated specimens substantially increased with the grain size refinement to less than 10 μm. Plastic deformation remarkably increased the hydrogen absorption capacity in accord with previous results shown in Fig. 3.2 for iron, but the total amount of tracer-hydrogen rather decreased with grain refinement. Subsequent annealing at 250 °C after straining almost totally eliminated the increment due to straining. The results are consistent with Fig. 3.2 and imply that vacancy-type lattice defects are the trap sites of the incremental amounts of tracer-hydrogen due to plastic deformation.

Fig. 8.6 The amounts of tracer-hydrogen introduced to medium carbon martensitic steels with various grain sizes. ○, as-heat-treated; ●, strained to 5 %; Δ, annealed at 250 °C for 1 h after straining (Fuchigami et al. [18])

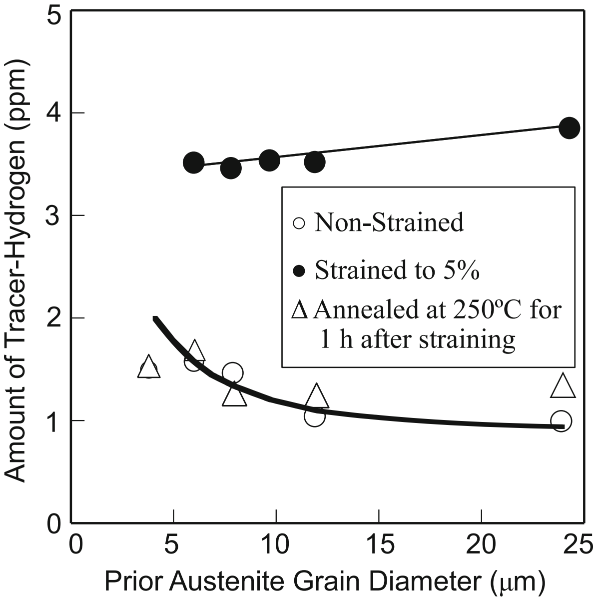

The lower solid line in Fig. 8.6 is the calculated curve of the total hydrogen concentration, C_{TOT}, which is the sum of hydrogen concentrations in prior austenite grain boundaries C_{GB} and that in the matrix C_{M} which includes hydrogen trapped in other lattice defects such as dislocations and martensite lath boundaries. The C_{GB} is the product of the total grain boundary surface area and the hydrogen mass in the unit area of boundaries. Then, C_{TOT} in mass ratio is given as

$$\begin{aligned} C_{\mathrm{TOT}} &= C_{\mathrm{GB}} + C_{\mathrm{M}} \\ &= 2a/\rho\overline{L} + C_{\mathrm{M}}, \end{aligned} \tag{8.1}$$

where a is the hydrogen mass in unit area, ρ is the density of the steel, and $\overline{L}$ is the mean lineal intercept of grains obtained experimentally. The numerical values of a and C_{M} were determined from six combinations of observed C_{TOT} for four grain sizes shown in Fig. 8.6. The fit of the calculated curve with experiments implies that the increase in the hydrogen absorption capacity associated with grain refinement is simply due to the increase in grain boundary surface area when the same hydrogen concentration in unit area was assumed. The estimated values of a corresponded to the site coverage of 0.14 in grain boundary areas when monolayer plane having the same nearest interatomic distance as in the bulk was assumed for boundaries. The magnitude of a less than unity is reasonable, but actual values might be less when the thicknesses of boundaries are taken into account.

An important result of Fig. 8.6 is that the strain-induced increment of the hydrogen absorption capacity is reduced by grain refinement, i.e., the grain refinement suppresses the strain-induced creation of vacancies. Then tensile tests were conducted with specimens with and without hydrogen precharging at the strain rate of $2.8 \times 10^{-5}\ \mathrm{s}^{-1}$. Cathodic hydrogen precharging was conducted under a mild condition in 3 % NaCl aqueous solution containing 3 g/l NH_4SCN at a current density of 10 $\mathrm{A/m^2}$ for 18 h. Since concurrent hydrogen charging was not employed, the tensile tests were conducted under a constant hydrogen concentration in the unit area of grain boundaries. Observed degradations of fracture stress and ductility were expressed in terms of the embrittlement indices, *EI*, defined as the fraction of the decrease in fracture stress σ_f or in reduction of area *RA* in the form of

$$EI_{\sigma_f} = \frac{\sigma_{fA} - \sigma_{fH}}{\sigma_{fA}}, EI_{RA} = \frac{RA_A - RA_H}{RA_A}, \tag{8.2}$$

where subscripts H and A denote specimens with and without hydrogen precharging, respectively.

Figure 8.7 [18] shows the dependence of *EI* on the increment of the amount of tracer-hydrogen with straining to 5 %. Together with the annealing effect shown in Fig. 8.6, the results of Fig. 8.7 imply that effects of grain size refinement on reducing the degradation are due to the decrease in the density of strain-induced vacancy-type defects. Generation of vacancies mostly results from mutual

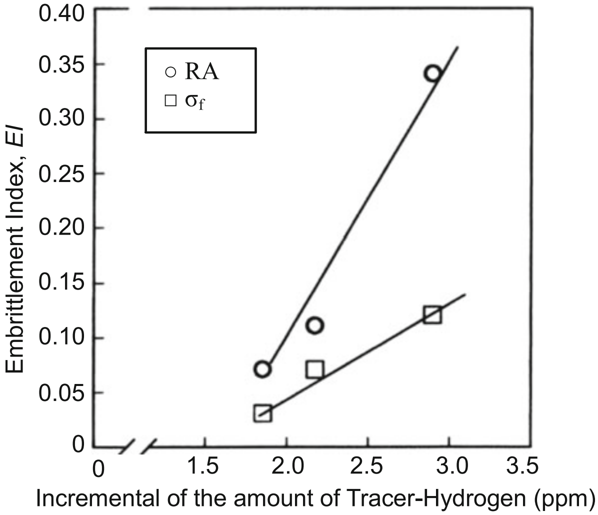

Fig. 8.7 Embrittlement index at tensile tests as a function of the increase in the amounts of tracer-hydrogen by straining to 5% (Fuchigami et al. [18])

interactions of dislocations. Grain refinement may reduce the length of slip and then the densities of dislocations in areas near grain boundaries that impede the slip extension. Correspondingly, the grain size refinement should diminish effects of hydrogen on the fracture morphology. Hydrogen effect to change the fracture mode from dimple to more flat QC was observed for specimens of 24 μm in grain size.

8.2 Impurities and Alloying Elements

Intergranular fracture (IG) is a typical fracture mode for severely embrittled high-strength steels. Temper embrittlement of martensitic steels is enhanced by step-cooling on tempering. It has been well established that step-cooling promotes the segregation of impurity elements mostly of 14th and 15th groups such as P, As, Sb, Sn in the periodic table. Hydrogen accumulates along grain boundaries as tritium autoradiography shows in Fig. 2.12, but the decrease in the Charpy impact fracture toughness that characterizes temper embrittlement does not appear in the case of hydrogen embrittlement (HE). Origins of IG fracture mode in temper embrittlement and HE are not certain to be identical. A cooperative relation between temper embrittlement and HE has been a subject of extensive studies as reviewed by McMahon [19].

The enhanced susceptibility to HE by temper embrittlement was demonstrated in delayed fracture tests of a HY 130 steel (0.1C-0.9Mn-0.35Si-5Ni-0.5Cr-0.5Mo-0.08 V in mass % and 900 MPa in the yield stress) in 0.1 N H_2SO_4 with As_2O_5 using edge-notched cantilever specimens [20] as described in Sect. 7.1(e). Step-cooling drastically decreased the lowest applied stress intensity, i.e., the threshold to cause fracture, from that of unembrittled specimens. The threshold stress intensity normalized by the fracture toughness in air was much lower for step-cooled specimens than that for unembrittled ones. Then, a cooperative function of hydrogen and temper embrittlement was concluded, taking into account a decrease of the initial stress intensity by temper embrittlement.

Effects of impurities were extensively examined by fracture mechanics tests for a 0.3C-3.5Ni-1.7Cr (mass %) steel doped with P, Sn, or Sb [21]. Grain boundary concentrations C_{gb} of impurity elements were controlled by varying the aging time at 480 °C on tempering and were estimated by means of Auger electron spectroscopy (AES). The threshold stress intensity K_{TH} for the first detectable crack extension at compact tension tests using precracked specimens and the threshold stress σ_{TH} for microcrack formation at four-point bend tests using notched specimens were measured. Both K_{TH} and σ_{TH} decreased with increasing C_{gb} of impurity elements for tests in air and 0.17 MPa hydrogen gas. Significant effects of hydrogen in reducing both K_{TH} and σ_{TH} appeared in partially embrittled specimens, but hydrogen effects were smaller for lower K_{TH} and σ_{TH} levels. The results are indicative of the presence of some limited plasticity in order that hydrogen-induced embrittlement plays a role.

Impurity elements play the primary role in temper embrittlement of steels, but common alloying elements Mn and Si also affect the susceptibility to HE [22]. Modified WOL tests were conducted for HY 130 steel in hydrogen gas of 0.21 MPa at room temperature. The threshold stress intensity K_{TH}, defined as the crack initiation on loading, decreased by step-cooling at 480 °C on tempering. The degradation was much smaller for a steel of very low Mn (0.02 %) and Si (0.03 %) contents than steels of standard compositions. Four-point bend tests in air and hydrogen gas were also conducted using notched specimens. A steel of the standard compositions and step-cooled at 480 °C for 1000 h exhibited a more prominent decrease in the fracture stress when tested in hydrogen gas than in air. Observations of the crack path revealed that the crack initiated along plastic hinges or slip lines for the pure steel with reduced Mn and Si. The extent of plastic region was diminished, and IG fracture mode prevailed by step-cooling for steels of standard compositions.

Effects of Mn and Si as well as P and S on the susceptibility to HE were extensively examined using modified WOL precracked specimens for AISI 4340-type steels of various combinations of Mn and Si contents [23]. The K_{th} values at the crack arrest in 0.11 MPa hydrogen gas exhibited a linear decrease against a parameter [Mn + 0.5Si + S + P (mass %)] up to 0.2. The decrease in K_{th} was associated with the increase in the area fraction of IG surface. Further, K_{th} values of commercial and high purity steels in various hydrogen gas pressures were plotted uniquely on a single curve against a parameter $[10^4 C_{\text{H}}]$ + [Mn + 0.5Si + S + P in mass %]. The hydrogen concentration C_{H} was evaluated according to Sieverts' law and the accumulation in the stress field ahead of the precrack using Eq. (1.10). Bandyopadhyay et al. claimed that the hydrogen and metalloid impurities additively operate for intergranular cohesion and that the function of Mn and Si is to control the segregation of P and S in austenite grain boundaries [23].

A cooperative function of P and Mn was observed for the threshold stress for no-failure on SSC tests of martensitic steels presented in Sect. 8.1(c) [17]. The

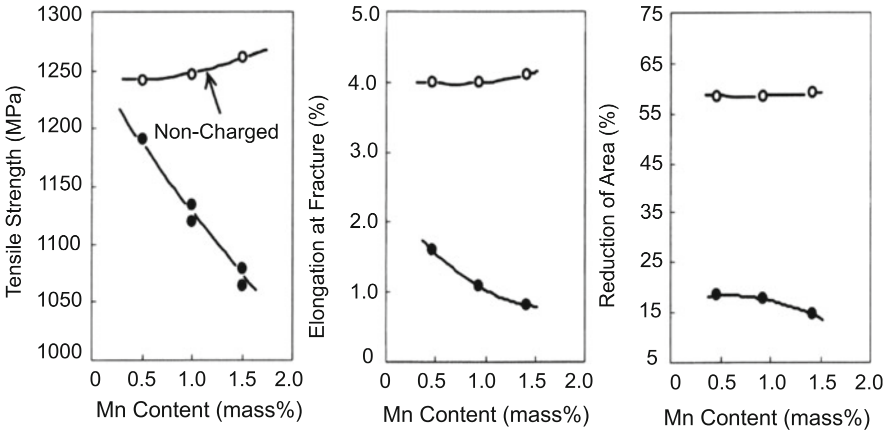

Fig. 8.8 Tensile properties of medium carbon martensitic steels with different Mn contents with/without hydrogen charging (Nagumo et al. [24])

threshold stress decreased with increasing P contents, and the decrease at a constant P content was pronounced with increased Mn contents. The yield strengths were almost the same, ~745 MPa, but the fracture surface changed from transgranular to partially IG associated with the decrease in the threshold stress.

Enhancement of IG fracture by hydrogen at tensile tests of medium carbon Cr-Mo martensitic steels containing different amounts of Mn are shown in Figs. 7.6, 7.7, 7.8 and 7.9 in Sect. 7.1(e). The fracture mode was mostly IG, and the higher Mn contents caused the smoother fracture surfaces and reduced accompanying fine tear patterns. Tensile test results under concurrent hydrogen charging are shown in Fig. 8.8 [24]. The Mn contents did not affect tensile properties when hydrogen was not present, but the fracture stress and tensile ductility decreased with increasing Mn contents in the presence of hydrogen, in accord with other studies on K_{th} for AISI 4340 steel [23].

On the other hand, high Mn contents pronounced the increase in the hydrogen absorption capacity after straining as shown in Fig. 7.8. The vacancy-type nature of the trap sites was revealed by TDA as shown in Fig. 7.9. The increase in the density of strain-induced trap sites is apparently against the reduction of plasticity that appeared on the fracture surface. However, the results are plausible when extremely localized strain in regions near prior austenite grain boundaries intensifies accumulation of damage, there leading to premature fracture. Constraint for slip extension across grain boundaries favors the creation of strain-induced vacancies as the result of mutual interactions of dislocations. The microstructural entity of Mn operating for strain localization is not definite quantitatively, but Mn likely affects structural factors such as impurity segregation and precipitation of carbides in grain boundaries, as suggested in preceding studies.

Boron is a unique element that intensifies the hardenability of steels with contents as low as ppm by segregating at austenite grain boundary. The states of B in steels are controlled by other alloying elements and thermal histories since B

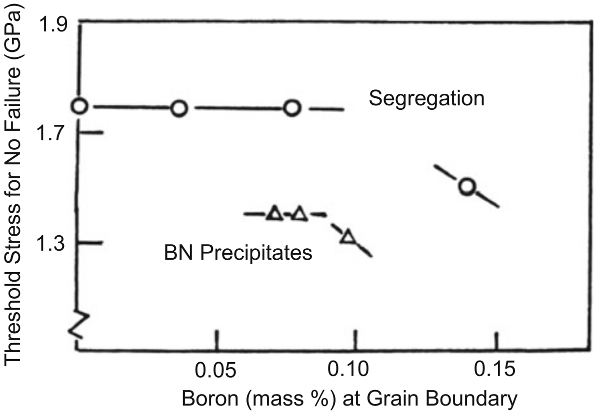

Fig. 8.9 Threshold stress for no-failure at delayed fracture for B-containing martensitic steels as a function of B concentrations at prior austenite grain boundaries. Segregation boron and BN precipitates are separated by Auger electron spectroscopy (Inoue et al. [26])

combines with nitrogen forming fine BN. Effects of B on HE was examined at delayed fracture tests for 0.15%C-Si-Mn (mass %) martensitic steels containing different amounts of B and N [25]. Two-step austenitization was occasionally employed in order to fix B as fine BN precipitates in the matrix. Constant-load delayed fracture tests were conducted using cantilever bend notched specimens under cathodic electrolysis in a 3 % NaCl solution at current densities of 2 ~ 10 A/m^2. The fracture mode was mostly IG, and Auger electron spectroscopy (AES) on the IG fracture surface revealed peaks due to B and BN separately. The threshold stresses for delayed fracture are shown in Fig. 8.9 [26] as a function of B concentrations at grain boundaries calculated from AES peak heights. The concentrations of B at grain boundaries were substantial, but segregated B was not harmful when its amount was limited. On the other hand, fine precipitates of BN at grain boundaries remarkably decreased the threshold stress. Addition of Ti to fix N as TiN and a two-step austenitization to precipitate BN in the matrix are useful means to suppress detrimental effects associated with B addition.

8.3 Heterogeneous Phases

The proper design of multiphase microstructures is an effective means to improve the strength and toughness of steels, and the susceptibility to HE is an item to be added for assessing the practical performance of such microstructures. Ferrite-martensite dual phase (DP) steels of (0.03–0.1) C-0.2Si-0.5Mn-0.5Mo (mass %) in compositions containing martensite of 5–45 % in volume fraction were prepared by brine quenching from the intercritical temperature region between 760 and 840 °C [27]. The tensile strengths of the steels increased from about 400 MPa to 900 MPa with increasing martensite volume fractions accompanying a decrease in ferrite grain size and an increase in martensite region size. The susceptibility to HE was evaluated by means of tensile tests using specimens hydrogen-charged in

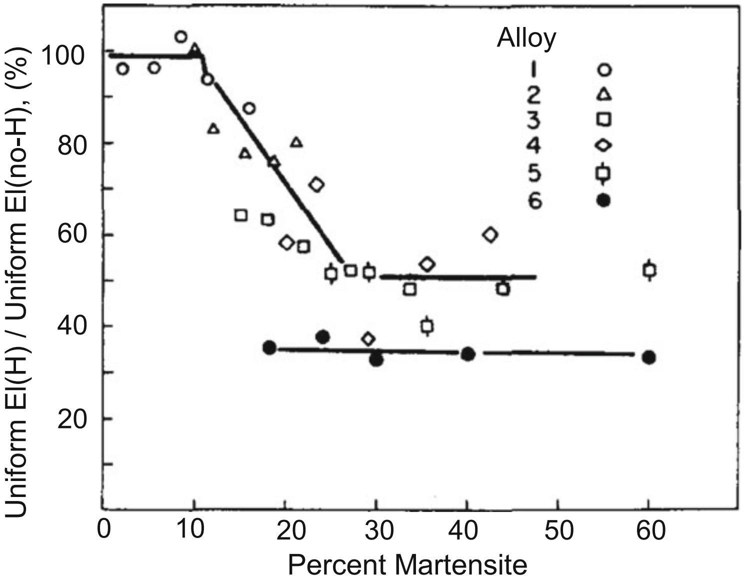

Fig. 8.10 Ratios of uniform elongations at tensile tests with/without hydrogen charging for ferrite-martensite dual phase steels. Alloys 1–5 contain about 0.5 % Mn and 0.5 % Mo, alloy 6 contains 1.46 % Mn and 0.08%V without Mo. Alloy #6 (●) is a commercial dual phase steel (Davies [27])

poisoned 4 % H_2SO_4 at a current density of 60 A/m^2. The ratio of the uniform elongation of specimens with and without hydrogen charging showed three ranges as shown in Fig. 8.10 [27]: (1) no embrittlement up to 10 % martensite, (2) advancing embrittlement from 10 to 30 %, (3) essentially independent of martensite contents above 30 %. Martensite regions were all at grain boundaries of ferrite. The regions were separated in the steels containing martensite up to 10 % but tended to form a network over the range of 10 to about 30 % with decreasing ferrite grain size and increasing martensite region size. Martensite likely acts as the easy path for crack propagation. Effects of martensite volume fraction differed by compositions of steel. As included in Fig. 8.10, a commercial DP steel of 0.1C-1.5Mn-0.55Si-0.08 V (mass %) in compositions with fine ferrite grain size of 3–5 μm showed a constant but lower susceptibility to HE than other steels, whereas the increase in the volume fraction of martensite from 20 to 40 % in the DP steel raised the tensile strength from 800 to 1100 MPa. The estimated carbon content in the martensite for the experiments was more than 0.2 %.

A similar study for HE for a ferrite-martensite DP steel containing about 18 % martensite revealed that the reduced tensile ductility by hydrogen was retrieved with increasing tempering temperatures and almost totally at 500 °C [28]. The tensile fracture surface of hydrogen-charged specimens exhibited cleavage-like transgranular facets of a scale much larger than martensite islands. Martensite regions are likely nucleation sites of cracks, but their existence also serves to prepare the easy crack path in neighboring ferrite grains in the presence of hydrogen. The no-failure critical stress for delayed fracture decreased by the presence of martensite, but it was above the macroscopic yield stress. It was then concluded that high carbon martensite is responsible to HE of dual phase steels, but considerable macroscopic deformation is involved in failure.

Details of deformation microstructures are presented in Sect. 7.3.1 about the creation of damage during plastic deformation for another ferrite-martensite DP steel with the martensite volume fraction of 55 % [29]. A substantial decrease in the total elongation by hydrogen charging appeared on tensile tests. Cracking of martensite took place in the early stage of failure for both hydrogen-charged and uncharged specimens, but effects of hydrogen was apparent in late stages of deformation. In hydrogen-charged specimens, the crack propagated along the prior austenite grain boundaries through a few neighboring ferrite grains associated with increased local orientation changes around the crack tip. When hydrogen was not present, the crack propagation inside the ferrite grains was not observed. The observations are consistent with earlier studies [27], [27] and suggest a cooperative function of martensite and ferrite in hydrogen-related changes of deformation microstructures. Fracture surfaces showed both dimple and brittle features. Hydrogen charging increased the size of brittle feature regions, but large brittle feature regions contained a considerable number of voids and dimples.

In martensitic or lower bainitic steels, some fractions of retained austenite γ_R often exist in the form of thin films along lath boundaries. The hydrogen absorption capacity of the steels increases with the amount of γ_R presumably due to a high solubility of hydrogen in austenite and to trapping of hydrogen at the γ_R/matrix interface [30]. Contradictory reports are found for the effects of γ_R on the susceptibility to HE. Some studies on HE of bainite-martensite DP steels [31] or transformation-induced plasticity (TRIP) steels [32] showed a superior resistance to delayed fracture or tensile elongation in the presence of γ_R compared with fully martensitic steels. On the other hand, comparisons of steels of different compositions showed that threshold strengths for no-failure in delayed fracture tests were lower for steels containing higher amount of γ_R [33]. Retained austenite partially decomposes when stress is applied. It has been often postulated that hydrogen ejected from γ_R associated with the decomposition enriches the local hydrogen concentration and promotes the crack nucleation and growth. However, the susceptibility to HE is affected by various factors. In the latter study [33], the contents of Mn, Si and P were different among steels and likely contributed the delayed fracture test results in addition to γ_R.

Suppression of IG fracture is a prospective means to reduce the susceptibility to HE for high-strength steels, and precipitation of proeutectoid ferrite along austenite grain boundaries has been attempted according to this notion [34]. Proeutectoid ferrite of 3.5 ~ 8.4 % in areal fraction on micrograph was precipitated in medium carbon martensitic steels by isothermal holding at intermediate temperatures during quenching from the austenitizing temperature. Tensile strengths were fixed at almost the same level of about 1300 MPa by varying tempering temperatures between 623 and 693 K. Sustained-loading delayed fracture tests were conducted

Fig. 8.11 Delayed fracture diagrams of high-strength martensitic steels. Solid and open marks denote steels with and without intergranular ferrite precipitation (Watanabe et al. [34])

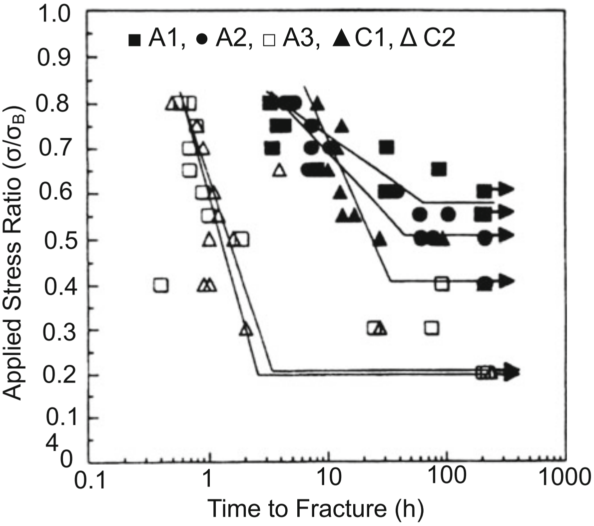

Fig. 8.12 Mean hydrogen occlusion rates per hour at sustained-loading delayed fracture tests at the applied stress of 0.8 of the tensile strength. Areal fractions of proeutectoid ferrite are 3.5, 8.4 and 0 % for A1, A2 and A3 steels, respectively (Watanabe et al. [34])

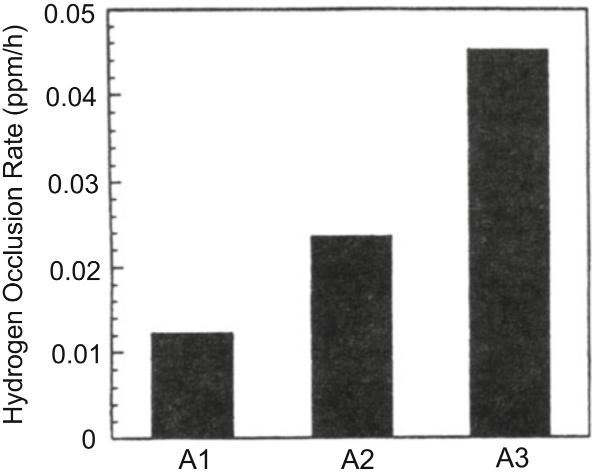

by immersing round bar specimens of 5 mm in diameter in 20 % NH_4SCN aqueous solution at 323 K. Figure 8.11 [34] shows for comparison tests results in which open marks denote steels without proeutectoid ferrite.

The presence of proeutectoid ferrite markedly improved delayed fracture characteristics. The IG fracture that appeared near the crack initiation site for fully martensitic steels was absent by the precipitation of proeutectoid ferrite, and IG was replaced by QC fracture mode. Proeutectoid ferrite increased the hydrogen absorption capacity, but the amounts of hydrogen at the time of fracture were not systematically correlated with delayed fracture characteristics for different steels even under the same applied stress. On the other hand, the mean hydrogen occlusion rates, defined as the hydrogen content in a failure specimen divided by the time to fracture, are shown in Fig. 8.12 [34] at the applied stress of 0.8 of the tensile strength. The time to fracture at a given applied stress substantially scattered, but the no-failure threshold stresses shown in Fig. 8.11 correlated well with the mean hydrogen occlusion rates. The hydrogen content corresponds to that of lattice defects that operate as trap sites of hydrogen. Since most hydrogen in failure specimens is diffusive and vacancies are major trap sites of increased hydrogen contents by straining, the hydrogen occlusion rate likely represents the ease of vacancy creation due to interactions between dislocations near grain boundaries. Local situations are difficult to estimate from thermal desorption analysis (TDA), but proeutectoid ferrite likely lowers the density of dislocations near grain boundaries.

8.4 Phase Stability and Deformation Microstructures of Austenitic Stainless Steels

Austenitic (γ-) stainless steels are an important group of steels with high corrosion and heat resistances. Basic behaviors of hydrogen in γ-steels are substantially different from those in ferritic steels as described in Sect. 1.1 on solubility and in Sect. 4.1 on diffusivity. Coupling of compositional and crystal-structural effects gives some specific situations for HE of high alloyed austenitic steels. An important notice is that the hydrogen distribution is often very inhomogeneous in γ-stainless steels due to the very low diffusivity of hydrogen at room temperature. On cathodic hydrogen charging to Type 310 stainless steel (21Ni-23Cr-2Mn-1Si in mass %) in 1 N H_2SO_4 with arsenic at a current density of 1000 A/m^2, the estimated hydrogen concentration in the near-surface layers amounted to 0.5 ~ 0.8 in H/M atomic ratio [35].

8.4.1 Hydrides and Phase Changes

Three types of hydrides have been reported on hydrogen charging to Ni-containing γ-stainless steels, β- and β'- phases of face-centered cubic (fcc) structures and η-phase of a hexagonal close-packed (hcp) structure [36]. The η-phase is also denoted as ε' since η is the phase with the lattice constant some percent larger than that of ε-martensite. Hydrides are formed when hydrogen concentration is high enough, and Fig. 8.13 [37] shows X-ray diffraction patterns of Type 304 steel specimens of 0.8 mm in thickness cathodic hydrogen-charged in poisoned 1 N H_2SO_4 at current densities of 100 ~ 1000 A/m^2 at 20 °C. At an early stage of charging, ε' and an fcc Y-phase appeared. With increasing the charging time, Y-phase disappeared and ε' decomposed into body-centered tetragonal α'-martensite and ε phases. The lattice constant of ε' is almost constant, implying that ε' is a hydride, whereas that of ε was larger than that of ε formed on cooling or straining. Hydrogen charging at 60 °C

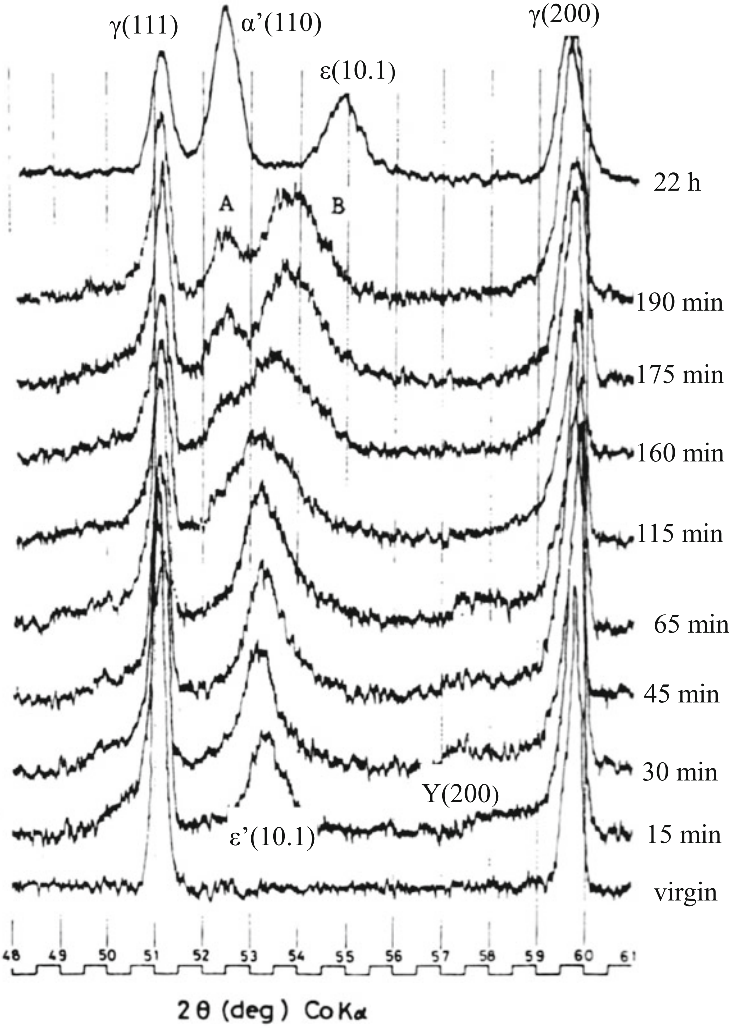

Fig. 8.13 Change in X-ray diffraction patterns with the progress of hydrogen charging at 20 °C into Type 304 γ-stainless steel sheet (Kamachi [37])

induced two fcc phases instead of Y, likely corresponding to β and β'. The phase separation into ε' and fcc γ'-phase from γ was also reported for Type 310S steel when hydrogen concentration was 18 and 25 at.% at 35 °C and 75 °C, respectively [38]. The Y-phase reported by Kamachi [37] may correspond to γ'-phase reported by Ulmer and Altstetter [38].

The presence of α' which is susceptible to HE is an issue as the origin of HE of unstable γ-stainless steels as described in the following Sect. 8.4.2. Crack path associated with α' is often observed in failure specimens. In this respect, an

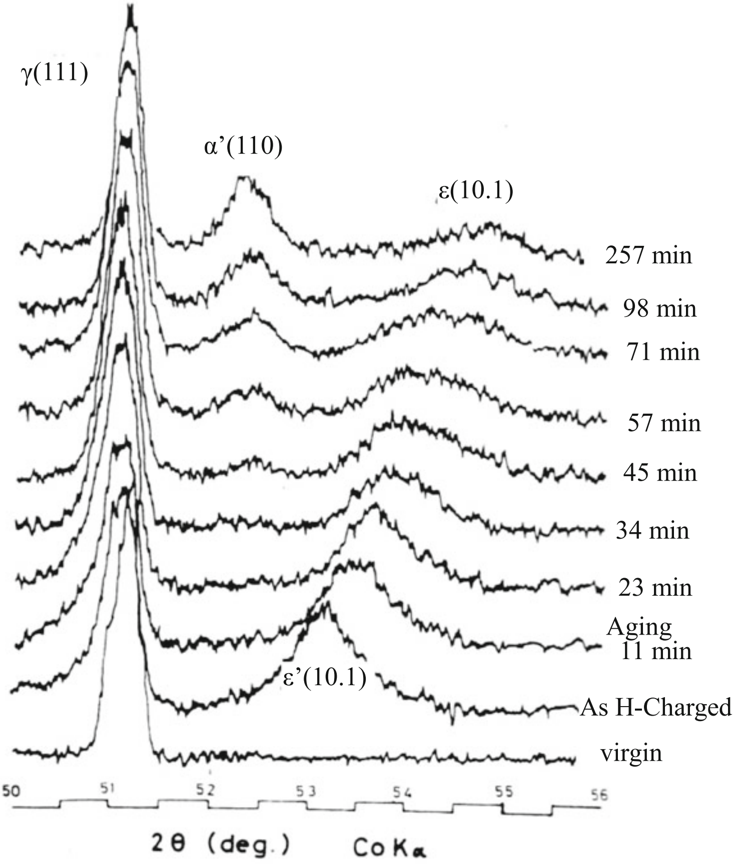

Fig. 8.14 Change in X-ray diffraction patterns from hydrogen-charged Type 304 γ-stainless steel during aging at room temperature (Kamachi [37])

important finding is the reversible phase change of ε' to α' and ε during aging at room temperature as shown in Fig. 8.14 [37]. Simultaneously conducted transmission electron microscopy observations revealed the formation of band-like α' within ε [37]. A similar formation of α' together with γ' and ε' was reported by Narita et al. during aging hydrogen-charged Type 304 [39]. The formed α' disappeared when hydrogen was recharged, indicating that α' and ε are reversible. The fact implies that an observed crack path through or along α' might be actually through or along ε at the time of crack extension. For Type 310S the formation of α' was not observed both at hydrogen charging and outgassing.

The driving force of hydrogen-induced phase changes has been ascribed to two different functions of hydrogen. The one is the stress-induced effects due to a large lattice expansion associated with solute hydrogen. The evolution of stress induced by the entry of hydrogen appeared as the formation of fine surface cracks associated with shrinkage on degassing hydrogen-charged Types 304 and 310S [39]. Very high concentrations of hydrogen favor such situations to take place. In this case, the stress-induced phase change is not expected for Type 310 because the deformation-induced martensite start temperature, M_d, is well below room temperature.

Alternatively, some intrinsic effects of hydrogen on the thermodynamic stability of γ-phase have been discussed [40]. In analogy to other interstitial solute atoms such as carbon and nitrogen, hydrogen was assumed to stabilize γ-phase, retarding the transformation to martensite. Some observations such as the larger amount of retained austenite associated with the higher hydrogen content were in accord with the notion. However, no effects of hydrogen were observed for the martensite start temperature, M_s, of Fe-30Ni alloy for hydrogen up to 400 at. ppm [41]. Also, volume fractions of deformation-induced α' and ε in Type 304 L [41], and of α' in Types 301 and 310S [42] were not affected by hydrogen.

Narita et al. postulated that hydrogen stabilizes ε [39]. Since hcp ε-phase may form as the result of the motion of partial dislocations leaving arrays of stacking faults, increases in M_S and M_d are feasible if hydrogen lowers the stacking fault energy. However, reported hydrogen effects are not always consistent. Hydrogen effects on γ-steels are affected by experimental conditions such as hydrogen concentration, temperature and specimen thickness. Careful examinations are necessary for employed experimental procedures.

8.4.2 Compositional Effects on Hydrogen Embrittlement

The susceptibilities to HE of γ-stainless steels vary by the type of steels. Figure 8.15 [43] shows tensile test results of Types 304 and 310 steels under hydrogen charging following precharging to about 12 mass ppm. Unnotched smooth plate specimens of 0.1 mm in thickness were cathodic hydrogen-charged in poisoned 0.5 N H_2SO_4 at current densities ranging from 0 to 300 A/m^2. The yield stress was not affected by hydrogen, whereas the elongation to fracture and the area under the tensile stress-strain curve decreased with increasing current densities. The degradation appeared for both steels but more pronouncedly for Type 304 steel.

The stability of γ-stainless steels against martensite transformation is a crucial factor for HE. Effects of test temperatures and nickel contents on hydrogen degradation are shown in Fig. 8.16 [44] for three steels containing 18 % Cr and different nickel contents. The contours in Fig. 8.16 show equal fracture strain in percent. The filled marks and the region under the dotted line indicate the presence of α' after the test. The region of significant degradation overlaps, though not exactly, that of α' formation.

The specification of a type of steels admits certain compositional ranges. Table 8.1 shows chemical compositions of two Type 304 steels. Steel B is slightly more stable than Steel A against the deformation-induced α'-transformation according to magnetic measurements [42]. Susceptibilities to HE differed between the two steels. Hydrogen effects on the threshold stress intensity K_{TH} for the crack initiation and the crack growth rate were measured using single-edge-notched

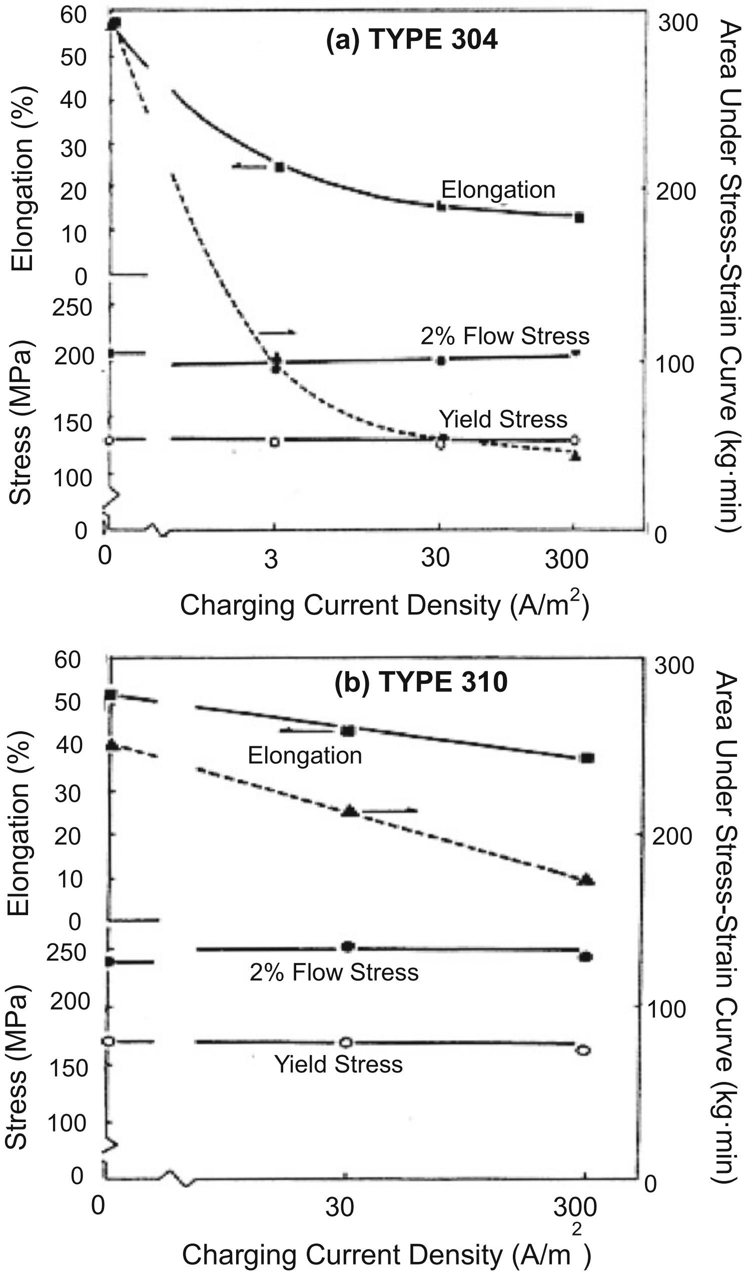

Fig. 8.15 Tensile properties of Type 304 and Type 310 steels under hydrogen charging at various current densities (Inoue et al. [43])

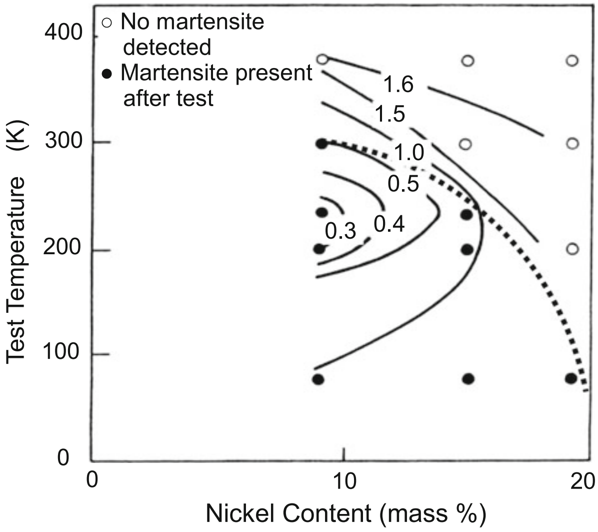

Fig. 8.16 Isoductility diagram for hydrogen-charged Fe-Cr-Ni alloys. Contours show equal values of plastic strain (Caskey Jr. [44])

Table 8.1 Chemical compositions of two Type 304 stainless steel (in mass %) (Singh et al. [42])

Alloy	C	N	Cr	Ni	Mn	Si	Mo	Cu
A	0.061	0.041	18.0	8.54	1.72	0.58	0.18	0.28
B	0.061	0.027	18.2	9.42	1.33	0.59	0.14	0.26

specimens under constant load at room temperature. Hydrogen up to 50 mass ppm was precharged uniformly by cathodic electrolysis in a molten salt bath at 280 °C. The K_{TH} decreased with increasing hydrogen contents, but K_{TH} was higher and Stage II crack growth rate was lower for steel B than steel A at the same hydrogen contents. However, the amounts of deformation-induced α' were not affected by hydrogen for these steels. It may suggest that the stability of γ-phase is crucial to HE, but the effect is not necessarily due to the formation of α'-martensite.

The susceptibility to HE of stainless steels is also affected by thermal histories. Sensitization, i.e., isothermal heat treatments in the temperature range between 773 and 1123 K, enhances intergranular corrosion and stress corrosion cracking of γ-stainless steels. It is caused by the precipitation of chromium carbides at grain boundaries resulting in depletions of Cr and C around the precipitates. Enhanced susceptibilities to HE by sensitization were reported for Type 304 steels [42]. On delayed fracture tests using smooth bar tensile specimens under cathodic hydrogen charging, the lowest applied stress to cause delayed fracture decreased by the sensitization associated with IG fracture mode.

Susceptibilities to HE on tensile tests of various γ-stainless steels at low temperatures in 1 MPa hydrogen and He gases are shown in Fig. 8.17 [45] in terms of the ratio of the reduction of area in the two environments. Notations (S) and (SD) in Fig. 8.17 respectively indicate “sensitized” and “desensitized” by annealing at

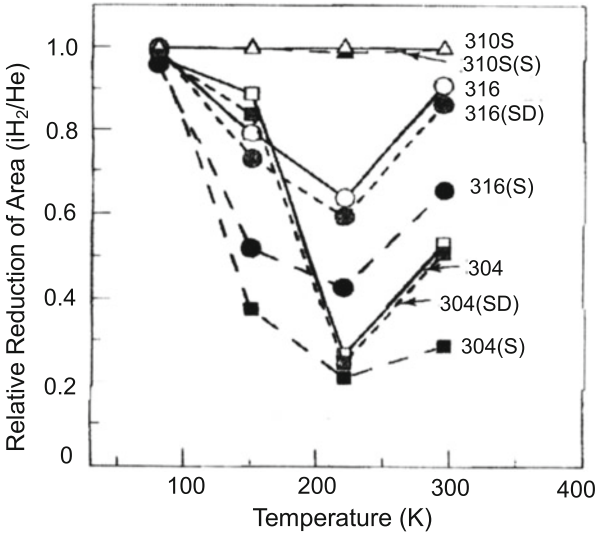

Fig. 8.17 Temperature dependencies of the susceptibility to hydrogen embrittlement of sensitized (S) and desensitized (SD) γ-stainless steels. The susceptibility to hydrogen embrittlement is expressed in terms of the ratio of reduction of areas in H_2 and He gas environments (Han et al. [45])

1193 K for 8 h. The maximum degradation by hydrogen occurred at around 220 K and the degradation was larger for Type 304 than Type 316. However, further degradations by sensitization and its recovery by desensitization were more significant for Type 316 than Type 304. Fracture modes were IG for sensitized and QC for desensitized specimens for both Type 304 and Type 316 steels. Transmission electron microscopy revealed $Cr_{23}C_6$ and α' along grain boundaries in sensitized Type 304. For desensitized specimens, discontinuous carbides along grain boundaries still existed, but no α' was identified. Fractographic features of sensitized and desensitized specimens are described in following Sect. 8.4.3.

In Fig. 8.17, stable Type 310S did not exhibit HE. Type 309S (0.06C-14Ni-23Cr in mass %) was also stable without showing degradation at tensile tests in 69 MPa hydrogen gas at room temperature [46]. However, thermal hydrogen precharging to 425 at. ppm, about six times as large as the solid solubility, lowered the reduction of area from 45 % to 27 % and from 43 % to 30 % at notched-tensile tests for normal and sensitized specimens, respectively [46]. The sensitizing heat treatment was at 975 K for 15 or 300 min. The relative reductions by hydrogen were almost the same for normal and sensitized specimens. It implies no cooperative effects between hydrogen and the sensitization for Type 309S.

Strain-induced α' has been often postulated to play the primary role in HE of unstable γ-stainless steels. Actually, a unique correlation between the susceptibilities to HE and the amounts of deformation-induced α' on tensile fracture surfaces was shown for Types 304, 316 and 316 L steels tested in high pressure 90 MPa hydrogen gas at -45 ~ 85 °C [47]. However, contrary findings that the larger amounts of α' introduced by prestraining reduced more pronouncedly slow crack growth rates were reported for Type 301 (6 ~ 8Ni-16 ~ 18Cr) steel [48]. For the experiments, prestrain was given by rolling to 30 % in the reduction of thickness either at room temperature and 110 °C. The amounts of α' were respectively 57 and 0.5 % at the two temperatures. Increased amount of α' elevated the threshold stress intensity K_{TH} for the crack initiation and reduced Stage II crack growth rate at sustained-loading tests in 108 kPa hydrogen. The results are against the notion that α' provides a favorable crack path. On the other hand, the suppression of martensite transformation by prestraining is well known. The reduced susceptibility by prestraining will be feasible if alterations of microstructures of γ-phase preceding the martensite transformation are suppressed by prestraining and if dislocation dynamics associated with martensite transformation, rather than martensite itself, are crucial for causing embrittlement.

Compositional effects appear in deformation microstructures and are described in Sect. 8.4.4.

8.4.3 Fractographic Features

Fractographic features of hydrogen-degraded γ-stainless steels are quite similar to those of ferritic steels stated in Sect. 7.1, such as fine dimple size on hydrogen-charged and tensile-fractured Type 309S [47], striations on facets in transgranular fracture surfaces of severely hydrogen-charged and tensile-fractured Type 316 steel [49]. Facets containing slip lines that correspond to {111} planes were observed for hydrogen-charged and tensile-fractured Type 310S steel specimens [37]. Facets are likely due to cracking along grain or twin boundaries. Cracks at intersections of slip bands were observed on the side surface of tensile-fractured Type 304 steel specimens containing about 10 at. ppm hydrogen [37]. Quasi-cleavage (QC) appeared at slow elongation-rate tests of Type 301 steel in 108 kPa hydrogen gas at room temperature, and the fraction of QC decreased and fine dimples increased as the test temperature was raised [50]. Transgranular QC surfaces associated with secondary cracks were also reported on slow crack growth regions of hydrogen-charged Type 304 steel [51]. Tensile fracture surfaces of Type 304 steel specimens used for Figs. 7.13, 7.14, 7.16 and 7.17 are shown in Fig. 8.18 [52]. Hydrogen of 30 ~ 35 mass ppm was uniformly charged. Coarse dimples for the hydrogen-free specimen changed to mixture of fine dimples, QC and facets for the hydrogen-charged specimen.

Hydrogen degradation appears even for stable Type 310 steels without forming α' as shown in Fig. 8.15, but the enhanced embrittlement associated with the instability of γ-stainless steels has been ascribed often to strain-induced α'. Enhanced degradation by sensitization is an example that claimed the role of α'. In fact, strain-induced α' was observed along grain boundaries for sensitized Type 304. However, a substantial degradation by hydrogen still occurred for desensitized specimens while no α' was observed at grain boundaries. It indicates that α' is not essential for the large hydrogen degradation of Type 304 at 220 K.

The fracture mode of sensitized specimens was macroscopically IG accompanying secondary cracks vertical to the fracture surface along grain boundaries for

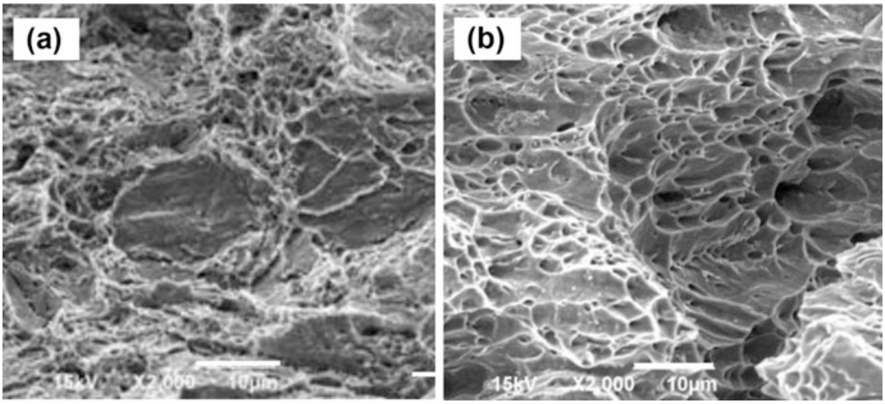

Fig. 8.18 Tensile fracture surfaces of Type 304 stainless steel (**a**) with and (**b**) without hydrogen charging (Hatano et al. [52])

both Types 316 and Type 304 and in both helium and hydrogen gases [45]. Close examinations of IG fracture surfaces revealed that macroscopically IG surfaces were not quite smooth with different morphologies depending on steels and environments. Microvoid coalescence (MVC) covered IG-like surfaces of both Types 304 and 316 when tested in helium. In hydrogen gas, dimples on IG-like surfaces of sensitized Type 304 were extremely fine and the apparent surfaces were brittle-like.

Very fine dimples on IG surfaces are ascribed to the increase in the nucleation sites of fine voids. Desensitization of sensitized steels hardly changed MVC fracture mode in helium gas, but it changed IG to QC in hydrogen gas for both Types 316 and 304. The change from MVC in helium to QC in hydrogen also appeared on transgranular fracture surfaces of solution-treated specimens. Promotion of the nucleation of voids and their premature coalescence associated with plastic deformation are possibly the essential function of hydrogen common to both sensitized and desensitized specimens. Compositional effects are to be examined with respect to deformation microstructures in γ-phase.

8.4.4 Deformation Microstructures

Besides the high susceptibility to HE of strain-induced α', deformation microstructures in γ-phase are important factors for degradation. Transmission electron microscopy (TEM) is a powerful tool to reveal deformation microstructures associated with the crack propagation that constructs fracture surface. A high density of dislocations and the formation of ε and α' martensite were observed near the crack tip in Type 304 and Type 310 steel specimens tensile strained under cathodic hydrogen charging [43]. The formation of stacking fault and ε-martensite was enhanced with increasing current densities, and the crack path was mainly along the interface between γ and ε phases. The crack propagation along the interface between γ and ε phases was also reported using high-voltage TEM for Type 304 steel specimens tensile strained after cathodic hydrogen precharging [53].

As for α' produced at the transformation, Debye rings of selected area diffraction (SAD) from Type 304 steel foils tensile fractured in an environmental cell of 108 kPa hydrogen gas showed completely α-phase in front of the crack tip and along the crack [54]. The finding suggested that α-phase was the precursor of crack extension. Narita and Birnbaum pointed out two possible hydrogen effects, the increase in M_d temperature favoring transformation to α' and enhanced plasticity at the crack tip. However, more stable Type 310 also showed SAD patterns consisting of Debye rings characteristic of a very fine-grain γ-phase at the crack tip and along the crack.

On the other hand, stacking fault and ε-martensite are sites along which strain localization and associated damage accumulation preferentially take place. Accumulation of damage is the precursor of the crack nucleation and growth as described in Sect. 7.3. Deformation-induced deterioration of crystallinity along grain and annealing-twin boundaries and the void nucleation at intersections of deformation bands with obstacles in γ-stainless steels [52] are described in Sect. 7.3.1. Crack propagation along twin boundaries was also revealed for hydrogen-assisted failure of twinning-induced plasticity (TWIP) steel [55].

A difference in deformation microstructures between Type 304 and Type 316 L appeared in strain localization shown in Figs. 7.13 and 7.14 for specimens given 24 % plastic strain [52]. Hydrogen-enhanced strain localization was more prominent in Type 304 than Type 316 L. The observed strain localization was associated with the planarity of dislocation slip and with barriers for the slip extension. TEM micrograph Fig. 8.19 [52] for hydrogen-charged Type 304 strained to 5 % shows

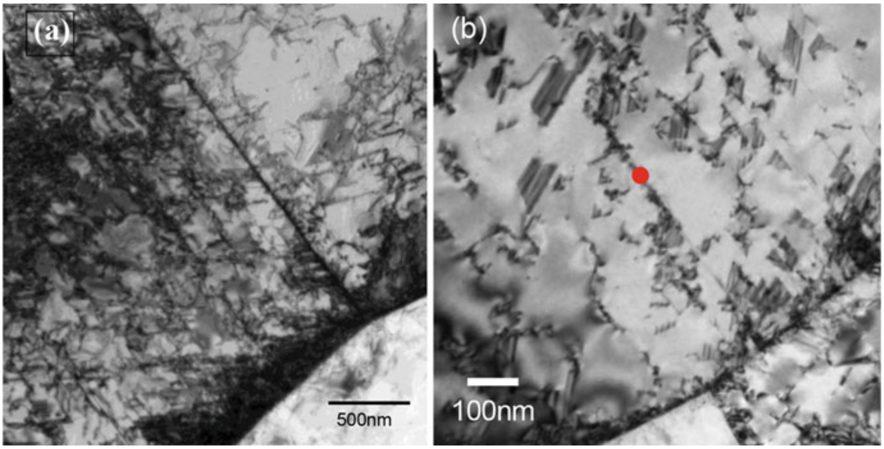

Fig. 8.19 TEM micrograph of hydrogen-charged Type 304 steel strained to 5 %, showing (**a**) annealing-twin band and high dislocation densities along twin and grain boundaries. Magnified view (**b**) shows high densities of stacking fault and ε-martensite (Hatano et al. [52])

high densities of stacking faults and fine streaks of ε-martensite. High dislocation densities along grain boundaries and annealing-twin boundaries were also revealed. Inhomogeneous microstructures made quantitative comparisons difficult, but stacking faults, twins and ε-martensite were observed much more frequently in hydrogen-charged Type 304 than Type 316 L. Further, dislocation structures in Type 316 L were tangled with a few stacking faults [52].

Formations of stacking fault and ε-martensite in γ-steels are dominated by the stacking fault energy (SFE). The SFEs of Type 304 and Type 316 L estimated according to a first-principles calculation [56] were about 2 and 30 $\mathrm{mJ \cdot m^{-2}}$, respectively [52]. Experimentally, sensitization of Type 309S steel reduced SFE in the area near grain boundaries from 35 to 22 $\mathrm{mJ \cdot m^{-2}}$ due to Cr depletion [49]. Reductions in SFE of γ-stainless steels by hydrogen are presented in Sect. 7.2.1(a). Reductions of SFE of about 20–30 % by hydrogen were reported for Type 304 [43] and Type 310 [57]. The stability of γ-phase surely originates in SFE, which dominates deformation microstructures.

Plausible functions of hydrogen on the susceptibility to HE of γ-stainless steels are twofold: one is the enhancement of strain localization through the decrease of SFE and the other is that of strain-induced creation of vacancies common to other types of steels. Effects of hydrogen in various γ-stainless steels possibly originate in deformation microstructures in γ-phase.

References

1. N.R. Moody, S.L. Robinson, W.M. Garrison Jr., Res Mechanica **30**, 143–206 (1990)
2. I.M. Bernstein, G.M. Pressouyre, in *Hydrogen Degradation of Ferrous Alloys*, ed. by R.A. Oriani, J.P. Hirth, M. Smialowski (Noyes Pub, Park Ridge, 1985), pp. 641–685
3. W.W. Gerberich, T. Livne, X.-F. Chen, M. Kaczorowski, Metall. Trans. A **19A**, 1319–1334 (1988)
4. N. Owada, H. Majima, T. Eguchi, in *Advances in Delayed Fracture Solution* – Report of Research Group, Iron Steel Inst. Jpn (1997), pp. 111–114
5. H.K.D.H. Bhadesia, *Bainite in Steels*, 2nd edn. (The Institute of Materials, London, 2001)
6. F. Nakasato, F. Terasaki, Tetsu-to-Hagané **61**, 856–868 (1975)
7. I.-G. Park, A.W. Thompson, Metall. Trans. A **21A**, 465–477 (1990)
8. R.A. Oriani, P.H. Josephic, Scr. Metall. **13**, 469–471 (1979)
9. J.C. Charbonnier, H. Margot-Marette, A.M. Brass, M. Aucouturier, Metall. Trans. A **16A**, 935–944 (1985)
10. S. Yamazaki, T. Takahashi, Tetsu-to-Hagané **83**, 454–459 (1997)
11. M. Nagumo, T. Tamaoki, T. Sugawara, in *Hydrogen Effects on Materials Behavior and Corrosion Deformation Interactions*, ed. by N.R. Moody, A.W. Thompson, R.E. Ricker, C.W. Was, K.H. Jones (TMS, Warrendale, 2003), pp. 999–1008
12. T. Tsuchida, T. Hara, K. Tsuzaki, Tetsu-to-Hagané **88**, 771–778 (2002)
13. J.F. Lessar, W.W. Gerberich, Metall. Trans. A **7A**, 953–960 (1976)
14. N.R. Moody, R.E. Stoltz, M.W. Perra, Scr. Metall. **20**, 119–122 (1985)
15. J. Kameda, Acta Metall. **34**, 1721–1735 (1986)
16. S.K. Banerji, C.J. McMahon Jr., H.C. Feng, Metall. Trans. A **9A**, 237–247 (1978)
17. H. Asahi, Y. Sogo, M. Ueno, H. Higashiyama, Corrosion **45**, 519–527 (1989)
18. H. Fuchigami, H. Minami, M. Nagumo, Philos. Mag. Lett. **86**, 21–29 (2006)

19. C.J. McMahon Jr., Eng. Fract. Mech. **68**, 773–788 (2001)
20. K. Yoshino, C.J. McMahon, Metall. Trans. **5**, 363–370 (1974)
21. J. Kameda, C.J. McMahon Jr., Metall. Trans. A **14A**, 903–911 (1983)
22. Y. Takeda, C.J. McMahon Jr., Metall. Trans. A **12A**, 1255–1266 (1981)
23. N. Bandyopadhyay, J. Kameda, C.J. McMahon Jr., Metall. Trans. A **14A**, 881–888 (1983)
24. M. Nagumo, H. Matsuda, Philos. Mag. A **82**, 3415–3425 (2002)
25. T. Inoue, K. Yamamoto, M. Nagumo: in Hydrogen Effects in Metals", ed. by I.M. Bernstein, A.W. Thompson (Metall. Soc. AIME, Warrendale, 1981), pp. 777–784
26. T. Inoue, K. Yamamoto, M. Nagumo, K. Miyamoto, in *Hydrogen in Metals*, Proceedings of the 2nd International Symposium, Supplement of Trans. Jpn. Inst. Metals, **21**, 433–436 (1980)
27. R.G. Davies, Scr. Metall. **17**, 889–892 (1983)
28. R.G. Davies, Metall. Trans. A **12A**, 1667–1672 (1981)
29. M. Koyama, C.C. Tasan, E. Akiyama, K. Tsuzaki, D. Raabe, Acta Mater. **70**, 174–187 (2014)
30. S.L.I. Chan, H.L. Lee, J.R. Yang, Metall. Mater. Trans. A **22A**, 2579–2586 (1991)
31. J.L. Gou, K.D. Chang, H.S. Fang, B.Z. Bai, ISIJ Int. **42**, 1560–1564 (2002)
32. T. Hojo, K. Sugimoto, Y. Mukai, H. Akagi, S. Ikeda, Tetsu-to-Haganè **92**, 83–89 (2006)
33. T. Hojo, K. Sugimoto, Y. Mukai, S. Ikeda, Tetsu-to-Haganè **93**, 234–239 (2007)
34. J. Watanabe, K. Takai, M. Nagumo, Tetsu-to-Haganè **82**, 947–952 (1996)
35. K. Farrell, M.B. Lewis, Scr. Metall. **15**, 661–664 (1981)
36. A. Szummer, in *Hydrogen Degradation of Ferrous Alloys*, ed. by R.A. Oriani, J.P. Hirth, M. Smialowski (Noyes Pub., Park Ridge, 1985), pp. 512–534
37. K. Kamachi, Trans. ISIJ **18**, 485–491 (1978)
38. D.G. Ulmer, C.J. Altstetter, Acta Metall. Mater. **41**, 2235–2241 (1993)
39. N. Narita, C.J. Altstetter, H.K. Birnbaum, Metall. Trans. A **13A**, 1355–1365 (1982)
40. K.J.L. Iyer, Scr. Metall. **6**, 721–726 (1972)
41. A.W. Thompson, O. Buck, Metall. Trans. A **7A**, 329–331 (1976)
42. S. Singh, C. Altstetter, Metall. Trans. A **13A**, 1799–1808 (1982)
43. A. Inoue, Y. Hosoya, T. Masumoto, Trans. ISIJ **19**, 171–178 (1979)
44. G.R. Caskey Jr., in *Hydrogen Degradation of Ferrous Alloys*, ed. by R.A. Oriani, J.P. Hirth, M. Smialowski (Noyes Pub., Park Ridge, 1985), pp. 822–862
45. G. Han, J. HE, S. Fukuyama, K. Yokogawa, Acta Mater. **46**, 4559–4570 (1998)
46. A.W. Thompson, Mater. Sci. Eng. **14**, 253–264 (1974)
47. T. Omura, M. Miyahara, H. Senba, M. Igarashi, H. Hirata, J. High Pressure Inst. Jpn. **46**, 205–213 (2008)
48. T.-P. Perng, C.J. Altstetter, Metall. Trans. A **19A**, 145–152 (1988)
49. H. Hänninen, T. Hakkarainen, Metall. Trans. A **10A**, 1196–1199 (1979)
50. T.P. Perng, C.J. Altstetter, Metall. Trans. A **18A**, 123–134 (1987)
51. C.L. Briant, Metall. Trans. A **10A**, 181–189 (1979)
52. M. Hatano, M. Fujinami, K. Arai, H. Fujii, M. Nagumo, Acta Mater. **67**, 342–353 (2014)
53. T. Nakayama, M. Takano, Corrosion-NACE **38**, 1–9 (1982)
54. N. Narita, H.K. Birnbaum, Scr. Metall. **14**, 1355–1358 (1980)
55. M. Koyama, W. Akiyama, K. Tsuzaki, D. Raabe, Acta Mater. **61**, 4607–4618 (2013)
56. L. Vitos, J.-O. Nilson, B. Johansson, Acta Mater. **54**, 3821–3826 (2006)
57. P.J. Ferreira, I.M. Robertson, H.K. Birnbaum, Mater. Sci. Eng. **207–209**, 93–96 (1996)

Chapter 9
Mechanistic Aspects of Fracture I ~ Brittle Fracture Models

Fracture of materials is a mechanistic event, and the mechanistic scheme and description are required for the function of hydrogen in the fracture process. Materials failure under stress is classified into two basic types; the one is the decohesion of material without plastic flow and the other is the split by necking down to a chisel point. Actual failure of steels due to hydrogen is more or less associated with plasticity as described in Chap. 7, but various models have been proposed from both "brittle" and "ductile" fracture viewpoints according to the presumed function of hydrogen in the fracture process. For "brittle" fracture models, the thermodynamic instability of a crack is the critical stage. On the other hand, hydrogen plays its role in "ductile" fracture models in the initiation of microvoids and plastic instability that leads to coalescence of voids.

The mechanism of hydrogen embrittlement (HE) of steels is not yet conclusive. Experimental difficulties, particularly of detecting hydrogen behaviors and of revealing fine details of microstructures, have made early works on the function of hydrogen rather conceptual. Some notices are necessary. Firstly, hydrogen behaviors in materials depend on the hydrogen fugacity as described in Chaps. 1 and 2, and a model derived for a specific experimental situation cannot be straightly applied to other cases. Secondly, deformation microstructures under a given hydrogen fugacity differ by materials as described in Sects. 7.1 and 7.2. Thirdly, mechanistic models inevitably assume some parameters so as to fit theoretical and observed behaviors. Thus determined parameters must be reasonable with respect to actual environmental and materials conditions.

Recent advances in experimental techniques are supplying new information to identify the operating function of hydrogen as described in preceding sections. In the following, major brittle fracture models so far proposed are reviewed from mechanistic viewpoints complementing their ideas on applying brittle fracture models.

M. Nagumo, *Fundamentals of Hydrogen Embrittlement*,
DOI 10.1007/978-981-10-0161-1_9

9.1 Internal Pressure Theory

Historically, internal cracks named as "snow flake", "fisheye" or "white spots" are the earliest known hydrogen-induced defects in steels. Bright and shiny facets suggested precipitation of high pressure molecular hydrogen, and the precipitation sites were assumed to be "interblock disjunctions" in crystals causing local cleavage and rupture [1]. The hydrogen source is mostly moisture in atmosphere during the fabrication process of steels. The hydrogen solubility in bcc iron in thermal equilibrium with hydrogen gas of pressure P is given by Sieverts' law in Eq. (1.1). For iron, when hydrogen is introduced under a hydrogen atmosphere of 0.1 MPa at 1000 °C and is quenched to room temperature, the expected pressure of internally precipitated hydrogen gas is 4×10^6 MPa in equilibrium with the supersaturated lattice hydrogen concentration, enough to cause cracking. Estimated hydrogen fugacity at various cathodic electrolysis methods is shown in Table 2.1.

The internally pressurized crack can act as an incipient crack for brittle fracture. The basic notion of brittle fracture is the Griffith condition that describes thermodynamic instability of an elliptical hole in a homogeneous linear elastic solid under tensile stress as illustrated in Fig. 9.1. The unstable crack growth is expected when the decrease in the potential energy, which is supplied by the internal strain and external force, exceeds the increase in the surface energy. The Griffith condition for the initiation of brittle fracture from a crack of half-length a in a solid of surface energy γ and Young's modulus E in plane strain condition is given as,

$$\sigma_f = \sqrt{2E\gamma/\pi(1 - \nu^2)a}, \tag{9.1}$$

where σ_f is the fracture stress and ν is Poisson's ratio. The surface energy is defined as the energy to create a unit area of the new surface. The lower γ and/or the longer a causes the lower σ_f.

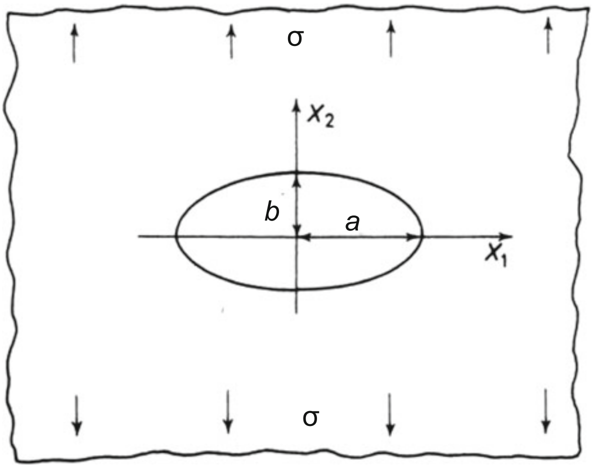

Fig. 9.1 Geometry of an elliptical hole in homogeneous linear elastic solid under tensile stress σ

Tetelman and Robertson observed microcracks of 10^{-4} m in length on {100} planes of 3% Si-Fe single crystals when hydrogen was introduced by strong cathodic-charging in 4 % H_2SO_4 with CS_2 and As_2O_3 at a current density of 160 A/m^2 at room temperature [2]. Arrays of decorated dislocations were revealed indicating intermittent growths of cracks associated with plastic deformation. Buildup of internal pressure by hydrogen and its decrease associated with the crack growth are reasonable as the origin. Tetelman et al. replaced σ_f in Eq. (9.1) with the internal pressure P for a penny-shaped crack and calculated stress fields around the crack tip. Calculated results matched well the observed growth of the crack and slip traces. The deduced ratio of energy expended in restarting the crack to the energy expended in moving it was of the order of unity for cracks 10^{-4} m long, implying a small contribution of plasticity that blunted the crack in this case. The internal pressure estimated from Eq. (9.1) neglecting the contribution of plasticity was about 100 MPa.

The existence of an incipient crack is a crucial premise for brittle fracture. The void formation at non-metallic inclusions like elongated MnS in particular has been well known in terms of hydrogen induced cracking (HIC) for line-pipe steels exposed to humid environments containing H_2S [3]. The void formation results from the molecular precipitation of hydrogen entering from environments. On the other hand, some models for the plasticity-induced nanocrack formation for brittle fracture have been proposed as schematically shown in Fig. 9.2; (a) Stroh's model for pileup of dislocation groups at interface such as grain boundaries [4], and (b) Cottrell's model for coalescence of dislocations moving on intersecting slip planes [5]. In the former, the critical shear stress τ_c acting on pileup of n dislocations to coalesce into a crack is given as

$$\tau_c = \tau_i + \left(\frac{12\gamma}{nb}\right), \tag{9.2}$$

where τ_i is the friction stress in the slip plane, γ is the surface energy and b is the Burgers vector. The smaller n needs the larger τ_c to coalesce piled-up dislocations.

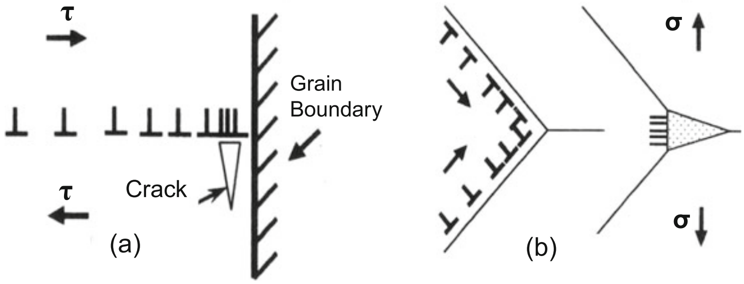

Fig. 9.2 Dislocation models for nanocrack formation. (**a**) Stroh's model for pileup of dislocations at interface such as grain boundaries. (**b**) Cottrell's model for coalescence of dislocations moving on intersecting slip planes

Cottrell pointed out the importance of hydrostatic tension for the growth of a crack nucleus [5]. The instability of a microcrack under external stress in addition to internal pressure was given by Garofalo et al. [6] and Bilby et al. [7]. The basic idea is the same as the Griffith model, *i.e*. the catastrophic growth of a crack takes place when the change of the Gibbs free energy is negative. For a wedge-shape crack produced by n dislocations running into the crack on a slip plane, the instability condition under an internal pressure p and applied external stresses that produce a normal stress σ_1 and a shear stress σ_2 was given in the form,

$$\left[(\sigma_1 + p)^2 + \sigma_2^2\right]^{1/2} + [(\sigma_1 + p)\sin\theta - \sigma_2\cos\theta] \geq \frac{4\gamma}{nb}, \tag{9.3}$$

where θ is the angle between the crack and the slip plane, γ is the surface energy and b is the Burgers vector of the dislocations [7]. The critical length $2c*$ of the crack was expressed as

$$2c^* = 4\mu\gamma\{\pi(1 - v)\varphi[\varphi + (\sigma_1 + p)\sin\theta - \sigma_2\cos\theta]\}^{-1}, \tag{9.4}$$

where μ and v are the shear modulus and Poisson's ratio, respectively, and ϕ is defined as

$$\varphi^2 = (\sigma_1 + p)^2 + {\sigma_2}^2. \tag{9.5}$$

Another expression in terms of n is

$$2c^* = nb\mu[\pi(1 - v)\varphi]^{-1}. \tag{9.6}$$

Computations of $2c^*$ were conducted for Eq. (9.4) assuming hydrogen pressures corresponding to the lattice hydrogen concentration of 8 mass ppm and values of γ taking into account an expected decrease due to hydrogen adsorption on the crack surface (described in Sect. 9.2). For the observed fracture stresses of a mild steel at −115 °C, the calculated $2c^*$s were about 6 or 4 nm using assumed γ of 0.83 or 0.52 J/m^2. The values are much shorter than actually observed 1 ~ 4 μm for hydrogen-free cases [6]. However, the assumed hydrogen concentration needs an unrealistic p value as high as 3100 MPa. Also, the magnitude of γ should be much higher than assumed γ when plastic deformation around the crack is taken into account.

Observed hydrogen concentrations are mostly of trapped hydrogen rather than hydrogen in solution, and nanoscale cracks predicted by the models in Fig. 9.2 have not been observed experimentally. Application of Stroh's model to actual brittle fracture have some other difficulties such as the sharpness of the crack tip, the relaxation of high stresses on piled-up dislocations due to the activation of secondary slip systems and complex microstructures particularly near grain boundaries in high strength steels.

9.2 Surface Adsorption Theory

The instability of a crack is promoted when the surface energy γ in the Griffith condition Eq. (9.1) decreases. Lowering of γ of metals by the adsorption of hydrogen on the surface is given as Eq. (5.10) in Sect. 5.3.3 according to the Gibbs adsorption isotherm and the Langmuir adsorption. Petch assumed a crack ahead of arrays of n edge dislocations held up at some obstacle under a shear stress τ [8]. The Stroh model for the microcrack formation gives a relationship among τ, n and γ in the form

$$\tau = 12\gamma/nb. \tag{9.7}$$

The arrays of dislocations produce normal stress as a part of the fracture stress superposing the external stress. Assuming also that the length of the arrays is one half of the grain diameter, Petch calculated γ as a function of the hydrogen concentration using Eq. (5.10) and Sieverts' law that related the internal pressure to the hydrogen concentration. The results for α-iron at room temperature are shown in Fig. 5.8.

The calculated decrease in γ at very low hydrogen concentrations amounts to about 40 % of the true surface energy γ_0, ~ 2 J/m^2, of metals, but it is still a very small fraction for effective surface energies of the order of kJ/m^2 which is estimated from fracture toughness data of steels. Decrease in γ due to the surface adsorption of hydrogen is viable, but its quantitative contribution to observed degradation is an issue as described in Sect. 5.3.3. Petch explained observed fracture stresses of mild steels with different grain sizes according to his surface energy theory [8]. However, the amount of hydrogen was as much as 10 mass ppm. Hydrogen was introduced under a very strong condition, *i.e.* cathodic electrolysis in 4 % H_2SO_4 containing poison at a current density of 3200 A/m^2, surely producing extraneous defects at the time of electrolysis.

Changes in γ of α-iron due to adsorption of hydrogen were calculated by Tromans more precisely using a suitable adsorption isotherm [9]. The calculated decrease in γ from the value in vacuum was 0.5 J/m^2 at 100 MPa hydrogen gas at 25 °C. Tromans also showed the effects of local stress on γ instead of internal pressure. The presence of hydrostatic stress increased the activity of hydrogen, and the calculated decrease in γ by local hydrostatic stress of 1 GPa was 0.2 J/m^2.

Actually, fracture surfaces in HE often exhibit a fine mixture of plastic shearing-off and cleavage-like fracture. As described in Sect. 6.2.2(a) on the crack growth rate, the model by Vehoff and Roth on the crack-tip opening assumed that the fractional hydrogen coverage of special sites right at the tip of a stressed crack controls crack propagation in HE [10].

9.3 Lattice Decohesion Theory

9.3.1 *Cohesive Strength*

The Griffith condition, Eq. (9.1), is a thermodynamic criterion for the instability of a crack without stating microscopic processes of the crack extension. The crack extension by breaking atomic bonds is expected when the stress concentration at the crack tip exceeds the cohesive force. This is the stress-controlled criterion of brittle fracture. For an elliptical hole of $2a$ in length and ρ in radius of curvature, the condition of the bond separation by the stress concentration at the edge is expressed as

$$\sigma_{\max} = \sigma_a\left(1 + 2\sqrt{\frac{a}{\rho}}\right) \approx 2\sigma_a\sqrt{\frac{a}{\rho} > \sigma_{th} \approx \frac{E}{6}}, \tag{9.8}$$

where σ_a is the applied stress, σ_{th} is the ideal strength of metals and E is Young's modulus. In order to satisfy the condition for $\sigma_a = 100$ MPa, $2a = 10$ μm and $E = 300$ GPa, ρ must be atomically sharp as small as 1.6×10^{-10} m. Further, the bond separation itself is not a sufficient condition for the unstable crack extension. The Griffith condition must be satisfied in this case with γ low enough close to the true surface energy of metals of ~2 J/m^2 without involving plasticity.

Troiano assumed the decrease in the cohesive strength by hydrogen for delayed fracture of high strength steels, but the formation of fracture embryo was thought to be due to activated dislocation arrays [11]. Oriani and Josephic formulated a criterion for stress-controlled unstable crack advance for HE [12]. The work for cutting n atomic bonds per unit area is twice the true surface energy γ,

$$2\gamma = n\int_{z_0}^{\infty} F(z)\,dz, \tag{9.9}$$

where $F(z)$ is the cohesive force, z is the interatomic distance and z_0 is the stress-free equilibrium value of z. The critical condition for a crack to start is that the concentrated stress at the crack tip exceeds the maximum cohesive force expressed as

$$k'\sigma(L/\rho)^{1/2} = nF_m\left(c'\right), \tag{9.10}$$

where σ is the applied tensile stress, L is the crack length, ρ is the crack tip radius, n is the number of atoms per unit area of crystallographic plane, $F_m(c')$ is the maximum cohesive force at a local hydrogen concentration c' and k' is a numerical parameter. The assumption that Oriani and Josephic made was that F_m decreases in proportion to hydrogen concentration c,

$$F_m(c) = F_m^0 - \alpha c, \tag{9.11}$$

where $F_m{}^0$ is F_m of the hydrogen-free lattice and α is an unknown parameter. The model was thus designated as the hydrogen enhanced decohesion (HEDE) theory.

The estimation of $F_m(c)$ is difficult, but it is included in the stress intensity factor K, a parameter to express stress fields near the crack-tip, described in following Sect. 9.3.2. Using Eq. (9.10) for the stress-controlled brittle fracture, K is written as,

$$K = k'' \rho^{1/2} n F_m\left(c'\right), \tag{9.12}$$

where k'' is a numerical parameter. Buildup of c' by hydrostatic stress at the crack tip was taken into account for the calculation. Oriani et al. embedded $F_m(c')$ in the critical stress intensity K_{cr} at the onset of unstable fracture and used experimental parameters to determine numerical values of $F_m(c')$. The local hydrogen concentration c is a function of the hydrostatic stress. Oriani et al. derived a relation between the environmental hydrogen gas pressure and K using $F_m(c)$ and crack tip radius as parameters. The ad hoc parameters were determined so as to fit the calculation using the formula with the experimental dependence of the critical hydrogen pressure on K.

Experiments were conducted using WOL specimens of AISI 4340 steel in hydrogen and deuterium gases of pressures lower than 0.1 MPa at room temperature. Examples of thus determined parameters at K_{cr} of 20 $\text{ksi} \cdot \text{in}^{1/2}$ ($=22\ \text{MPa} \cdot \text{m}^{1/2}$) were 2.49×10^3 ksi (=17.4 GPa) for the hydrostatic pressure, $6.75 \times 10^{-6}\beta$ (H/M) for the local hydrogen concentration and 0.34 for $F_m(c)/F_m{}^0$. Experimental data Oriani et al. referred were for intergranular fracture, and the unknown parameter β for the local hydrogen concentration was estimated to exceed 10^3 at grain boundaries. The fit between experimental and theoretical dependencies of p on K was good, but the estimated values of the hydrostatic stress and the local hydrogen concentration are not likely realistic.

9.3.2 Local Stress Intensity Approach

Stress fields near the crack-tip in the regime of linear elasticity are expressed in terms of the stress intensity factor K as

$$\sigma_{ij} = \frac{K}{\sqrt{2\pi r}} f(\theta) \tag{9.13}$$

in polar coordinates. Events that take place near the crack tip are controlled by K. For a through-crack of length $2a$ in an infinite plane at right angles to a uniform stress field σ, K is expressed as

$$K = \sigma\sqrt{\pi a}. \tag{9.14}$$

The critical value of K gives a failure criterion and is useful as a parameter to express fracture toughness of materials for engineering purposes. However, the viability of expressing stress fields in terms of K breaks down in regions very close to the crack tip and in the presence of local plasticity. Some modifications have been presented for such local situations. It is also to be noticed that observed critical values of K for fracture do not specify microscopic processes that cause the fracture event. Equation (9.12) is for the case of the stress-controlled fracture.

Dislocations near the crack tip affect the crack-tip stress fields. When a crack is figured to occupy the negative real axis in the complex plane and dislocations are situated at points ζ_{j}, the stress at a point z is the superposition of the stresses exerted by the crack and the dislocations as expressed in the form

$$\sigma = \frac{K}{\sqrt{2\pi z}} + \sum_{j} \frac{\mu b_j}{2\pi}\sqrt{\frac{\xi_j}{z}\frac{1}{z - \varsigma_j}}, \tag{9.15}$$

if, for simplicity, the distribution is symmetric about the x-axis [13]. The second term in the right-hand side is due to dislocations. By defining k_{D} and the local stress intensity factor k as

$$k_D = \frac{\mu b}{\sqrt{2\pi\varsigma}}, \tag{9.16}$$

$$k = K - \sum_{j} k_D(j)\,, \tag{9.17}$$

$\sigma(\mathrm{z})$ near the crack tip is expressed as [14]

$$\sigma(z) \approx \frac{k}{\sqrt{2\pi z}}. \tag{9.18}$$

Then, k is the effective stress intensity factor that determines the local stress fields in the presence of a dislocation group.

Marsh and Gerberich derived a relation between the plane-strain fracture toughness K_{IC} and the plane-strain Griffith local stress intensity for fracture k_{G} [15]. A simplified approximation was developed from computer simulations for the closest approach of the nearest dislocation to the crack tip. Thus obtained relation is

$$K_{IC} \approx \frac{1}{\beta'}\exp\left(\frac{k_{IG}^2}{\alpha'\,\sigma_y}\right), \tag{9.19}$$

where α' and β' are parameters and σ_{y} is the yield stress. Marsh and Gerberich assumed that k_{IG} could be lowered to k_{IH} proportionately to the local hydrogen concentration C_{H} in the form

$$k_{IH} = k_{IG} - \alpha C_H \, . \tag{9.20}$$

The estimation of k_{IH} under hydrogen gas environments was made by equating k_{IH} with $\sqrt{E\gamma}$ using about $1.5 \sim 1$ J/m^2 for γ calculated according to Tromans' first-principles method [9]. Then, K_{IC} in the presence of hydrogen was calculated from Eq. (9.19) replacing k_{IG} by estimated k_{IH}. Using also separately determined parameters α' and β' in Eq. (9.19) so as to fit fracture toughness data of steels, the calculated threshold K decreased with increasing hydrogen gas pressures along a curve nearly coincident with observed data for AISI 4340 steel in hydrogen gas [12]. The fracture mode for the observed data was intergranular as described in Sect. 7.1(e). The local stress intensity factor does not explicitly incorporate F_{m}, but Gerberich et al. ascribed the fit to the hydrogen-enhanced decohesion mechanism expressed by Eq. (9.11) [16].

9.4 Theories of Intergranular Fracture

9.4.1 Interface Decohesion

Enhanced embrittlement associated with segregation of impurities in prior austenite grain boundaries is well known with temper embrittlement of steels [17]. Enrichment of hydrogen along grain boundaries of steel has been revealed by means of tritium autoradiography [18, 19] and discussed with respect to intergranular fracture [20]. Thermodynamic treatments of the impurity adsorption at interface and its effects on interfacial embrittlement have been presented in the literature [21–23].

Transition of a system from non-equilibrium to equilibrium states is associated with a net decrease in energy as expressed by the Griffith condition. When a crack extends under external force, the internal strain energy U is released while the external force does work F. The driving force of the crack extension is the net change of the energy. The energy release rate or the crack driving force or the crack extension force, $\mathcal{G}$, is defined as

$$\mathcal{G} = -\frac{d}{dA}(U - F), \tag{9.21}$$

where A is the crack area.

The net change of the energy is transferred to the work to create new surfaces, W_{s}, and the equilibrium condition for the crack is

$$-\frac{d}{dA}(U - F) = \frac{dW_s}{dA} \, . \tag{9.22}$$

In the Griffith condition, the right-hand side of Eq. (9.21) is 2γ and thus the surface energy term in the Griffith condition expresses the crack extension force. A general

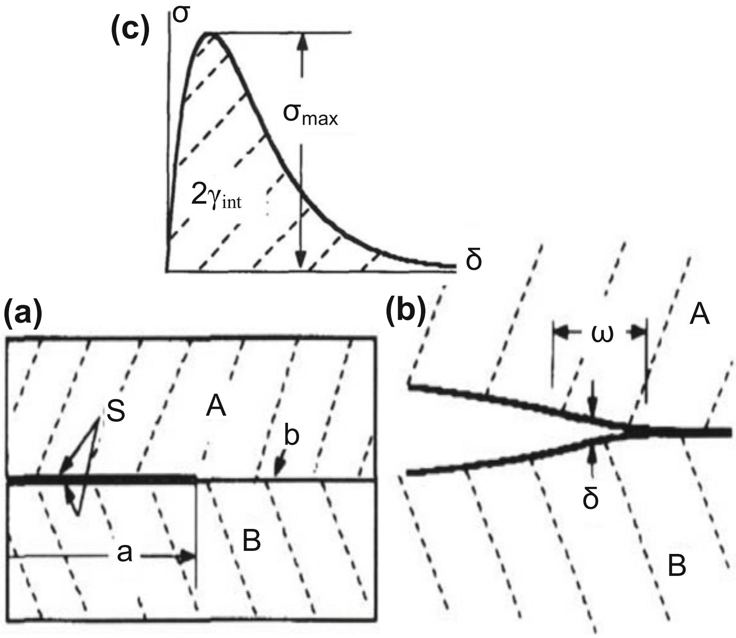

Fig. 9.3 Model of interface decohesion. (**a**) Interfacial brittle crack between phases A and B. (**b**) Region of gradual decohesion neat tip over size scale ω. (**c**) Tensile stress σ *vs.* separation distance δ normal to the interface (Rice et al. [22])

energy balance criterion for the crack extension was presented by Rice [24]. When the separation of material surfaces incorporates microstructural processes associated with plasticity, the meaning of the right hand side of Eq. (9.21) is not identical to the surface energy. Descriptions on Rice's model are in the end of Sect. 9.4.2(a).

For the crack advance with gradual interface decohesion, Rice and Wang proposed a model as schematically shown in Fig. 9.3 [22]. The crack extension force $\mathcal{G}$ along the transition zone of length ω between two elastic solids is defined as

$$\mathcal{G} = \int_{\delta_0}^{\infty} \sigma(\delta)\, d\delta \equiv 2\gamma_{\mathrm{int}}, \tag{9.23}$$

where δ is the local interfacial opening. In this model the separation is reversible on stressing, i.e. separated faces rejoin when applied stress is removed, and the thermodynamic threshold for growth $2\gamma_{\mathrm{int}}$ does not include plastic work.

Impurity segregation at the interface increases the energy of the interface by potential energies of segregants. The energy change d*u* associated with the reversible change of state is

$$du = Tds + \sigma d\delta + \sum_i \mu_i d\Gamma_i, \tag{9.24}$$

where T is temperature, s is entropy and μ_i and Γ_i are respectively the equilibrium chemical potential and concentration of *i*-segregant. Using Eqs. (9.22) and (9.23), Rice and Wang formulated the change of $2\gamma_\mathrm{int}$ for the interface separation under constant concentration or constant chemical potential of a segregant. The segregation of impurities was assumed to follow the Langmuir-McLean theory that derived the fractional monolayer segregation to minimize the energy of the system,

$$\frac{\Gamma}{\Gamma^\mathrm{max} - \Gamma} = x \exp\left(-\frac{\Delta g}{RT}\right), \tag{9.25}$$

where x is the fraction of available sites occupied in the bulk by the segregant and Δg was the Gibbs free energy of segregation per mole of segregant. Rice and Wang derived an approximate form of $2\gamma_\mathrm{int}$ for the case of fixed and low Γ in the form,

$$2\gamma_\mathrm{int} = (2\gamma_\mathrm{int})_0 - \left(\Delta g_b^0 - \Delta g_s^0\right)\Gamma, \tag{9.26}$$

where suffixes *0*, *b*, *s* abbreviate respectively segregant-free, boundary and surface. Reported values of $(\Delta g_\mathrm{b}{}^0 - \Delta g_\mathrm{s}{}^\mathrm{o})$ for P, Sn and Sb are in the range 50 ~ 100 kJ/mol. When one assumes that one quarter of possible adsorption sites are occupied by segregants, the second term of the right-hand side of Eq. (9.22) is 0.35 ~ 0.70 J/m^2, a substantial fraction of the true surface energy of metals.

Following Rice-Wang's theory, Novak et al. analyzed hydrogen embritlement of AISI 4340 steel of 1760 MPa in tensile strength [25]. Experimentally, the fracture stress of thermally hydrogen-precharged specimens at four-point bending tests decreased with increasing hydrogen concentrations associated with changes of fracture modes from ductile microvoid coalescence for uncharged specimens to intergranular for hydrogen-precharged ones. The model by Novak et al. was that the impingement of dislocation arrays at the carbide/matrix interface formed there an incipient crack of brittle intergranular fracture by decohesion. Assumed functions of hydrogen were in two ways, the one was to reduce the reversible work of decohesion along the carbide/matrix interface and the other was to enhance dislocation motion thus increasing the number of piled-up dislocations.

Many assumptions and numerical estimations as listed below were made for the quantitative analyses:

1. For the second term in the right-hand side of Eq. (9.25), $(\Delta g_\mathrm{b}{}^0 - \Delta g_\mathrm{s}{}^\mathrm{o})$ of hydrogen was set to 74.5 kJ/mol in the same range as that for P, Sn and Sb.
2. Hydrogen trapped in dislocations rather than other stronger trap sites such as grain- or interface boundaries was effective for decohesion. The hydrogen occupancy for dislocations $\theta_T^{(d)}$ was used for the interfacial coverage Γ

$$\Gamma = \eta \theta_T^{(d)} \Gamma_{\max}, \tag{9.27}$$

with the fitting parameter η. The number of trap sites per unit area of the interface, $\Gamma_{\max}$, was determined from observed carbide size and frequency.

3. The hydrogen concentration at the interface was estimated assuming transport by dislocations. The density of dislocations near the notch root was calculated using a finite element method.
4. The weakest-link model was applied to estimate the fracture stress due to the carbide/matrix interface decohesion.
5. The effective surface energy γ_{eff} in the Griffith condition for the instability of the interface-crack included plastic work γ_{p} in the form

$$\gamma_{eff} = 2\gamma_{\mathrm{int}} + \gamma_p\,, \tag{9.28}$$

$$\gamma_p = A(2\gamma_{\mathrm{int}})^q \tag{9.29}$$

with parameters A and q.

The parameters were determined so as to fit calculated fracture stresses with observed ones for various hydrogen concentrations. The reduction in $2\gamma_{\mathrm{int}}$ by the segregation of hydrogen was expressed by the second term in the right-hand side of Eq. (9.25). The expression of Γ is given in Eq. (9.26).

According to assumed or calculated values [25] of $\Delta g_{\mathrm{b}} = -25.5$ kJ/mol, $\Delta g_{\mathrm{s}} = -100$ kJ/mol, $\theta_T^{(d)} = 5 \times 10^{-4}$, $\eta = 0.01$, $\Gamma_{\max} = 6.17 \times 10^{24}$ /m^2, the value of Γ is 5×10^{-5} mol/m^2 (= 3×10^{-19}/m^2) for the average hydrogen concentration of 1 at. ppm and the estimated reduction in $2\gamma_{\mathrm{int}}$ by hydrogen is 3.8 J/m^2. The value is about one order of magnitude larger than the values by the segregation of P and Sn and almost completely cancels out the true surface energy of metals. When the energy dissipation due to plasticity is taken into account, the effective surface energy is obtained from Eqs. (9.28) and (9.29). Taking $A = 0.02$ and $q = 6$, the estimated magnitude of γ_{p} is 82 J/m^2 for $2\gamma_{\mathrm{int}}$ of 4 J/m^2.

Experimental determination of the Gibbs free energy of segregation, Δg, for hydrogen is difficult and Yamaguchi et al. conducted first-principles calculations on grain boundary embrittlement in metal-hydrogen systems [26]. Instead of the Gibbs energy Δg, they calculated the total segregation energy changes, $\Delta E_{\mathrm{gb}}{}^{\mathrm{seg}}$ and $\Delta E_{\mathrm{s}}{}^{\mathrm{seg}}$, when hydrogen atoms move from the bulk to grain boundary or free surface. They used the unit cell that includes 76 Fe atoms and $\sum 3(111)$ symmetrical tilt grain boundary in bcc lattice. One hydrogen atom was successively inserted at each interstitial site in the unit cell until the segregation energy reached a constant value. Calculated values of $\Delta E_{\mathrm{gb}}{}^{\mathrm{seg}}$ on Fe$\Sigma 3(111)$ grain boundary and $\Delta E_{\mathrm{s}}{}^{\mathrm{seg}}$ on Fe(111) are -45 and -79 kJ/mol, respectively. The total segregation energy decreased with the hydrogen concentration and the resulted decrease in $2\gamma_{\mathrm{int}}$ was as much as 40 % when six immobile hydrogen atoms were present in a unit cell area of 0.278 nm^2 on a Fe$\Sigma 3(111)$ boundary. Yamaguchi et al. also showed a more pronounced decrease in $2\gamma_{\mathrm{int}}$ when hydrogen atoms were mobile, and the concentrations in the boundary and free surface in thermal equilibrium were the same as in the bulk [27]. However, $2\gamma_{\text{int}}$ that Yamaguchi et al. used was the difference of the total energies before and after the interface separation. Their definition is not the crack extension force in Eq. (9.25) and Fig. 9.3(c) defined by Rice and Wang.

Kirchheim et al. applied the DEFACTANT mechanism described in Sect. 3.1.2 to the grain boundary or interface decohesion [28]. The reduction of the interfacial energy by impurity segregation is expressed by Eq. (3.11) in terms of the excess and the chemical potential of impurities. However, large chemical potentials or hydrogen pressures are requisite for any remarkable reduction of the work to fracture, which is defined as the difference between the newly created surface energy and the interface energy before separation, to take place. Quantitative estimations for iron-hydrogen system predicted above 1GPa in pressure or 10^8 bar in fugacity of hydrogen to decrease the work to fracture. The vapor pressure of liquid water of about 20 mbar at room temperature gives about 20 MPa or 200 bar hydrogen fugacity in iron [28]. When dislocations or vacancies are present, enhancements of both the generation and movement rates by hydrogen are expected.

9.4.2 Formation of Incipient Crack – Meaning of Surface Energy in Fracture Criteria

(a) Effective surface energy

A key problem on applying the Griffith condition to intergranular fracture is the physical meaning of the surface energy γ. Observed K_{th} values for steels are normally of the order of 10 $\text{MPa} \cdot \text{m}^{1/2}$, and the effective surface energy "γ" derived from Eqs. (9.1) and (9.14) are of the order of 1 kJ/m^2. The value is about three orders of magnitude higher than the true surface energy γ of metals. A common explanation of the discrepancy is the involvement of plastic work γ_{p} in γ as conventionally shown by Eq. (9.28). However, plastic processes that compose γ_{p} are difficult to be figured for estimating γ_{p}.

McMahon and Vitek took into account the work done by plastic deformation around the crack tip [29]. Firstly, they proposed a model that related γ_{p} with dislocation dynamics in the way that the plastic region associated with the crack growth was formed as a strip laid down along either side of the crack path. The plastic work W_{p} is proportional to the effective applied tensile stress σ_{eff} and plastic strain ε_{p},

$$W_p \propto \sigma_{\text{eff}} \varepsilon_p V_p, \tag{9.30}$$

where V_{p} is the volume of the plastic region. McMahon and Vitek considered dynamics of crack advance and related γ_{p} with the change of W_{p}. The change of W_{p} with the crack extension gives γ_{p} as

$$\gamma_p = \frac{d\,W_p}{d\,a}. \tag{9.31}$$

The plastic strain rate $\dot{\varepsilon}_p$ associated with the crack extension is proportional to $\partial\varepsilon_p/\partial a$ and $\dot{\varepsilon}_p$ is empirically related to stress σ as

$$\dot{\varepsilon}_p \propto \sigma_{\text{eff}}^m, \tag{9.32}$$

Since γ_{p} is related to $\dot{\varepsilon}_p$ according to Eqs. (9.30) and (9.31), γ_{p} is also related to σ_{eff}. Then, utilizing differentiation of logarithmic functions,

$$\frac{d\gamma_p}{\gamma_p} \approx (m+1)\frac{d\sigma_{\text{eff}}}{\sigma_{\text{eff}}}. \tag{9.33}$$

Secondly, the impurity segregation reduces the ideal surface energy γ. Then, a crucial problem for IG fracture is the relation between γ and γ_{p} that dominates γ_{eff}. McMahon and Vitek assumed that two processes at the crack tip, one is bond stretching and rupture and the other is dislocation emission and motion, are independent and that the crack extension is very fast with bond stretching occurring only at the crack tip [29]. The assumption was to separate the true surface energy γ from $\gamma_{\text{p.}}$ The local stress at the crack tip dominates the bond-breaking and is proportional to σ_{eff}. Then, since the true surface energy γ is the work done by the local stress, γ is proportional to σ_{eff}. From Eq. (9.33), a relation between γ and γ_{p} was obtained in the form

$$\frac{d\gamma_p}{\gamma_p} \approx (m+1)\frac{d\gamma}{\gamma}. \tag{9.34}$$

The reduction by hydrogen of not only the reversible work but also the attendant plastic work is the underlying assumption of Eq. (9.29) that Novak *et al* used [25] for decohesion of carbide/matrix interface.

Alternatively, Jokl et al. considered a moving microcrack under loading and assumed concomitant bond breaking and dislocation emission from the crack tip [30]. In their model, the stress ahead of the crack and the microcrack opening displacement varied with time, and the plastic work γ_{p} was ascribed to the energy consumed by dislocation emission. Jokl et al. derived a thermodynamic criterion for the unstable microcrack extension taking into account movement of newly created dislocations. Using the relationship between stress and dislocation velocity of the form of Eq. (9.32), γ_{p} was numerically computed as a function of the ideal work for fracture γ with several values of adjustable parameters. Thus calculated γ_{p} values were about 2 ~ 5 times as large as γ.

The model by McMahon and Vitek succeeded to correlate a large change of γ_{p} with a small change of γ. However, the instability of a crack is determined by the crack-tip condition. A general crack instability criterion *incorporating plastic work* was formulated by Rice under a thermodynamical scheme in early days

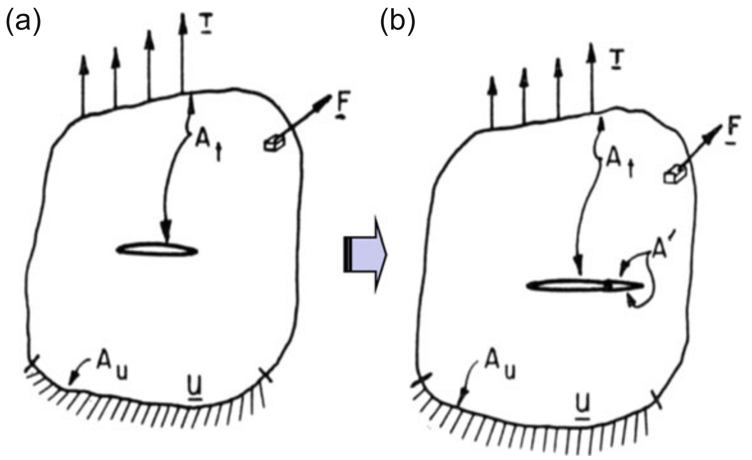

Initial state with extension Imminent.

Crack surface extended by area A'.

Fig. 9.4 Model of cracked continuum loaded by surface and body forces and imposed displacement on the portion of bounding surface. The crack extension increases the traction-free crack surface (Rice [24])

[24]. His model is shown in Fig. 9.4 [24]. In contrast with the Griffith model of Fig. 9.1, a cracked continuum is loaded by forces per unit area $\underline{T}$ on the portion of bounding surface A_T and forces per unit volume $\underline{F}$ throughout the region V occupied by the body. Displacements $\underline{U}$ are imposed on the portion of bounding surface A_U. No particular assumptions are made to the form of constitutive equations relating stresses and strains. The crack extension increases the traction-free crack surface by an amount of A′.

The energy balance criterion is that the work of applied forces during crack extension is equated to the change in stored elastic energy, dissipated energy, change in kinetic energy and energy of the newly created surface. The last term is expressed in terms of γA′. The fracture criterion is then expressed as

$$\lim_{A' \to 0} \frac{1}{A'}\int_{V_0}\left\{\int_{(a)}^{(b)}\left[\left(\sigma_{ij}^{b}-\sigma_{ij}\right)d\varepsilon_{ij}+\rho\left[\left(\ddot{u}_i^{b}-\ddot{u}_i\right)du_i\right]\right]\right\}dV=\gamma, \tag{9.35}$$

where V_0 denotes any arbitrary small region surrounding the crack tip and ρ is the mass density. Superscript a or b on any mechanical quantity denotes its value in the initial or extended states, respectively in Fig. 9.4.

Rice calculated each term of the energy change with the configurations depicted in Fig. 9.4 for an infinitesimal crack extension. Thus derived fracture criterion states that the crack instability is determined *solely by singularities* in the stress and deformation fields at the crack tip, *i.e*. by the local stresses and deformations in the immediate vicinity of the crack tip. The *immediate vicinity* means an arbitrarily small portion that surrounds the crack-tip and contains A′. The physical meaning of $\gamma A'$ is the work done by the new crack surfaces against forces tending to hold them together. The value of $\gamma A'$ is determined independently of the changes of elastic and dissipated energies and its estimation needs *microstructural considerations* of the separation of material surfaces.

(b) Energy to form incipient crack

The presence of an incipient crack is a premise of energy balance criteria. Observed fracture toughness values include energies dissipated in forming the incipient crack in addition to energies needed for the crack instability. McMahon and Vitek considered the brittle crack nucleation at carbides in grain boundaries located a distance x from the precrack tip [29]. The crack was assumed to be formed by pileup of dislocations at the carbide/boundary interface. When the length of the crack along the interface is c and the length of the dislocation pileup is L, the Griffith condition for the crack is expressed using Eq. (9.28) in the form [31],

$$\sigma_L^2 + \tau_{\text{eff}}^2 \left[\left(\frac{L}{c} \right)^{1/2} + \frac{4\,\tau_f}{\pi \tau_{\text{eff}}} \right]^2 \geq \frac{4E(2\gamma + \gamma_p)}{\pi(1 - \nu^2)\,c}, \tag{9.36}$$

where σ_{L} is the local stress ahead of the precrack, τ_{eff} is the effective shear stress on the dislocation pileup, E is Young's modulus and ν is Poisson's ratio.

In this case, the local stress σ_{L} at the carbide is expressed in terms of the critical stress intensity K_C as

$$\sigma_L = \frac{K_C}{\sqrt{2\pi x_0}}, \tag{9.37}$$

where x_0 is the distance from the precrack tip to the point of microcrack nucleation. Equation (9.36) is the instability criterion for the newly created microcrack, but the magnitude of γ_{p} can be expressed in terms of the macroscopic fracture toughness K_{IC} or crack extension force $\mathcal{G}_{\text{IC}}$ that characterizes stress fields around the precrack under plane strain condition. Using Eq. (9.36) and assuming $\tau_{\text{f}} << \tau_{\text{eff}}$ and $\gamma << \gamma_{\text{p}}$, $\mathcal{G}_{\text{IC}}$ is approximated as

$$\mathcal{G}_{\text{Ic}} = \frac{K_{\text{IC}}^2(1 - \nu^2)}{E} = 32 \left(\frac{x_0}{L + 4\,c} \right) \gamma_p\,. \tag{9.38}$$

If the magnitude of $x_0/(L + 4c)$ were of the order of 10 to 10^2, $\mathcal{G}_{\text{IC}}$ would be of the order of 10^2 to $10^3\gamma_{\text{p}}$. The multiplying factor of γ_{p} in Eq. (9.38) originates in stress fields that act on the pileup of dislocations at carbides. McMahon and Vitek adopted the idea that related γ_p to dislocation dynamics as described for Eqs. (9.30) and (9.31) [28]. Then, it was deduced that a small change in γ results in a large change in observed K_{IC} or $\mathscr{G}_{IC}$ according to the interrelation between γ and γ_p expressed by Eq. (9.28). Their model rationalized hydrogen-enhanced intergranular fracture to be caused by the reduction in γ due to enriched hydrogen in grain boundaries.

As described above, plasticity has been taken into account in various ways for instability criteria of a crack. Actually, a substantial part of observed fracture toughness is the plastic work dissipated prior to the formation of an incipient crack. The initiation site of brittle fracture is not the crack tip, but normally locates in a region ahead of the notch or precrack associated with plasticity. Instrumented Charpy impact tests for medium strength steels exhibited that the temperature dependence of the fracture toughness in ductile to brittle transition temperature regions was determined by the initiation stage of brittle fracture [32]. However, observed impact toughness values were dominated by the energy dissipated prior to the onset of brittle fracture, apart from the crack instability criterion. Functions of hydrogen in fracture must be examined not only for the macroscopic crack initiation and growth stages but also throughout the process that lead to the final fracture.

9.5 Summary of Brittle Fracture Models

Most brittle fracture models for HE address hydrogen-induced cracking and intergranular fracture of high strength steels. The crack formation by the precipitation of molecular hydrogen is feasible in case of high hydrogen fugacity, but the key issue is the function of hydrogen in triggering the unstable crack extension.

The basis of brittle fracture models is the thermodynamic energy balance criterion for the crack extension, developed as the Griffith condition or the interface decohesion model. The thermodynamic criteria do not specify microscopic processes of the crack extension. The stress-controlled criterion is not the sole mechanism of brittle fracture, but most models implicitly postulate the function of hydrogen to reduce the cohesive strength of metallic atoms. Some ab initio calculations have shown a decrease in the cohesive force or the surface and interface energies by hydrogen. Experimentally, on the other hand, hydrogen effects are evaluated in terms of the critical stress intensity factor or the crack extension force. Crack extension forces derived from observed fracture toughness are two or three orders of magnitude higher than the true surface energy of metals γ that originates in the cohesive force. The discrepancy between observed crack extension forces and the true surface energy has been ascribed to plastic energy γ_p associated with the crack extension.

The entity of γ_p is difficult to define, but some models have been proposed for the interplay of γ with γ_p. The formation of an incipient crack is a crucial step in brittle fracture. Assuming the microcrack formation by pileup of dislocations at grain boundary carbides, a numerically reasonable relation between macroscopic crack extension force and γ_p has been derived. However, the generalized energy balance criterion by Rice notices that plasticity in the immediate vicinity of the crack tip solely determines the crack instability. The origin of γ_p that affects the instability criterion is limited within this small region. It is to be noticed that observed fracture toughness values include energies dissipated in forming the incipient crack independent of the surface energy in the instability criteria.

Another problem of the bond-breaking model for the crack instability is that the crack-tip must be atomically sharp. The reduction in γ, rather than γ_p, in the energy balance criteria implies the reduction in the cohesive strength that constitutes γ. However, the cohesive strength is still very large and an expected high tensile stress exceeds the yield stress of the material. The situation makes difficult to keep the sharpness of the crack tip to satisfy stress-controlled instability criteria.

The hydrogen effect on the crack instability criteria through plasticity is a crucial issue, but apparently macroscopic fracture appearances of HE do not rule out fracture process dominated by mechanisms other than brittle bond breaking or interface separation.

References

1. C.A. Zapffe, J. Member, C.E. Sims, Trans. AIME **145**, 225–263 (1941)
2. A.S. Tetelman, W.D. Robertson, Acta Metall. **11**, 415–426 (1963)
3. A. Ikeda, Tetsu-to-Hagané **70**, 792–802 (1984)
4. A.N. Stroh, Proc. Roy. Soc. London A **232**, 548–560 (1955)
5. A.H. Cottrell, Trans. Metall. Soc. AIME **212**, 192–203 (1958)
6. F. Garofalo, Y.T. Chou, V. Ambegaokar, Acta Metall. **8**, 504–512 (1960)
7. B.A. Bilby, J. Hewitt, Acta Metall. **10**, 587–600 (1962)
8. N.J. Petch, Philos. Mag. **1**, 331–337 (1956)
9. D. Tromans, Acta Metall. Mater. **42**, 2043–2049 (1994)
10. H. Vehoff, W. Rothe, Acta Metall. **31**, 1781–1793 (1983)
11. A.R. Troiano, Trans. ASM **52**, 54–80 (1960)
12. R.A. Oriani, P.H. Josephic, Acta Metall. **22**, 1065–1074 (1974)
13. R.M. Thomson, J.E. Sinclair, Acta Metall. **30**, 1325–1334 (1982)
14. I.-H. Lin, R. Thomson, Acta Metall. **34**, 187–206 (1986)
15. P.G. Marsh, W.W. Gerberich, Acta Metall. Mater. **42**, 613–619 (1994)
16. W.W. Gerberich, P.G. Marsh, J.W. Hoehn, in *Hydrogen Effects in Materials*, ed. by A.W. Thompson, N.R. Moody (TMS, Warrendale, 1996), pp. 539–551
17. R.A. Mulford, C.J. McMahon Jr., D.P. Pope, H.C. Feng, Metall. Trans. A **7A**, 1184–1195 (1976)
18. M. Aoki, H. Saito, M. Mori, Y. Ishida, M. Nagumo, J. Jpn. Inst. Metals **58**, 1141–1148 (1995)
19. T. Asaoka, C. Dagbert, M. Aucouturier, J. Galland, Scr. Metall. **11**, 467–472 (1977)
20. C.J. McMahon Jr., Eng. Fract. Mech. **68**, 773–788 (2001)
21. J.P. Hirth, J.R. Rice, Metall. Trans. A **11A**, 1501–1511 (1980)
22. J.R. Rice, J.-S. Wang, Mater. Sci. Eng. **A107**, 23–40 (1989)
23. Y. Misin, P. Sofronis, J.L. Bassani, Acta Mater. **50**, 3609–3622 (2002)
24. J. R. Rice, in *Proceedings of International Conference of Fracture*, vol. 1, (The Jpn Soc. Promotion Sci., Tokyo,1965), pp. A269–A318

25. P. Novak, R. Yuan, B.P. Somerday, P. Sofronis, R.O. Ritchie, J. Mech. Phys. Solids **58**, 206–226 (2010)
26. M. Yamaguchi, K. Ebihara, M. Itakura, T. Kadoyoshi, T. Suzudo, H. Kaburaki, Metall. Mater. Trans. A **42A**, 330–339 (2011)
27. M. Yamaguchi, J. Kameda, K. Ebihara, M. Itakura, H. Kaburaki, Philos. Mag. **92**, 1349–1368 (2012)
28. R. Kirchheim, B. Somerday, P. Sofronis, Acta Mater. **99**, 87–98 (2015)
29. C.A. McMahon Jr., V. Vitek, Acta Metall. **27**, 507–513 (1979)
30. M.L. Jokl, V. Vitek, C.J. McMahon Jr., Acta Metall. **28**, 1479–1488 (1980)
31. E. Smith, in *Proceedings of Conference of Physical Bases of Yield and Fracture* (Inst. Phys., Phys. Soc., Oxford, 1966), pp. 36–46
32. T. Tani, M. Nagumo, Metall. Mater. Trans. A **26A**, 391–399 (1995)

Chapter 10
Mechanistic Aspects of Fracture II ~ Plasticity-Dominated Fracture Models

10.1 Outline of Elemental Concepts of Ductile Fracture

The contrastive picture to decohesion is the so-called microvoid coalescence (MVC) that designates the process in which fracture proceeds by the successive nucleation, growth and linkage of voids. The surface of MVC fracture is characterized by dimple patterns. However, MVC process can take place in very fine scale with macroscopically irregular or crack-like appearances. Most theories of ductile fracture address the growth and coalescence process, but the void or crack nucleation and its precursory process seriously affect final fracture.

10.1.1 Void Nucleation

Two models of the dislocation-originated crack formation are shown in Fig. 9.2. Stroh's model assumed pileup at grain boundaries of dislocations moving along a slip band. Difficulties of the model to operate as an incipient crack in hydrogen-induced brittle fracture are stated in Sect. 9.1, but strain incompatibility between the matrix metal and second phase particles is viable to cause separation of the interface. Void nucleation at second phase particles are commonly observed for various metals and alloys as documented in a review article [1]. Cracking and interface decohesion of second phase particles often appear on fracture surfaces.

Some theoretical models have been presented for the cavity formation from second phase particles [2, 3]. The criterion proposed by Argon et al. for the cavity formation is that the interfacial stress reaches the ideal shear strength of the interface provided that sufficient elastic energy available to create new surfaces is stored [2]. The size and distribution of particles are parameters in the criterion originating in interactions of stress fields produced by particles. Argon et al. noted

M. Nagumo, *Fundamentals of Hydrogen Embrittlement*,
DOI 10.1007/978-981-10-0161-1_10

that small cavities less than about 100 nm are difficult to open up spontaneously because the stored elastic energy is insufficient.

The energy criterion for the formation of cavity at a particle by interface separation is given as,

$$\Delta E_{el} + \Delta E_s \leq 0, \tag{10.1}$$

where ΔE_{el} and ΔE_{s} are respectively the internal elastic energy of the particle and the energy increase in forming the new internal surfaces [3]. ΔE_{el} is a function of the stress acting at the particle. Goods and Brown expressed the criterion in terms of the critical strain taking into account the local stress exerted by dislocations near the particle [3]. The critical strain is proportional to the particle size and also depends on the particle shape, coarseness of slip and temperature.

On the other hand, fine dimples not associated with second phase particles are often found, and the refinement of the dimple size characterizes fracture surfaces of hydrogen embrittlement as described in Sect. 7.1(b). Void nucleation without second phase particles was revealed at grain and twin boundaries in titanium alloys [1], at the crack front in AISI 310 stainless steel foils [4] and in high purity single crystal silver foils [5]. Intense strain localization likely characterizes the sites for the void nucleation. A feasible origin of voids is the condensation of vacancies [4]. Generation of vacancies by interactions of moving dislocations is described in Sect. 3.2.1(b), and calculated concentration of vacancies generated by jogged dislocations is shown in Fig. 3.3 [6] as a function of axial plastic strain.

Excess vacancies might diffuse away or annihilate at sinks, but Cuttiño and Ortiz pointed out possible mechanisms to stabilize vacancy aggregates [6]; (1) the reduction in the free energy of the system by condensation of vacancies into clusters or voids, and (2) the reduction in the surface energy by chemisorption of impurity gas such as oxygen. However, the size of voids resulted from vacancy agglomeration is still very small and some mechanisms must operate to induce their growth and/or their link with the main crack.

10.1.2 Void Growth and Coalescence

Cuttiño and Ortiz simulated using a finite element method (FEM) the growth of an initial void by successive diffusing-in of vacancies and its coalescence with the main crack for Cu bicrystal [6]. Assuming the void nucleation by jogged dislocations, the growth of the void radius a during the time interval Δt was expressed as

$$\Delta a = \frac{1}{a} D(c_0 - c_s)\mathrm{d}t, \tag{10.2}$$

where D is the diffusion coefficient of vacancy, c_0 and c_{s} are respectively vacancy concentrations in remote areas and at the boundary of the void. The void grows until it reaches a critical size and then coalesces with the main crack. When *D* was assumed to be 10^{-6} m^2/s, the void was predicted to grow from the initial radius of 0.6 nm to the maximum of 230*b* with the vacancy concentration of 6.3×10^{-5}. The assumed magnitude of *D* was very large as the value at room temperature, and Cuttiño et al. postulated pipe diffusion of vacancies along dislocation lines.

The void growth is strongly affected by stress states. Deformation of fully plastic materials containing sets of cylindrical holes of elliptical cross section was calculated by McClintock in the regime of continuum mechanics [7]. In the model, a hole of semiaxes *a* and *b* with a cylindrical axis in the *z*-direction is surrounded by a cylindrical cell whose dimensions are of the order of the mean spacing between the holes. For plane-strain deformation of a hole in an infinite media, the relative growth factor is defined as

$$F_{zb} = \left(\frac{b}{l_b}\right) \Big/ \left(\frac{b^0}{l_b^0}\right), \tag{10.3}$$

where *b*, *l* and the superscript *0* denote radius, spacing and the initial value, respectively. The condition of fracture is that the growth of the holes is such that each hole touches a pair of its cell walls. The relative hole-growth factor at fracture due to *z* holes growing together in the *b* direction is

$$F_{zb}^{f} = \left(\frac{1}{2}\right) \Big/ \left(\frac{b^0}{l_b^0}\right). \tag{10.4}$$

Fracture occurs on the *ij*-plane when the *ij* growth factor is the first to reach F_{ij}^{f}. For tests with a varying stress history, fracture is thought to occur when accumulation of “damage”, defined as

$$d\eta_{ij} = d\left(\ln F_{ij}\right)/\ln\ F_{ij}^{f}, \tag{10.5}$$

reaches unity.

The hole growth with increasing strain was calculated in terms of F_{zb} for viscous and plastic materials under different stress ratios. Stress triaxiality and strain hardening strongly affect fracture strain. Strain hardening is expressed as

$$\overline{\sigma} = \sigma_1 \overline{\varepsilon}^n \tag{10.6}$$

for equivalent stress $\overline{\sigma}$ and strain $\overline{\varepsilon}$. The smaller *n* enhances the more pronouncedly hole growth. The increase in damage with increasing strain is expressed approximately as

$$\frac{d\eta_{zb}}{d\bar{\varepsilon}} = \frac{\sinh\left[(1-n)(\sigma_a+\sigma_b)/\left(2\bar{\sigma}/\sqrt{3}\right)\right]}{(1-n)\ln F_{zb}^{f}}. \tag{10.7}$$

When ratios between components of applied stress are constant, integration of Eq. (10.7) gives the fracture strain required for z-axis holes to coalesce in the b direction as

$$\bar{\varepsilon}^{f} = \frac{(1-n)\ln\left(l_b^0/2b^0\right)}{\sin\mathrm{h}\left[(1-n)(\sigma_a+\sigma_b)/\left(2\bar{\sigma}/\sqrt{3}\right)\right]}. \tag{10.8}$$

Equations (10.7) and (10.8) indicate strong effects of the transverse principal stress on reducing fracture strain rather than solely the mean stress or the maximum principal stress. The equations also show interaction between stress triaxiality and strain hardening. The effect of triaxiality is the more significant by the smaller hardening exponent.

On tensile straining of materials, necking of specimens is a crucial stage of ductile fracture. Thomason applied the notion to the coalescence of voids within materials [8]. His internal necking model is schematically shown in Fig. 10.1 [8] for initially a square array of small square holes in a plane-strain plastic field. The material is non-hardening rigid-plastic under the hydrostatic pressure P. A tension applied in the X_1 direction causes the deformation of holes. The deformation of the region between adjacent holes is constraint by outside regions of the holes against necking to take place. The constraint changes by straining associated with the change of the geometry of holes. Unstable plastic flow begins when the load L_n to

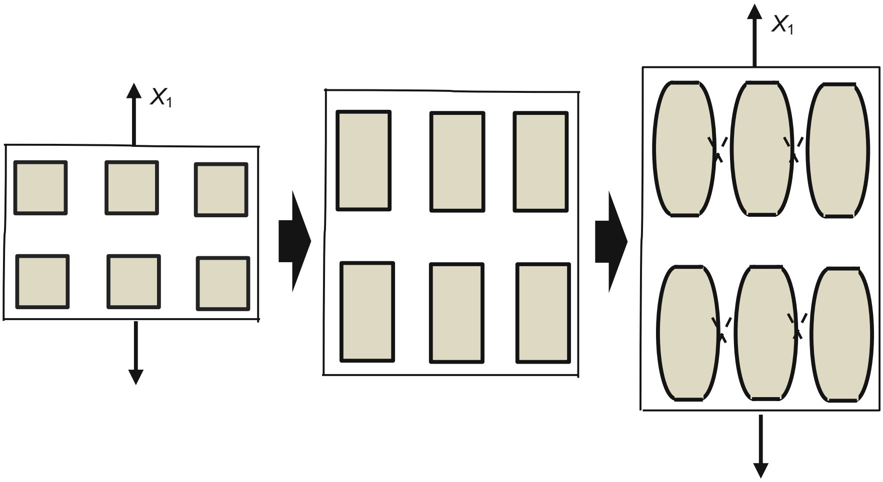

Fig. 10.1 Model of void linking by internal necking. Initially, a square array of small square holes is placed within a matrix (After Thomason [8])

cause internal necking is less than the load L_{u} for uniform flow. The mean tensile stress σ_{n} in the X_1 direction to start internal necking was given as,

$$\sigma_n\left(1-\sqrt{V_f}\right)+P<\sigma_{22}+2\tau_y, \tag{10.9}$$

where V_{f} is the volume fraction of holes, σ_{22} is any tensile stress applied in the X_2 direction and τ_{y} is the yield shear stress. Effects of V_{f}, P and σ_{22} on the post-instability strain, *i.e.* the amount of strain from the onset of macroscopic instability to the start of internal necking, were computed. The post-instability strain is significantly reduced by larger V_{f} and σ_{22} while P suppresses the reduction.

10.1.3 Plastic Instability

Internal necking is a localized breakdown of stability causing strain localization. The treatment of the problem by Thomason regarded the void coalescence as a discontinuous transition in material response from incompressible to dilatational plasticity [9]. Plastic instability that appears in hydrogen embrittlement is described in Sect. 7.2.2 about strain localization. Various factors which influence premature failure associated with plastic instability are reviewed by Onyewuenyi [10]. Plastic instability in homogeneous deformation is characterized by jump discontinuities in displacement gradient across certain surfaces such as shear bands, and it is predicted from continuum mechanics. Plastic instability is induced by materials flow in specific crystallographic planes and directions, microstructural or geometrical inhomogeneities such as inclusions, voids and free surfaces.

Rudnick and Rice assumed that instability is a bifurcation from homogeneous deformation of an initially uniform material to the localization of deformation into a planar band [11]. In an incipient non-uniform field, deformation rates vary with positions across the band but remain uniform outside the band. The coordinate system for the band is shown in Fig. 10.2 [11].

The macroscopic constitutive relation of the material is crucial. The treatment by Rudnick and Rice originally addressed fracture of brittle rock masses. For the material, elastic-plastic constitutive relations were adopted in a pressure and temperature regime showing apparent macroscopic inelastic strain and dilatancy. Shear and volumetric strain increments $d\gamma$ and $d\varepsilon$, respectively, and their plastic portions, $d^{\,p}\gamma$ and $d^{\,p}\varepsilon$, are written as

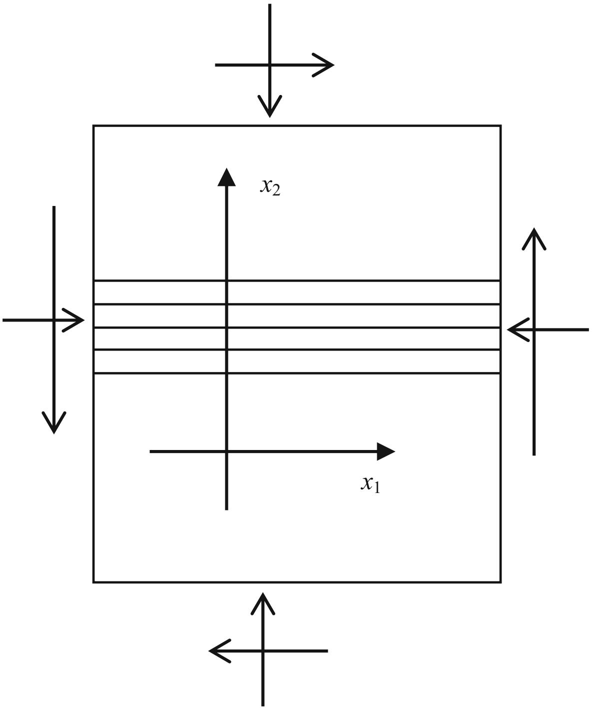

Fig. 10.2 Coordinate system for the band of localization (Rudnicki et al. [11])

$$d\varepsilon = -(d\sigma/K) + d^p\varepsilon, \;\; d\gamma = (d\tau/G) + d^p\gamma, \tag{10.10}$$

and

$$d^p\varepsilon = \beta d^p\gamma, \tag{10.11}$$

where σ is the hydrostatic stress, K and G are bulk and shear moduli, respectively, and β is the dilatancy factor. Further, the plastic hardening modulus h is defined as

$$d\tau = hd^p\gamma, \tag{10.12}$$

for constant σ. The shear stress τ *vs.* shear strain γ curve is shown in Fig. 10.3 [11].

The condition for instability was derived from the continuity of stress equilibrium to be satisfied until the start of bifurcation. The hardening modulus h varies by the orientation of the potential plane of localization and plays an important role in the instability condition. The orientation of the plane of localization requires h to be the maximum with respect to the components of the unit normal to the plane in the principal directions. The magnitude of h is a decreasing function of the amount of strain and instability takes place at the critical value h_{cr}. Stress states, values of β, and the slope of the τ *vs.* σ curve are factors that determine h_{cr}. Rudnick and Rice noted that the start of rupture was feasibly modeled as a constitutive instability.

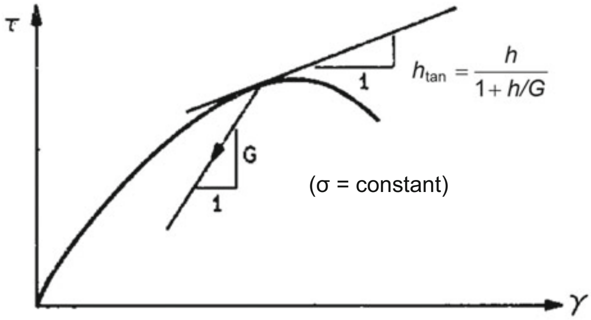

Fig. 10.3 Shear stress τ *vs.* shear strain γ curve showing the geometric interpretation of the hardening modulus h (= $\mathrm{d}\tau/\mathrm{d}^{\mathrm{p}}\gamma$), the tangent modulus h_{tan} and the elastic shear modulus G. $^{\mathrm{p}}\gamma$ denotes plastic portion of shear strain Rudnicki et al. [11])

The presence of voids is essential for ductile fracture. A constitutive relation in terms of the yield function Φ for porous material was given by Gurson [12, 13], and a form modified by Tvergaard for the bifurcation instability problem is

$$\Phi = \frac{\sigma_{eqv}^{2}}{{\sigma_y}^{2}} + 2f\,q_1 \cos\mathrm{h}\left(\frac{3q_2\sigma_m}{2\sigma_y}\right) - \left(1 + q_3 f^2\right) = 0 \tag{10.13}$$

where σ_{eqv} is the equivalent tensile stress, σ_{y} is the matrix flow stress, σ_{m} is the macroscopic mean stress, f is the void volume fraction and qs are numerical parameters [14]. $\Phi = 0$ must be satisfied at any stage of the deformation.

Needleman and Tvergaard applied Eq. (10.13) to ductile fracture of materials containing voids adopting $q_1 = q_3 = 1.5$ and $q_2 = 1$ [15]. Equation (10.13) implies that the increase in the void volume fraction lowers flow stress. The void volume fraction f increases during straining by the nucleation of new voids and the growth of existing voids. Then, the increasing rate $\dot{f}$ consists of two terms,

$$\dot{f} = \dot{f}_{\text{nucleation}} + \dot{f}_{\text{growth}}. \tag{10.14}$$

Each term in the right-hand side was given in forms of

$$\dot{f}_{\text{growth}} = (1 - f)G^{ij}\,\dot{\eta}_{ij}^{\,p}, \tag{10.15}$$

and

$$\dot{f}_{\text{nucleation}} = B\left(\dot{\sigma}_y + \dot{\sigma}_m\right) + D\,\dot{\varepsilon}_M^{\,p}. \tag{10.16}$$

where G^{ij} is the metric tensor that defined the stress deviator $s^{\mathrm{ij}} = \sigma^{\mathrm{ij}} - G^{\mathrm{ij}}\,\sigma_{\mathrm{m}}$, The $\dot{\eta}_{ij}^{\,p}$ is the plastic part of the macroscopic strain rate and $\dot{\varepsilon}_M^{\,p}$ is the effective plastic strain rate. For plastic strain-controlled void nucleation, the increasing rate of void volume fraction is written as,

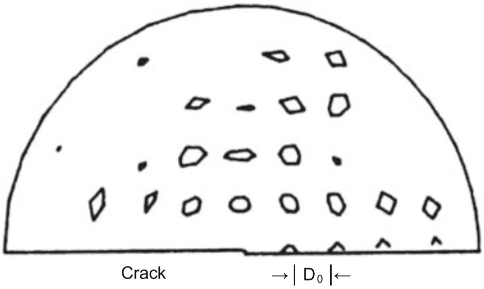

Fig. 10.4 The distribution of large particles near the initial crack tip in model material. Contours depict a constant value (=0.004) of the stress-controlled void nucleation amplitude f_N in Eq. (10.18). D$_0$ is the initial distance between particles center (Needleman et al. [15])

$$\dot{f}_{\text{nucleation}} = \frac{f_N}{s_N\sqrt{2\pi}} exp\left[-\frac{1}{2}\left(\frac{\varepsilon_M^p - \varepsilon_N}{s_N}\right)^2\right]\dot{\varepsilon}_M^p, \tag{10.17}$$

where f_N is the volume fraction of void nucleating particles, ε_N is the mean strain for nucleation and s_N is the corresponding standard deviation. For stress-controlled void nucleation with the mean stress σ_N for nucleation,

$$\dot{f}_{\text{nucleation}} = \frac{f_N}{s_N\sqrt{2\pi}} exp\left[-\frac{1}{2}\left(\frac{(\sigma_y + \sigma_m) - o_N}{s_N}\right)^2\right]\left(\dot{\sigma}_y + \dot{\sigma}_m\right). \tag{10.18}$$

The model material that Needleman and Tvergaard employed contained two types of particles: large particles that nucleate voids at relatively small strains and small particles that nucleate voids at much greater strains. The large particles were placed in regular arrays and the void nucleation was assumed stress-controlled. On the other hand, small particles were uniformly distributed and the void nucleation was strain-controlled. Figure 10.4 [15] shows an example of the model distributions of large particles near the initial crack which is represented by a semi-circular notch. Contours in the figure denote a constant value (=0.004) of the volume fraction of void-nucleating particles and D$_0$ is the initial distance between particle centers.

Stress and strain fields were computed using a finite element method, and the crack growth in ductile fracture was ascribed to the coalescence of the nearest large void with the crack tip. Ductile fracture is dominated by the interaction between the crack tip and the nearest large void, or between two neighboring large particles. An important implication is that the nucleation of small voids in the ligament between the crack tip and the large void is crucial and that the void volume fraction remains very low in the material near the surface of the growing crack. The criterion for the coalescence is that the void volume fraction in the ligament reaches a critical value, implicitly imaging the loss of the stress-carrying capacity.

The coalescence of the crack tip with a neighboring large void is characterized by the appearance of a small jog in the crack opening displacement *vs* *J*-integral curves as schematically shown in Fig. 6.11 [15]. The prediction was experimentally justified for the stable crack growth initiation at three-point bending tests of low carbon steel [16]. Hydrogen effects promoting the onset of the slow crack growth without a large step-wise advance are described in Sect. 6.2.1 with Fig. 6.12. Needleman and Tvergaard assumed homogeneously distributed small particles as the nucleation sites of small void [15]. Uniformly distributed strain-controlled nucleation sites are essential, but their model does not specify the origin of voids and allocates aggregates of vacancies.

10.2 Hydrogen-Enhanced Localized Plasticity Theory

Beachem observed a pronounced decrease in torque by hydrogen for torsion tests of AISI 1020 steel pipe specimens [17] as described in Sect. 5.2(b). Simultaneously conducted wedge-loaded compact tension tests for AISI 4340 steel revealed successive changes in the fracture mode with decreasing stress intensity factor, as described in Sect. 7.1(f). Beachem postulated that hydrogen in solid solution increases dislocation activity and expands a plastic zone ahead of the crack tip containing more inclusions that act as void nuclei. The model is hydrogen-assisted cracking, HAC, rather than the intrinsic embrittlement by hydrogen. However, the effects of hydrogen on the macroscopic flow stress are not yet conclusive and hardening rather than softening has been commonly reported for bulky specimens of commercial grade steels.

Many experiments that exhibit involvement of plasticity in HE, even for apparently brittle-like fracture, are described in Sect. 7.1. Enhanced mobility of dislocations revealed by in situ observations under hydrogen atmosphere, described in Sect. 5.4, is a strong base of notions that claim the primary role of plasticity in HE. The hydrogen enhanced localized plasticity (HELP) has been theoretically rationalized with respect to the shielding of elastic interactions between dislocations and between dislocations and other stress centers as shown by Eq. (5.11) in Sect. 5.5.1. However, numerical estimations showed that fairly high hydrogen concentrations over 0.01 are necessary to exhibit the shielding effects by hydrogen. First-principles calculations have been conducted on interactions between hydrogen and screw dislocations, Sect. 3.1.2, and on the mobility of dislocations, Sect. 5.5.2.

The defect acting agent (DEFACTANT) mechanism described in Sect. 3.1.2 for the stabilization of lattice defects by hydrogen is a general concept from thermodynamic viewpoint. With respect to HELP, the DEFACTANT mechanism predicts that the decrease in the formation energy by hydrogen activates dislocation sources [18]. It was then deduced that newly generated dislocations push former dislocations together with the ease of kink pair formation and that the sequence appears as the observed enhanced mobility of dislocations by hydrogen [19].

The HELP mechanism is viable, but the enhanced dislocation mobility per se is a deformation mechanism, not the mechanism of plastic fracture. As described in Sect. 7.1(d), Martin et al. postulated that the formation of very small ~50 nm mounds immediately beneath the fracture surface of pipe-line steels is a consequence of either near-surface relaxations of newly created surfaces or reflections of underlying dislocation structures [20]. However, the proposed function of HELP in forming the mounds is no more than to prepare high dislocation densities and hydrogen concentrations [20]. Strain discontinuities brought about at internal boundaries or deformation bands are viable to create voids as Nibur et al. postulated [21], but the conditions for the void nucleation such as Eq. (10.1) must be satisfied. Further, close examinations of similar fracture surfaces revealed nanovoid nucleation and growth [22] rather than "mound-on-valley" separation that Martin et al. claimed. The findings are against the interface separation induced by strain discontinuity as the result of the HELP mechanism.

A notion that relates the HELP mechanism to promoted fracture is a synergistic interplay of the HELP and HEDE mechanisms as proposed by Novak et al. [23] described in Sect. 9.4.1. There, the fracture criterion was essentially that of brittle fracture models. The idea was extended as the HELP-mediated decohesion model to mound-like quasi-cleavage fracture surfaces of pipeline steels [20]. The model postulates that hydrogen transported by activated dislocations causes decohesion at grain boundaries or martensite lath boundaries [24, 25].

On the other hand, a mechanistic consequence of the HELP mechanism to promote fracture was presented by Liang et al. [26] following the theory of plastic instability presented by Rudnicki and Rice [11]. Liang et al. employed a constitutive relation expressing the flow stress σ as a function of the total hydrogen concentration c (in H/M) in the form

$$\sigma(\varepsilon^p, c) = \sigma_0(c)(1 + \varepsilon^p/\varepsilon_0)^N, \tag{10.19}$$

where $\sigma_0(c)$ is the yield stress, ε^{p} is the effective plastic strain, ε_0 is the yield strain and the hardening exponent N was assumed to remain unaltered by hydrogen. The form of σ_0 (c) was tentatively assumed using a softening parameter ξ in the form

$$\sigma_0(c) = \sigma_0\{(\xi - 1)c + 1\}. \tag{10.20}$$

Stress-strain curves in terms of the normalized effective stress σ_e/σ_0 plotted against ε^{p} are shown in Fig. 10.5 [26] taking $\xi = 0.1$, $N = 0.1$, and σ_0 (the yield stress for $c = 0) = 400$ MPa.

Hydrogen-induced lattice dilatation due to the partial molar volume of hydrogen was included in the deformation rate tensor. An important assumption was that hydrogen is supplied from environment during the test keeping the chemical potential of lattice hydrogen constant at c_0. It was assumed that the total hydrogen concentration c increases due to trapping by the increasing density of dislocations during straining. The assumptions imply that hydrogen trapped in dislocations decreases the flow stress and enhances the decrease in strain hardening.

The employed condition of plastic instability is the model by Rudnicki-Rice for the bifurcation from continued homogeneous deformation to a localized deformation in a band of intense shear. The results of calculations following Rudnicki-Rice's procedure are shown in Fig. 10.6 [26] in terms of the hardening modulus

Fig. 10.5 Normalized effective stress σ_{eff} *vs.* plastic strain ε^{p} curves at various initial hydrogen concentrations c_0 calculated using Eqs. (10.19) and (10.20). The hardening exponent $N = 0.1$, the softening parameter $\xi = 0.1$ and σ_0 is the yield stress in the absence of hydrogen (Liang et al. [26])

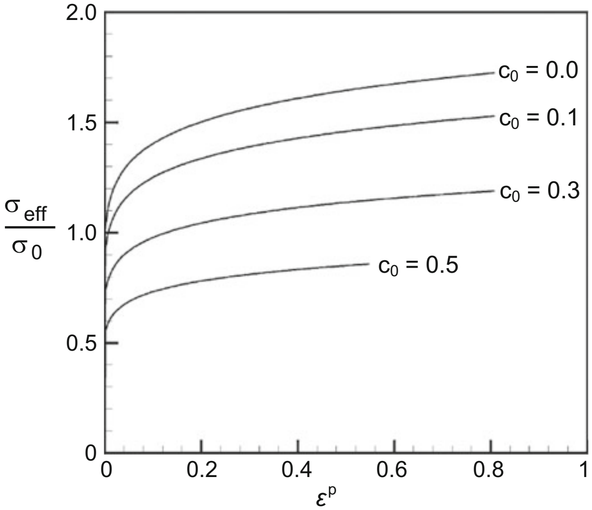

Fig. 10.6 Plot of the tangential modulus h and the critical tangent modulus h_{cr} against the normalized applied macroscopic strain $\varepsilon_{22}/\varepsilon_{\text{o}}$ at various initial hydrogen concentrations. The hardening exponent $N = 0.1$ and the softening parameter $\xi = 0.1$, and shear localization occurs when $h = h_{\text{cr}}$ (Liang et al. [26])

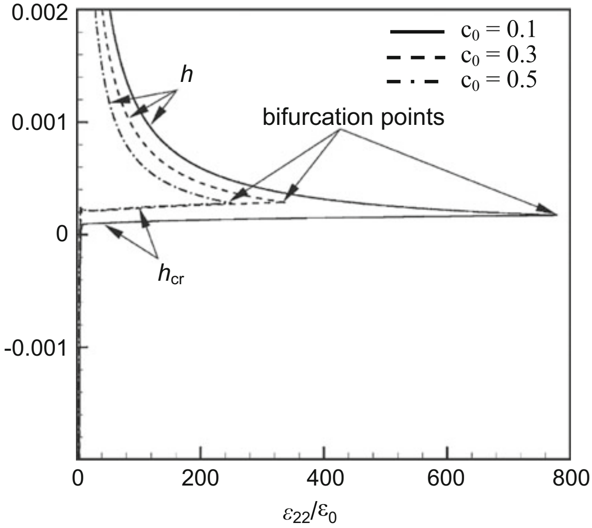

h against the normalized applied macroscopic strain for three initial hydrogen concentrations. The modulus h is defined as

$$h = \left[\frac{\partial \sigma_e}{\partial \varepsilon^p} + \left(\frac{\partial \sigma_e}{\partial c}\right)\left(\frac{\partial c}{\partial \varepsilon^p}\right)\right] \Big/ 3. \tag{10.21}$$

External tensile stress is applied along the x_2 direction, and the bifurcation takes place when h that decreases with increasing ε_{22} reaches the critical value h_{cr}. The higher initial hydrogen concentrations decrease *h* the more promptly and reduce the critical strain for the bifurcation the more prominently.

Hydrogen-induced softening and lattice dilatation at micro-scale regions can induce shear localization even though the material as a whole continues to exhibit positive hardening. The idea might be qualitatively reasonable, but Fig. 10.6 indicates that unrealistically high initial hydrogen concentrations, ≥ 0.2 in atomic ratio, are required to cause discernible reductions in the uniform elongation. The misfit with experimental observations might be improved by modified flow rules, but consistency with characteristic features of hydrogen embrittlement, such as fracture surfaces described in Sect. 7.1, is a subject to be further examined.

10.3 Adsorption-Induced Dislocation Emission Theory

Fractographic features such as fine, shallow dimples, striations, quasi-cleavage with steps and tear ridges that characterize hydrogen embrittlement (Sect. 7.1) are quite similar to the features of stress corrosion cracking (SCC) and liquid-metal embrittlement (LME). Since LME occurs even at high crack velocities and for systems of very low mutual solubilities, Lynch proposed that some surface effects such as the adsorption of hydrogen at crack tips play a critical role in hydrogen embrittlement [27, 28]. For LME, adsorption must occur only at crack tips and Lynch proposed a model that adsorbed hydrogen enhances the injection of dislocations from the crack tip and promotes the coalescence of the crack with voids ahead of the crack.

The elementary fracture mode envisaged is the microvoid coalescence (MVC) process. The qualitative explanation is that adsorbed hydrogen at crack-tip reduces the interatomic strength of metals and facilitates the dislocation nucleation and injection into the bulk. This adsorption-induced dislocation emission (AIDE) mechanism also claims that hydrogen at subsurface sites is able to contribute to bond-weakening. Void nucleation at small and large particles was assumed in areas of large strain such as localized slip around crack tips, slip band intersections or dislocation-cell boundaries.

Both the HELP and AIDE mechanisms consider the function of hydrogen in fracture from the viewpoint of strain localization for inducing void nucleation. The difference between the two mechanisms is that HELP focuses on the dislocation mobility enhanced by hydrogen while AIDE considers the enhancement of the dislocation injection from the surface. The mechanism addressed to transgranular fracture was also applied to apparently smooth intercrystalline facets that exhibited small dimples. Lynch assumed second phase particles as the void source, but he noticed the existence of dimples not associated with particles, smaller than dimples produced in air, sometimes difficult to resolve by scanning electron microscopy. The origin of such mall voids was not inquired. The AIDE model addresses fractographic features that associate with the crack extension. However, similar fractographic features appear for embrittlement caused by internal hydrogen which also promotes accumulation of damage as described in Sect. 7.3 characterizing hydrogen embrittlement.

10.4 Autocatalytic Void-Formation and Shear-Localization Theory

Flow localization into shear band induced by plastic instability is a critical stage in ductile fracture as described in Sect. 10.1.3. In terms of continuum mechanics, a low macroscopic strain-hardening rate favors instability. However, very large strain and hydrogen concentrations are necessary to initiate flow bifurcation in a homogeneous material according to a computation based on the HELP mechanism as shown in Fig. 10.6. On the other hand, microstructural or geometrical inhomogeneities also cause flow localization. Hydrogen effects on enhancing strain localization along characteristic slip lines at the U-notch root of a bend specimen of spheroidized steel are shown in Fig. 7.15 in Sect. 7.2.2. Reentrant portions of a roughened surface as well as particles within slip bands act as trigger sites of plastic instability, but the onset of surface rumpling occurred well before the profuse void formation was attained in the bulk [29]. Associated degradation in fracture toughness is shown in Fig. 6.10 in Sect. 6.2.1 about mixed mode I/III compact tension tests. It was then deduced that the major role of hydrogen is to promote plastic instability directly [29].

Hirth et al. proposed the autocatalytic model of hydrogen embrittlement, claiming that the nucleation of voids enhances the formation and propagation of shear bands in which voids are further formed [30, 31]. The function of hydrogen was ascribed to promote particle decohesion or cracking at second phase particles. The model does not require the HELP mechanism for the dislocations activity but implicitly assumes high hydrogen fugacity for the interface decohesion. As stated in Sect. 7.2.2, the steels used for experiments had a substantial ductility before fracture. A similar U-notch bend test was conducted for a high strength AISI 4340 steel of 1.35 GPa in tensile strength. The midspan-deflection at the onset of load drop was progressively reduced with the increasing current density of cathodic electrolysis [32]. In the midplane section of precharged specimens, a narrow mode II crack extended following characteristic slip paths and the length of the spiral part of the crack increased with decreasing charging current. The extending crack connected to mode I intergranular cracks in a region apart from the notch surface. In contrast to low strength steels, it was considered that the crack initiated internally first and connected to the surface. However, the critical notch-root strain at the crack initiation was nearly constant for three different notch-root radii.

It was deduced that the dominant role of hydrogen is to promote plastic instability and that the crack nucleation within the plastic zone is the consequence of a combination of the hydrogen concentration and the total stress. On the fracture surface, MnS was observed at the bottom of large dimples, but the origin of small dimples that became smaller and more uniform by hydrogen charging was not definitely mentioned. Experiments that the theory based on were mostly conducted under a high hydrogen fugacity, but the underlying idea of the autocatalytic model about plastic instability will be generally provided that the void source is not limited to second phase particles as will be stated in the following section.

10.5 Hydrogen-Enhanced Strain-Induced Vacancy Theory

Plastic deformation is deeply involved in hydrogen embrittlement (HE), and the primary player of plasticity is the dynamics of dislocations. Functions of dislocations in fracture are multiple. The increase in the density of dislocations and their interactions set up substructures and local stress and strain fields in which fracture events take place. On the one hand, dislocation dynamics also bring about damage that deteriorates mechanical performance of materials. The term "damage" here denotes in a broader sense deterioration of crystallinity rather than flaws such as cracks and voids. The function of hydrogen in embrittlement is to be considered in the context of dislocation dynamics and resultant microstructural changes.

The hydrogen-enhanced strain-induced vacancy (HESIV) mechanism proposed by Nagumo [33] claims that hydrogen enhances the strain-induced creation of vacancies leading to premature fracture. Excess vacancies are stabilized and their mobility is reduced by combining with hydrogen, thus forming clusters that act as void sources or reducing the stress-carrying capacity of the material. Figure 10.7 illustrates the creation and clustering of vacancies forming microcracks in strain-concentrated area close to a barrier for the slip extension. The HESIV mechanism has shifted the viewpoint on HE from hydrogen itself to hydrogen-related damage that leads to premature fracture.

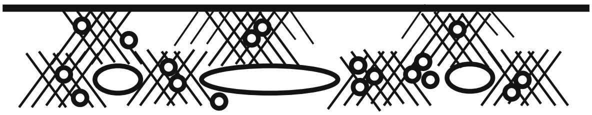

Fig. 10.7 Illustration of the HESIV model for the creation and clustering of vacancies forming microcracks in strain-concentrated area close to a barrier for slip extension

10.5.1 Brief Summary of Findings

(a) Hydrogen-enhanced creation of strain-induced vacancies

The creation of vacancies associated with plastic straining has been exhibited by means of thermal desorption analysis of hydrogen as shown in Fig. 3.2 for iron and in Fig. 2.4 for eutectoid steel. Hydrogen was introduced as the tracer of lattice defects, and the increase is fairly general for other steels and alloys. The vacancy-type nature of the lattice defects trapping hydrogen was demonstrated by annealing experiments of strained materials by means of thermal desorption analysis (TDA) as shown in Fig. 3.2 and in Figs. 3.8, 3.9 and 3.10. The vacancy-type nature of strain-induced defects is confirmed by positron annihilation spectroscopy (PAS) which is a more direct method to identify vacancies and their clusters. The PAS results shown in Figs. 3.11 and 3.12 are consistent with TDA results. The crucial finding is that hydrogen enhances preferentially the creation of vacancies as shown in Table 3.4.

Ion-implantation experiments shown in Fig. 3.6 and Table 3.3 validate high densities of vacancies due to the stabilization by hydrogen. Ion-implantation experiments also revealed the decrease in the mobility of vacancies by coupling with hydrogen and by forming clusters. Theoretical estimations of high densities of vacancies resulting from interactions between dislocations are described in Sect. 3.2.1(b). Binding of hydrogen with vacancies reduces the formation energy and then increases the density of vacancies as described in Sect. 3.2.3(b). Further, a first-principles calculation on the mobility of vacancies predicted a high density of vacancies left behind jog-dragging of screw dislocations as the result of coupling with hydrogen. The findings support the notion that interactions between hydrogen and excess vacancies result in high densities of vacancies and their clusters.

(b) Correlations with the susceptibility to hydrogen embrittlement

Compositions and microstructures strongly affect the susceptibility to hydrogen embrittlement of steels even of the same strength levels. The origins are ascribed to the extent of the strain-induced creation of vacancies. Good correlations between the susceptibility and the amount of strain-induced vacancies are demonstrated for high strength martensitic steels with the prior austenite grain size effects in Figs. 8.6 and 8.7 and manganese content effects in Figs. 7.8 and 8.8. Positron annihilation spectroscopy revealed more prominent clustering of vacancies in Type 304 austenitic stainless steel than in Type 316 L as described in Sect. 7.2.1(b) corresponding to their different susceptibilities to HE.

Strain-rate and temperature dependences of the susceptibility to HE, shown in Fig. 6.3, characterize HE of steels. In tensile tests of cold-worked eutectoid steel, it was demonstrated that the enhanced degradation by reducing the strain rate was associated with increasing amounts of strain-induced vacancies, as shown in Fig. 6.4. In experiments to investigate cumulative effects of loading-modes, cyclic prestressing in the presence of hydrogen degraded tensile properties of martensitic steel. The degradation was more prominent with lower strain rate at cyclic prestressing as shown in Fig. 7.18, and the effects of strain rates at cyclic prestressing were well related to the absorption capacity of tracer-hydrogen trapped in vacancies, *i.e*. the density of strain-induced vacancies as shown in Fig. 7.19.

(c) Damage accumulation and superposing effects of loading-modes

Deterioration of materials under external stress precedes fracture to take place. Hydrogen-enhanced strain localization and deterioration of crystallinity along twin boundaries are shown in Figs. 7.13 and 7.16, respectively, for Type 304 austenitic stainless steel. Creation of vacancies in the incubation period prior to the onset of fracture was revealed as damage in materials. In sustained-loading delayed fracture tests of high strength steels, the increase in absorbed hydrogen is not monotonic as shown in Figs. 6.23 and 6.24. Time-dependent change of the amount of lattice defects during the incubation period was detected by means of TDA of hydrogen used as the tracer. As shown in Fig. 6.25, the amount of tracer-hydrogen gradually increased with loading-time after an initial drop and its final amount was very high in portions close to the fracture surface. Simultaneously conducted positron annihilation spectroscopy revealed the vacancy-type nature of the defects. Hydrogen enhancement of the creation of defects was revealed in the incubation period of fatigue failure by means of TDA as shown Fig. 6.17 for rotational bending fatigue tests of high strength Si-Cr steel. The results are consistent with the promotion of fatigue failure in the presence of hydrogen.

Hydrogen degradation appears in mechanical tests with various loading-modes, but deterioration of materials preceding the onset of fracture will be common for various tests. Then, hydrogen effects on degradation are cumulative for a material subjected to various loading histories as described in Sect. 7.3.2. Fig. 7.20 for delayed fracture tests of prefatigued Si-Cr martensitic steels demonstrates that damage accumulated during prefatigue promotes fracture in delayed fracture tests. Annealing experiments shown in the figure indicate that damage concerned is vacancies. Figure 7.21 for tensile tests of high strength steel initially subjected to sustained-loading in a corrosive solution shows degradation of tensile properties due to vacancy-type defects introduced by the preceding sustained-loading. Further, the effects of cyclic stressing prior to tensile tests, shown in Figs. 7.18 and 7.19, show the essential role of strain-induced vacancies in degradation through accumulation of damage.

(d) Model experiments for the role of vacancies

Most studies so far conducted for the mechanism of HE remark hydrogen effects on the crack initiation and growth. The HESIV mechanism addresses deterioration of materials rather than hydrogen itself as the essential factor of degradation. A more direct demonstration of the essential role of vacancies in HE was the intermediate unloading and annealing experiments conducted during tensile tests of hydrogenated iron and Inconel 625, shown in Fig. 6.6. It demonstrates that the degradation at tensile tests was caused by vacancy-originated damage produced in the sustained-loading stage while hydrogen was absent at the time of fracture.

10.5.2 Crack Growth Resistance and its Microscopic Origin

The functions of vacancies in the susceptibility to HE must be incorporated in the mechanics of fracture. The crack propagation in ductile fracture proceeds sequentially following the nucleation, growth and linkage of voids. The crack growth resistance curve, *R*-curve, described in Sects. 6.2.1 and 6.2.2(c), gives a link between the total energy dissipation rate and microscopic processes of fracture through the constitutive relation in calculating the *J*-integral.

Figure 10.8 [34] shows *R*-curves obtained by three-point bend tests of three low carbon ferrite-pearlite steels of about 450 MPa in tensile strength. The three steels contain 2 mass % of (Mn + Ni) with varied Mn/Ni ratios, and the compositions resulted in different amounts of carbides along grain boundaries. The steels used for Figs. 6.14 and 7.5 are Steel B and Steel A, respectively, used for Fig. 10.8. The constraint factor, η, is defined as the fraction of grain boundaries length occupied by hard phases, such as carbides and pearlite that block slip extension across grain boundaries, to the total grain boundary length. The values of η are 58.1, 33.2 and 43.5 % for steel A, B and C, respectively.

Lattice defects induced by plastic straining were detected using hydrogen as the tracer. Figure 10.9 [34] shows thermal desorption curves of tracer-hydrogen (tritium in this case) introduced to the three steels strained to 20 % at room temperature. When straining was not given, hydrogen (tritium) absorption capacities were almost the same in the three steels. For strained steels, the amounts of tracer-tritium were the larger for steels with the higher constraint factors, and the tracer-tritium was diffusive at room temperature.

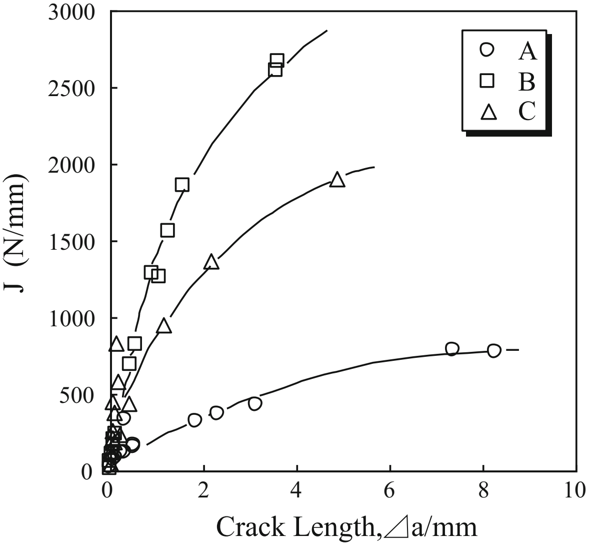

Fig. 10.8 *R*-curves of three low carbon steels of similar compositions except Mn/Ni ratios.for 2 mass % of (Mn + Ni). Three steels have different constraint factors for slip extension across grain boundaries. Tests are conducted at 20 °C (Nagumo et al. [34])

Fig. 10.9 Thermal desorption profiles of tritium introduced to the three steels used in Fig. 10.7 strained to 20 % at 20 °C (Nagumo et al. [34])

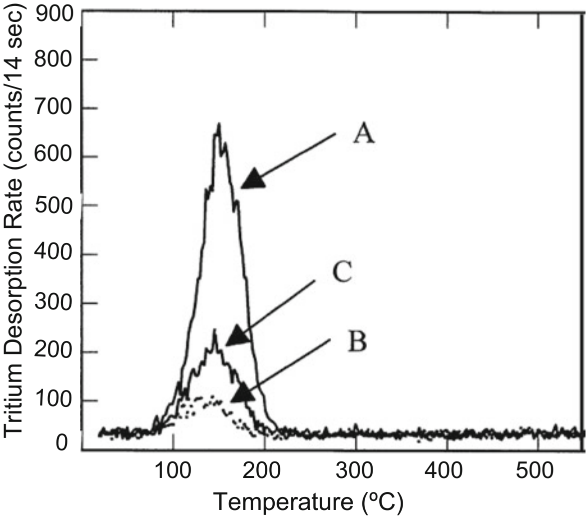

Fig. 10.10 Correlation between the constraint factor and the total amount of the thermally desorbed tritium from the three steels in Fig. 10.7 strained to 20 % at different temperatures (Nagumo et al. [34])

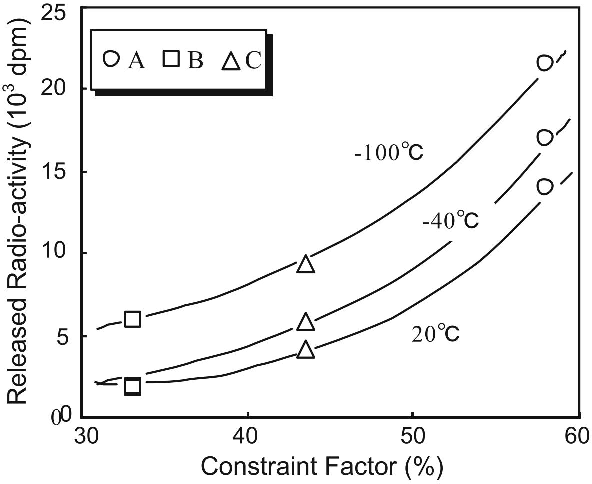

A critical issue is the function of the constraint phases on R-curves. The three steels are characterized by different constraint factors, and Fig. 10.10 [34] plots the amounts of tracer-hydrogen in terms of the released radio-activity (the disintegration per minute, dpm) as a function of the constraint factor for specimens strained to 20 % at different temperatures. The amounts of tracer-hydrogen correspond to those of strain-induced defects. The results imply that the constraint of slip extension, likely due to grain-boundary carbides, causes strain concentration and enhances the creation of strain-induced vacancies that trap tracer-hydrogen. A high density of vacancies leads to the formation of voids and promotes fracture to proceeds. The results correspond to the dependence of *R*-curves on slip constraint shown in Fig. 10.8.

10.5.3 Simulation of R-Curve and Strain Localization Near the Crack-Tip

The correspondence between *R*-curves and the density of strain-induced vacancies relates macroscopic mechanics to microscopic processes of fracture. The *J*-integral is calculated from the stress and strain fields near the crack tip as described in Sect. 6.2.1. Yoshida computed the stress and strain fields near the crack tip by means of a finite element method using the constitutive relations Eq. (10.13) for porous materials and experimentally obtained flow stress [35]. Equation (10.17) was adopted for the calculation of the plastic strain-rate controlled void-nucleation rate using experimentally determined volume fractions of void nucleating particle, f_N. Actually, f_N was measured by a scanning electron microscope on a vertical cross section of specimens subjected to tensile straining up to ε_N just before the maximum stress. The experimental value of f_N for Steel B was 0.02. Void nucleating particles were hard phases such as cementite layer or pearlite existing along grain boundaries.

The *J*-integral values were calculated at successive extensions of a crack and Fig. 10.11 [35] plots calculated *J*-integral values on the experimental *R*-curves for Steel B in Fig. 10.8 at two test temperatures. The agreement between the calculation and experiment is satisfactory. Insensitivity to test temperature is a characteristic feature of *R*-curve. The simulation of *R*-curve shown in Fig. 10.11 validated the feature. The origin is the opposite temperature dependencies of the flow stress and strain by canceling each effect on the buildup of strain energy for *J*-integral [35].

Hydrogen effects on the *R*-curve shown in Fig. 6.14 are observed with a steel of quite similar compositions as Steel B in Fig. 10.8. Both experimental and computed

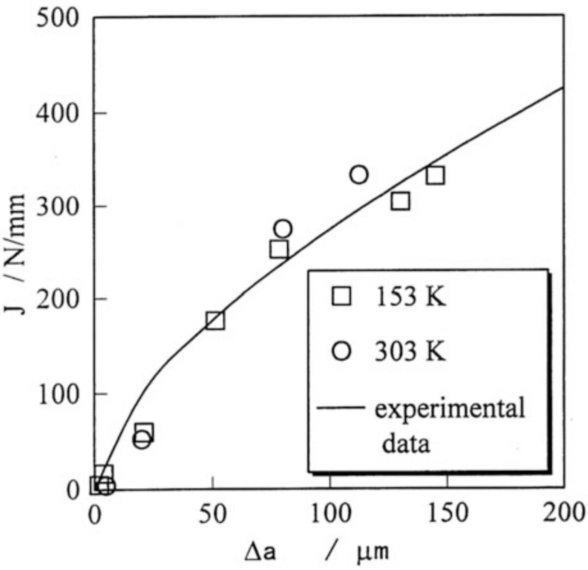

Fig. 10.11 Comparison between calculated and experimental R-curves for Steel B in Fig. 10.7 tested at different temperatures (Yoshida et al. [35])

J-integral values are plotted and the computation was conducted in a similar way as for Fig. 10.11 using values of f_N raised from 0.02 for the hydrogen-free to 0.035 for the hydrogen-charged specimens [36]. It is to be noticed that the constraint phases in the original microstructure were not affected by hydrogen-charging when straining was not applied. The increase in f_N takes place at the time of straining in the presence of hydrogen, and the coincidence of experimental and computational results in Fig. 6.14 represent the mechanistic effect of the HESIV mechanism on the crack growth.

The constitutive relation Eq. 10.13 was also successfully applied to the analysis of the start of stable crack from the pre-crack as described in Sect. 6.2.1. The steel used for Fig. 6.12 is Steel A in Fig. 10.8. The notion common to the crack initiation and propagation is that the increased density of small voids reduces the stress-carrying capacity of the matrix in front of the crack and promotes the onset of plastic instability.

Strain localization is a feature that characterizes deformation at hydrogen embrittlement as described in Sect. 7.2.1, and the intense creation of vacancies is closely related to strain localization. The FEM calculation using the constitutive relation Eq. 10.13 revealed a substantial enhancement of strain localization near the crack-tip when hydrogen was present [36]. Distributions of voids ahead of the crack after the advance of 200 μm were computed for Steel B [36]. Figure 10.12 [36] shows the distribution of the volume fraction of nucleation voids $f_{\mathrm{nucleation}}$ with and without hydrogen charging. The enhanced localization of voids well explains fractographic features of HE such as the refinement of dimple size and quasi-cleavage fracture surface. However, simulations of R-curves shown in Figs. 10.11 and 6.14 are for low carbon ferrite-pearlite steel of a medium strength level. Further examinations for high strength steels are necessary.

10.6 Summary of Ductile Fracture Models

Features characterizing hydrogen embrittlement of steels indicate involvement of plasticity in most cases even for IG fracture of high strength steels. The function of hydrogen on the role of dislocations has been ascribed to either the increase in either the mobility (HELP) or the density (AIDE and DEFACTANT) of dislocations. The mechanistic outcome of activated dislocations, however, is not straightforward to fracture events. Postulated mechanisms are the decrease in the flow stress promoting plastic instability or the increase in the number of piled-up dislocations resulting in the interface decohesion at second phase particles. Alternatively, the HELP-mediated decohesion model postulates enhanced hydrogen transport by activated dislocations to cause decohesion at grain boundaries or martensite lath boundaries. The autocatalytic model remarks synergistic effects of particle cracking by hydrogen and plastic instability induced by the cracks, resulting in the void sheet formation along slip lines. The viability of a model

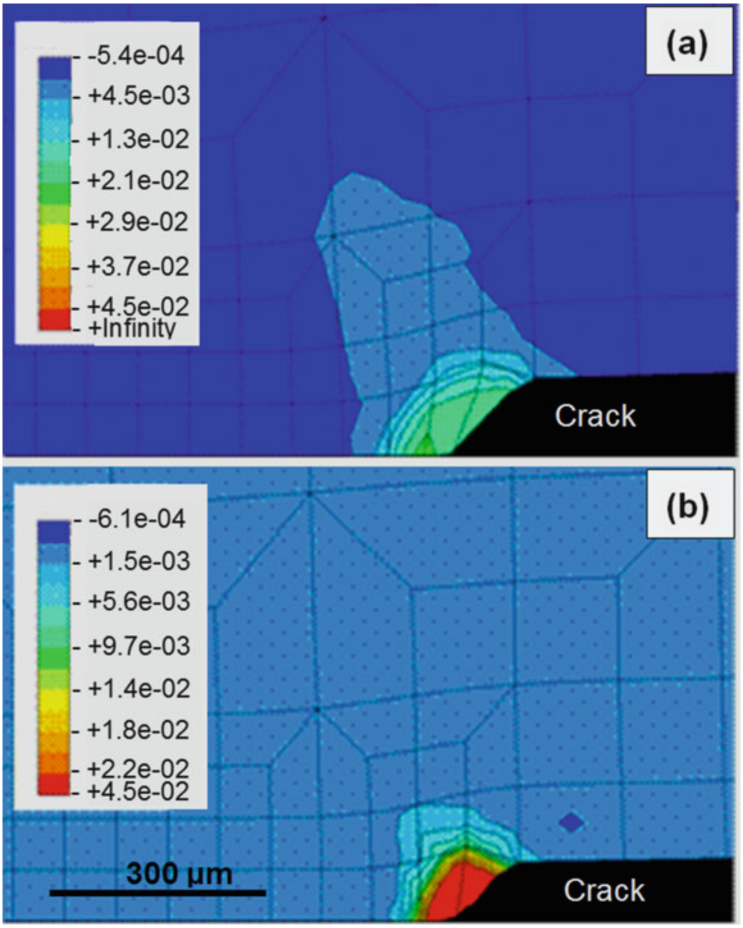

Fig. 10.12 Calculated distributions of nucleation void volume fractions ahead of the crack in Steel B in Fig. 10.7 after the crack advance of 200 μm (**a**) without and (**b**) with hydrogen (Nagumo et al. [36])

should depend on situations where the concentration and the fugacity of hydrogen satisfy fracture criteria.

The HESIV model, on the other hand, remarks on the role of vacancies and their clusters created by interactions between moving dislocations. Hydrogen effects are ascribed to the stabilization of vacancies increasing the density of vacancies and promoting their clustering. The model addresses hydrogen effects in successive stages of fracture; accumulation of damage, initiation of microvoids or cracks and their growth. The constitutive relation that incorporates the void volume fraction that increases with strain for porous materials well describes observed mechanistic behaviors. Clustering of vacancies is postulated as the embryo of voids, but the promoted plastic instability is essential for premature fracture. The function of high

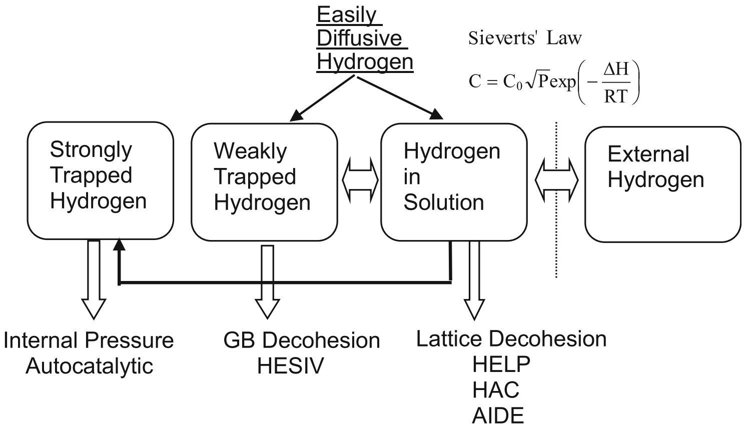

Fig. 10.13 Positions of proposed models for hydrogen embrittlement with respect to states of hydrogen in materials (Nagumo [33])

densities of vacancies on instability caused by deteriorated crystallinity is expected to be described by some other mechanistic treatments.

Major models so far presented on the mechanism of HE are positioned in Fig. 10.13 [33] with respect to the states of hydrogen concerned with each model. Both the HELP and HESIV models premise the role of activated dislocations, but the HESIV claims the primary role of vacancies created by interactions between moving dislocatons. Deformation microstructures that characterize HE such as fractographic features and localized deformation are difficult to discriminate between the two models. For a definite understanding, revealing the entity of nanoscale damage in the entire fracture process would be decisive.

References

1. R.H. Van Stone, T.B. Cox, J.R. Row Jr., J.A. Psioda, Int. Metals Rev. **30**, 157–179 (1985)
2. A.S. Argon, J. Im, R. Safoglu, Metall. Trans. A **6A**, 825–837 (1975)
3. S.H. Goods, L.M. Brown, Acta Metall. **27**, 1–15 (1979)
4. Q.-Z. Chen, W.-Y. Chu, Y.-B. Wang, C.-M. Hsiao, Acta Mater. **43**, 4371–4376 (1995)
5. R.L. Lyles Jr., H.G.F. Wilsdorf, Acta Metall. **23**, 269–277 (1975)
6. A.M. Cuttiño, M. Ortiz, Acta Mater. **44**, 427–436 (1996)
7. F.A. McClintock, Trans. ASME, J. Appl. Mech. **35**, 363–371 (1968)
8. P.F. Thomason, J. Inst. Met. **96**, 360–365 (1968)
9. P.F. Thomason, Acta Metall. **29**, 763–777 (1981)
10. O.A. Onyewuenyi, in *Hydrogen Degradation of Ferrous Alloys*, ed. by R.A. Oriani, J.P. Hirth, M. Smialowski (Noyes Pub, Park Ridge, 1985), pp. 414–453
11. J.W. Rudnicki, J.R. Rice, J. Mech. Phys. Solids **23**, 371–394 (1975)
12. A.L. Gurson, Trans. ASME, J. Eng. Mater. Tech. **99**, 2–15 (1977)
13. A.L. Gurson, in *Fracture 1977, Proc. The 4th Int. Conf. Fracture*, ed. by D.M.R. Taplin, vol. 2 (University Waterloo Press, Wateloo, 1977), pp. 357–364
14. V. Tvergaard, J. Mech. Phys. Solids **30**, 399–425 (1982)

15. A. Needleman, V. Tvergaard, J. Mech. Phys. Solids **35**, 151–183 (1987)
16. Y. Fujii, A. Kikuchi, M. Nagumo, Metall. Mater. Trans. A **27A**, 469–471 (1996)
17. C.D. Beachem, Metall. Trans. **3**, 437–451 (1972)
18. R. Kirchheim, Scr. Mater. **62**, 67–70 (2010)
19. R. Kirchheim, Acta Mater. **55**, 5139–5148 (2007)
20. M.L. Martin, I.M. Robertson, P. Sofronis, Acta Mater. **59**, 3680–3687 (2011)
21. K.A. Nibur, B.P. Somerday, D.K. Balch, C. San Marchi, Acta Mater. **57**, 3795–3809 (2009)
22. T. Neeraji, R. Srinivasan, J. Li, Acta Mater. **60**, 5160–5171 (2012)
23. P. Novak, R. Yuan, B.P. Somerday, P. Sofronis, R.O. Ritchie, J. Mech. Phys. Solids **58**, 206–226 (2010)
24. A. Nagao, C.D. Smith, M. Dadfarnia, P. Sofronis, I.M. Robertson, Acta Mater. **60**, 5182–5189 (2012)
25. M.L. Martin, B.P. Somerday, R.O. Ritchie, P. Sofronis, I.M. Robertson, Acta Mater. **60**, 2739–2745 (2012)
26. Y. Liang, P. Sofronis, N. Aravas, Acta Mater. **51**, 2717–2730 (2003)
27. S.P. Lynch, Acta Metall. **32**, 79–90 (1984)
28. S.P. Lynch, Acta Metall. **36**, 2639–2661 (1988) (overview)
29. O.A. Onyewuenyi, J.P. Hirth, Metall. Trans. A **14A**, 259–269 (1983)
30. J.A. Gordon, J.P. Hirth, A.M. Kumar, N.E. Jr. Moody, Metall. Trans. A **23A**, 1013–1020 (1992)
31. J.P. Hirth, in *Hydrogen Effects on Materials*, ed. by A.W. Thompson, M.R. Moody (TMS, Warrendale, 1996), pp. 507–522
32. T.D. Lee, T. Goldenberg, J.P. Hirth, Metall. Trans. A **10A**, 439–448 (1979)
33. M. Nagumo, Mater. Sci. Tech. **20**, 940–950 (2004)
34. M. Nagumo, T. Yagi, H. Saitoh, Acta Mater. **48**, 943–951 (2000)
35. H. Yoshida, M. Nagumo, ISIJ Int. **38**, 196–202 (1998)
36. M. Nagumo, H. Yoshida, Y. Shimomura, T. Kadokura, Mater. Trans. **42**, 132–137 (2001)